NEW APPLICATIONS OF MICRO- AND NANOTECHNOLOGIES

NOI APLICAȚII ALE MICRO- ŞI NANOTEHNOLOGIEI

NEW APPLICATIONS OF MICRO- AND NANOTECHNOLOGIES

EDITORS:

MARIA ZAHARESCU, LIVIU GIURGIU, DAN DASCĂLU

EDITURA ACADEMIEI ROMÂNE
Bucureşti, 2009

The responsibility for originality and the contents
of the articles lies exclusively with the authors.

Address: EDITURA ACADEMIEI ROMÂNE
Calea 13 Septembrie nr. 13, sector 5,
050 711, Bucureşti, România,
Tel. 40-21-3188146, 40-21-3188106
Fax: 40-21-3182444
E-mail: edacad@ear.ro
Internet: http://www.ear.ro

Descrierea CIP a Bibliotecii Naţionale a României

New applications of micro- and nanotechnologies / Editors:
Maria Zaharescu, Liviu Giurgiu, Dan Dascălu. - Bucureşti :
Editura Academiei Române, 2009
ISBN 978-973-27-1576-xxx

I. Zaharescu, Maria (ed.)
II. Giurgiu, Liviu (ed.)
III. Dascălu, Dan (ed.)

xxxxxxxxxxx

Editorial assistant: Mihaela Marian
Computer operator: Ioana Plăviţu
Cover: Elena Trică, Mircea Ciocioc

Passed for press: 04.2009. Size: 16 / 70 × 100.
Printed sheets: 16.25
D.L.C. for large libraries xxxxxxxxx
for small libraries xxxxxxxxx

CONTENTS

FOREWORD

This volume, "New applications of micro-and nanotechnologies", is Number 14 in the "Micro-and nanoingineering" series, edited by the Publishing House of the Romanian Academy. This volume contains a number of papers selected from the programme of the 7th Annual National Seminar for Nanoscience and Nanotechnologies (Bucharest, 20th of March, 2008).

The papers published in this volume are original, written specially for this purpose. They are focused on a variety of subjects related to nanomaterials and nanotechnologies. In a few cases, they reflect the so-called "convergent technologies": micro-nano-bio-info, a domain of outstanding importance for a variety of applications. The reader will find in this volume a relevant image about the status of research of this field in Romania.

The Editors,

April 2009

Magnetic – Based Microfluidic Platform for Biomolecular Separation

Andrei AVRAM[1], Marioara AVRAM[1], Marius VOLMER [2], Daniel Puiu POENAR[3], Ciprian ILIESCU[4]

[1]National Institute for Research and Development in Microtechnologies (IMT), Bucharest, Romania
[2]University Transilvania Braşov, Physics Department, Romania
[3]Nanyang Technological University, Singapore
[4]Institute of Bioengineering and Nanotechnology, Singapore

Abstract. The motivation of the research work is to realize a spin valve array for manipulating, sorting and testing biomolecules. The spin valve arrays allow the application of torsion forces to a large number of individual biomolecules simultaneously. A novel microfluidic platform for manipulation of micro/nano magnetic particles was designed, fabricated and tested for applications dealing with biomolecular separation. At the present moment we are studying of the interaction of the magnetic particles used in biological applications with the GMR sensor. The fractional change in resistance, and hence the sensitivity, will be maximized by matching, as far as possible, the size of the sensor to the size of the beads and by carefully positioning the beads over the sensor. We found, by micromagnetic simulations, that the amount of surface coverage with magnetic particles may affect the magnetization curve of the sensor and will change the field dependence of his GMR response.

1. Introduction

In recent years there has been a great progress in applying microfabrication and soft lithographic techniques in the separation of biomolecules and in studying biosystems. The manipulation and sorting of biocells still poses unique challenges to microfabrication because of the complex physical properties of biological objects and their interaction with the surface and the designed structures in microfluidic devices. Lab-on-a-chip devices [1–3] are very attractive because they allow shrinking the entire chemical or biochemical assays down to small microfluidic chips. Cell separation is one of the most important steps in the study and prevention of diseases. Without cell separation many analyses would be impaired by the extremely high concentration of some cells in comparison to the other cell types. The actual cells separations methods are based on complicated procedure of mag-

netic beads labeling and centrifugation to separate blood cells, which is a time consuming procedure taking up several hours. There is a need for a system, which can collect, sort and manipulate different types of cells and measure the concentration of the clinically relevant species in continuous, real time fashion. Because GMR detectors can resolve single micrometer-sized magnetic beads [4–6] and are compatible with silicon technology, they can be easily integrated to build arrays of sensors able to detect different biological molecules [5, 7–9]. The bonding of the magnetic beads to the sites – GMR sensors – via the molecules to be detected has been described in many studies [4, 5]. Single molecule manipulation and measurement is desired because information that is obscured in ensemble measurements and statistical distribution can be probed when molecules are observed individually. On the other hand, magnetic tweezers, which trap magnetic microparticles in magnetic field gradients, can impart torque and torsional motion to the bio-molecules in addition to lateral movement. High gradient magnetic separation has advantages over existing cell separation methods; when it is implemented in a passive magnetophoretic microsystem that can be fabricated using established methods, it can be applied to different cells with the use of pre labeling with magnetic beads or using the native magnetic susceptibilities of the biosamples. It is faster than the actual magnetic separation methods and it doesn't need the use of a great quantity of material to be tested.

2. Theoretical considerations

A uniform external magnetic field applied normal to the plane is deformed near the spin valve, and generates a high gradient magnetic field, experienced by the magnetic particles moving around the spin valve. Therefore, cells flowing near the spin valve experience a magnetic force created by the high gradient magnetic field. The magnetic force on a magnetic cell placed in a buffer solution can be calculated as:

$$F_{BC} = -\frac{2k\mu_0\chi V_{BC}a^2}{r^3}\left[k\left(\frac{w}{h}\right)\frac{a^2}{r^2}+\cos 2\varphi\right]\left(\frac{w}{h}\right)H^2 a_r - \frac{2k\mu_0\chi V_{BC}a^2}{r^3}\sin 2\varphi\left(\frac{w}{h}\right)H^2 a_\phi,\ r>a$$

with:

$$k=\frac{\mu_w-\mu_B}{\mu_w+\mu_B}, \tag{1}$$

where χ is the relative magnetic susceptibility of a blood cell relative to the buffer solution; μ_w and μ_B are the permeability of the ferromagnetic wire and the buffer solution, respectively; V_{BC} is the volume of the blood cell; a is the radius of a circular ferromagnetic wire; r and φ are the cylindrical coordinates of the distance and

angle; H is the external magnetic field; and a_r and a_φ are unit vectors for the distance and angle in the cylindrical coordinate.

If the wire is magnetically saturated, the first term of the magnetic force in equation (1) is independent of the external magnetic field, H, and proportional to the square of the saturation magnetization field. The second and third terms of the magnetic force are linearly proportional to the magnetization field saturation and the external magnetic field.

For magnetic particles placed on the x-axis ($\varphi \approx 0$), $\sin 2\varphi \approx 0$, $\cos 2\varphi \approx 1$, the ferromagnetic wire attracts paramagnetic particles and repels diamagnetic particles. For magnetic particles placed on the y-axis ($\varphi \approx 90$), $\sin 2\varphi \approx 0$, $\cos 2\varphi \approx -1$, the wire attracts diamagnetic particles and repels paramagnetic particles. The first geometric configuration has been called the paramagnetic capture (PMC) mode; the latter has been called the diamagnetic capture (DMC) mode.

To summarize, the main parameters that influence the magnetic force applied on the particles affected by an external magnetic field are: the intensity and orientation of the magnetic field H; the permeability of the buffer solution and the ferromagnetic wire; the susceptibilities of the cells and the buffer solution and the dimension of the device and of the cells.

In order to pump and precisely control small volumes of sample, micropumps need to be integrated into miniaturized total analysis systems (μTAS). Microfabricated pumps are shown to generally fall into one of two main categories [4]. The "displacement pumps" exert pressure forces on the working fluid through one or more moving boundaries. The "dynamic pumps" continuously add energy to the working fluid in a manner that directly increases either its momentum or its pressure. Magnetohydrodynamic (MHD) micropumps fall into the "dynamic pumps" category. They operate without moving parts, and require only low voltages (less than 10 V) for their actuation. The liquid flow does not depend on the chemical nature of the capillary surface unlike in electro-osmotic flow. Forward and reverse flows are possible by changing the voltage or magnetic field polarity. It is for all these reasons that MHD pumping has attracted a growing interest for the handling of conductive fluids in microchannels over the past few years. The operating principle of the MHD pumps is based on the Lorentz force, F_L, which is acting on charged species that are moving in a magnetic field. When a current is flown across the width of a microchannel filled with an electrolyte solution, the Lorentz force exerts a body force on the fluid that is proportional to both the current density j in the liquid and the magnetic flux density B which is perpendicular on the current density in order to obtain a maximum efficiency [4]:

$$\vec{F}_L = \vec{j} \times \vec{B} \cdot V_D, \tag{2}$$

where V_D is the device volume (the active part, through which the current is flowing). It is assumed that B is homogeneous, j is constant, the bulk solution is elec-

troneutral, and that the Hartmann number is close to zero (poor conductivity of the medium, compared to metals or plasma fluids). The flow along the length of the channel resulting from the Lorentz force has a flow profile similar to that of pressure-driven flow, and obeys Poiseuille law in microchannels [4]:

$$\Delta P = Q \cdot R_{hy} = \frac{F_L}{A} = j \cdot B \cdot l \,, \tag{3}$$

where ΔP is the pressure drop in the channel, Q is the volumetric flow rate, R_{hy} is the hydraulic resistance of the channel, A is the channel cross-section, and l is the length of the channel along which the current is applied across it. Generally l does not equal L, the total length of the channel. R_{hy} depends on the channel geometry (channel length L and the cross-section shape) and the fluid viscosity, η. For example, if the channel has a semi-circular cross-section, R_{hy} is expressed by [4]:

$$R_{hy} = \frac{127\eta L}{3\pi h^4}, \tag{4}$$

where h is the height of the channel. Usually, the maximum flow rate which can be obtained with these kinds of pumps is about 63 μl/min, corresponding to a pressure difference of 170 Pa in the capillary [4, 5].

An experimental MHD device made by the authors will be presented in the next section.

The fluid which is actuated by the MHD micropump can be a carrier of magnetic beads labelled with different biological structures. Detection of such small magnetic fields generated by magnetic particles encapsulated in plastic, carbon or ceramic spheres which are coated with chemical or biological species such as DNA or antibodies that selectively bind to the target analysed can be made using giant magnetoresistive effect (GMR) or Hall effect sensors. Because GMR detectors can resolve single micrometer-sized magnetic beads [6–8] and are compatible with silicon technology, they can be easily integrated to build arrays of sensors able to detect different biological molecules [7, 9–11]. The bonding of the magnetic beads to the sites – GMR sensors - via the molecules to be detected has been described in many studies [6, 7] and is showed schematically in Fig. 1.

The magnetic microbeads and the GMR sensors will be coated with identical probes such as DNA or antibodies which are specifically bonded together by the molecule to be analyzed. The microbeads in suspension were allowed to settle onto the GMR sensor array where specific beads bonded to specific sensors only if the probes were designed to attract each other. Nonbinding beads can be removed by applying a small magnetic field. The beads are then magnetized by a DC or an AC electromagnet and detected by the GMR sensors. The microbeads are made up of nm sized iron oxide particles that have little or no magnetization in the absence of an applied field.

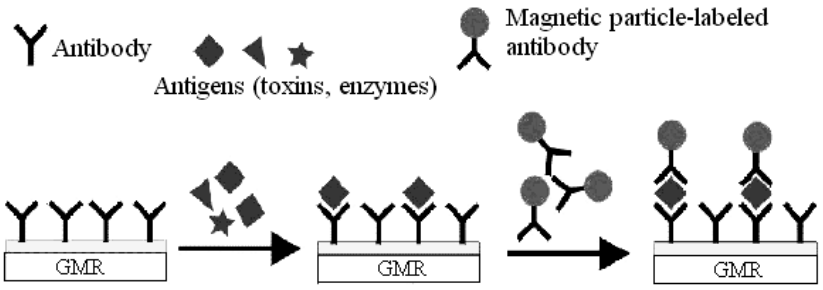

Fig. 1. Antigens are detected by flowing them over a sensor coated with antibodies to which they bind. The magnetic particle-labeled antibodies then bind to the antigens providing a magnetic indication of the presence of those antigens.

The field generated by the beads is proportional to the volume of magnetic material and inversely proportional to the cubed distance from the bead to the sensor. Basically two detection schemes can be used: (i) the external magnetic field is applied parallel to the GMR sensor and (ii) the magnetic field is applied perpendicular on the GMR sensor which will detect the in-plane component of the field produced by the beads. In both cases a differential measurement setup has to be used in order to extract, from the total field, the contribution corresponding due to the magnetic moment of the beads and to avoid the influence of other external magnetic fields and thermal variations.

3. Device Design

The structure of the device is presented in Fig. 2. A glass die with inlet/outlet holes and a 60 μm deep microfluidic channel is bonded to another glass die, on which a magnetic platform consisting of magnetic tweezers and spin valves array was patterned. A permanent magnet generates an external magnetic flux of 0.2 T perpendicular on the flow direction. Potential advantages of this design include the ability to manipulate both ends of the molecules, the capability to sort and probe a large number of molecules, and the potential to apply torsional forces to a large number of individual biological molecules simultaneously.

4. Numerical Simulations

In this paper we report the micromagnetic simulation regarding the sensor behaviour for both orientations of the applied magnetic field. First we shall consider the case when the magnetic field is applied parallel to the GMR sensor and the magnetic beads are located above the sensor as sketched in Fig. 2. The stray field produced by the beads will change the effective field inside the GMR sensor

and will affect the field behaviour of the GMR effect. Using a differential setup, i.e., a second GMR sensor which is placed in the same external applied field, H, we can extract the change of the GMR response due to the stray field produced by the beads. In our simulations regarding the sensor response we'll assume a total thickness of the layers (immobilization layer and protection layer – Si_3N_4) between the bead and the GMR sensor of 0.2 μm.

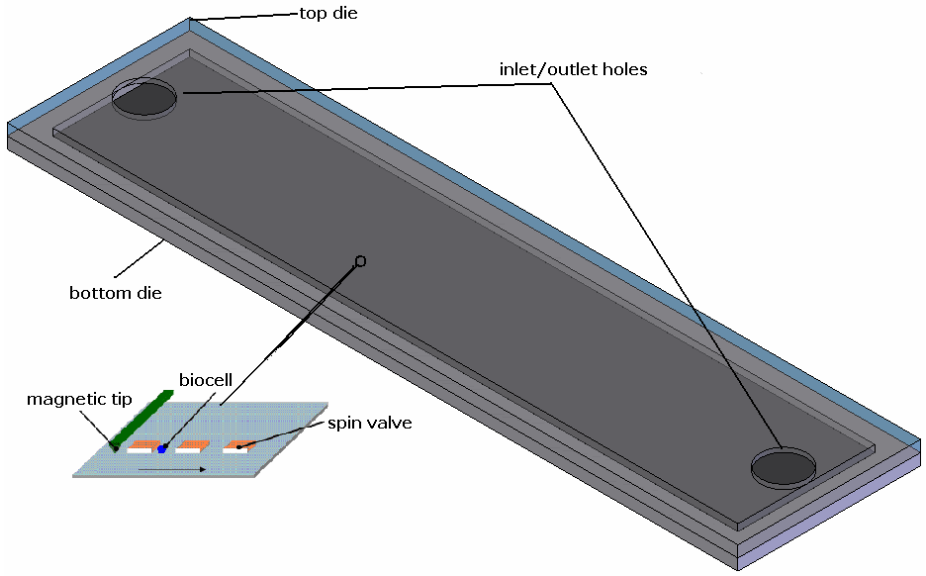

Fig. 2. Schematic view of the microfluidic device.

Each bead is assumed to be a sphere with a diameter of about 0.2 μm. Because the magnetization of magnetite is lower by a factor of 2–3 than for other ferromagnetic materials (e.g. cobalt or iron) [5], we assumed, in our simulations, for the saturation magnetization of the micro-magnetic bead a value of 400 emu/cm^3 (the saturation magnetization for Co is 1300 emu/cm^3). The GMR sensor is a multilayer structure FeMn/$Ni_{80}Fe_{20}$ (10 nm)/Cu(4 nm) $Ni_{80}Fe_{20}$(10 nm). To simulate the magnetic behaviour and the GMR response of such a multilayer film, we take a square region of 1×1 μm^2. Each magnetic layer of this region was divided into 10×10 single domains of $Ni_{80}Fe_{20}$, 10 nm thick and 95 nm each side, Fig. 3. The distance between the adjacent domains is d = 5 nm which is equivalent with an inter-grain spacing [10]. The distance between this two ferromagnetic layers is set to be equal with the real interlayer thickness, t_{Cu} = 4 nm. The coupling constant, for t_{Cu} > 1.5–2 nm, is well described by the Néel model for positive magnetostatic interlayer coupling [10, 11] and the resulting coupling field is H_0 = 2 457 A/m (31 Oe) for our system. Because of NiFe bridges that exist trough the spacer, in real structures, the coupling may have local variations that exceed 31 Oe [11]. Be-

tween the top and the bottom layers we introduced coupling fields that have random values from 30 to 60 Oe. The pinning field between the FeMn layer and the NiFe(10 nm) layer was set at H_{pin} = 200 Oe, a value which is consistent with experimental data.

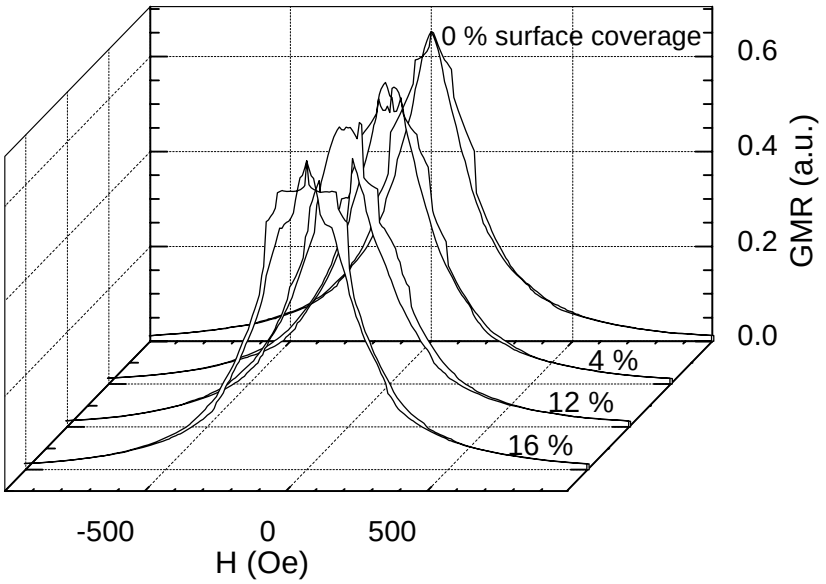

Fig. 3. The field dependence of the GMR effect for different amounts of the surface coverage with magnetic particles. The field is applied in the film plane over the easy axis.

The uniaxial anisotropy field is perpendicular on the pinning field and the value was fixed at H_K = 5 Oe. The beads are placed above the centre of the free layer at distance of 200 nm from its surface. They are equally spaced. In our simulations the distance between the nearest beads is 200 nm. Applying the magnetic field in the film plane over the easy axis, like in Fig. 2, we obtained by micromagnetic simulations [10, 12], the GMR response for different number of beads placed above the sensor. The data is plotted in Fig. 3 and the results are presented in terms of surface coverage with magnetic beads. Taking into account the dimension of the considered region (1 μm^2) and the bead dimension we get 4 % surface coverage for 1 bead, 12 % for 3 beads and 16 % for 4 beads respectively. When the magnetic field is applied upon the easy axis, the magnetization from the free layer will reverse at a value which is dependent on the anisotropy field, the coupling field and the strength of the magnetostatic interaction between the free layer and the magnetic beads. The presence of the magnetic beads above the sensor will bring an additional field, H_{bead}, which alters the *GMR* response. These perturbations can be seen using a reference sensor in a differential setup. The output of the differential setup is presented in Fig. 4.

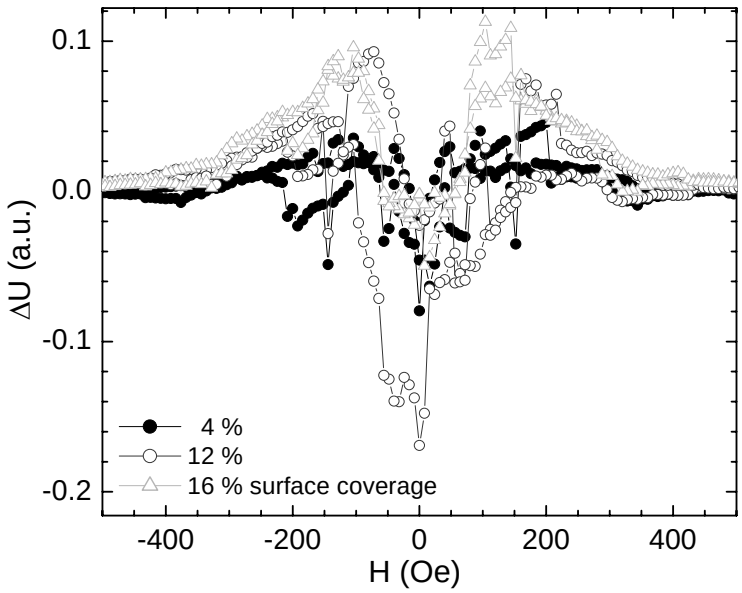

Fig. 4. The output of the differential setup for different amounts of the surface coverage with magnetic particles. The field is applied in the film plane over the easy axis.

Because the output voltage, ΔU, depends on some parameters like the amplitude of the GMR effect, the resistance value of the GMR sensors, the driving currents through the sensors and the gain of the instrumentation amplifier, the vertical axis is quoted in arbitrary units (a.u.). Our simulations revealed the fact that the positions of the low field peaks, depend on the surface coverage ratio with magnetic beads. For this reason the best detection method is to sweep the magnetic field between the limits illustrated in Fig. 3 and Fig. 4, i.e. to perform a complete magnetization curve. However, these simulations reveal the fact that it is difficult to extract a signal which can be a measure of the magnetic moment because what is changed is mainly the shape and not the amplitude of field dependence of the GMR effect. This is because the external magnetic field, which is applied in the film plane, is much higher than the contribution of the stray field produced by the beads.

Now, we shall consider the case when the magnetic field is applied perpendicular to the sensor surface. Because of the high value of the demagnetizing coefficient over this direction, the magnetic moments remain in the film plane and magnetization curve shows a line with a very small slope. For this reason, the GMR effect is field insensitive in this case. When magnetic beads are located over the sensor, like in Fig. 2, the horizontal component of the stray field, generated by them, can change the magnetic state of the sensor and hence can produce a GMR effect. However, for a large number of particles, located over the centre of the sensor, the horizontal components of the stray fields will cancel each other and will be a very weak GMR response as we can see in Fig. 5.

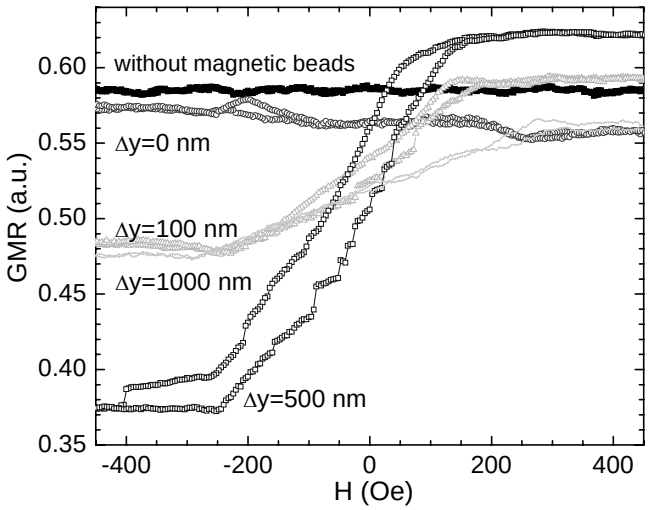

Fig. 5. The field dependence of the GMR effect, for different positions of the magnetic beads, when the field is applied perpendicular to the film surface.

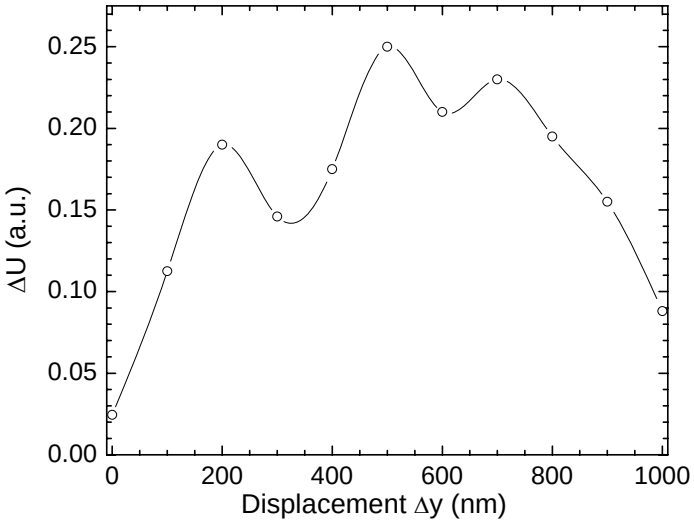

Fig. 6. The output of the differential system upon the position, Δy, of the particles ensemble relative to the centre of sensor. The field is applied perpendicular to the film surface.

Now, if the ensemble of particles, as sketched in Fig. 2, is moved from the centre toward the margin of the sensor, following the y direction, the horizontal components of the stray fields will not cancel entirely and an increases of the net field applied in the film plane is expected. A GMR response will appear as we can

see in Fig. 5, for three values, Δy = 100, 500 and 1000 nm, of the ensemble displacement relative to the sensor centre. It is important to emphasis the fact that taking into account the geometry presented in Fig. 2, the horizontal components of the stray fields will be directed over the hard direction of magnetization and will produce a smooth variation of the GMR effect. The output of the differential system depends on the position Δy of the particles ensemble relative to the centre of sensor and is plotted in Fig. 6. As is expected the maximum sensitivity is achieved for Δy = 500 nm. The secondary peaks seams to appear because of the discrete structure made by magnetic beads distributed uniformly inside. The advantage of this configuration, i.e. magnetic field applied perpendicular to the sensor surface, is a net GMR response when magnetic beads are presented and located in a position for which is achieved a maximum sensitivity. For this position we can plot, Fig. 7, the dependence of the output signal (the amplitude of differential signal due to GMR effect for a loop field scan) in function of the number of magnetic beads. Taking the above specified data, we can estimate a value of the magnetic moment at saturation, $m_b = 1.67 \cdot 10^{-12}$ emu/magnetic bead. It is natural to assume a small number of magnetic particles located over a surface of 1 μm^2 of the sensor.

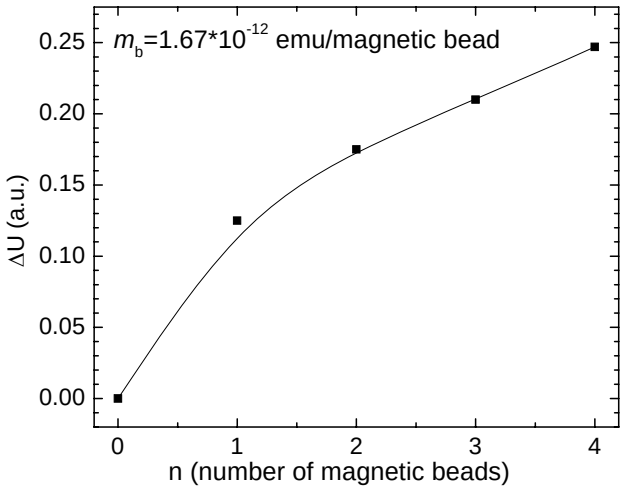

Fig. 7. The dependence of the output signal, ΔU, in function of the number of magnetic beads located over the sensor. The field is applied perpendicular to the film surface.

Obviously, the results of these micromagnetic simulations can be extended by multiplying the selected 1 μm^2 region to the entire sensor. In conclusion, we performed micromagnetic simulations regarding the response of the GMR sensor covered with magnetic beads used for biomedical applications. We found that a net signal can be obtained when the magnetic field is applied perpendicular on the film surface and the beads are located in a given position for which a maximum sensi-

tivity is achieved. From these simulations, Fig. 7, a calibration curve can be build in order to perform quantitative measurements.

Figure 7 presents the calculated temperature dependence of the reverse current. Symbols used in the table are the generation, diffusion, surface, and respectively, tunnelling components of the reverse current density at two reverse bias voltages, 500 V and 700 V. The reverse bias considered in Fig. 7, is $V_R = -10$ V. For comparison, experimental data are shown. As it is seen, the generation in the space charge is dominant up to a temperature of 1000K, when the current density approaches the limit of 10^{-2} A/cm^2. In spite of the high electrical field in the junction, the tunnelling component is still negligible in this temperature range.

5. Device fabrication

By exploiting the surface micromachining and applying functionalization of the surfaces to generate controlled hydrophobicity, we have developed a smart microfluidic system capable of sampling, dispensing, sorting and delivering biological fluids to the sensing unit. The microdevice (Fig. 1) contains: microchannels with input and output reservoirs for fluid transport and a microfluidic platform that can trap, measure, manipulate and sort magnetic marked biomolecules in an array of magnetophoretic spin valves. The fabrication process of the device consists of three important steps: fabrication of the top wafer with the inlet/outlet holes and the microfluidic channel, fabrication of the bottom wafer with ferromagnetic concentrators and assembling of the wafers.

The fabrication of the top wafer is presented in Fig. 8. A 4" glass wafer Corning 7740 was used. A Cr/Au/ photoresist masking layer (Fig. 8a) was used for the fabrication of the microfluidic channel. A wet etching process in HF/HCl was used for 60 μm deep-etching in glass (Fig. 8b). During the wet etching process the backside of the wafer was protected by a dummy silicon wafer bonded with wax on the glass wafer. The debonding of the wafer was performed on a hot plate. After removing of the Cr/Au/photoresist mask (Fig. 8c) using classical resist stripper (NMP) – for photoresist and residual wax and Au and Cr etchants, a second Cr/Au/photoresist mask was applied on the other surface of the glass wafer (Fig. 8d). Similar, a second wax bonding process will assure the protection of the microfluidic channel, while the wax served also as etch-stop layer for the deep wet etching process in HF/HCl (Fig. 8e). Finally, the glass wafer was debonded from the dummy silicon wafer and the masking layer was removed with a similar procedure as was described before.

The fabrication of the bottom wafer consists of a simple lift off process presented in Fig. 9. On a 4" glass wafer (Corning 7740) a 5 μm-thick photoresist mask (AZ4620 from Clariant) was deposited (Fig. 9a). The metal layer Ti/Ni (50 nm/2 μm) was deposited in a CHA e-beam evaporator – (Fig. 9b). The photoresist masking layer was finally removed in an ultrasonic bath using acetone.

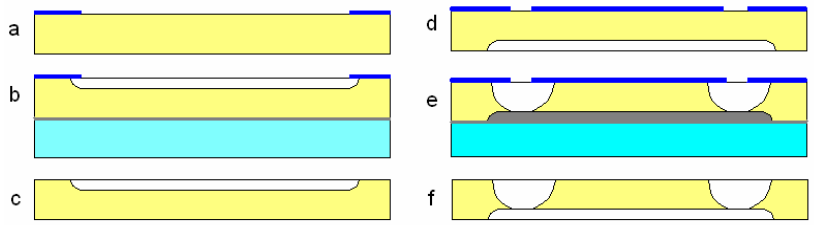

Fig. 8. Main steps of the fabrication process of the top wafer: a) processing of the Cr/Au/ photoresist masking layer, b) wet etching of the microfluidic channel, c) removing of the masking layer, d) processing of the Cr/Au/photoresist masking layer for inlet/outlet holes, e) wet etching of inlet/outlet holes, f) removing of the second masking layer.

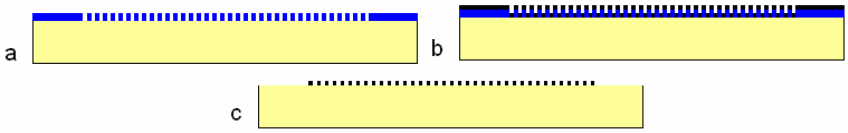

Fig. 9. Main steps of the bottom wafer fabrication process: a) deposition of the photoresist mask, b) deposition of Ti/Ni layer, c) removing of the photoresist mask.

For the assembling of the glass wafers a simple adhesive bonding, using SU8-5, photoresist process was used. The technique consists of imprinting of an SU8-5 layer initially spun on a dummy silicon wafer (Fig. 10a) on a Teflon cylinder (Fig. 10b) and transferring further the adhesive from the cylinder to the top glass wafer (Fig. 10c). This contact imprinting technique allowed deposition of a thin adhesive layer only on the bonding regions. In the last step, the wafers are manually align and bonded at 150ºC for 30 minutes with an applied pressure of 1000 N (Fig. 10d).

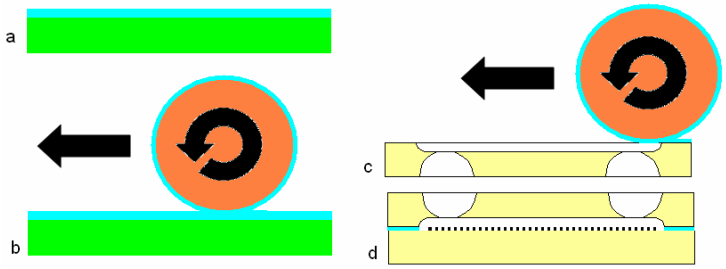

Fig. 10. Assembling of the wafers: a) deposition of SU8 on a dummy wafer, b) imprinting of the SU8 on a Teflon cylinder, c) imprinting SU8 on the bonding area, d) alignment and bonding.

Finally, the wafer is diced. An image of the fabricated device is presented in Fig. 11. The dimensions of the chip are 32 mm×9 mm.

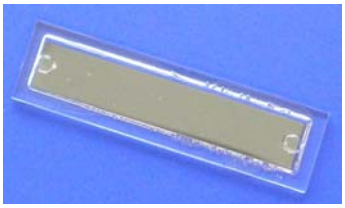

Fig. 11. Photo of the microfluidic chip for RBCs trapping.

The microfluidic platform consists of an array of spin valves so that many biomolecules can be manipulated simultaneously (Fig.11). A spin valves array that can be switched between bistable states is integrated in the microfluidic device, in order to provide a local magnetic field gradient large enough to trap magnetic particles, to capture and sort biological molecules for gene sequencing or bioassay applications. The spin valve has a twelve layer composition [22]: 5 nm Ta/ 15 nm $Ni_{80}Fe_{20}$/5 nm Co/10 nm CuAuAg/5 nm Co/15 nm $Ni_{80}Fe_{20}$/5 nm FeMn/ 5 nm T.The multilayer is patterned to make structures 2 μm wide and 4 μm long with variable spacing depending on the dimension of the biomolecule to be studied. The first Ta layer promotes the adhesion of the structure to the surface and the last Ta layer acts as a barrier to oxidation and to provide an ohmic contact. The Co layer has a double purpose: diffusion barrier between the $Ni_{80}Fe_{20}$ and the Cu spacer; the interface Co/Cu gives a higher GMR ratio. To the Cu layer was added small quantities of Ag(5%) and Au(5%). Both silver and gold atoms have significantly higher mobility than copper atoms. Au is incorporated in the bulk of Cu lattice, whereas Ag tends to segregate upon the free surface, enhancing its potency as a boundary layer. Au and Ag reduce the Ehrlich – Schwoebel barrier for Cu promoting a sequential flow growth mode [23].

6. Results and discussions

6.1. DC MHD micropump

The MHD micropump presented here is made in glass, and is operated in the DC mode using a permanent magnet. This solution reduces power consumption and reduces heating effects which appear when electromagnets are used. On the other hand, the use of AC electromagnets can produce induction heating effects in biological solutions. This pump is intended to be integrated together with planar coils and GMR sensors in a microfluidic system, part of a lab-on-chip analysis solution. The channel was processed using photolithography processes in a clean room. A NdFeB rare earth permanent magnet was used to create the magnetic field. The structure of the MHD pump is presented in Fig. 12.

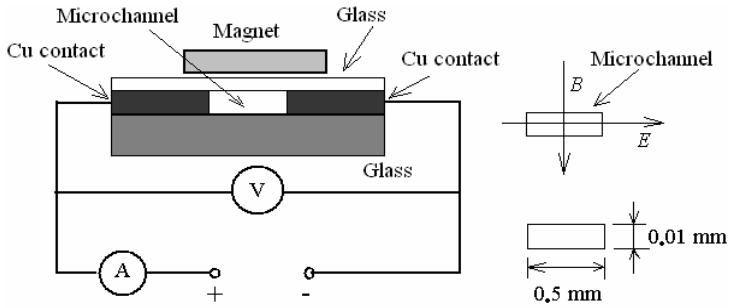

Fig. 12. Schematic diagram of the as build MHD micropump. Here, $l = L = 5$ mm and $B = 0.022$ T inside the micro channel.

Using the above setup, for a DC supply voltage of 3 V and a current of about 0.5 mA through the fluid, the measured flow rate was $2.5 \cdot 10^{-3}$ mL/min. As a working fluid was used buffer matrix (natrii chloridum).

6.2. Detection of magnetic particles employed in biological applications

In this subsection we describe the detection of different biological structures labelled with magnetic beads. First we shall consider the case (i) when the magnetic field is applied parallel to the GMR sensor and the magnetic beads are located above the sensor as sketched in Fig. 13a. The stray field produced by the beads will change the effective field inside the GMR sensor and will affect the field behaviour of the GMR effect. Using a differential setup, presented in Fig. 3b, and a second GMR sensor which is placed in the same external applied field, H, we can extract the change of the GMR response due to the stray field produced by the beads [13, 14]. The driving voltage, U_C, sets constant currents, $I_1 = U_C/R_1$, $I_2 = U_C/R_2$, through the sensors GMR1 and GMR2. From basic electronics, we have for the output voltage that is applied to the data acquisition system the expression:

$$\Delta U = A_I\left[\left(U_{GMR1} + U_C\right) - \left(U_{GMR2} + U_C\right)\right] = A_I\left[U_{GMR1} - U_{GMR2}\right] = f\left(H_{bead}\right), \quad (4)$$

where H_{bead} denotes the strength of the stray field generated by the magnetic beads in the sensor region and A_I is the gain of the instrumentation amplifier, A.I., which can be set using digital signals or a resistor, R_G. Because our design is to integrate on the same substrate the electronics and the GMR sensors, the A.I. uses a resistor to set the gain.

In our simulations regarding the sensor response we'll assume a total thickness of the layers (immobilization layer and protection layer – Si_3N_4) between the bead and the GMR sensor of 0.2 μm. Each bead is assumed to be a sphere with a diameter of about 0.2 μm. Because the magnetization of magnetite is lower by a factor of 2–3 than for other ferromagnetic materials (e.g. cobalt or iron) [7], we

assumed, in our simulations, for the saturation magnetization of the micro-magnetic bead a value of 400 emu/cm^3 (the saturation magnetization for Co is 1300 emu/cm^3).

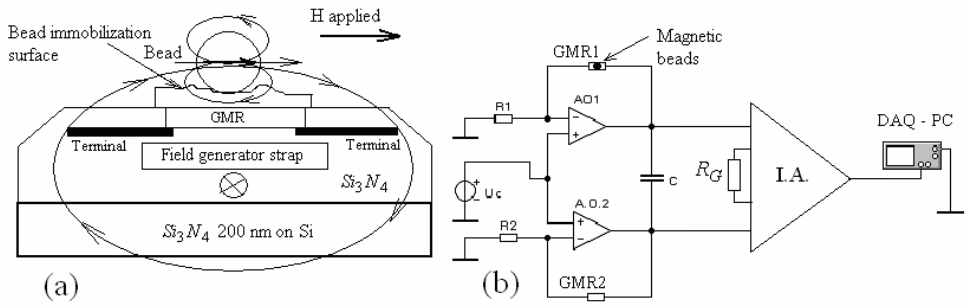

Fig. 13. (a) The schematic setup for a GMR sensor that detects the stray field generated by a bead and (b) the differential measurement setup used to measure the stray field produced by the magnetic bead. The sensor GMR2 is used as reference. The magnetic field is applied parallel with the sensor surface.

Diluted blood (1:20 in PBS) was used for testing purpose. The permanent magnet creates an external magnetic flux of 0.2 T and the flow rate was set in the range between 0.5 and 0.7 ml/h (using a peristaltic pump). Two connectors fabricated by polymer printing secured the inlet and outlet connections. The results are based on the analysis of the quantity of red cells collected at the output of the device. Experimental results show an average of 5% of red blood cells collected at the output of the device. Figure 14 presents the image with the field densities of cells before and after flowing the sample through the microfluidic device.

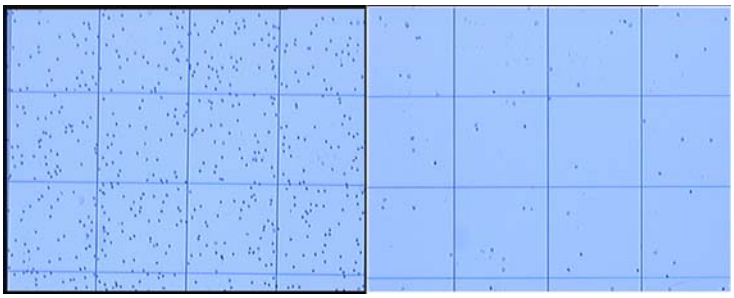

Fig. 14. Image of the field density of the cells on Neubauer hemocytometer before and after flowing the blood sample through the microfluidic device.

The magnetic field gradient is used in the magnetic force determination. As in the case of the magnetic field the force can be separated in two components, F_x and F_y, which act, respectively, in the flow direction and perpendicular to the flow, being responsible for cell separation.

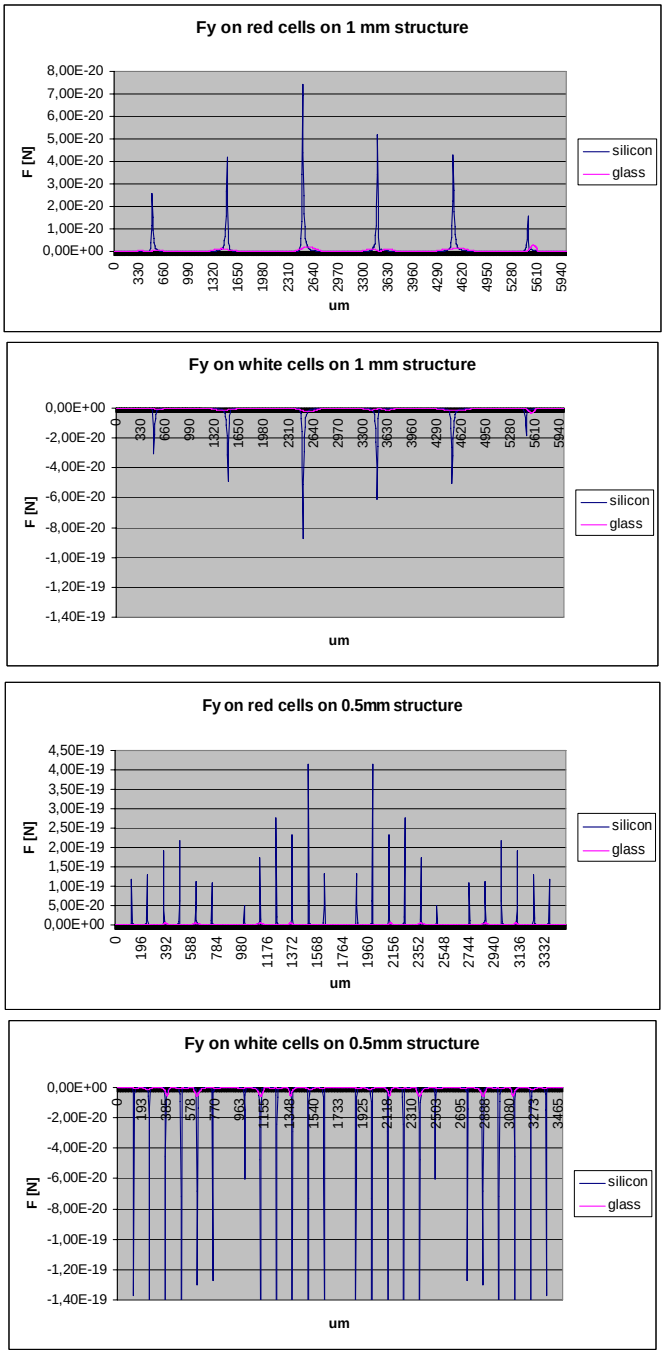

Fig. 15. F_y force component on red and white cells in 1 mm and 0.5 mm structure.

References

[1] FIGEYS D., PINTO D., Anal. Chem. **72** (9) (2000) 330A–335A.
[2] GIJS M. A. M., Microfluidics Nanofluidics 1, 22–40 (2004), DOI 10.1007/s10404-004-0010-y.
[3] *Microfluidics and Their Applications to Lab-on-a-Chip*, in Springer *Handbook of Nanotechnology*, edited by Bharat Bhushan, Springer Verlag, 2004, ISBN 3-54-001218-4, pp 270–277.
[4] TONDRA M.,. PORTER M,. LIPERT R. J, Journal of Vacuum Science & Technology A: Vacuum, Surfaces, and Films **18**(4) (2000) 1125-1129.
[5] SCHOTTER J., KAMP P.B., BECKER A., PÜHLER A., REISS G.,. BRÜCKL H, Biosensors and Bioelectronics **19** (2004) 1149–1156.
[6] BRZESKA M., PANHORST M., KAMP P. B., SCHOTTER J., REISS G., PÜHLER A., BECKER A., BRÜCKL H., Journal of Biotechnology **112** (1–2) (2004) 25–33.
[7] KRICKA L.J., Clin. Chim. Acta **307** (2001) 219–223.
[8] MILLER M.M., SHEEHAN P.E., EDELSTEIN R.L., TAMANAHA C.R., ZHONG L., BOUNNAK S., WHITMAN L.J., COLTON R.J., J. Magn. Magn. Mater. **225** (2001) 138–144.
[9] FERREIRA H. A., GRAHAM D. L., FREITAS P. P., J. Appl. Phys. **93** (10) (2003) 7281.
[10] MILLER M.M., SHEEHAN P.E., EDELSTEIN R.L., TAMANAHA C.R., ZHONG L., BOUNNAK S., WHITMAN J., COLTON R.J., J. Magn. Magn. Mater., **225** 138 (2001).
[11] FERREIRA H. A., GRAHAM D. L., FREITAS P. P., J. Appl. Phys., **93** (10) 7281 (2003).
[12] OTI J. O. in: *SimulMag Version 1.0*, *Micromagnetic Simulation Software*, *User's Manual*, Electromagnetic Technology Division, National Institute of Standards and Technology Boulder, Colorado 80303, December 1997.
[13] VOLMER M., AVRAM M., Journal of optoelectronics and advanced materials, **9**(6) 1808 (2007).
[14] VOLMER M.,. AVRAM M., *Detection of Magnetic-Based Bio-Molecules using MR Sensors*, accepted to be published in AIP Conference Proceedings, 2008.
[15] ILIESCU C., JING J., TAY F. E. H., MIAO J., Sun T. T., *Characterization of masking layers for deep wet etching of glass in an improved* HF/HCl *solution*, Surf Coatings Technol. 198/1–3:314–318 (2005).
[16] ILIESCU C., YU L., XU G., TAY F. E. H., *A dielectrophoretic chip with a* 3D *electric field gradient*, J.Microelectromech Syst **15**/6:1506–1513 (2006).
[17] ILIESCU C., XU G., LOE F., ONG P. L., TAY F. E. H., *A 3 dimensional dielectrophoretic filter chip*, Electrophoresis 28 /7: 1107–1114 (2007).
[18] ILIESCU C., CHEN B., MIAO J., *On the wet etching of Pyrex glass*, S& A, **A 143**/1: 154–161 (2008).
[19] INGLIS D. W., RIEHN R., AUSTIN R. H., STURM J. C., *Continuous microfluidic immunomagnetic cell separation*, Appl. Phys. Lett. **85**/21:5093–5095 (2004).
[20] INGLIS D. W., RIEHN R., STURM J. C., AUSTIN R. H., *Microfluidic high gradient magnetic cell separation*, J. Appl. Phys. **99**/8:08K101 (2006).
[21] POENAR D. P., ILIESCU C., CARP M., PANG A. J., LECK K. J., *Glass-based microfluidic device fabricated by Parylene wafer-to-wafer bonding for impedance spectroscopy*, S&A, **A 139**/1–2:162–171 (2007).
[22] RAMADAN Q., YU C., SAMPER V., POENAR D. P., *Microcoils for transport of magnetic beads*, Appl. Phys. Lett. **88**/3: 032501 (2006).
[23] M. AVRAM, J. Optoel. Adv. Materials, 6, 987–990 (2004).

On the Bending and Torsion of Carbon Nanotubes Ropes

Veturia CHIROIU[1], Ligia MUNTEANU[1],
Viorel Puiu PAUN[2], Petre P. TEODORESCU[3]

[1]Institute of Solid Mechanics of the Romanian Academy
C-tin Mille Street, No. 15, Bucharest 010141
E-mail: veturiachiroiu@yahoo.com
[2]University Politehnica, Bucharest
E-mail: paun@physics.pub.ro
[3]University of Bucharest, Faculty of Mathematics, Bucharest
E-mail: petre_teodorescu@hotmail.com

Abstract. This paper presents some results concerning the applicability of carbon nanotubes to the space elevator concept. After the development of carbon nanotubes in the 1990s, the high strength of these materials made the concept of an orbital skyhook feasible. A coupled atomistic-continuum theory for describing the bending and torsion of ropes made from single-walled carbon nanotubes is proposed in this article. The model couples a region described with full atomistic detail to a surrounding region modeled with the continuum concepts. The shifted Chebyshev polynomials of the second kind and a generalization of Vekua and Nikagadze methods are performed on the base of a nonclassical parametrization of the transition region.

1. Introduction

The concept of the space elevator was introduced by russian scientist Konstantin Tsiolkovsky in 1895, based on the Eiffel Tower in Paris. This space elevator must be able to launch objects into orbit without a rocket. The Tsiolkovsky's concept is a compression structure, rather than a tension structure. After the development of carbon nanotubes in the 1990s, it was realized that the small dimensions, strength and remarkable mechanical properties of carbon nanotubes make them a very unique material which might make the concept of an orbital skyhook feasible [1]–[4].

The carbon nanotube was discovered in 1991 as a direct consequence of the synthesis of buckminsterfullerene, C_{60} and other fullerenes [5], [6]. These cylindrical carbon molecules, which exhibit extraordinary strength properties, are one of the most promising building blocks for future development of functional nanostructures. The carbon nanotubes have novel properties that make them potentially use-

ful in a wide variety of applications in nanotechnology, and other fields of material science [7]–[11]. Carbon nanotubes have the potential to be 100 times stronger than steel and are as flexible as plastic. Once scientists are able to make fibers from carbon nanotubes, it will be possible to create threads that will form ropes for the space elevator.

To identify the types of single wall carbon nanotubes we refer to rolling up the graphene sheet. The geometric parameter associated with this process is the roll-up vector r, which is a linear combination of the lattice basis a and b, with (n,m) a particular integer pair (Fig. 1.1)

$$r = na + mb.$$

For $m = 0$, we have the zigzag form, for $n = m$, the armchair form, and for other, chiral. Fig. 1.2 shows some carbon nanotubes.

Advances in multi-scale computational methods for nanostructured materials are made by coupling the continuum-models with more-realistic details at quantum and atomistic scales [12], [13]. In atomistic case, there is no direct consideration of the continuum concepts of strain or displacement. The motion of individual atoms is followed without reference to their original positions, and the occurred deformations may violate many assumptions about the continuity of deformations.

The methods at the atomic-scale is governed by quantum mechanics [14]–[16]. The total energy is a function of the all coordinates, which are the electronic degrees of freedom. The energy functional is minimized with respect to the electronic degrees of freedom for fixed coordinates. The force on an individual nucleus is obtained by the derivative of the total energy with respect to the considered coordinate. The total atomic energy E^a can be expressed as a sum of individual atom energies [10]:

$$E^a = \sum_i E_i^a \,, \tag{1.1}$$

where E_i^a is the energy of an atom i.

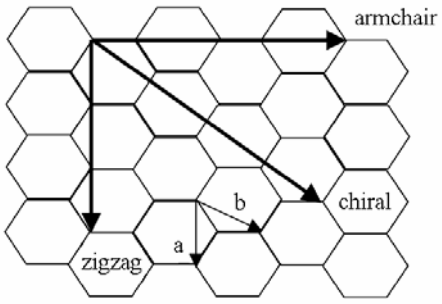

Fig. 1.1. The roll-up vector.

Continuum mechanics assumes that, for a material, there exists a strain energy density functional W, and the energy in a volume $\mathrm{d}V$ around point X is $W(X)\mathrm{d}V$. The overall potential energy of the material is then an integral over the volume Ω of the body:

$$E^c = \int_{\Omega} W(X)\mathrm{d}V, \tag{1.2}$$

If X is a point in the undeformed state of the body, by some applied forces or imposed displacements on the body, the point X moves to the point x. The displacement referenced to the original state of the body $u(X) = x - X$. The difference $\mathrm{d}x - \mathrm{d}X$ describes the local deformation with reference to X. The deformation gradient is:

$$F(X) = x_{,X} = I + \nabla u(X), \tag{1.3}$$

where ∇ is the gradient with reference to X. The Lagrangian strain is given by:

$$E = 1/2(F^T F - I), \tag{1.4}$$

which becomes $\varepsilon = 1/2(\nabla u + (\nabla u)^T)$, for the infinitesimal deformations.

Fig. 1.2. Carbon nanotubes.

The locality of $W(X)$ implies that the strain energy density at X is equal to the strain energy per unit volume of an infinite perfect crystal deformed according to a homogeneous deformation gradient $F(X)$. The locality of $W(X)$ is a key assumption for constructing the coupled methods, because the real atomistic energy is nonlocal. When ∇F is large, the nonlocality plays an important role and the local $W(X)$ cannot describe this nonlocality. When $W(X)$ is calculated in the continuum model, it does include the nonlocality of atomic interactions, by assuming

of a homogeneous deformation around any given element, and not rather than considering the true inhomogeneous deformation.

To determine the equilibrium strain field for applied forces and displacements in the body, the energy E^c must be minimized. The transition or boundary region between the atomistic and continuum regions is a very important aspect of the modeling. At the interface between the atoms and the nodes of the continuum region, we construct a one-to-one correspondence with the aid of the Chebyshev polynomials of the second kind [17]–[19].

The concept of length scale is important in studying the damping because damping is working different at different length scales. The decoupling of different length scales makes it possible to have a self-consistent theory for damping that only describes the relevant length scales for a given problem.

The spatial scales may run from angstroms to centimeters (range of 10^8). In quantum mechanics the length scale of a given phenomenon is related to its de Broglie wavelength $l = h/p$ where h is the reduced Planck's constant and p is the momentum. At the microscopic level, the typical bond distance between atoms is of the order of Ångstroms (the lattice constant), and atoms vibrate with a frequency of approx. 10^{13} 1/s.

The time scale required by quantum mechanical oscillations may be of a femtosecond (10^{-15}s), whereas protein folding requires microseconds (a range of 10^9).

The dynamics of a double-walled carbon nanotube is characterized by different intrinsic time scales [15]: (1) a short time (the correlation time t_c) of the order of the vibrational period of the carbon atoms around their equilibrium positions. It can be evaluated in terms of the Debye frequency ω_D as $t_C = \frac{2\pi}{\omega_D}$, which is of the order of 50 fs; (2) the period of oscillations t_P that is the main time scale of the dynamics of double-walled carbon nanotubes, which is of the order of 10 ps ; (3) the damping or relaxation time t_R that is the time over which the mechanical oscillations are damped, which is of the order of 1 ns.

These times are therefore ordered as:

$$t_C \ll t_P \ll t_R . \tag{1.5}$$

Generally, the nanoropes are made from fullerene single-wall carbon nanotubes. These materials are produced of more than 70 percent by condensation of a laser-vaporized carbon-nickel-cobalt mixture at 1200°C. X-ray diffraction and electron microscopy showed that these carbon nanotubes are nearly uniform in diameter and that they self-organize into ropes, which consist of 100 to 500 carbon nanotubes in different arrangements. Figure 1.3 shows such a carbon nanotube rope made from 6 subropes, each subrope being composed from 7 groups of single wall carbon nanotubes. Each group contains 25 carbon nanotubes with two different

radii (zigzag and armchair 6.26A, h = 0.617 A and 16.33 A, h = 0.998 A), and the core group consists of 49 chiral carbon nanotube with the same radius (3.22 A and h = 0.6 A), into a polymeric matrix.

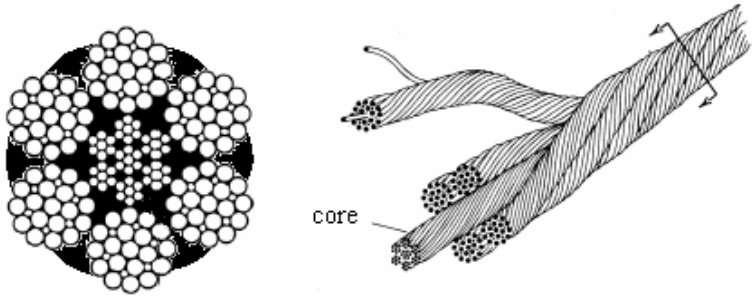

Fig. 1.3. The structure of nanorope.

2. Chebyshev Polynomials

The polynomial Chebyshev of second kind on the interval $[-1,1]$ are given by [17]–[19]:

$$U_n(x) = [1/(n+1)]T'_{n+1}(x),\ -1 \le x \le 1,\ n \in \mathrm{N}_0. \tag{2.1}$$

In (2.1), $T_n(x) = \cos(n \arccos x)$ are the Chebyshev polynomials of the first kind, and N_0 is a set of natural numbers. The shifted Chebyshev polynomials are defined as:

$$U_n^*(t) = U_n(2t-1) = \{1/[2\sqrt{t(1-t)}]\}\sin[(n+1)\arccos(2t-1)],\ 0 \le t \le 1.$$

The functions

$$F^*(r,t) = 1/[1+r)^2 - 4rt],\ h^*(x) = 2\sqrt{2(1-t)},\ |r| \le 1,\ 0 \le t \le 1, \tag{2.2}$$

are the generating and weighting functions for these polynomials.

To obtain the basic recurrence relations, the first can be derived for $U_n(x)$ and then for $U_n^*(t)$ by substituting $2t-1,\ 0 \le t \le 1$ for x. As a result, it is obtained:

$$4tU_n^*(t) = U_{n-1}^*(t) + 2U_n^*(t) + U_{n+1}^*(t),$$

$$2tU_n^{*\prime}(t) = 2nU_n^*(t) + 2U_{n-1}^{*\prime}(t) + U_n^{*\prime}(t),\ n \ge 1, \tag{2.3}$$

$$U_n^{*\prime}(t) = 4nU_{n-1}^*(t) + U_{n-2}^{*\prime}(t),\ n \ge 2.$$

On the base of (2.3) additional recurrence relations are obtained:

$$2^{2s}t^{s}U_{k}^{*}(t)=\sum_{p=0}^{2s}C_{2s}^{p}U_{k-s+p}^{*}(t)\,,\ k-s\geq 0\,,\ k\in \mathrm{N}_{0}\,, \tag{2.4}$$

$$2^{2(k+1)}t^{k+1}U_{k}^{*}(t)=\sum_{p=0}^{2k+2}C_{2k+2}^{p}U_{p-1}^{*}(t)\,,\ k\in \mathrm{N}_{0}\,, \tag{2.5}$$

$$2^{2(k+s)}t^{k+s}U_{k}^{*}(t)=-\sum_{q=2}^{s}C_{2k+2s}^{q-2}U_{s-q}^{*}(t)+\sum_{p=s}^{2k+2s}C_{2k+2s}^{p}U_{p-s}^{*}(t)\,,\ k\in \mathrm{N}_{0}\,,\ s\geq 2\,, \tag{2.6}$$

$$2^{2s}t^{s}U_{m}^{*}(t)U_{n}^{*}(t)=\sum_{p=0}^{m}\ \sum_{q=0}^{2s}C_{2s}^{q}U_{n-m-s+2p+q}^{*}(t)\,,\ n-m-s\geq 0\,, \tag{2.7}$$

$$U_{n}^{*\prime}(t)=4\sum_{k=0}^{[(n-1/2]}(n-2k)U_{n-(2k+1)}^{*}(t)=4\sum_{k=0}^{[(n-1/2]}(2k+1+a)U_{2k+a}^{*}(t)\,,\ n\geq 1\,, \tag{2.8}$$

$$\begin{aligned}&U_{n}^{*\prime\prime}(t)=2^{4}\sum_{k=0}^{[(n-1/2]}(k+1)(n-k)(n-2k-1)U_{n-(2k+2)}^{*}(t)\\&=2^{2}\sum_{k=0}^{[(n-2/2]}(2k+2-a)[(n+1)^{2}-(2k+2-a)^{2}]U_{2k+1-a}^{*}(t),\quad n\geq 2,\end{aligned} \tag{2.9}$$

$$\begin{aligned}&2^{2s}t^{s}U_{n}^{*\prime}(t)=4\sum_{k=0}^{(n-s-2)/2}\sum_{p=0}^{2s}(n-2k)C_{2s}^{p}U_{n-s-2k-1+p}^{*}(t)\\&+4\sum_{k=(n-s+2)/2}^{[(n-1/2]}(n-2k)\left[-\sum_{q=2}^{2k+1-n+1}C_{2s}^{q-2}U_{2k+1-n+s-q}^{*}(t)+\sum_{p=s}^{2s}C_{2s}^{p}U_{p-1}^{*}(t)\right],\\&n-s=2l+1,l\geq 0,\ n\geq 0,\ s\geq 0,\end{aligned} \tag{2.10}$$

$$\begin{aligned}&2^{2s}t^{s}U_{n}^{*\prime}(t)=4\sum_{k=0}^{(n-s-2)/2}\sum_{p=0}^{2s}(2k+1+a)E_{0}\\&+4\sum_{k=(s-a)/2}^{[(n-1/2]}\sum_{p=0}^{2s}(2k+1+a)C_{2s}^{p}U_{2k+a-s+p}^{*}(t),\\&E_{0}=\left[-\sum_{q=2}^{s-2k-a}C_{2s}^{q-2}U_{s-2k-a-q}^{*}(t)+\sum_{p=s-2k-a}^{2s}C_{2s}^{p}U_{p-s+2k+a}^{*}(t)\right],\\&n-s=2l,l\geq 0,n\geq 1,\ s\geq 0,\end{aligned} \tag{2.11}$$

$$2^{2s}t^sU_n^{*\prime}(t)=4\sum_{k=0}^{(n-s-2)/2}(2k+1+a)E_1,$$
$$E_1=\left[-\sum_{q=2}^{s-2k-a}C_{2s}^{q-2}U_{s-2k-a-q}^{*}(t)+\sum_{p=s-2k-a}^{2s}C_{2s}^{p}U_{p-s+2k+a}^{*}(t)\right], \qquad (2.12)$$
$$s-l\geq 1, n\geq 1,$$

$$2^{2s}t^sU_n^{*\prime\prime}(t)=2^4\sum_{k=0}^{(n-s-2)/2}\sum_{p=0}^{2s}(k+1)(n-k)(n-2k-1)C_{2s}^{p}U_{n-s-2k-2+p}^{*}(t)$$
$$+2^4\sum_{k=(n-s)/2}^{[(n-1/2]}(k+1)(n-k(n-2k-1))E_2, \qquad (2.13)$$
$$E_2=\left[-\sum_{q=2}^{2k+2-n+s}C_{2s}^{q-2}U_{2k+1-n+s-q}^{*}(t)+\sum_{p=2k+2-n+s}^{2s}C_{2s}^{p}U_{n-s-2k-2+p}^{*}(t)\right],$$
$$n-s=2l,\ l\geq 0,\ n\geq 2,\ s\geq 0,$$

$$2^{2s}t^sU_n^{*\prime\prime}(t)=2^2\sum_{k=0}^{[(n-2/2]}(2k+2-a)[(n+1)^2-(2k+2-a)^2]E_3,$$
$$E_3=\left[-\sum_{q=2}^{n-2k-1+a}C_{2s}^{q-2}U_{n-2k-1+a-q}^{*}(t)+\sum_{p=n-2k-1+a}^{2s}C_{2s}^{p}U_{2k+1-a-s+p}^{*}(t)\right], \qquad (2.14)$$
$$s-n\geq 1,\ l\geq 0,\ n\geq 2,$$

$$2^{2s}t^sU_n^{*\prime\prime}(t)=2^4\sum_{k=0}^{(n-s-3)/2}\sum_{p=0}^{2s}(k+1)(n-k)(n-2k-1)C_{2s}^{p}U_{n-s-2k-2+p}^{*}(t)$$
$$+2^2s[(n+1)^2-s^2]\sum_{p=1}^{n}C_{2s}^{p}U_{p-1}^{*}(t)+2^4\sum_{k=(n-s+1)/2}^{|(n-2)/2|}(k+1)(n-k)(n-2k-1)E_4, \qquad (2.15)$$
$$E_4=\left[-\sum_{q=2}^{2k+2+s-n}C_{2s}^{q-2}U_{2k+2+s-n-q}^{*}(t)+\sum_{p=2k+2+s-n}^{2s}C_{2s}^{p}U_{n-s-2k-2+p}^{*}(t)\right],$$
$$n-s=2l,\ l\geq 0,\ n\geq 2,\ s\geq 0.$$

In these expressions $a=n-1-2\left[(n-1)/2\right]$ with $[x]$ the integer part of x. The expressions (2.3)–(2.15) with the exception of (2.7) contain the orthogonal Chebyshev polynomials $\{\widehat{U}_k^*\}_{k=0}^{\infty}$ of the second kind, defined as $\widehat{U}_k^*=\|U_n^*\|^{-1}U_k^*$, with U_n^* the shifted polynomial Chebyshev of second kind on the interval [0,1]

and $\|U_k^*\| = \sqrt{\pi}/2$, the norm of U_k^*. Relation (2.7) can be written for orthogonal polynomials as:

$$2^{2s} t^s U_m^*(t) U_n^*(t) = \widehat{U}_0^* \sum_{p=0}^{m} \sum_{q=0}^{2s} C_{2s}^q \widehat{U}_{n-m-s+2p+q}^*(t), \; n-m-s \geq 0. \qquad (2.16)$$

3. Macroscopic Modeling

At the macrosopic, the carbon nanorope displayed in Fig. 1.3 is modeled as a rod of length *l*, with circular cross section of radius less than its length $a \ll l$. The geometry of the nanorope is presented in Fig. 3.1.

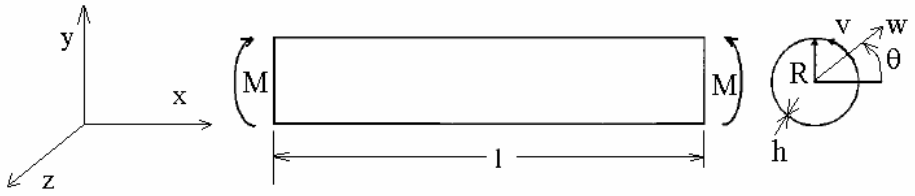

Fig. 3.1. Geometry of the nanotube.

A new parametrization is applied to the region occupied by the body $x \in [-a,a]$, $s \in [0,l]$, for a given time interval $t \in [0,T]$. Instead of $x \in [-a,a]$ we can use $x \in [0,1]$. For any integrable function $A(x,s)$, $x \in [0,1]$, $s \in [0,l]$, $t \in [0,T]$, we consider an expansion of the form:

$$A(x,s,t) = \sum_{k=0}^{\infty} A^{(k)}(s,t) \widehat{U}_k^*(x), \; x \in [0,1], \; s \in [0,l], \; t \in [0,T], \qquad (3.1)$$

where $A^{(k)}(s,t)$ is the *k*th coefficient in the expansion of $A(x,s,t)$ in the orthonormal Chebyshev polynomials $\{\widehat{U}_k^*(x)\}_{k=0}^{\infty}$ of the second kind. Let us to consider the integral:

$$I^{(k)}(A) = \int_0^1 A(x,s,t) \widehat{U}_k^*(x) h(x) \mathrm{d}x, \; k \in \mathrm{N}_0, \; s \in [0,l], \qquad (3.2)$$

where $h(s)$ is a properly chosen weighting function. This integral verifies the property of linearity [17]:

$$I^{(k)}[\alpha(s)A + \beta(s)B] = \alpha(s) I^k(A) + \beta(s) I^k(B), \qquad (3.3)$$

for any functions A and B of the form (3.1). Also, it is easily to show that $I^{(k)}(A)$ defined by (3.3) is equal to the *k*-th coefficient in the expansion of A in these polynomials with respect to x:

$$I^{(k)}(A)=\int_0^1 A(x,s,t)\widehat{U}_k^*(x)h(x)\mathrm{d}x=A^{(k)}(s,t)\,,\ \text{with}\ k\in \mathrm{N}_0\,. \tag{3.4}$$

External moments fix the ends of the tube. We suppose the rope deforms in space by bending and torsion.. The rod occupies at time $t=0$ the region $\vartheta=27°$. After motion takes place at time t, the rod occupies the region $\vartheta=27°$. At the macroscopic scale, we know the motion of the rod between $t=0$ and r_{ij} if and only if we know the mapping:

$$S(0,t),\ \ \forall t\in[0,t_1]\,, \tag{3.5}$$

which takes a material point in Ω_0 at t = 0 to a spatial position in $\Omega(t)$ at t = t_1.

The mapping (3.5) is single valued and possess continuous partial derivatives with respect to their arguments. The position of a material point in Ω_0 may be denoted by a rectangular fixed coordinate system $X\equiv(X,Y,Z)$ and the spatial position of the same point in $\Omega(t)$, by the moving coordinate system $x\equiv(x,y,z)$.

Following the current terminology, we shall call *X* the material or Lagrange coordinates and *x* the spatial or Euler coordinates. The origin of these coordinate systems is lying on the central axis of the rod. The motion of the rod carries various material points through various spatial positions. This is expressed by:

$$x=f_i(X,t),\ \ i=1,2,3\,. \tag{3.6}$$

We take *s* to be the coordinate along the central line of the natural state. The orthonormal basis of the Lagrange coordinate system is denoted by (e_1,e_2,e_3), and the orthonormal basis of the Euler coordinate system by (d_1,d_2,d_3). The basis $\{d_k\}$, $k=1,2,3$ is related to $\{e_k\}$, $k=1,2,3$ by the Euler angles θ,ψ and φ. These angles determine the orientation of the Euler axes relative to the Lagrange axes [20]:

$$\begin{aligned}
d_1&=(-\sin\psi\sin\varphi+\cos\psi\cos\varphi\cos\theta)e_1+\\
&+(\cos\psi\sin\varphi+\sin\psi\cos\varphi\cos\theta)e_2-\sin\theta\cos\varphi e_3,\\
d_2&=(-\sin\psi\cos\varphi-\cos\psi\sin\varphi\cos\theta)e_1+\cos\psi\cos\varphi-\\
&-\sin\psi\sin\varphi\cos\theta)e_2+\sin\theta\sin\varphi e_3,\\
d_3&=\sin\theta\cos\psi e_1+\sin\theta\sin\psi e_2+\cos\theta e_3.
\end{aligned} \tag{3.7}$$

The *Z*-axis coincides with the central axis. The plane (xy) intersects the plane (*XY*) in the nodal line *ON*. The motion of the rod is described by three vector functions:

$$R \times R \ni (s,t) \to r(s,t), d_1(s,t), d_2(s,t) \in E^3 . \tag{3.8}$$

The material sections of the rod are identified by the coordinate *s*. The position vector $r(s,t)$ can be interpreted as the image of the central axis in the Euler configuration. The functions $d_1(s,t)$, $d_2(s,t)$ can be interpreted as defining the orientation of the material section *s* in the Euler configuration. The function:

$$d_3(s,t) = d_1(s,t) \times d_2(s,t) , \tag{3.9}$$

represents the unit tangential vector along the rod. We introduce the strains y_1, y_2, y_3 by:

$$r' = y_k d_k , \tag{3.10}$$

where $(')$ means the partial differentiation with respect to *s*. Since $\{d_k\}$, $k = 1,2,3$, is orthonormal, there is a vector u that measures the bending of the bar, such as:

$$d_k' = u \times d_k , \; u_3 = 0 , \tag{3.11}$$

with

$$\begin{gathered} u_1 = \theta' \sin\varphi - \psi' \sin\theta \cos\varphi, \; u_2 = \theta' \cos\varphi + \psi' \sin\theta \sin\varphi, \\ u_3 = \varphi' + \psi' \cos\theta = 0, \end{gathered} \tag{3.12}$$

where θ, φ and ψ are Euler angles. The exact 3D equilibrium equations of the nanotube with the ends fixed by the external moment $M = -\lambda$ are obtained from (3.7)–(3.12):

$$A(\psi'^2 \sin\theta\cos\theta - \theta'') - \lambda \sin\theta = 0, \; \frac{\partial}{\partial s}(A\psi' \sin^2\theta) = 0, \tag{3.13}$$

where $A = \frac{1}{4}\pi R^4 E$ is the bending stiffness. The curvature C, in the longitudinal direction, the nondimensional curvature c, the deformation parameter ζ, are defined as:

$$C = \frac{2ch}{\sqrt{3}R^2(1-\nu^2)} , \; c = \frac{\sqrt{3\zeta}}{2} , \; \zeta = \frac{R - R_c}{R} , \tag{3.14}$$

where R and R_c, are the radius before and after deformation. The strain energy per unit length Π is given by:

$$\Pi = \Pi_0 + \frac{1}{2}\pi R^3 hC^2 E\sum_{k=1} a_k \zeta^k,\ \Pi_0 = \frac{3\pi Eh\hat{h}^2\zeta^2}{8R} + \frac{5\pi Eh\hat{h}^2\zeta^4}{16R},\ \hat{h} = \frac{h}{\sqrt{1-\nu^2}}. \quad (3.15)$$

The energy (3.15) can be expressed under the form (3.1):

$$\Pi(x,s,t) = \frac{1}{2}\sum_{k=0}^{\infty} L^{(k)}(s,t)\widehat{U}_k^*(x), \quad (3.17)$$

where $x_c \in [0,1]$, $s_c \in [0,l]$ represents the region occupied by the body, where the continuum theory is valid, for $t \in [0,T]$. In (3.17), $L^{(k)}(s,t)$ is the *k*-th coefficient in the expansion of $\Pi(x,s,t)$ in the orthonormal Chebyshev polynomials $\{\widehat{U}_k^*(x)\}_{k=0}^{\infty}$ of the second kind. These coefficients can be calculated with (3.4). The total energy of the tube Π_t and the bending moment M can be written as:

$$\Pi_t = \Pi l,\ M = \frac{\mathrm{d}\Pi_t}{\mathrm{d}\vartheta}, \quad (3.18)$$

where ϑ is the bending angle. The critical compressive stress $\sigma_{cr} = \frac{N}{h}$, where N is the axial load, and the critical bending moment M_{cr} in local buckling can be also calculated. This theory is valid up to the point of local buckling at a specific value for the bending angle ϑ.

4. Atomistic Modeling

Secondly, the atomistic modeling of the bar is analyzed. The total atomic energy E^a can be expressed as a sum of individual atom energies by (1.1). The energy of an atom is:

$$E_i^a = F_i(\bar{\rho}_i) + \frac{1}{2}\sum_{j\neq i}\alpha_i V_{ij}(r_{ij}), \quad (4.1)$$

where F_i is an electron-density dependent embedding energy, V_{ij} is a pair potential between i-th and j-th and r_{ij} is the interatomic distance, and α_i unknown constants. The electron density at atom *i*, $\bar{\rho}_i$ is the superposition of density contributions from each of the neighbours $\bar{\rho}_i = \sum_{j\neq i}\rho_j(r_{ij})$.

The van der Waals force refers to the attractive or repulsive forces between molecules or between parts of the same molecule, other than those due to covalent bonds or to the electrostatic interaction of ions with one another or with neutral

molecules. In this article this force is introduced to model the interaction between the opposite walls of the nanotube when they approach each other. This force depends on the distance between the atoms.

For large distances, the van der Waals force is attractive, but when the separation between the atoms is below the critical equilibrium distance, it becomes strongly repulsive. The van der Waals force between atom *i* and *j* can be expressed by the Lennard-Jones 6-12 potential as:

$$V_{ij}(r_{ij}) = A\left(\frac{1}{2}\frac{d_0^6}{r_{ij}^{12}} - \frac{1}{r_{ij}^6}\right). \tag{4.2}$$

where $A = 24.3\times10^{-79}\,\mathrm{Jm}^6$ and $d_0 = 0.383\,\mathrm{nm}$ are parameterized to describe interlayer forces in graphite [21], [22]. For the energy field $E^a(x,s)$ we consider an expansion of the form (3.1):

$$E^a(x,s) = \sum_{k=0}^{\infty} E^{a(k)}(s)\widehat{U}_k^*(x)\,, \tag{4.3}$$

where $x_a \in [0,1]$, $s_a \in [0,l]$ represents the region where the atomistic theory is valid. In (3.3), $E^{a(k)}(s)$ is the *k*-th coefficient in the expansion of E^a in the orthonormal Chebyshev polynomials $\{\widehat{U}_k^*(x)\}_{k=0}^{\infty}$ of the second kind. These coefficients can be calculated with (3.4).

For nanoropes, the inclusion of non-bonded interactions is important, because this explains the inter tube rotational mode as a result of long range van der Waals forces. Figure 4.1 plots the potential as a function of the relative rotational angle between two nanotubes, shown in Fig. 1.4, i.e. zigzag and armchair 6.26A, with *h* = 0.617 A and 16.33 A, with *h* = 0.998 A. The space between them is 3.48 Å, which is close to the graphite inter layer distance (3.3545 Å).

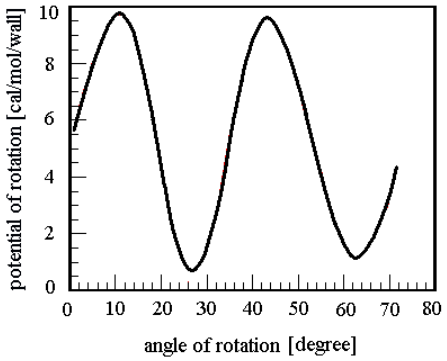

Fig. 4.1. The rotational potential as a function of relative rotational angle between two nanotubes.

5. Interface Modeling

Thirdly, the transition region between continuum and atomistic regions are modeled. The transition region between the atomistic and continuum regions is displayed in Fig. 5.1. On one side of the transition boundary is the atomistic region in which every atom is explicitly represented and treated by using interatomic potentials. The transition or boundary region between the atomistic and continuum regions is a very important aspect of the modelling [23]–[25].

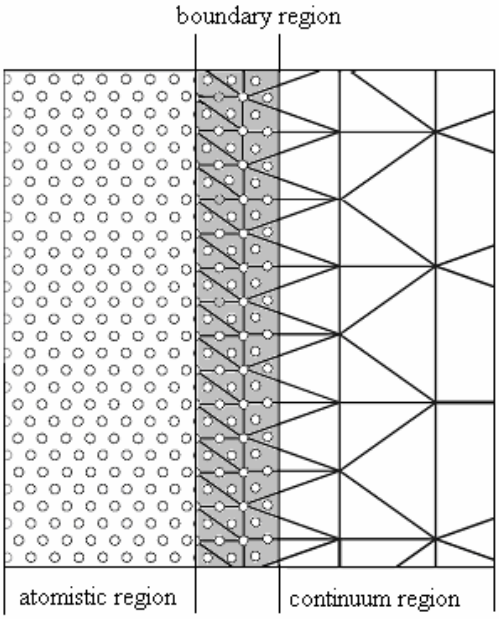

Fig. 5.1. The atomistic-continuum transition region.

At the interface between the atoms and the nodes of the continuum region, we construct a one-to-one correspondence with the aid of the Chebyshev polynomials of the second kind. The parametrization of the transition region $x_{tr} \in [0,1]$, $s_{tr} \in [0,l]$ is constructed such that the following assertion is valid.

***Assertion* 1.** *The energy field* $E^{tr}(x,s)$ *of the transition region verifies the conditions:*

$$E^{tr}(x,s) \to E^{c}(x,s) \text{ for } x_{tr} \to x_c,\ s_{tr} \to s_c, \tag{5.1}$$

and

$$E^{tr}(x,s) \to E^{a}(x,s) \text{ for } x_{tr} \to x_a,\ s_{tr} \to s_a, \tag{5.2}$$

where:

$$E^{tr}(x,s)=\sum_{k=0}^{\infty}E^{tr(k)}(s)\widehat{U}_k^*(x)\,, \tag{5.3}$$

with $x_{tr}\in[0,1]$, $s_{tr}\in[0,l]$.

In (5.3) $E^{tr(k)}(s)$ is the *k*-th coefficient in the expansion of $E^{tr}(x,s)$ in the orthonormal Chebyshev polynomials $\{\widehat{U}_k^*(x)\}_{k=0}^{\infty}$ of the second kind. These coefficients can be calculated as:

$$E^{(k)tr}(s)\to\int_0^1 E^a(x,s)\widehat{U}_k^*(x)h_a(x)\mathrm{d}x\,,\ k\in\mathrm{N}_0\,,\text{ for }x_{tr}\to x_a\,,\ s_{tr}\to s_a\,, \tag{5.4}$$

and:

$$E^{(k)tr}(s)\to\int_0^1 E^c(x,s)\widehat{U}_k^*(x)h_c(x)\mathrm{d}x\,,\ k\in\mathrm{N}_0\,,\text{ for }x_{tr}\to x_c\,,\ s_{tr}\to s_c\,, \tag{5.5}$$

with unknown functions $h_a(x)$ and $h_c(x)$ that are determined from an inverse problem such that (5.1) and (5.2) hold.

The total potential energy of the coupled atomistic-continuum model is obtained by summing the energies associated with the atomistic, continuum and transition regions as:

$$\begin{aligned}&E(x,s)=E^c(x_c,s_c)+E^a(x_a,s_a)+E^{tr}(x_{tr},s_{tr}),\\&(x_c,s_c)\in I_c,(x_a,s_a)\in I_a,(x_{tr},s_{tr})\in I_{tr},\\&I_c\cup I_a\cup I_{tr}=[0,1]\times[0,l],I_i\cap I_j=O,i,j=a,c,tr.\end{aligned} \tag{5.6}$$

6. The Solitonic Mechanism

In this section we consider some of the numerical results obtained for bending and torsion of nanoropes (Fig. 1.3) by applying the coupled atomistic-continuum theory. The model couples a region described with full atomistic detail to a surrounding region modeled with the continuum concepts. The shifted Chebyshev polynomials of the second kind and a generalization of Vekua and Nikagadze methods are performed on the base of a nonclassical parametrization of the transition region [26]–[28].

While deformating, with the increase in the bending angle ϑ, the atomistic theory must be considered in the area, which becomes a solitonic mechanism of deformation. In the rest of the tube the macroscopic modeling (3.13) remains valid. The interface between the continuum region of the nanotube and the solitonic re-

gion, where the atomistic modelling is applied, is modeled using an inverse problem. The unknown functions $h_a(x)$ and $h_c(x)$ are determined from an inverse problem such that (5.1) and (5.2) hold. The inverse problem is solved with a genetic algorithm based on the condition of matching the continuum and atomistic solutions.

Solitons or solitary waves are localized functions with no change in shape. In the mathematics literature the word *soliton* refers to solitary traveling waves, which preserve their identities after a pair-wise collision [29], [30]. The solutions of (3.13) are:

$$\cos\theta = -1 + 2\frac{|\lambda_3|}{A}\operatorname{sech}^2\sqrt{\frac{|\lambda_3|}{A}}s\ ,\ \ \psi = \arctan(4A\tanh(-\sqrt{\frac{|\lambda_3|}{A}}s))\ . \qquad (6.1)$$

These equations are valid up to the point of local buckling at $\vartheta = 25.58°$. For larger angles, the macroscopic modeling must be coupled with an atomistic theory. When the external bending moment increases, the axial compression in the tube increases too, and when the compressive stress reaches a critical value, the tube will locally buckle. The value of ζ at the point of local buckling is around 0.14.

With the increase in the bending angle ϑ, the top and bottom parts of the kink get closer to each other, and at a certain stage, the distance between them reaches the critical equilibrium distance. Upon additional bending, this distance remains unchanged because there are no external normal loads applied on the walls to prevail over the repulsive van der Waals forces.

For $\vartheta > 25.58°$, the atomistic theory put into evidence a region in which a solitonic mechanism of deformation appears. Figure 6.1 shows the nucleation of a solitonic mechanism of deformation in the nanotube for $\vartheta = 25.58°$. In according to experiments and molecular dynamics simulations, the pattern of the deformation resembles the soliton mechanism similar to that of a macrorope. A portion of the wall flattens and forms a domain that rotate about a central hinge line. This portion is treated by the molecular dynamic. Once the solitonic mechanism starts, the nanorope becomes a mechanical mechanism and the formulas (6.1) are no longer valid in the solitonic domain.

The remaining part of the tube remains circular although it flattens and decreases its curvature. This part is treated by the equations (6.1).

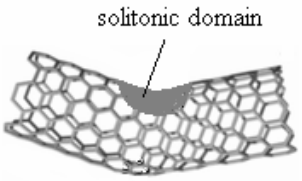

Fig. 6.1. The nucleation of the solitonic mechanism of deformation at $\vartheta > 25.58°$.

Figure 6.2 represents the solitonic domain (gray region) for $\vartheta = 27°$. Figure 6.3 represents the solitonic deformations (Å) into the solitonic domain for $\vartheta = 27°$, in the local coordinates.

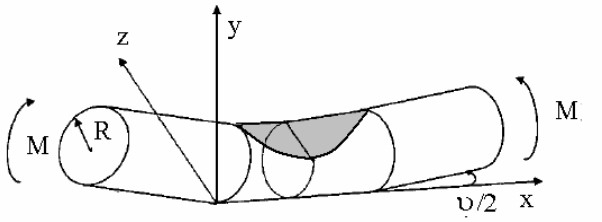

Fig. 6.2. The solitonic domain for $\vartheta = 27°$.

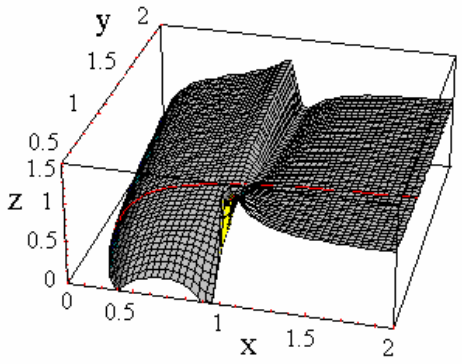

Fig. 6.3. The solitonic deformations (Å).

The generation of the solitonic deformations is presented in Figs. 6.4. Figure 6.5 shows the cross section of the nanorope for different values of ζ.

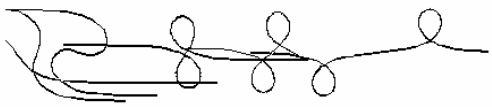

Fig. 6.4. The generation of solitonic deformations.

The consequence of the solitonic deformation mechanism is the rippling configuration of the nanorope. For a curvature large enough, our coupled atomistic-continuum analysis leads to a solution corresponding to a rippling configuration. Figure 6.6 presents the rippling configuration. A detailed configuration of the rippling phenomenon by interacting of the two soliton functions of the type (6.1), is

represented in Fig. 6.7. The result of this iuteraction is the rippling configuration shown in Fig. 6.6.

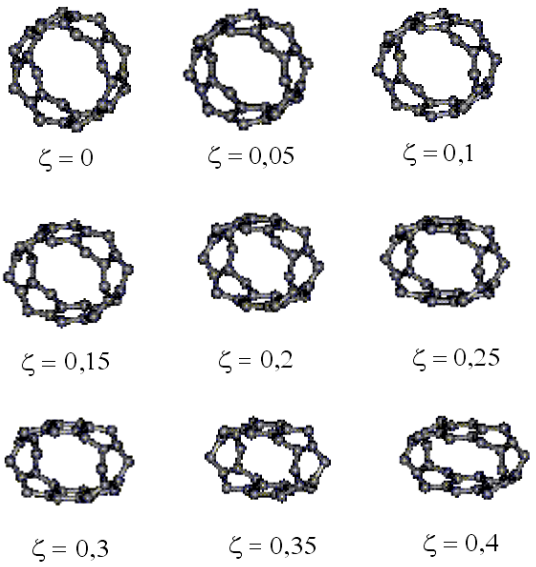

Fig. 6.5. Cross section of the nanotube for different values of ζ.

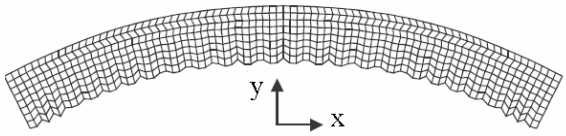

Fig. 6.6. The rippling configuration of the nanorope.

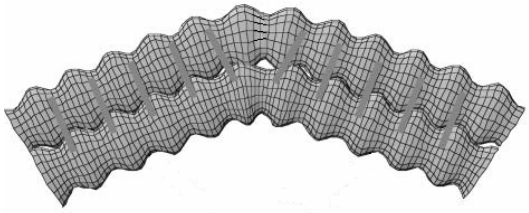

Fig. 6.7. The rippling interactions between two soliton solutions.

Finally, upon complete unloading from angles below 110° the nanorope completely recovers. At a very large bending angle of 120°, atomic bonds break and the deformation of the nanotube becomes irreversible.

7. Conclusions

In this paper, a coupled atomistic-continuum theory is performed for describing the bending and torsion of ropes made from single-walled carbon nanotubes. The rope is made from 6 subropes, each subrope being composed from 7 groups of single wall carbon nanotubes. Each group contains 25 carbon nanotubes with two different radii (zigzag and armchair 6.26 A, h = 0.617 A and 16.33 A, h= 0.998 A), and the core group consists of 49 chiral carbon nanotube with the same radius (3.22 A and h = 0.6 A), into a polymeric matrix.

The model couples a region described with full atomistic detail to a surrounding region modeled with the continuum concepts. The shifted Chebyshev polynomials of the second kind and a generalization of Vekua and Nikagadze methods are performed on the base of a nonclassical parametrization of the transition region.

When the external bending moment increases, the axial compression increases in the nanorope, and when the compressive stress reaches a critical value, the nanorope will locally buckle at $\vartheta = 25.58°$, where ϑ is the bending angle. For $\vartheta > 25.58°$, a solitonic deformation mechanism is starting and a portion of the nanorope becomes to rotate about a central hinge line. For large distances, the van der Waals force is attractive, but when the separation between the atoms is below the equilibrium distance of 3.42 Å, it becomes strongly repulsive. Upon complete unloading from angles below 110° the nanorope completely recovers. At a very large bending angle of 120°, atomic bonds break and the deformation of the nanorope becomes irreversible.

Acknowledgement

The authors acknowledge the financial support of the PNII project-Idei, Grant nr. 106/2007, code ID-247/2007.

References

[1] LEONARD D., *The space elevator comes closer to reality*, University of Phoenix, report, 2002.
[2] PEARSON J.,*The orbital tower: a spacecraft launcher using the Earth's rotational energy*, Acta Astronautica, 2, 785–799, 2000.
[3] YU M.F., LOURIE O., DYER M.J., MOLONI K., KELLY T.F., RUOFF R.S., *Strength and Breaking Mechanism of Multiwalled Carbon Nanotubes Under Tensile Load, Science*,. 287 (5453), 637–640, 2000.
[4] MORAVEC H.P., *A Non-Synchronous Orbital Skyhook,Journal of the Astronautical Sciences*, Vol. **25**, October-December 1977.
[5] IIJIMA S., *Helical microtubules of graphitic carbon*, Nature, London**, 354**, 56–58, 1991.
[6] IIJIMA S., ICHIHASHI, T., *Single-shell carbon nanotubes of 1 nm diameter*, Nature, London, **363**, 603–605, 1993.
[7] SRIVASTAVA D., MENON M., CHO K., *Nanoplasticity of Single-Wall Carbon Nanotubes under Uniaxial Compression*, Physical Review Letters, **83,** 15, 2973–2976, 1999.

[8] GAO G., CAGIN T, GODDARD W. A., *Energetics, structure, mechanical and vibrational properties of single-walled carbon nanotubes*, Nanotechnology, **9**, 184–191, 1998.
[9] RUOFF R.S., QIAN D., LIU W.K., *Mechanical properties of carbon nanotubes: theoretical predictions and experimental measurements*, Comptes Rendus Physique, **4**, 993–1008, 2003.
[10] CURTIN W.A., MILLER F., *Atomistic/continuum coupling in computational material science*, Modelling and Simulation in Materials Science and Engineering, **11**, R33–R68, 2003.
[11] HUGHES T. J. R., *The Finite Element Method: Linear Static and Dynamic Finite Element Analysis*, Englewood Cliffs, NJ: Prentice-Hall, 1987.
[12] ZIENKIEWICZ O. C., *The Finite Element Method*, 4-th edition, vol. **1–2**, London: McGraw-Hill, 1991.
[13] SHENOY V. B., *Multi-scale modeling strategies in material science – the quasicontinuum method*, Bull. Mater. Sci., **26**, 1, 53–62, 2003.
[14] SHENOY V. B., *Quasicontinuum models of atomic-scale mechanics*, Ph. D. thesis, Brown University, Providence, RI, USA, 1998.
[15] TADMOR E. B., *The quasicontinuum method*, Ph. D. thesis, Brown University, Providence, RI, USA, 1996.
[16] RAFII-TABAR H., *Modelling the nano-scale phenomena in condensed matter physics*, Phys. Rep., **325**, 239–310, 2000.
[17] NIKABADZE M.U., *Application of Chebyshev polynomials to the theory of thin bodies*, Moscow University Mechanics Bulletin, **62**, 5, 56–63, 2007.
[18] NIKABADZE M.U., *A system of equations of the thin-body theory*, Vestn. Mosk. Univ., Ser.1: Mat.Mekh., **1**, 30–35, 2006.
[19] NIKABADZE M.U., *The unit tensors of second and fourth ranks under a new parametrization of a shell space*, Vestn. Mosk. Univ., Ser.1: Mat.Mekh., **6**, 25–28, 2000.
[20] MUNTEANU L., DONESCU ST., *Introduction to Soliton Theory: Applications to Mechanics*, Book Series "Fundamental Theories of Physics", vol. **143**, Kluwer Academic Publishers, 2004.
[21] RUOFF R.S., QIAN D., LIU W.K., *Mechanical properties of carbon nanotubes: theoretical predictions and experimental measurement*s, Comptes Rendus Physique, **4**, 993–1008, 2003.
[22] WANG Q., VARADAN V.K., QUEK S.T., *Small scale effect on elastic buckling of carbon nanotubes with nonlocal continuum methods*, Physics Letters A, **357**, 130–135, 2006.
[23] TEODORESCU P.P., CHIROIU V., *On the nanomechanics of carbon nanotubes*, Trends and Challenges in Applied Mathematics ICTCAM 2007, Bucharest 20-23 June, 117–123, 2007.
[24] TEODORESCU P.P., CHIROIU V., MUNTEANU L., *On the soliton mechanism of bending for carbon nanotube*, Proc. Int. Conf. on Structural Analysis of advanced materials (ICSAM2005) Bucharest, 151–157.
[25] TEODORESCU P.P., CHIROIU V., MUNTEANU L., *The pseudosherical reduction of an uniaxial deformation of the Carbon nanotubes*, Proceedings of the 5th Conference of Balkan Society of Geometers, Geometry Balkan Press, BSG Proc., 2006 (ed. C. Udriste), 157–165, 2006.
[26] VEKUA I.N., *Shell theory: General methods of construction*, Nauka, Moscow, 1982.
[27] SUETIN P.K., *Classical orthogonal polynomials*, Nauka, Moscow, 1976.
[28] DANILOV YU. A., *Chebyshev polinomials*, Editorial Moscow, 2003.
[29] TEODORESCU P.P., CHIROIU V., *On the nanomechanics of carbon nanotubes*, Trends and Challenges in Applied Mathematics ICTCAM 2007, Bucharest 20-23 June, 117–123, 2007.
[30] TEODORESCU P.P., CHIROIU V., MUNTEANU L., *On the soliton mechanism of bending for carbon nanotube*, Proc. Int. Conf. on Structural Analysis of advanced materials (ICSAM2005) Bucharest, 151–157, 2005.

Correlations between Nanostructure and Thermodynamic Properties of $NiAlMe_x$-Alumina Composites

Roxana Mioara PITICESCU[1], Radu ORBAN[2], Speranta TANASESCU[3], Radu PITICESCU[1], Viorel BADILITA[1], Mariana LUCACI[4]

[1]National R&D Institute for Nonferrous and Rare Metals, Pantelimon, Ilfov, Romania
[2]Technical University Cluj Napoca, Romania
[3]Institute of Physical Chemistry I.G.Murgulescu Romanian Academy, Bucharest
[4]INCDIE – ICPE CA Bucharest, Romania

Abstract. The paper presents a part of the performed researches to synthesise new types of nanostructured composite materials with controlled distribution of the phases and multifunctional applications. Two innovative directions are squared up to: high temperature auto propagation synthesis of $NiAlMe_x$ (where Me = Fe or Co; x = 5 or 10) inter-metallic compounds and synthesis of metal-ceramic nanostructured composites by a soft solution process (SSP).

Nanostructured powders with core ($NiAlMe_x$ inter-metallic compounds)-shell (alumina) distribution were obtained and characterised by chemical quantitative analysis, X ray diffraction, thermal analysis and scanning electron microscopy.

1. Introduction

Nanotechnology is generally defined as an instrument to create and use the materials, devices and systems by materials manipulation at a scale lower than 100 nm. Mechanical and thermal response of compositional and microstructure spatial graded materials are of great interest for many technological domains, such as: tribology, biomechanics, nanotechnology and high temperature technology. Functional graded materials are very interesting for a series of applications, namely: aero spatial structures, solid oxide fuel cells, energy conversion, systems that use thermoelectric and thermo ionic materials (thermal barrier coatings), piezoelectric and thermoelectric applications, dental and orthopaedic implants in bioengineering, infusible doors, armour vest. Metal-ceramic composites retained the specialists attention from industry and research due to the excellent combination of their properties, namely: high specificity mechanical properties, high and predefined electrical and thermal conductivity, low to moderate thermal shrinkage coef-

ficient, good wear resistance, good behaviour at high temperatures. Two classes of composite materials could be distinguished: ceramic matrix composites (CMC) and metal matrix composites (MMC). Ceramic matrix composites can be reinforced with metallic or/and ceramics inclusions. A new class of CMC with interpenetrate microstructures is described in the literature (e.g. alumina /Al alloys; titanium dioxide/Al alloys; alumina/ Me_xAl_y). Ceramic coatings represent a separate class of composite materials. Bedded structures based on different structural ceramic materials present enhanced fracture strength. Microstructure graded layers or coatings, with grain sizes modifications can be obtained by different processing techniques. Functional graded materials are multifunctional materials because on one side present hard surfaces, temperature and corrosion resistance and on the other side the surfaces are ductile and easy workable. Electrical conductivity or / and magnetic properties are demonstrated by only one component of functional graded materials. Functional graded materials can be obtained by: a) metal infiltration (without pressure, compression casting or with gas pressure) in a preform with controlled porosity; b) together sintering of different metal and ceramic ratios.

The progress in the development and optimization of the new functional graded materials for the thermal barrier coatings (TBC) is depending on the development of new synthesizing and characterization methods and the questions have to be solved by a complex approaching of the correlation between composition and properties. The determination of the thermodynamic data and the thermo chemical investigation of the behaviour under the thermal treatment are essential for evaluating the long term stability and compatibility when the compounds are used in applications.

In the paper new types of nanostructured composite materials with controlled distribution of the phases and multifunctional applications are described. Nanostructured composite materials are formed from intermetallic compound $NiAlMe_x$ (where Me = Fe or Co and x = 5 or 10) synthesised by high temperature auto propagation procedure and a ceramic phase α-Al_2O_3 deposited as a superficial layer by sol-gel method (synthesis in solution at low pressures and temperatures). The correlation between microstructure and thermodynamic properties of these materials is described.

The study is focused on two important issues

– the re-evaluation of the energetic of the Al_2O_3 –based ceramic component of the nanocomposite material, taking into account the factors influencing the phase transformations characteristics
– the consideration of the inter-relations between the metallic substrate and oxide particles in the conditions of some discrepancies in microstructural homogeneity and inter-particle distance of the powder system.

Corundum, α-Al_2O_3, is the thermodynamically stable phase of coarsely crystalline aluminum oxide, but syntheses of nanocrystalline Al_2O_3 usually result in γ-Al_2O_3. Transition alumina powders are intrinsically nanocrystalline and can be synthesized from a variety of precursors. The most common precursors for α-Al_2O_3

thesized from a variety of precursors. The most common precursors for α-Al_2O_3 are boehmite (γ-AlOOH) and γ-Al_2O_3. Boehmite and the less ordered `pseudo-boehmite' are aluminium hydroxides, which decompose to form polycrystalline γ-Al_2O_3 upon heating above 450°C [1]. Upon heating, γ-Al_2O_3 undergoes a series of polymorphic phase transformations from a highly disordered cubic close packed lattice to the more ordered cubic close packed θ-Al_2O_3. When heated to 1200°C, θ-Al_2O_3 undergoes a reconstructive transformation by nucleation and growth, where the oxygen atoms rearrange into a hexagonal close packed structure to form thermodynamically stable α-Al_2O_3 [2].

From the thermodynamic point of view, due to the correlation between the increasing metastability of the polymorphic phases and the surface energies, the crossover of the stability domains is a specific phenomenon at nano level. Blonski si Garofalini [3] performed molecular dynamics simulations of various α-Al_2O_3 and γ-Al_2O_3 (Table 1). The surface energies for α-Al_2O_3 were significantly greater than those of γ-Al_2O_3. Using their data, and assuming preferential exposure of the surfaces with lowest energy, McHale et al. predicted that γ-Al_2O_3 should become energetically stable polymorph as specific areas exceed ~125 m^2/g^{-1}. The thermodynamic stability of γ-Al_2O_3 should be even greater than implied by this energy. Due to the presence of tetrahedral and octahedral sites in its spinel-type structure, and fairly random distribution of Al^{3+} and vacancies over these sites, γ-Al_2O_3 has a greater entropy than α-Al_2O_3. The entropy change of the α-Al_2O_3 to γ-Al_2O_3, $\Delta S_{\alpha\rightarrow\gamma}$, is about +5,7 $JK^{-1}mol^{-1}$ [5]. Therefore, at room temperature, γ-Al_2O_3 could be thermodynamically stable with respect to α-Al_2O_3 at specific areas >100 m^2g^{-1}, and at 800K (a temperature typical of a hydroxide decomposition) γ-Al_2O_3 might become thermodynamically stable at specific surface areas greater than only 75 m^2g^{-1}.

Table 1. Surface and transformation enthalpy for different aluminium oxide polymorphic forms

Oxide	ΔH_s (Surface enthalpy) [J/m^2]	ΔH_{transf} (Phase transformation enthalpy) [kJ/mol]	Specific surface [m^2/mol]
α-Al_2O_3	2.6 ± 0.2	0	<10000
γ-Al_20_3	1.7 ± 0.1	13.4 ± 2.0 ($\alpha - \gamma$)	>10000 at 298 K >7500 at 800 K
AlOOH (boehmite)	0.5 ± 0.1	–17±1	5140

The energetic parameters involved in the synthesis of α-Al_2O_3 could be influenced also by the impurities content. A large number of investigators have attempted to control the kinetics and microstructure evolution of the θ to α-Al_2O_3 phase transformation with the addition of small amounts of metal oxide seed particles [6–8]. In unseeded boehmite, the intrinsic nucleation density is 108±1011 nu-

clei/cm^3 γ-Al_2O_3 and 1200°C is required to fully transform the material to α-Al_2O_3 in 100 min. The addition of seeds, which are isostructural with α-Al_2O_3, provide low energy sites for heterogeneous nucleation and thus reduce the activation energy barrier required for transformation, and the transformation temperature [7, 8].

The inhomogeneity of the samples and the inter-particle distance variation could be important factors for the characterization of the phase transformations in the analysed systems. The θ- to α-Al_2O_3 phase transformation is considered to occur though a nucleation and growth process. Once the θ-crystallite grows to the critical size of phase transformation then the α-Al_2O_3 nucleus occurs. The process is one θ-crystallite transforming to one α-Al_2O_3 nucleus and results in an exothermic reaction at temperatures from near 900 to 1300°C. The critical size of θ-crystallite, dcθ is ~ 22 nm and the correspondingly transformed α-crystallite dcα is ~ 17 nm. The literature data and thermodynamic estimations presented above supported the development of the experimental part.

2. Experimental procedure

Inter-metallic compounds of $NiAlMe_x$ type (where Me = Fe or Co; x = 5 or 10) were synthesised by a high temperature auto propagation method. After screening on 125 μm sieve, the metallic mixtures of nickel, aluminium and iron or cobalt have been pre-alloyed by wet mechanical milling. The process has been conducted in a planetary ball mill at balls to powder ratio of 3:1, for 8 hours. Milled powders have been pressed in pellets and sintered 1 h at 1100ºC in protective atmosphere. Inter-metallic powders were than obtained by wet milled for 4 hours [9]. Nanostructured metal ceramic composites with core ($NiAlMe_x$ inter-metallic compounds)-shell (alumina) distribution have been synthesised by a soft solution process based on controlled precipitation of Al (III) on the dispersed inter-metallic powders. The procedure is described in details elsewhere [9].

Nanostructured metal-ceramic composites thus obtained were compositionally analysed by inductively coupled plasma (ICP- Spectroflame apparatus) and atomic absorption spectroscopy (AAS – Zenith 700 spectrometer). Powders microstructure and morphology were determined by X ray diffraction analysis (XRD-Brucker D8 Advance diffractometer), scanning electron microscopy (SEM- JEOL 5400 LV microscope, endowed with EDS compositional analyzer - Oxford Instruments) and thermal analysis (DSC-Netszch Maya F200 and Setsys evolution TGDTADSC Setaram calorimeter respectively).

3. Results and discussions

In Figures 1–4 are presented the XRD spectra for some representative nanostructured composite samples synthesised by a soft solution process. In Table 2 are synthetically presented the results of XRD analysis.

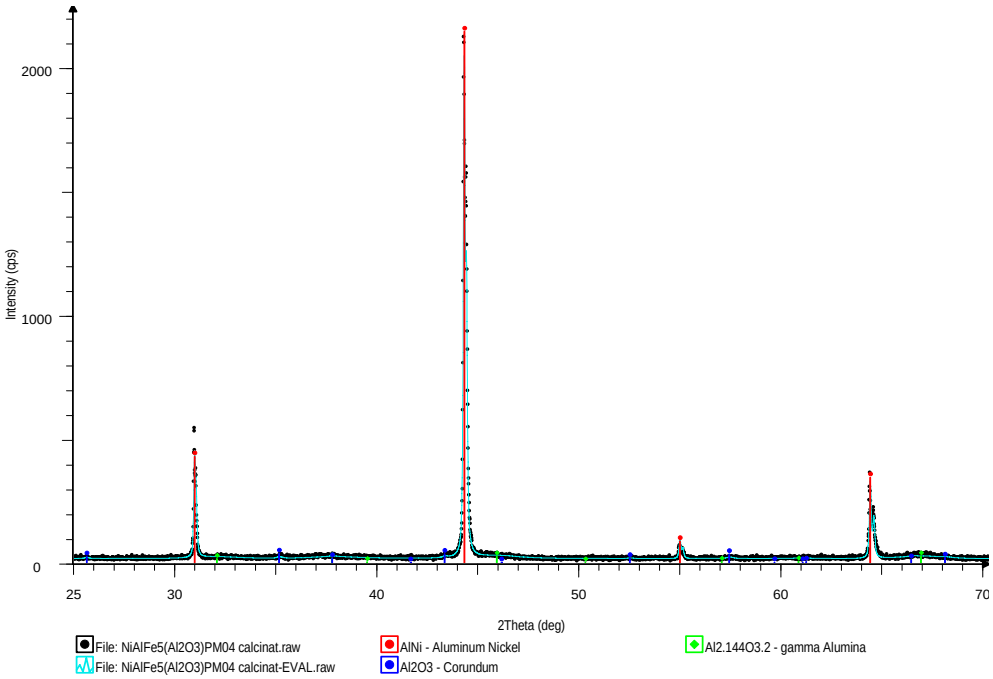

Fig. 1. XRD spectra for composite sample $NiAlFe_5$-alumina.

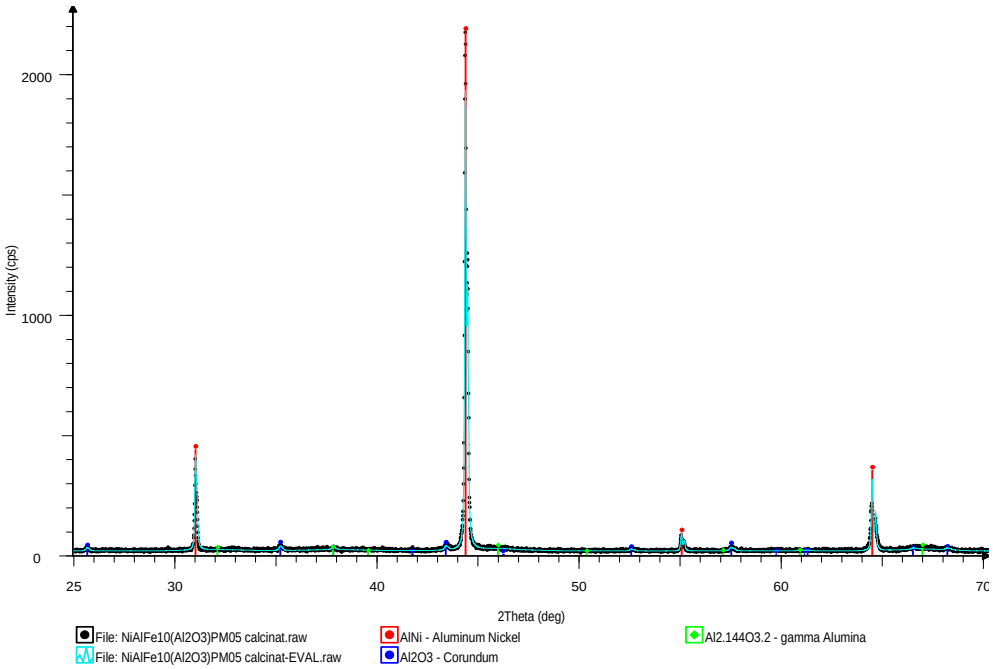

Fig. 2. XRD spectra for composite sample $NiAlFe_{10}$-alumina.

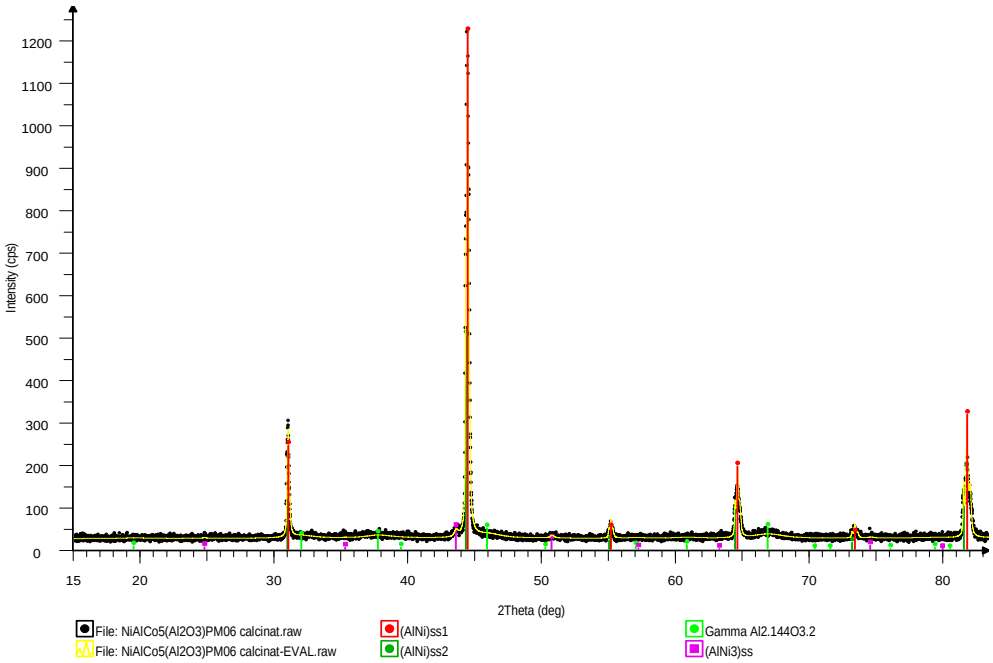

Fig. 3. XRD spectra for composite sample $NiAlCo_5$-alumina.

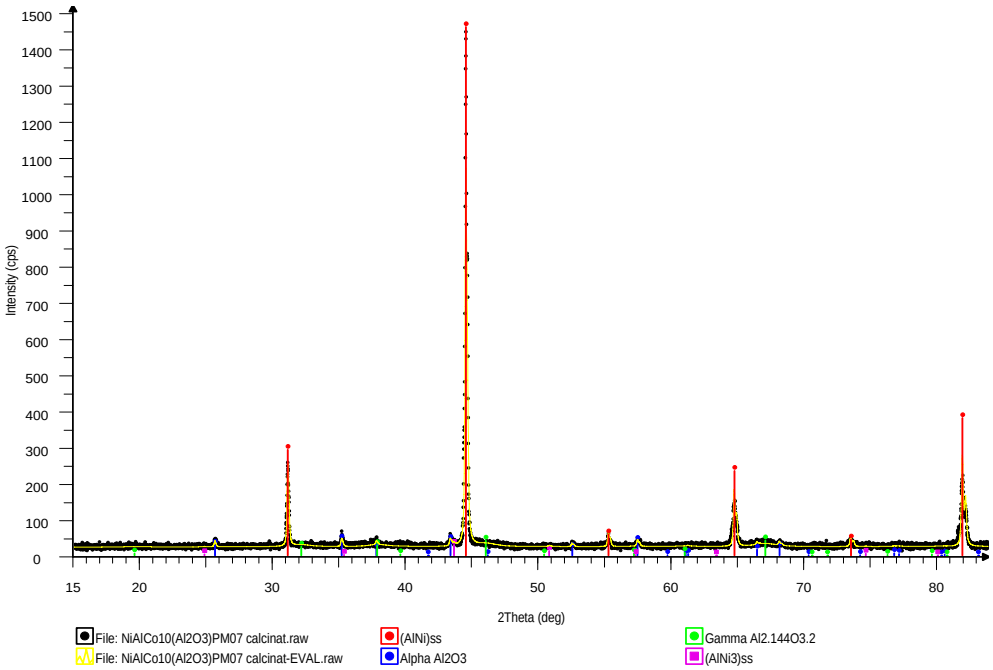

Fig. 4. XRD spectra for composite sample $NiAlCo_{10}$-alumina.

Table 2. Phase analysis and crystallite sizes for nanostructured composite samples

Phase	**Phase semiquantitative analysis (weight %)**			
	$NiAlFe_5(Al_2O_3)$	$NiAlFe_{10}(Al_2O_3)$	$NiAlCo_5(Al_2O_3)$	$NiAlCo_{10}(Al_2O_3)$
(AlNi)ss1	67.5 *a* = 2.88734 Å d crystallite = 85 nm	65.0 *a* = 2.88664 Å d crystallite = 98 nm	52.8 *a* = 2.87802 Å d crystallite = 54 nm	65.8 *a* = 2.87553 Å d crystallite = 62 nm
(AlNi)ss2	–	–	14.9 *a* = 2.88510 Å d crystallite = 104 nm	–
(AlNi3)ss	–	–	1.5 *a* = 3.59217 Å d crystallite = 31 nm	0.5 *a* = 3.59022 Å d crystallite = 31 nm
$Al_{2.144}O_{3.2}$ Gamma Alumina / Amorphous alumina	29.3	27.3	15.9 *a* = 7.8978 Å d crystallite = 4 nm	23.6 *a* = 7.88178 Å d crystallite = 5 nm
α Al2O3 (hex)	3.2	7.7	Possible traces	10.1 4.75970/12.99350 d crystallite = 65 nm

In Figures 5–8 are presented some representative examples of the scanning electron microscopy (SEM) analysis corresponding to inter-metallic compounds synthesised by high temperature auto propagation process and nanostructured composite samples obtained by a soft solution process respectively.

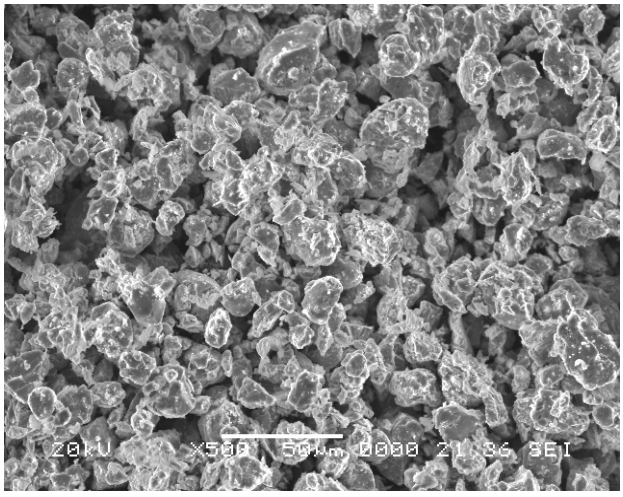

Fig. 5. SEM micrograph for $NiAlFe_5$ inter metallic compounds.

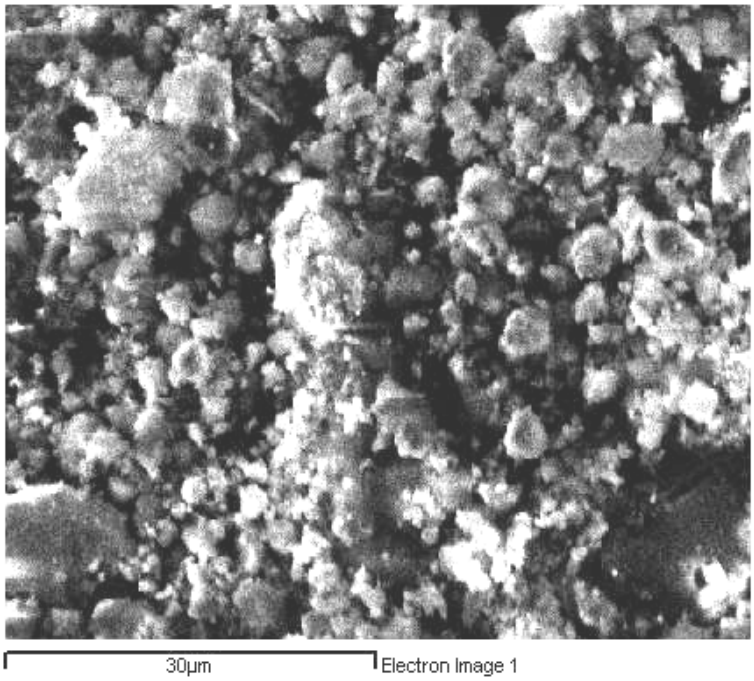

Fig. 6. SEM micrograph for composite sample $NiAlFe_5$-alumina.

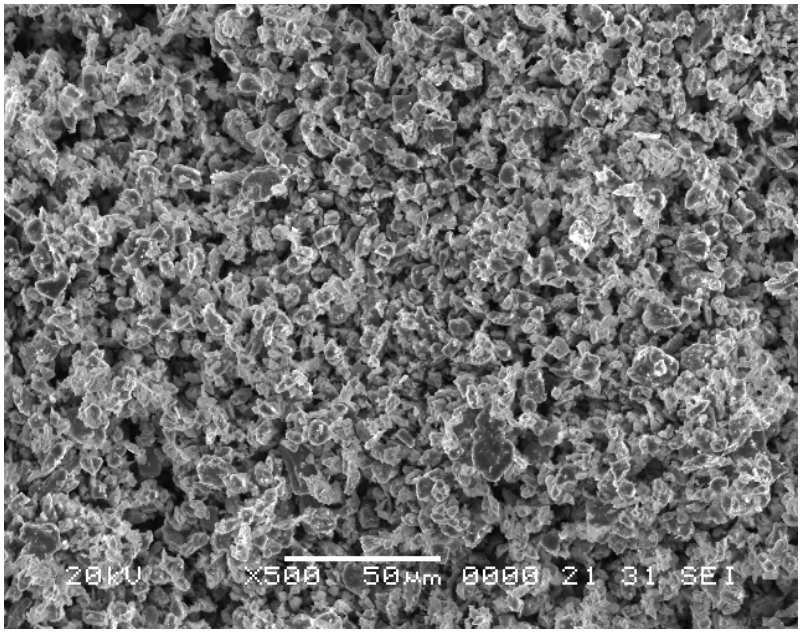

Fig. 7. SEM micrograph for composite sample $NiAlFe_{10}$ inter-metallic compounds.

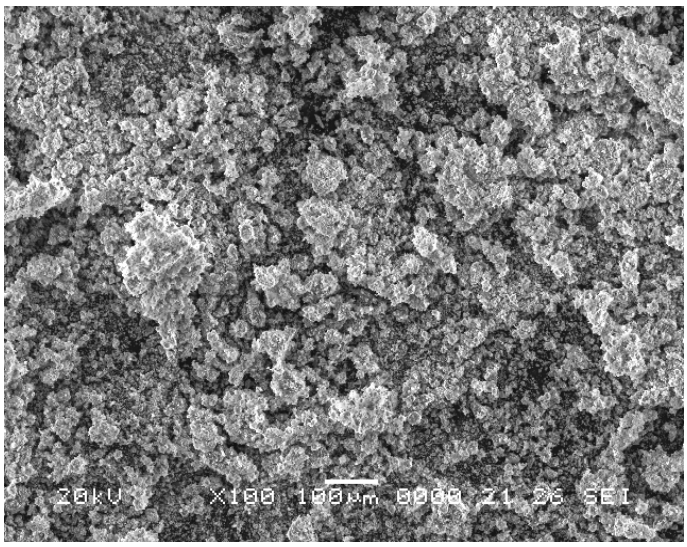

Fig. 8. SEM micrograph for composite sample $NiAlFe_{10}$-alumina.

Figure 5 revealed a particle conglomerate with narrow sizes distribution, polyhedral shape with bright facets- fracture cleavage-as a result of mechanical disintegration process. Round edges and corners can be observed as a consequence of friction forces between particles.

Figure 6 revealed small particles with variable sizes (from 5-10 μm to submicron values). Round edges can be observed proving that coating with alumina took place.

Figure 7 revealed the morphology of $NiAlFe_{10}$ inter-metallic compounds. Very fine powder conglomerate can be observed. Higher Fe amount influence the grain sizes distribution. Particles with almost uniform coarse grained with round fracture cleavage facets and edges, in a small amount comparing to $NiAlFe_5$ inter-metallic compounds can be observed.

In Figure 8 a fine and higher coarse grained powder comparing to $NiAlFe_5$-alumina powder is revealed. Lower conglomerates amount and small conglomerates sizes can be observed.

DSC techniques have long been the common method to examine the thermal properties of materials. In general, with reactions that occur in a material during thermal treatment, the energy changes can be identified and measured through temperature differences relative to a thermally inert material. However, this kind of reaction may inherently be attributed to phase transformations and grouped into endothermic reactions and exothermic reactions, demonstrated by DSC profiles in a macroscopic sense. Recent studies on the θ- to α-phase transformation of nano-scaled Al_2O_3 powder systems reveal that the profiles obtained by DSC techniques may release additional information rather than the phase transformation. The ex-

periments were done on ceramic samples with different grain size, measuring on heating and cooling runs; the observed endothermic, as well as the exothermic processes will evidence the phase transformations and the corresponding temperatures of the phase transitions.

In the Figures 9 and 10 and Table 3 are presented the representative results obtained for the nanocomposite samples.

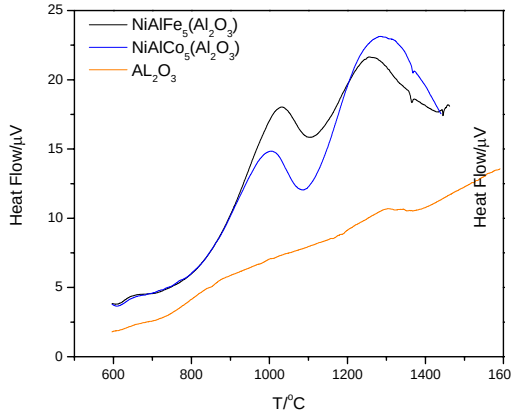

Fig. 9. The influence of the dopant nature.

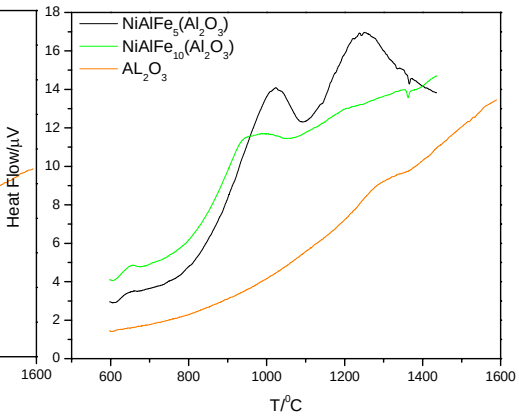

Fig. 10. The influence of the dopant concentration.

Table 3. Heat of transformations and phase transformation temperature for the nanocomposite materials

Sample	Heat rate (°C/min)	Heat of transf. (Peak 1) (J/g)	T_{Onset} (°C)	T_{Peak} (°C)	Heat of transf. (Peak 2) (J/g)	T_{Onset} (°C)	T_{Peak} (°C)
$NiAlFe_5(Al_2O_3)$	20	–469.322	881	1013	–638.067	1138	1255
$NiAlCo_5(Al_2O_3)$	20	–478.231	851	988	–1362.05	1124	1266
$NiAlFe_{10}(Al_2O_3)$	20	–342.283	842	940			

The results reveal the reconstructive transformation by nucleation and growth, where the oxygen atoms rearrange into a hexagonal close packed structure to form thermodynamically stable alpha alumina. At the same time, the influence of both the nature and concentration of dopants is observed.

The values of the heat of transformation, as well as the phase transformation temperature are presented in the Table 2. At the same concentration of the dopant (5%) and at the same heating rate (20 K min^{-1}), in the Fe containing sample, the exothermic effect is more pronounced than in the sample in which Co is present. The phase transformation temperature is higher in Fe doped sample (1237°C) comparatively with the sample containing Co (1217°C).

NiAlFe(Co)(Al2O3) nanocomposite materials present a microstructure inhomogeneity and the inter-relations between metallic substrate particles and oxide particles have to be taken into account. The ab initio study of the NiAl(110) oxidation revealed that the selective oxidation of its surface requires the redistribution of the atomic species near the surface. In the presence of oxygen, exchange defects formation near the NiAl surface and the Ni vacancy segregation at the exterior layer are extremely increased. The analysis of possible sequences for NiAl oxidation demonstrates the appearing of an energetic barrier on the Ni rich side comparing to Al rich side. While the oxygen diffusion took place (due to the beginning of the thermal treatment) and aluminium oxides begin to be formed, Ni remains chemically unaffected by the oxygen presence. This could be a possible explanation of the exothermic process showing a reconstructive transformation through nucleation. Oxygen atoms are re-arranged in a hexagonal structure to form thermodynamic stable α-alumina. In the same time Fe presents two components, namely: a low energy component that could be attributed to Fe-Fe or Fe-Al interactions and a higher energy component attributed to NiAlFe compound. The reduction –dissolution process of the substrate leads to the diffusion of oxygen in the outer layer surface and the alumina formation at NiAlFe-Al_2O_3 interface. Al and Ni will be present as an inter-metallic compound. The samples' heating thus induces oxidation at the surface followed by the formation of alumina layer. This inter-phase morphology should lead to optimal properties of the composite material. However, due to the inhomogeneity of the initial powders, a quasi homogeneous phase transformation is possible. The presence of point defects (thermal vacancies, constitutional vacancies and anti-site atoms) as well as the concentration variation with temperature may be also directly correlated with the possible precipitation of doping metal (especially Fe) thus explaining the changing of phase transformation temperature with the doping element concentration.

4. Conclusions

New types of nanostructured composite materials with controlled distribution of the phases and multifunctional applications were obtained. Nanostructured composite materials are formed from intermetallic compound $NiAlMe_x$ (where Me = Fe or Co and x = 5 or 10) synthesised by high temperature auto propagation procedure and a ceramic phase - α Al_2O_3 deposited as a superficial layer by sol-gel method (synthesis in solution at low pressures and temperatures). The results reveal the reconstructive transformation by nucleation and growth, where the oxygen atoms rearrange into a hexagonal close packed structure to form thermodynamically stable alpha alumina. At the same time, the influence of both the nature and concentration of dopants is revealed.

Acknowledgement

Authors thanks AMCSIT POLITEHNICA for financial support in the frame of CEEX 290 NANOGRAF project.

References

[1] WEFERS K., MISRA C., *Oxides and Hydroxides of Aluminium*, ALCOA Technical Paper No. 19, Rev. ALCOA Labs, 1987.

[2] YANG X., PIERRE A.C., UHLMANN D.R., *TEM study of boehmite gels and their transformation to a-Alumina*, J. Non-Cryst.Sol. **100**(1–3) (1988) 331–337.

[3] BLONSKI S, GAROFALINI SH, *Molecular dynamics simulation of a-alumina and g-alumina surfaces*, Surface Sci. **295**, 263–297, 1993.

[4] MCHALE J. M., NAVROTSKY A, PERROTTA A. J., *Effects of Increased Surface Area and Chemisorbed* H_2O *on the Relative Stability of Nanocrystalline* γ-Al_2O_3 *and* α-Al_2O_3, J Phys Chem B. 1997;101:603–613. doi: 10.1021/jp9627584.

[5] MCHALE J. M., AUROUX A, PERROTTA A. J., NAVROTSKY A., *Surface Energies and Thermodynamic Phase Stability in Nanocrystalline Aluminas*, Science, **277**, 5327, **7**88–791, 1997.

[6] KUMAGAI M., MESSING G. L., *Enhanced densification of boehmite sol-gels by a-Alumina seeding*, J. Am. Ceram. Soc., **67** (11), C-230-31, 1984.

[7] SHELLEMAN R. A., MESSING G. L., KUMAGAI M., *Alpha Alumina transformation in seeded boehmite gels*, J. Non-Cryst. Sol. **82**(1–3), 277–285, 1986.

[8] SUWA Y., KOMARNENI S., ROY R., *Solid-state epitaxy demonstrated by thermal reactions of structurally diphasic xerogels: the system* Al_2O_3, J. Mater. Sci. Lett. **5**(1), 21–24, 1986.

[9] PITICESCU R. M., LUCACI M., TANASESCU S., ORBAN R., LUNGU C., PITICESCU R., *Innovative Routes for Functionally Graded Materials Synthesis*, AMCSIT POLITEHNICA, CEEX Conference 2007 Brasov, ISSN 1843-5904, Ed.Tehnica.

Thermal Properties of Mesoscopic Amorphous Membranes

Dragoş-Victor ANGHEL

Department of Theoretical Physics, National Institute for Physics
and Nuclear Engineering–"Horia Hulubei", Str. Atomistilor no. 407,
P.O.BOX MG-6, Bucharest - Magurele, Romania

Abstract. We calculate thermal properties of amorphous nanoscopic membranes. We assume that such membranes contain dynamical defects like amorphous materials, which can be described at low temperatures by an ensemble of two-level systems. For the interaction of the two-level systems with the phonon modes we use the model introduced in Phys. Rev. **75**, 64202 (2007). In this way we find that at higher temperatures, the heat conductivity, κ, is proportional to T^2, whereas in the limit of low temperatures – when the dominant phonon wavelength is longer than the thickness of the membrane – κ is proportional to T.

1. Introduction

Research of low temperature properties of glassy materials has already a long history. In 1971, Zeller and Pohl [1], collecting the experimental data on specific heat and thermal conductivity that existed at that time for amorphous solids, and making new measurements for vitreous SiO_2, Se, and silica- and germanium-based glasses, observed that the Debye model calculations, which are typical for crystalline materials, fail to describe the amorphs. The Debye model predicts a specific heat proportional to T^3, whereas the heat conductivity, although in general proportional also to T^3, is very dependent on the material properties, quality of the crystalline lattice, and the type of the defects or impurities that exist in the solid.

In contrast to this, in glasses, the specific heat is linear in temperature, whereas the heat conductivity is proportional to T^2 and quite insensitive of the chemical composition of the material. Obviously, the Debye model could not describe such systems and there was need for a new model. The new model was introduced independently by Philips [2] and Anderson, Halperin and Varma [3]. They proposed that the amorphous materials contain dynamical defects that, at low temperatures, are modeled by an ensemble of two-level systems (TLS). A TLS is

imagined as an atom or a group of atoms in a two-well potential. The two wells are positioned in such a way that the energy difference between the two lowest energy levels of the system is much smaller then the energy difference between any other two energy levels–thus the name of two-level system.

Nevertheless, the model of Philips and Anderson, Halperin and Varma [2, 3] was mainly used to describe amorphous, isotropic bulk systems, where the phonon modes are simple, transversely and longitudinally polarized plane-waves. In such problems it is enough to consider a simple interaction hamiltonian between the TLS and the phonons, which contain two coupling terms: one for the interaction with the transversal modes and another for the interaction with the longitudinal modes.

Despite of the success of this model to describe amorphous, isotropic solids, other challenges appeared in the field. In the 1980s is was observed that crystals (especially the ones with defects) and quasicrystals may have glassy properties as well [4, 5, 6, 7, 8, 9, 10, 11, 12, 13]. This is surprising, since glassy properties were assumed to be a consequence of the amorphous structure. Moreover, these properties are anisotropic, which brings additional challenges to the theory, since the scalar model cannot be applied.

The scalar model cannot be applied also to the description of mesoscopic systems, like nanodevices. These devices become irreplaceable in more and more branches of physics and technology, where they are supposed to work very close to the fundamental limits of precision and accuracy. Therefore there is a strong demand to describe them in great detail, using models which are very realistic and reliable. But in mesoscopic systems, like in anisotropic crystals, the phonon modes are most of the time complicated superpositions of longitudinally and transversely polarized waves and therefore the scalar model is again useless.

In [14] we introduced a model that generalizes the standard tunneling model and allows one to describe the interaction of TLSs with any strain field. With this model we are able to describe both, the anisotropy of the glassy properties of disordered crystals [15, 16] and mesoscopic amorphous systems [17, 18].

In the next section we are going to describe briefly the STM, in order to introduce the reader into the subject and define the notations. In the subsection 2.1 we generalize the STM, which we then apply to mesoscopic membranes in section 3. In section 4 we present the conclusions.

2. The STM and its generalization

A two-level system in described in a two-dimensional (2D) basis, by the hamiltonian:

$$H_0 = \frac{\Delta}{2}\sigma_z - \frac{\Lambda}{2}\sigma_x = \frac{1}{2}\begin{pmatrix} \Delta & -\Lambda \\ -\Lambda & \Delta \end{pmatrix}, \tag{1}$$

where Δ is called the *asymmetry of the potential* and Λ, the *tunnel splitting*. As we mentioned in the Introduction, the TLS is imagined to be an atom or a group of atoms which tunnels between the two minima of a two-well potential. In this picture, the asymmetry of the potential represents the difference between the ground state energies of the two wells, taken separately, whereas the tunnel splitting is the tunneling hamiltonian of the system from one well to another.

The interaction of the TLS with a strain field perturbs H_0. However, it does not affect all its elements, but only the diagonal ones [2, 3, 19]. The perturbation hamiltonian is:

$$H_{TLS} = O^T H_{TLS} O = \frac{\varepsilon}{2}\sigma_z = \frac{1}{2}\begin{pmatrix} \varepsilon & 0 \\ 0 & -\varepsilon \end{pmatrix}, \tag{2}$$

where δ is linear in the strain field, [20, 19]. If we denote the symmetric strain field tensor by S_{ij}, then we can write $\delta \equiv 2\gamma_{ij}S_{ij}$, where γ_{ij} is a tensor that characterizes the TLS. Everywhere in this paper we shall assume summation over repeated subscripts, unless otherwise specified.

Here we can introduce the simplification of the STM: instead of the whole tensor of coupling constants, γ_{ij} , are used only two constants, γ_l and γ_t. The first constant determines the strength of the coupling of the TLS with a longitudinal phonon and the second determines the coupling of a TLS with a transversal phonon; therefore we write $\delta_\sigma = 2\gamma_\sigma S_\sigma$ (no summation over $_\sigma$), where S_σ is the amplitude of the phonon mode of polarization σ.

Although the interaction hamiltonian, H_1 is assumed to be the same for all the TLSs, the parameters of the bare hamiltonian, H_0, varies from one TLS to another, with the distribution $V\,P(\Delta,\Lambda)$, where V is the volume and P is of the form:

$$P(\Delta,\Lambda) \equiv P_0/\Lambda, \tag{3}$$

with P_0 a constant.

The TLS excitation energy – let's call it ε – is obtained by diagonalizing the matrix of H_0. If we denote by O the transformation that diagonalizes H_0, then:

$$H_{TLS} = O^T H_{TLS} O = \frac{\varepsilon}{2}\sigma_z = \frac{1}{2}\begin{pmatrix} \varepsilon & 0 \\ 0 & -\varepsilon \end{pmatrix}, \tag{4}$$

where $\varepsilon = \sqrt{\Delta^2 + \Lambda^2}$ is the excitation energy of this TLS and by the superscript ^{T} we denote in general the transpose of a matrix.

A very useful parameter that characterized the TLS is $u = \Lambda/\varepsilon$. In terms of the two new parameters, ε and u, the distribution of TLSs is:

$$P(\varepsilon,u)\mathrm{d}\varepsilon\mathrm{d}u = \frac{P_0}{u\sqrt{1-u^2}}\mathrm{d}\varepsilon\mathrm{d}u\,. \tag{5}$$

We have now all the ingredients to calculate the specific heat and heat conductivity of the sample. If we represent by ↑ an excited TLS, by ↓ a TLS in its

ground state, and we denote by $n_{\mathbf{k}\sigma}$ the population of the phonon mode with the wavevector k and polarization σ, then an obvious transition amplitude is:

$$\left\langle n_{\vec{k}\sigma}+1,\uparrow\right| H_1 \left| n_{\vec{k}\sigma},\downarrow\right\rangle = -\gamma_\sigma \frac{\Lambda}{\varepsilon}\sqrt{\frac{\hbar k(n_{\vec{k}\sigma}+1)}{2V\rho c_\sigma}}, \tag{6}$$

where ρ is the density of the solid. Using (6) we obtain the deexcitation rate of a TLS, by the emission of a phonon of wavevector k and polarization σ,

$$\Gamma^{em}(\varepsilon) = \gamma_\sigma^2 \frac{\pi k}{V\rho c_\sigma}\cdot\frac{\Lambda^2}{\varepsilon^2}(n_{k\sigma}+1)\delta(\hbar c_\sigma k-\varepsilon). \tag{7}$$

The rate of phonon absorption by the TLS is, obviously:

$$\Gamma^{abs}(\varepsilon) = \Gamma^{em}(\varepsilon) n_{k\sigma}/(n_{k\sigma}+1).$$

2.1. The extension of the STM

In [14] the STM was extended, starting from the expression $\delta=2\gamma_{ij}S_{ij}$. Since γ_{ij} characterizes the TLS and the strength of its interaction with the strain field, it was splited in two, writing $\gamma_{ij}=T_{kl}R_{klij}$; the 2D tensor T_{ij} characterizes solely the TLS, whereas R_{ijkl} is a constant 4D array that determines the strength of the interaction of the TLS with the field. Going even further, in [14] it was proposed that to each TLS it is associated a direction, $\hat{\vec{t}}$ (all the unit vectors in this paper will carry a hat), of components (t_1, t_2, t_3) and these components determine the components of the tensor T_{ij} by the relation, $T_{ij}=t_i\, t_j$.

It is more convenient to work with abbreviated subscripts [21], which transform the second rank tensors [T] and [S] into 6D vectors, **T** and **S**, and the 4D array into a 6 × 6 2D symmetric array, [R]. In the new notations, δ is calculated simply, using matrix multiplication, $\delta = \mathrm{T}^t \cdot [R] \cdot S$.

One of the key aspects of this model is that the structure of [R] is determined by the symmetry of the lattice that incorporates the TLSs, in the same way as the tensor of elastic stiffness constants [c] [21] is determined by the symmetry of the lattice [14, 22]. For example if the solid is isotropic or has a cubic symmetry, then the matrix [R] has a block diagonal form. We shall be consistent with the notations used before and we write:

$$[R] \equiv \tilde{\gamma}\cdot\begin{pmatrix} 1 & \zeta & \zeta & 0 & 0 & 0\\ \zeta & 1 & \zeta & 0 & 0 & 0\\ \zeta & \zeta & 1 & 0 & 0 & 0\\ 0 & 0 & 0 & \xi & 0 & 0\\ 0 & 0 & 0 & 0 & \xi & 0\\ 0 & 0 & 0 & 0 & 0 & \xi \end{pmatrix} = \tilde{\gamma}\cdot[r], \tag{8}$$

where $\tilde{\gamma} = R_{11}$, $\varsigma = R_{12} / R_{11}$, and $\xi = R_{44} / R_{11}$. If [R] characterizes an isotropic lattice, then an extra condition is satisfied [14, 16], namely:

$$\zeta + 2\xi = 1 \tag{9}$$

Nevertheless, Eq. (9) may be satisfied also for a cubic lattice, as it seems to be the case for the Ca stabilized Zirconium [15].

3. The description of thin amorphous membranes

Our research in this area was triggered by the development of ultra sensitive detectors of electromagnetic radiation for space-born astrophysical experiments [23–34]. One cell of such a detector consists roughly of some metallic films, of thicknesses of the order of 10 nm deposited on free-standing dielectric, amorphous membranes, like the ones depicted in Fig. 1 [18]. The metallic films form the thermal sensing element, which is the actual detector, and the cooler, which has the role of keeping the membrane at working temperature of some hundreds of mK. To be able to design such a detector and to calculate its response, we have first to calculate and characterize with good accuracy the thermal properties of the supporting membrane.

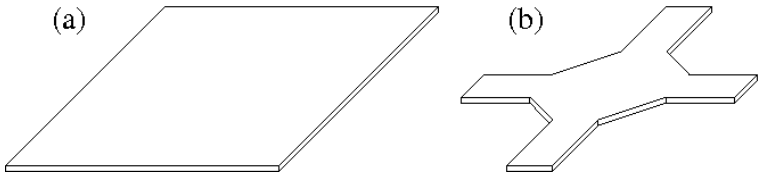

Fig. 1. (a) The full, dielectric membrane; (b) the membrane is cut, for better insulation.

Although this is well known [17, 21, 35, 36, 37], for the sake of consistency of the presentation and to introduce the notations we explain here some of the properties of the phonon modes in membranes. The phonon modes of a free standing, infinite membrane are the eigenmodes of the elastic equations and are divided into three groups, according to their symmetry properties. One group is formed of simple, transversely polarized modes, called the horizontal shear modes (*h*). The two other groups are the symmetric (*s*) and antisymmetric (*a*) Lamb modes. Together, these modes form a complete, orthonormal set of functions for the elastic displacement fields and their proper quantization has been carried out in [36]. Here we shall use the results and notations from there and we shall call the three different types of phonons – i. e., *h*, *s* and *a* – as polarizations.

We assume that the membrane of thickness d is placed parallel to the (*xy*) plane and its parallel surfaces cut the *z* axis at ± *d*/2. The phonons propagate in the (*xy*) plane with the wave-vector $\mathbf{k}_{\|} = k_{\|} \cdot \hat{\vec{k}}_{\|}$, of real $k_{\|}$. We use hat to denote unit vectors.

Along the z direction, the phonon modes are stationary. The h modes are transversal waves, and their wavevector component along the z direction will be denoted by kh. The s and a waves are superpositions of transversal and longitudinal waves, of wave vector components along the z direction denoted by k_t and k_l, respectively. Due to the boundary conditions, which demand that the membrane surfaces are stress-free, k_h takes the discrete values $m\pi/d$, with m taking all integer values between 0 and ∞, whereas k_t and k_l satisfy the more complicated relations [21]:

$$\frac{\tan(k_t d/2)}{\tan(k_l d/2)} = -\frac{4k_t k_l k_{\|}^2}{(k_t^2 - k_{\|}^2)^2}, \tag{10a}$$

for the symmetric modes and

$$\frac{\tan(k_l d/2)}{\tan(k_t d/2)} = -\frac{4k_t k_l k_{\|}^2}{(k_t^2 - k_{\|}^2)^2} \tag{10b}$$

for the antisymmetric modes.

Equations (10) plus Snell's law, $\omega^2 = c_t^2(k_{\|}^2 + k_t^2) = c_l^2(k_{\|}^2 + k_l^2)$, enable us to write k_l as a function of k_t for each of the polarizations s and a. Like in the case of the h modes, the dispersion relations, $\omega \equiv \omega(k_{\|})$ for the symmetric and antisymmetric modes split into branches, i. e. Eqs. (10) and Snell's law do not give only one function $k_l(k_t)$ for either set of modes, but produce an infinite, countable set of such functions. These functions will be called phonon branches and we shall number them with m=0,1,…, where branches of bigger m lie above branches of smaller m (see [35, 36]). Note also that $k_t(k_{\|})$ and $k_l(k_{\|})$ may take both, real and imaginary values [21, 35, 36].

As stated in the Introduction, we cannot apply a scalar model to characterize such a membrane, so we shall apply the model of section 2.1. The membrane is amorphous, so we use for $[R]$ the form (8), with the extra condition (9). In this model, the amplitude of absorption of a phonon of quantum numbers ($\mathbf{k}\sigma$) by an unexcited TLS is

$$\left\langle n_{\tilde{k}\sigma}, \uparrow \middle| \tilde{H}_1 \middle| n_{\tilde{k}\sigma} + 1, \downarrow \right\rangle = -\frac{\tilde{\gamma}\Lambda}{\varepsilon}\sqrt{n_{\tilde{k}\sigma}} \cdot (\vec{T}^t \cdot [r] \cdot \vec{S}_{\tilde{k}\sigma}) \tag{11}$$

where $n_{\mathbf{k}\sigma}$ is the population of the phonon mode. By applying the Fermi's golden rule, Eq. (11) gives a phonon emission rate by one TLS (or TLS deexcitation rate) [14, 16, 17, 38],

$$\bar{\Gamma}_{|n_{\tilde{k}\sigma},\uparrow\rangle \to |n_{\tilde{k}\sigma}+1,\uparrow\rangle} = \frac{(n_{\tilde{k}\sigma}+1)\pi k}{V\rho c_{\sigma}} \cdot \frac{\Lambda^2}{\varepsilon^2} \cdot (\vec{T}^t \cdot [r] \cdot \vec{s}_{\tilde{k}\sigma}) \delta(\hbar\omega_{\tilde{k}\sigma} - \varepsilon). \tag{12}$$

To make the comparison between the isotropic and anisotropic models more transparent, in Eq. (12) we took out a factor $N = \sqrt{(\hbar k)/(2V\rho c_{\hat{k},\sigma})}$ from the expression of S (**S** ≡ N**s**, where N is the normalization constant of the phonon mode, multiplied by k). Now note the difference between Eqs. (7) and (12). In the isotropic model (Eq. 7) Γ^{em} depends only on the TLS excitation energy, ε, whereas in the anisotropic model Γ^{em} depends on the more complicated expression,

$$M_\sigma(\hat{\vec{t}}) \equiv \vec{T} \cdot [r] \cdot \vec{S}_\sigma$$

Detailed expressions of $M_\sigma(\hat{\vec{t}})$ for different polarizations σ of the phonon modes are given in [17]. Here we show briefly how they were applied to the calculation of thermal properties of the membrane and state the main results.

First of all, averaging $|M_\sigma(\hat{\vec{t}})|^2$ over $\hat{\vec{t}}$ or over all the phonon modes, we calculate the TLS and phonon relaxation times,

$$\tau_\varepsilon^{-1} = \frac{\pi}{\rho} \cdot \left(\frac{\tilde{\gamma}\Lambda}{\varepsilon} \right)^2 \coth(\beta\varepsilon/2) \sum_\sigma \frac{1}{\omega_\sigma} \left\langle |M_\sigma(\hat{\vec{t}})|^2 \right\rangle, \tag{13}$$

and

$$\tau_\mu^{-1} = \frac{\pi\tilde{\gamma}^2 V P_0}{\rho\omega_\mu} \cdot \left(\frac{\tilde{\gamma}\Lambda}{\varepsilon} \right)^2 \tanh(\beta\varepsilon/2) \left\langle |M_\mu(\hat{\vec{t}})|^2 \right\rangle, \tag{14}$$

respectively, where by μ we denote the set of phonon quantum numbers, (**k**, σ).

Using Eq. (14) we can calculate the two-dimensional heat conductivity along the membrane:

$$\kappa = \frac{1}{A} \sum_\mu \hbar\omega_\mu \tau_\mu (c_\sigma)_x^2 \frac{\partial n_\mu}{\partial T} =$$

$$= \frac{\hbar^2 \rho}{16\pi^2 \tilde{\gamma}^2 V P_0} \cdot \frac{1}{k_B T^2} \sum_{n,\sigma} \int_0^\infty dk_\parallel \left(\frac{\partial\omega_\mu}{\partial k_\parallel} \right)^2 \frac{k_\parallel \omega_\mu^3}{\left\langle |M_\mu(\hat{\vec{t}})|^2 \right\rangle} \frac{\coth(\beta\hbar\omega/2)}{\sinh(\beta\hbar\omega/2)},$$

where A is the area of the membrane. At an arbitrary temperature, κ has to be calculated numerically. Here we present only the analytical low temperature approximation (for more details, see [17]).

3.1. Low temperature approximations

At low temperatures, the dominant phonon wavelength is much longer than the thickness of the membrane. In such a case, only the phonons from the lowest h,

s, and *a* branches contribute to the heat transport and specific heat. The calculation of the relaxation time for the h modes is trivial and gives

$$\tau_{h,0,k_\parallel} = \frac{\hbar\rho c_t^2}{\pi\tilde{\gamma}^2 P_0}\frac{1}{C_t}\frac{\coth(\beta\hbar\omega/2)}{\hbar\omega}. \tag{16}$$

For the *s* and *a* polarizations we use the assumption $\frac{k_t d}{2} \ll 1$ and $\frac{k_l d}{2} \ll 1$ in Eqs. (10) which we then expand in Taylor series to write analytical expressions for $k_l(k_t)$. With these we obtain the dispersion relation:

$$\omega_{s,0,k_\parallel} = 2\frac{c_t}{c_l}\sqrt{c_l^2 - c_t^2}\,k_\parallel \equiv c_s k_\parallel, \tag{17}$$

for the *s* modes, which gives:

$$\tau_{s,0,k_\parallel} = \frac{\hbar\rho c_t^2}{\pi\tilde{\gamma}^2 P_0}\frac{4c_l^2(c_l^2 - c_t^2)}{C_l c_t^4 + C_t c_l^2(c_l^2 - 2c_t^2)}\frac{\coth(\beta\hbar\omega/2)}{\hbar\omega} \equiv \frac{\hbar\rho c_t^2}{\pi\tilde{\gamma}^2 P_0}\frac{1}{C_s}\frac{\coth(\beta\hbar\omega/2)}{\hbar\omega}. \tag{18}$$

For the *a* modes, the dispersion relation for long wavelengths is:

$$\omega_{a,0,k_\parallel} = \frac{\hbar}{2m^*}\left(k_\parallel^2 - d^2\frac{27c_l^2 - 20c_t^2}{90c_l^2}k_\parallel^4\right), \tag{19}$$

where m^* is the effective mass of the long wavelength a phonons (see [35]). From (19) we finally get

$$\tau_{s,0,k_\parallel} = \frac{\hbar\rho c_t^2}{\pi\tilde{\gamma}^2 P_0}\frac{c_l^2(c_l^2 - c_t^2)}{C_l c_t^4 + C_t c_l^2(c_l^2 - 2c_t^2)}\frac{\coth(\beta\hbar\omega/2)}{\hbar\omega} \equiv \frac{\hbar\rho c_t^2}{\pi\tilde{\gamma}^2 P_0}\frac{1}{C_a}\frac{\coth(\beta\hbar\omega/2)}{\hbar\omega}, \tag{20}$$

with $C_a = 4C_s$. In the equations above, C_t and C_l are the constants that appear in the scattering of transversal and longitudinal plane waves, respectively, in bulk amorphous materials, $C_t = 4\xi^2/15$ and $C_l = (15-40\xi+32\xi^2)/15$; note that $C_l/C_t \geq 4/3$ for all ξ [14].

Using these asymptotic relations for the scattering times, we calculate the low temperature expression for heat conductivity and we obtain the expression [17]:

$$\kappa = \frac{\hbar^2}{16\pi}\frac{1}{k_B T^2}\sum_\sigma\int_0^\infty d\omega\frac{k_{\parallel,\sigma,0}(\omega)l_{\sigma,0,k_\parallel}\omega^2}{\sinh^2(\beta\hbar\omega/2)} =$$

$$= \frac{k_B^2\rho c_t^2}{16\pi^2\hbar\tilde{\gamma}^2 P_0}T\cdot\left(\frac{I(x_{h,0}^*)}{C_t} + \frac{I(x_{s,0}^*)}{C_s} + \frac{2I(x_{a,0}^*)}{C_a}\right) \tag{21}$$

where $x_{\sigma,0}^* \equiv \beta\hbar\omega_{\sigma,0}^*$ and by $I(x)$ we denoted the integral:

$$I(x)=\int_x^\infty \mathrm{d}y\,\frac{y^2\coth(y/2)}{\sinh^2(y/2)}=\frac{4x^2e^x}{(e^x-1)^2}+\frac{8x}{e^x-1}-8\ln(1-e^{-x})\,. \tag{22}$$

The lower limit of the integral, $\omega^*_{\sigma,0}$, was introduced because the heat conductivity is divergent if the integral is taken from zero to infinity. In real systems, this lower cut-off might be due either to other scattering mechanisms or to the finite (small) size of the membrane. On the other hand, the absence of the cut-off would mean that the heat transport in the membrane is ballistic and takes place by radiative heat transfer.

If the cut-off is small enough, then $I(x) \approx 12 - 8\ln(x)$ and the heat conductivity becomes:

$$\kappa=\frac{k_B^2\rho c_t^2}{16\pi^2\hbar\tilde{\gamma}^2P_0}T\cdot\left(\frac{3-2\ln(\beta\hbar\omega^*_{t,0})}{C_t}+\frac{3-2\ln(\beta\hbar\omega^*_{s,0})}{C_s}+\frac{6-4\ln(\beta\hbar\omega^*_{a,0})}{C_a}\right). \tag{23}$$

This expression means that in the limit of low temperatures, the heat conductivity in the membrane, if limited by the scattering of phonons on the TLSs, is proportional to $T(a + b\ln T)$.

4. Conclusions

We presented briefly the standard tunneling model, used to describe bulk amorphous solids. Nevertheless, this model is not enough to be used for disordered crystals or nanoscopic membranes. For these problems, a new model was introduced in [14], which can describe the interaction of a TLS with any strain field. In this model a direction in space is associated to each TLS and the coupling between the phonon and the TLS depends on the orientation of the TLS with respect to the strain field of the phonon. In section 3 we showed how the model is applied to calculate the heat conductivity of a nanoscopically thick membrane. The final result is very complicated and can be calculated only numerically, but here we presented the asymptotic low temperature analytic results.

References

[1] ZELLER R. C., POHL R. O., Phys. Rev. B, **4**:2029, 1971.
[2] PHILIPS W. A, J. Low Temp. Phys., **7**:351, 1972.
[3] ANDERSON P. W., HALPERIN B. I., VARMA C. M., Phil. Mag., **25**:1, 1972.
[4] LAERMANS C., VANELSTRAETE A., Phys. Rev. B, **34**:1405, 1986.
[5] VANELSTRAETE A., LAERMANS C., Phys. Rev. B, **38**:6312, 1988.
[6] VANELSTRAETE A., LAERMANS C., Phys. Rev. B, **42**:5842, 1990.
[7] LAERMANS C., KEPPENS V., Phys. Rev. B, **51**:8158, 1995.
[8] PARSHIN D. A., LAERMANS C., Phys. Rev. B, **58**:11099, 1998.

[9] CLASSEN J., ROHR I., ENSS C., HUNKLINGER S., LAERMANS C., Eur. Phys. J. B, **10**:623, 1999.
[10] TOPP K. A., *Effects of random strains on tunneling states in crystals*. PhD thesis, 1997.
[11] TOPP K. A., THOMPSON E. J., POHL R. O.. Phys. Rev. B, **60**:898, 1999.
[12] TOPP K. A., CAHILL D. G., Z. Phys. B: Condens. Matter, **101**:235, 1996.
[13] BERT F., BELLESSA G., GRUSHKO B., Phys. Rev. Lett., **88**:255901, 2002.
[14] ANGHEL D. V., KÜHN T., GALPERIN Y. M., MANNINEN M., Phys. Rev. B, **75**:064202, 2007.
[15] ANGHEL D. V., CHUROCHKIN D. V., arXiv:0804.1481, 2008.
[16] ANGHEL D. V., CHUROCHKIN D. V., arXiv:0804.1486, 2008.
[17] KÜHN T., ANGHEL D. V., GALPERIN Y. M., MANNINEN M., Phys. Rev. B, **76**:165425, 2007. cond-mat/07051936.
[18] ANGHEL D. V., KÜHN T., GALPERIN Y. M., Series in Micro and Nanoengineering, **11**:286, 2007.
[19] LEGGETT A. J., CHAKRAVARTY S., DORSEY A. T., FISHER M. P. A., GARG A., ZWERGER W., Rev. Mod. Phys., **59**:1, 1987.
[20] ESQUINAZI P., *Tunneling systems in amorphous and crystalline solids*, Springer, 1998.
[21] AULD B. A. , *Acoustic Fields and Waves in Solids*, 2nd Ed. Robert E. Krieger Publishing Company, 1990.
[22] ANGHEL D. V., KÜHN T., GALPERIN Y. M., MANNINEN M., J. Phys.: Conf. Series, **92**:012133, 2007.
[23] LEIVO M., *On-chip Cooling by Quasiparticle Tunneling Below 1 Kelvin*, PhD thesis, 1999.
[24] ANGHEL D. V., *Phases and phase transitions in mesoscopic systems*, PhD thesis, 2000.
[25] LUUKANEN A., *High Performance Microbolometers and Microcalorimeters: from 300 K to 100 mK*, PhD thesis, 2003.
[26] LEIVO M. M., PEKOLA J. P., Appl. Phys. Lett., **72**:1305–1307, 1998.
[27] LEIVO M. M., MANNINEN A. J., PEKOLA J. P., Appl. Supercond., **5**:227, 1998.
[28] ANGHEL D. V., PEKOLA J. P., LEIVO M. M., SUOKNUUTI J. K., MANNINEN M., Phys. Rev. Lett., **81**(14):2958–2961, Oct. 1998.
[29] ANGHEL D. V., MANNINEN M., Phys. Rev. B, **59**:9854, 1999.
[30] PEKOLA J. P., ANGHEL D. V., SUPPULA T. I., SUOKNUUTI J. K., MANNINEN A. J., MANNINEN M., Appl. Phys. Lett., **76**:2782, 2000.
[31] ANGHEL D. V., PEKOLA J. P., J. Low Temp. Phys., **123**:197, 2001.
[32] ANGHEL D. V., LUUKANEN A., PEKOLA J. P., Appl. Phys. Lett., **78**:556, 2001.
[33] LUUKANEN A., KINNUNEN K. M., NUOTTAJÄRVI A. K., HOEVERS H. F. C., BERGMANN TIEST W. M., PEKOLA J. P., Phys. Rev. Lett., **90**:238306, 2003.
[34] LUUKANEN A., PEKOLA J. P., Appl. Phys. Lett., **82**:3970, 2003.
[35] KÜHN T., ANGHEL D. V., PEKOLA J. P., MANNINEN M., GALPERIN Y. M., Phys. Rev. B, **70**:125425, 2004.
[36] ANGHEL D. V., KÜHN T., J. Phys. A: Math. Theor., **40**:10429, 2007. cond-mat/0611528.
[37] ANGHEL D. V., KÜHN T., GALPERIN Y. M., Series in Micro and Nanoengineering, **11**:286, 2007.
[38] ANGHEL D. V., arXiv:0710.0728, 2007.

Nanostructured Film Preparation by Thermionic Vacuum Arc

Cristian P. LUNGU

National Institute for Laser,Plasma and Radiation Physics,
Magurele-Bucharest, Romania
E-mail: cristian.lungu@inflpr.ro

Abstract. The paper presents the principle of the thermionic vacuum arc method developed at the National Institute for Laser, Plasma and Radiation Physics, Magurele-Bucharest, Romania and preparation of the of multifunctional nanostructured films with antifriction and magnetoresistive properties.

1. Introduction

Nowadays, multifunctional, nanostructured films are continuously developing in order to improve the properties of coated surfaces such as wear resistance, low friction coefficients, hardness, roughness, smoothness, chemical inertness and electrical/magneto-resistance.[1–6]. Thanks to these properties, nanocrystalls open up possibilities for applications in nanoelectronics, novel optical devices, integrated digital circuits, biomedical applications, etc. [7–10].

There are many methods for obtaining nanostructured materials as for example: Filtered Cathodic Vacuum Arc (FCVA) [11–13], Mass Selected Ion Beam (MSIB) [14], Pulsed Laser Deposition (PLD) [15–17], Laser Arc [18–19], etc.

The best control of the preparation of nanostructured materials can be achieved by the use of energetic species either by direct ion beam deposition or by bombardment of materials (ion beam-assisted methods). Most systems applying energetic species are characterized by a complex nature of precursor particles with a large distribution of energies [20]. This makes the controlled growth and study very difficult.

The original plasma-based method providing high energy ions (of hundreds eV) suitable for the preparation of pure elements or composites without gas inclusions is presented here. The method, developed at the National Institute for Laser, Plasma and Radiation Physics is known as Thermionic Vacuum Arc (TVA).

The method uses an electron beam emitted by an externally heated cathode (a tungsten grounded filament) accelerated by a high anodic voltage. The electron beam can evaporate the anode materials as neutral pure particles and facilitate their deposition on the substrate. When the anode potential is increased up to a certain value, the evaporation rate increases as much as to allow an electrical discharge to be ignited in the evaporated pure material and the discharge is maintained even when the discharge current is as low as a few hundreds mA. By using the TVA method, the metal deposition takes place in high or ultrahigh vacuum conditions, without the presence of any gas.

2. Thermionic vacuum arc method principle

The material that needs to be evaporated is introduced in a crucible made of graphite TiB_2, Mo, W, etc located at a few millimeter far from the cathode. On the cathode it is applied a positive voltage of 1–6 KV, depending on the material that needs to de deposited and on the conditions in which the deposit process takes place.

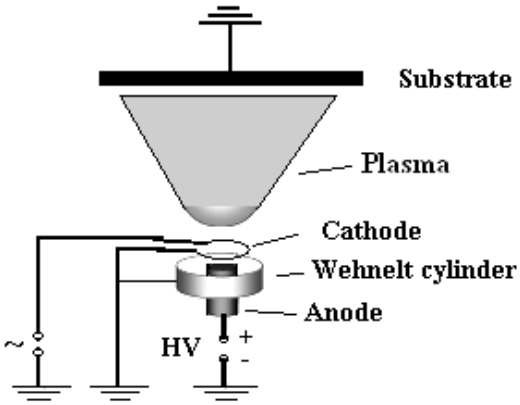

Fig.1. The experimental set-up of the thermionic vacuum arc method.

The external heating process of the cathode is done and that is why the lighting up process of the arc and it's maintaining can be done at 0.3 A and at anodic voltage of over few hundreds of V, even kV. Limiting the discharge current is done with the balast resistors. Thus it is reached the usual discharge in vacuum arc. By the current's external heating process of the cathode and of the voltage applied to the anode some, small current discharge and high voltage may be generated exclusively in the anode vapor material. The substrates being located in vacuum, the evaporated material deposits both under the form of atoms and ions. The measurements done have shown that the energy of the ions that arrive on the surface may

vary between 100 and 900 eV, depending on the heating of the cathode and on the voltage applied to the anode. The ionic current at the substracte surface may be of the μA order, depending on the some parameters. By the TVA method the atoms deposed on the substrate are extracted from the anode by electron bombardment, the electrons' mass being much smaller than the ions' one it is expected to be extracted from the anode especially atoms and not large clusters. The existence of an ionic bombardment in the film formation process is benefic for its adherence and compactness. In this case, the ions are of the same nature with the material that needs to be deposed and have high enough energies and intensities for their acceleration towards the surface. Due to the thickness of the prepared films that is of the hundred of nm order, and to the deposit rates that are of some nm/s order, the duration of the deposition is of the minutes order, which makes a possible heating of the surface, due to the thermal radiation of the TVA plasma, to be negligible, and the film integrity does not be affected during the deposition. The reaction chamber is cylindrical, having a volume of about 0.8 m^3. The access port is located in the front side of the deposition system. This is provided with a monitoring system of the thickness and deposition rate of the film working on the principle of the quartz balance crystal. The chamber is provided with a number of flanges to which may be attached the isolated or mechanical entries (for linear movements or rotations of the elements from the chamber). The side parts of the chamber have some stainless steel pipes attached which allows the activating of a water cooling or heating system. The anterior part of the chamber opens completely. It is provided with two circular windows through which one can view the phenomena from the inside of the chamber. The windows are protected by applying on the inferior part some glass screens of appropriate diameter. For ignition and maintaining the TVA arc are necessary two circuits: one for the heating of the cathode filament, where a relatively low voltage source (0–24 V) provides a 10–150 A current and another one that is designed for the running up of the arc discharge, being used for this an adjustable source of high voltage (0–5 kV) and a current up to 3 A.

If the breakdown conditions are accomplished, applying a high voltage between the heated cathode and the anode, in the space between the electrodes appears a bright discharge, extremely stable as far as the shape, the value of the discharge current and the emitted light intensity are concerned. From the moment of applying the voltage up to the ignition of the discharge it is necessary a time in which the anode material to melt, and then it begins to evaporate up to the settling of a stationary density of the anode material vapors in the inter-electrode space. Once with the ignition of the TVA arc, it will occur volume expansion of the plasma of the anode material vapors, the plasma having a density which will decrease with the distance (r) towards the crucible which contains the melted material. The number of the evaporated particles from a source of punctual evaporation which fall in the unit from the surface unit of the surface is in inverse ratio to the square of the distance from the source to the surface. The whole quantity of evapo-

rated material in a second towards all the directions from the surface if the source is m* (g/s) then the the dm* material quantity which passes through a solid angle $dw = ds \cdot \cos\theta / r^2$ is given by the relation :

$$dm^* = \frac{\left(\frac{m^*}{4\pi}\right) \cdot \cos\theta \cdot ds}{r^2} \quad (1) \tag{1}$$

which is the Knudsen-Lambert law relation, where ds is the elementary surface on which the deposition is done, θ – the incidental angle at the *ds* surface.

In the TVA, the cathodic fall reaches values of the kV order. This is due to the fact that for the starting the breakdown process, the voltage must, on one hand ensure the production of a sufficient number of electric charge carriers, and on the other hand, ensure the generation of the gas in which the discharge through an appropriate atom vapors density is produced. After the ignition of the discharge the distribution of the potential is set in the inter-electrodes space, the cathode fall having a much bigger value than in the case of the usual electric arc. The electron emission from the cathode is independent from the parameters of the TVA plasma. If the cathode – anode distance increases (for example due to the evaporation of the anode material), in order to maintain the electron current which comes from the cathode to the anode, the accelerating voltage must be raised which leads to the raising of the cathode fall. If the TVA electronic gun is inclined to an angle from which the anode is "seen" at a smaller solid angle, for collecting the same electron' current, we must rise the cathode fall. After the ignition of the TVA, the stable maintaining of the discharge requires a continuous generations, with a constant rate, of the anode material vapors. This is accomplished by the dissipated power at the anode, which is equal with the product between the anode fall (U_a) and the intensity (I_a) of the arc current:

$$P_a = U_a \cdot I_{arc} \tag{2}$$

The expansion of the plasma is produced on the walls of the chamber, the vapors' density according to Knudsen-Lambert law, from the anode on the radial direction. Next to the anode, the elementary processes that determine the expansion of the plasma are the collisions determined by the Coulomb forces, and also by the collisions between the isolated atoms and those through which the charge transfer takes place. The balance of the charge carriers is equilibrated on one hand by the losses determined by the bipolar -ambipolar transport and by the reactions in volume, and on the other hand, the main production process of the electric charges is the electronic impact. During the expansion of the plasma from the anode, the atoms' and the ions' densities decrease. The bipolar - ambipolar transport of electrons and the number of ions determine an electric field which slows the electrons and accelerates the ions. In the anode plasma's zone the transfer collisions have an

important role in the ions' transport. At small distances towards the anode of approximately 10 nm, only the Coulomb collisions influence the charge transfer towards the electrodes. For bigger distances, the plasma is expanded without the collisions. As far as the potential is concerned, the difference between the interelectrode plasma and the metallic chamber is equal to the cathode decrease, because the chamber and the cathode are tied to the ground. The ions produced in the plasma will end up on the chamber's walls with energy equally proportional with the cathode decrease. This one is influenced by the geometric and optional factors: the interelectrode distance (d), the relative position of the electrodes given by the φ angle and the cathode temperature determined by the intensity of the heating current of the filament (I_f).

The total decrease of voltage on the arc U_{arc} is given by:

$$U_{arc} = U_c + U_{pl} + U_a \,, \tag{3}$$

where U_c – the potential fall on the cathode: U_{pl} – the plasma total potential fall; U_a – the potential fall on the anode. U_a has such a value that the generation process of the atoms from the anode must be maintained at the same level with the one before the breackdown of the arc discharge, which means:

$$U_a \cdot I_{arc} = I \cdot U_s \tag{4}$$

where I_{arc} is the intensity of the current that passes through the arc: U_s – the breakdown intensity; I – the intensity of the current before the ignition process of the discharge on the U_{pl} plasma potential. The plasma's conductivity is big so as the cathode fall can be neglected in comparison with the other values of the potential falls on the anode and the cathode. The stability of the discharge is an important characteristic of the TVA method. The TVA plasma's peculiarities may be resumed: a pure discharge in the evaporated material's vapors in the anode crucible; the ionization degree is high due to high plasma density; the ions' energy is stable; the cathode fall reaches the kV level; the arc parameters adjustment may be done only modifying the operations' conditions (I_f, U_a, I_a).

3. Nanostructured, low friction C-Cu, C-Sn coatings

Nanostructured, low friction films in the system C-Cu, C-Sn were prepared using the TVA method [21–26] where the C-Cu, C-Sn systems were chosen because carbon-metal compounds had been known as promising components of antifriction layer to be applied on the plain bearing of the engine moving parts. They were simultaneously deposited on a set of substrates, including engine half-bearings positioned at different distances from the evaporation sources. Carbon and metal (Cu, Sn) atoms were directed to the substrates, the deposition rates and consequently the relative concentrations of carbon and metal in the prepared films being determined by the discharge parameters (I_f, U_a, I_a) and geometrical parameters

(deposition rates controlled by the $1/r^2$ rule, where r is the respective distance to the carbon or metal anodes).

The obtained films were compact, uniform and free from columnar structure. Scanning and transmission microscopies (SEM and TEM) analyses show that the morphology and structure of the samples depends strongly on the processing parameters.

The experimental set-up is shown schematically in Fig. 2. The cathode of each of two guns consisted of circular heated tungsten filament surrounded by a stainless steel Wehnelt cylinder, which had aperture of 50 mm in diameter for carbon and 76 mm in diameter for copper and tin evaporation.

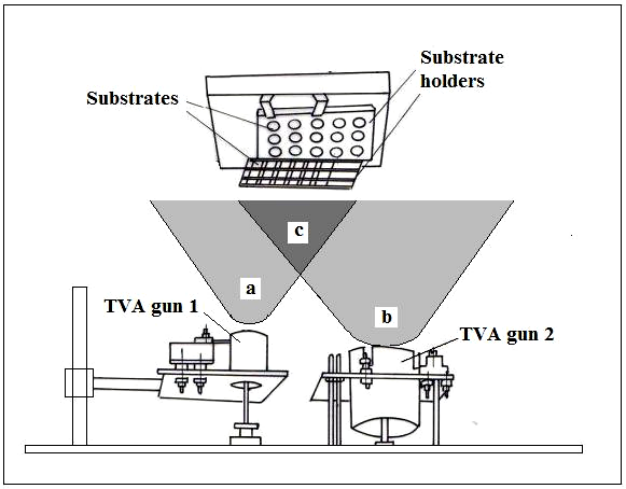

Fig. 2. Schematic sketch of C-metal (Cu, Sn) film preparation;
a) carbon plasma, b) metal plasma, c) mixed plasmas zone.

The filament for the carbon discharge was made of a tungsten wire of 0.8 mm in diameter while the filament for the Cu/Sn discharge was made of tungsten wire of 1 mm in diameter. The filaments were arranged in the apertures of the Wehnelt cylinders, about 100 mm bellow of the plane of their front surface. A hydrogen free graphite rod 50 mm in length and 20 mm in diameter was used as the carbon anode and Cu/Sn granules of 6–10 mm in diameter filed the anode crucible in the Cu/Sn case. The inter-electrode gap was adjusted in the range of 4–8 mm. The sample substrates, stainless steel discs of 25 mm in diameter and 3 mm thickness were settled in appropriate sample holders fixed on the surface of the heating device. The distance between anodes and sample holder was 260 mm. Substrates were situated on an imaginary line, parallel with the carbon and metal (Cu, Sn) evaporators, each sample situated at different distances relative to the evaporators. In this way in a single running deposition, were produced coatings with different relative carbon-

metal concentrations, in order to emphasize the role of metal inclusion in an amorphous carbon matrix.

The thickness of the film has been measured during the deposition with an *in situ* thickness monitor, which uses the quartz oscillators. After termination of the deposition, the anode voltage and the applied current to the TVA gun filament have been reduced to zero. The samples have been kept in the deposition chamber, under high vacuum for about 120 minutes, for the chamber's and substrate's temperature to cool down.

3.1. I-V characteristics in carbon and copper and tin vapors

In order to produce plasma in pure C vapors, the tungsten filament of the TVA gun 1 was heated by an a.c. of 50–60 A, 16–20 V. The emitted electrons were focused on the C anode by a Wehnelt cylinder.

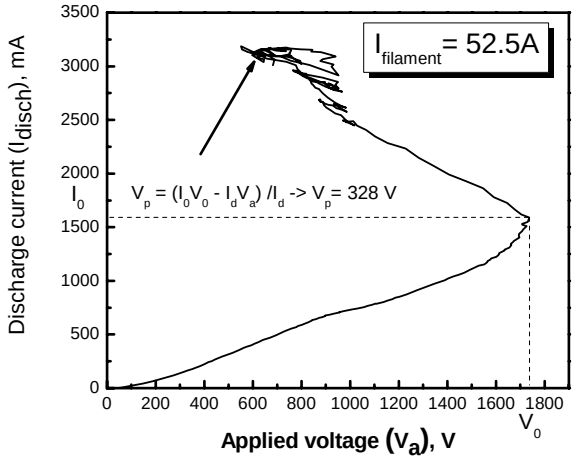

Fig. 3. The *I-V* characteristics in C vapors.

The anode applied voltage was increased up to about 2000 V in that a way that when the upper part of the C rod was heated up over 3500°C and the C vapor pressure exceeded 10^{-2} torr, a bright electrical discharge was ignited. After the ignition, the discharge voltage decreased to the 1000–2000 V as function of filament heating current. Figure 3 shows the *I-V* characteristic, the voltages and current of the vacuum arc in C vapors. An estimation of the plasma potential was made taking acoount of the following formula:

$$V_P = (I_0V_0 - I_{discharge}V_{ignition})/I_{discharge} \quad (5)$$

Using data taken from the Fig.'s 3 graph, the V_P = 328 V. The corresponding C ion energy is 328 eV. At this energy, the C ions are implanted into the sample surface determining strong adhesion and compactness of the film. The chemical

bonding of the formed carbon layer is affected to, leading on the formation of the sp^3 bonding. In the same way the plasma was running in Cu vapors. In this case the filament heating current was in the range of 55–65A at 18–22 V. On the *I-V* characteristics for a filament current of I_f = 55.5 A for different values of the cathode-anode distances (d_1–d_5: 5; 7; 9;11 and 13 mm respectively) we observed lower values of the ignition voltage; 650–900 V instead of 2000 V in the case of C. The Cu ion energy was in the range of 10–100 eV, enough to form stable composite layers C-Cu. In the Sn case, the ignition voltages were in the range of 400–700 V.

3.2. The control of the deposition rate

The deposition rate was measured during depositions using a Edwards, FTM-7 quartz balance monitor as function of the introduced power, cathode temperature, the cathode-anode distance. The automated acquisition system recorded simultaneously the I-V characteristics of the discharges (from which were extracted information concerning the vacuum arc breakdown voltage, the stable running parameters, including the introduced power into the arc discharge plasma) and the deposition rate displayed in the real time by the monitor. The deposition rate increases as the cathode temperature decreases (the heating current of the filament used as cathode) as well as the increase of the anode-cathode distance. The two parameters (the heating current filament and the anode-cathode distance) permit introduction of higher electrical power into the vacuum arc plasma, due to the possibility to increase the voltage of the stable running plasma in the pure material vapors. Figures 4–9 show the evolution of the breakdown power (the $I_{breakdown} \cdot V_{breakdown}$) and the stable running power ($I_{stable} \cdot V_{stable}$) as function of the cathode temperature (the intensity of the heating cathode current) and the anode-cathode distance for the studied elements.

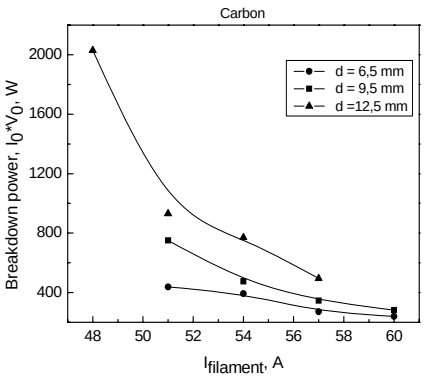

Fig. 4. The breakdown electrical power in carbon vapors as function of the intensity of the circular cathode filament current and anode-cathode distance (*d* = 6.5–12.5 mm).

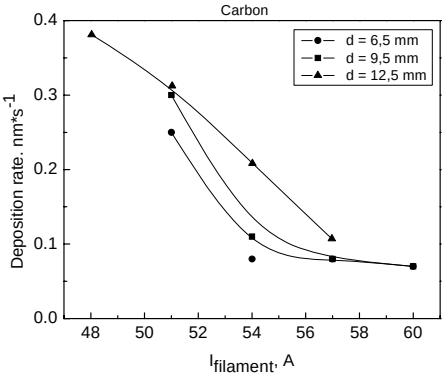

Fig. 5. Deposition rate of carbon film as function of the intensity (temperature) of the circular cathode filament current and anode-cathode distance (*d* = 6.5–12.5 mm).

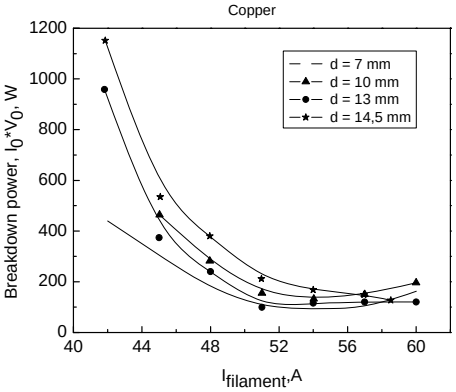

Fig. 6. Breakdown power in copper vapors as function of the intensity of the circular cathode filament current and anode-cathode distance (d = 7–14.5 mm).

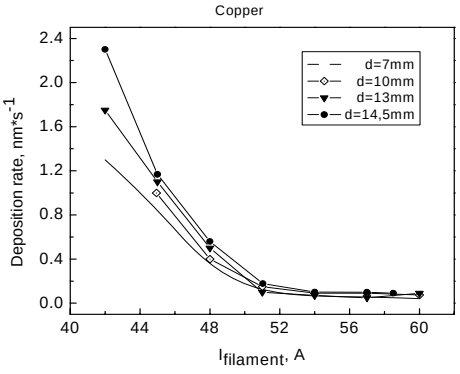

Fig. 7. Deposition rate of copper film as function of the intensity of the circular cathode filament current and anode-cathode distance (d = 7–14.5 mm).

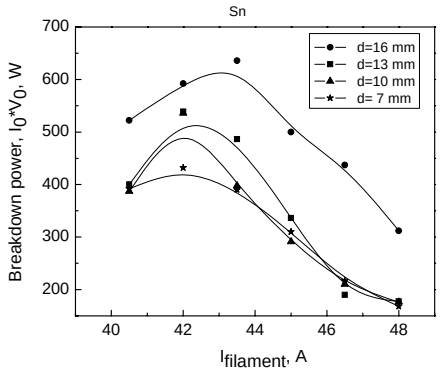

Fig. 8. Breakdown power in Sn vapors as function of the intensity (temperature) of the circular cathode filament current and anode-cathode distance (d = 7–16 mm).

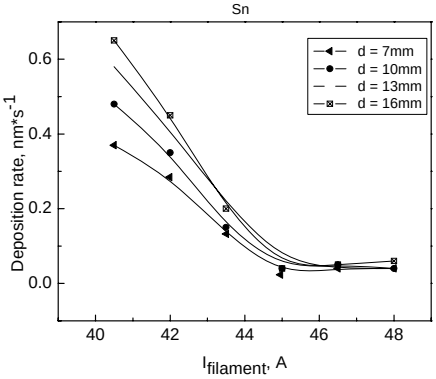

Fig. 9. Deposition rate of Sn film as function of the intensity (temperature) of the circular cathode filament current and anode-cathode distance (d = 7–16 mm).

3.3. SEM analysis of the C-Cu/C-Sn films

Using an optimized set of the working parameters (ensuring a maximum introduced power in the thermionic vacuum arc plasma), stainless steel substrates were coated with C-Cu and C-Sn films. The film morphology and composition were analyzed by scanning electron microscopy (SEM), a PHILIPS ESEM 120 model, having an electron dispersive spectroscopy (EDS) microprobe. The SEM images which present the surface morphology of the films settled in the closest position relative to the carbon plasma are shown in Fig. 10 and Fig. 11.

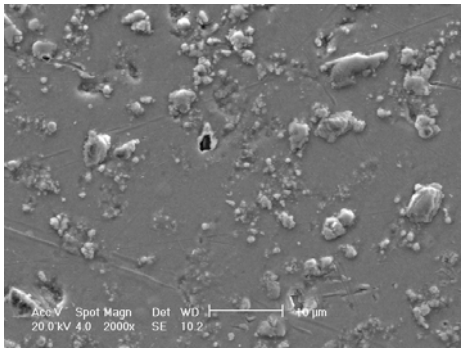

Fig.10. SEM image of the C-Cu film.

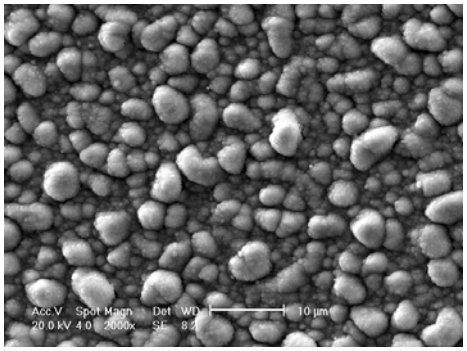

Fig. 11. SEM image of the C-Sn film.

The compositional analysis of the C-Cu and C-Sn films is presented in Table 1.

Table 1. Compositional analysis of the C-Cu and C-Sn Films

C-Cu (wt%)		C-Sn (wt%)	
C	6.15	C	15.91
O	2.63	O	4.25
Cu	91.22	Sn	79.84

3.4. TEM analysis of C-metal films

The prepared C-Cu, C-Sn films were analyzed by transmission electron microscopy (TEM) using a high resolution (up to 1.4 Å) PHYLIPS CM 120 apparatus. The samples were prepared for TEM observation in the following steps: a small film was removed by a sharp cutter from the sample surface and settled on a special amorphous carbon coated TEM grid. Figure 12 and Figure 13 show the images of the C-Cu and C-Sn structures: spherical features with about 10 nm and respective 20 nm diameter appear together with small grains with size of about 5 nm. The mentioned features are surrounded by a brighter matrix assigned to the amorphous carbon.

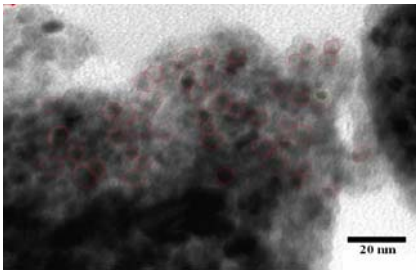

Fig. 12. TEM image of the C-Cu film.

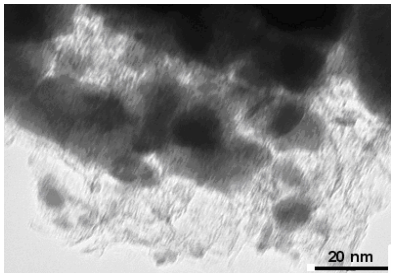

Fig. 13. TEM image of the C-Sn film.

3.5. XRD analysis of C-Cu/C-Sn films

In order to characterize the crystalline structure of the prepared films, the diffraction patterns were measured using following conditions: XRD device: TUR-M62, accelerating voltage: 40 kV; current intensity: 20 mA; copper anticathode (λ=1,54 Å), Filter: Ni; Angular step: 0.05° (theta); slits: 1.75; 1.75/1.09 mm. Analyzing the XRD pattern of the C-Cu and C-Sn films, shown in Fig. 14 and Fig. 15 can be assumed that the metallic grains embedded into the carbon matrix were polycrystalline with large size Cu/Sn crystals.

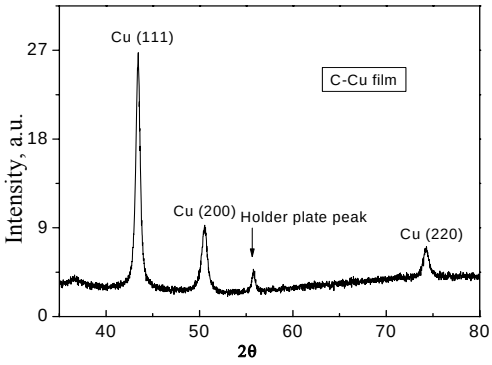

Fig. 14. XRD pattern of the C-Cu film.

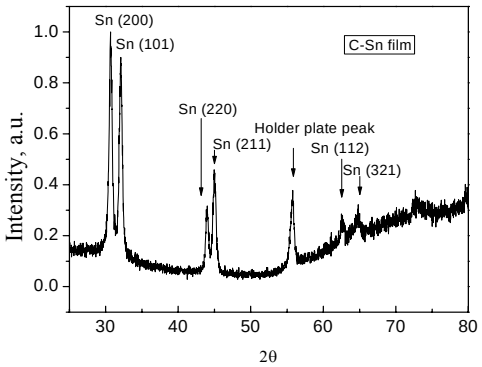

Fig. 15. XRD pattern of the C-Sn film.

The as-deposited C-Cu antifriction films have strong Cu (111) and Cu (200) texture normal to the surface located at 43.46°±0.01° and 50.56±0.01°, respectively, as well as a weak Cu (220) peak located at 74.29°±0.02°. This is due to the tilted texture from the substrate normal as a result of embedding Cu crystals into the amorphous, diamond like carbon (DLC) matrix. These peak positions are slightly larger than their equilibrium values of 43.30°, 50. 43° and 74.13° for the Cu (111), Cu (200) peaks and the Cu (220) peak, respectively. This corresponds to a lattice constant 3.606 Å, that is 0.25% smaller than the equilibrium value of 3.615 Å. We believe this is due to a tensile stress in the nanostructured carbon layer that reduces the lattice constant and pushes the XRD peaks to larger 2 positions. The tensile stress can originate from the thermal stress induced from the mismatch between thermal expansion coefficients of the substrate, the amorphous carbon matrix and the whole compound film. The similar behavior was observed on the C-Sn films, when only Sn XRD peaks were identified: strong (111), (101), (220), (211) and weak peaks: (112) and (321).

3.6. Tribological analysis

Frictional properties of the coatings were investigated using a CSM (Switzerland) ball-on-disc tribometer. The C-Cu and C-Sn films were deposited on 25 mm

diameter stainless steel discs. The tribometer counterpart was a 6-mm sapphire ball. The tests were performed in ambient atmosphere (50% humidity and 23ºC temperature). A load of 1 N was applied using a dead-weight, the track radii were 3 and 4 mm and the sliding speed was set to 5 mm/s. The duration of the tests was 30 min, giving a total of approximately 10 m of sliding. During the tests, the friction coefficient was recorded on a PC and after test completion; each wear track was studied using OM and SEM.

As shown in Fig. 16 and Fig. 17 the coefficient of friction of the prepared films drastically decreased (three to five times) compared to those of the substrate (stainless steel), showing the effect of dry lubrication of Cu and Sn embedded in an amorphous-carbon matrix.

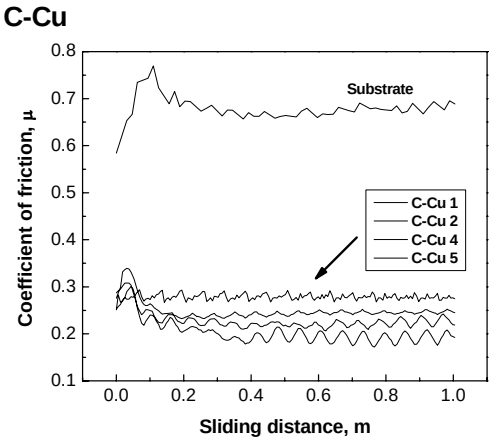

Fig.16. C-Cu film friction vs. sliding distance; Load: 1N, sliding speed: 0.1 m·s^{-1}.

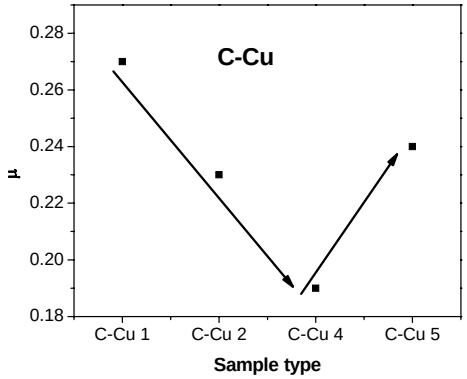

Fig. 17. Average friction coefficient of different C-Cu films.

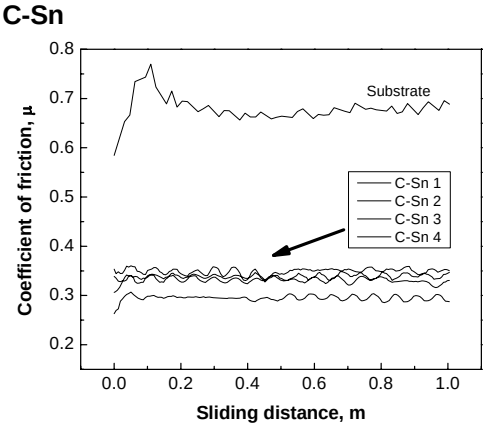

Fig. 18. C-Sn film friction vs. sliding distance; Load: 1N, sliding speed: 0.1 m·s^{-1}.

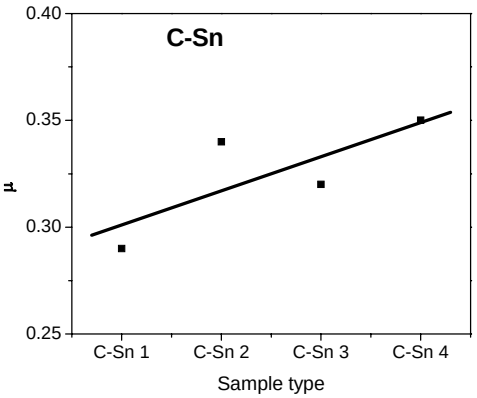

Fig. 19. Average friction coefficient of different C-Sn films.

4. Tunneling magnetoresistive films preparation

Granular thin films for tunneling magneto-resistance (TMR) applications can be made of 3d magnetic metal (e.g. iron, nickel or cobalt) clusters, uniformly distributed within an insulating matrix (e.g. magnesium or aluminum oxide). These films are able to provide both positive and negative electrical resistance variation under the influence of an external magnetic field. Due to the presence of the insulating matrix, the electrical resistance of such nanostructures is much higher than that of similar GMR structures with magnetic clusters dispersed in a conductive matrix. By similitude with layered systems, a much enhanced magneto-resistive effect would be also expected, making such structures more attractive for applications as magnetic memories or sensitive magnetic field sensors. In a layered system, the magnetoresitance coefficient, MR(θ), depends on the angle θ between the magnetic moments of the ferromagnetic layers sandwiching the dielectric layer, by (1−cos θ)/2 (in turn, angle θ depends on the magnetic field applied to the system). The proportionality coefficient is TMR = $(R_a - R_p)/R_p$, with R_a and R_p the resistances of the system in anti-parallel and parallel configuration of the ferromagnetic layers. This proportionality coefficient depends in a specific way on the geometrical/ structural parameters of the TMR structures [27, 28]. In the Julliere's simplified model [29], only the spin polarizations of the conduction electrons in the two electrodes influence the TMR coefficient. Electrons with a certain spin orientation in the first electrode should find empty states of similar spin orientation in the second electrode, in order to enhance the tunneling probability [30]. However, the spin polarization of the tunneling current between the ferromagnetic electrodes is extremely sensitive to surface and interface properties because of the short coherence length characteristic of the ferromagnetic state. Similitude with the case of TMR multilayered systems can be found also in the case of nanoglobular systems. The advantages are mainly related to the simplicity of the system and hence with the high productivity and lower production costs of such structures. The disadvantages are related to the more complex physics behind the systems, related to both the imperfections of the large interface between the magnetic nanoparticles and the dielectric structure as well as to the much more complex magnetic configuration of the nanometer-size magnetic grains. In the case of a nanoglobular system, the electrons will become spin polarized in the first magnetic cluster. Their associated wavefunction should tunnel towards a neighboring cluster with empty density of state of similar spin polarization and parallel orientation of the magnetic moment. The magnetic configuration of the ferromagnetic nanosized clusters is of main importance, but their response to an applied field is not so straightforward, due to their size distribution, possible intergranular couplings, possible superparamagnetic effects or impurities/ nonstoichiometry near the interface of the ferromagnet/dielectric phases.

The materials used for the simultaneous deposition were cobalt, as magnetic material, and MgO, as insulator. The TVA deposition method is described elsewhere [31, 32] as well as in the section 2 of this paper. In principle, it is based on the intense evaporation of the depositing materials placed in crucibles of high positive potential (anodes), under the bombardment of electrons emitted from a heated cathode filament.

The substrates were setled on an imaginary line between the two evaporators, the concentration of the magnetic metal in the MgO dielectric matrix will expectedly increase continuously, due to the different distances of the substrates to the two anode positions (e.g. the sample placed just in the front of the Co crucible will present the maximum amount of Co). The film substrates were 1cm^2 rectangular pieces of industrial glass. The composition of the obtained nanogranular films was analyzed by Energy Dispersive Spectroscopy (EDS) measurements, the film morphology and structure by Scanning Electron Microscopy (SEM) and High Resolution Transmission Electron Microscopy (HRTEM) and the magnetic properties were monitored via Magneto-Optic Kerr Effect (MOKE). Finally, the structural and the magnetic properties have been correlated with electron transport properties and TMR effects measured via the four point method with current in plane geometry.

4.1. Characterisation of the prepared magnetoresistive films

The relative amount of Co (at %), as obtained by EDS measurements on different samples, versus the distance from the Co crucible to the film supports, is presented in Fig. 20 (e.g sample P3 corresponds to a distance of 28 cm whereas sample with the highest index number, P7, is the sample placed to a distance Co crucible- film substrate of only 20 cm). One can observe the almost linear decrease of the cobalt concentration with the distance between the film substrate and the Co crucible.

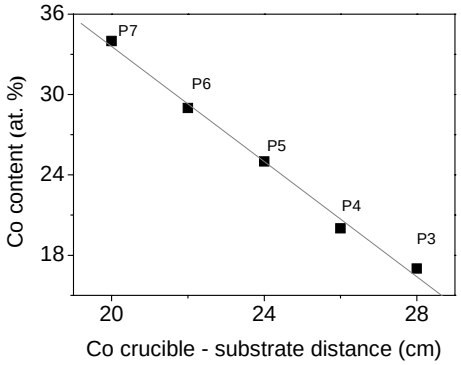

Fig. 20. The Co concentration against the distance between Co crucible and the film substrate.

As a consequence of the different Co contents in the different samples from P3 to P7, one can study the dependence of the TMR effect and the related structural and magnetic behaviors, versus the concentration of the magnetic element. It is worth mentioning that the thickness of the central sample, P_5, is 250 nm and the other samples present thicknesses of the same magnitude inside the measuring error bars.

The variation of the TMR effect at room temperature (RT) versus the relative content of cobalt in the magnesium oxide dielectric film is shown in Fig. 21. It is easily observed that the TMR effect has a maximum value at a given Co concentration (26 at % in this case) and decreases much faster at lower Co concentration as compared with the case of higher Co concentrations in the range from 17 to 34 at %. Most likely, this effect has to be related with different morphology or size distribution of the Co particles in the dielectric matrix and we will return to this point after presenting structural and magnetic data.

The MOKE hysterezis loops obtained at RT on samples of different Co contents are presented in Fig. 22. It might be observed that the magnetization in 0.1 T decreases continuously with the Co content. In order to get a hint about the correlation between TMR effect and magnetic data we will present in the following some structural and magnetic aspects of sample P_5, showing the highest TMR effect. Both the as prepared sample, as well as an annealed P_5 film processed by a post-deposition thermal treatment, performed at 300°C for one hour in high vacuum condition (10^{-5} torr), were analyzed.

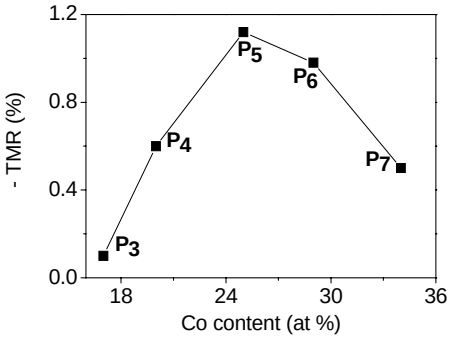

Fig. 21. The room temperature TMR effect for different Co concentrations in the MgO films.

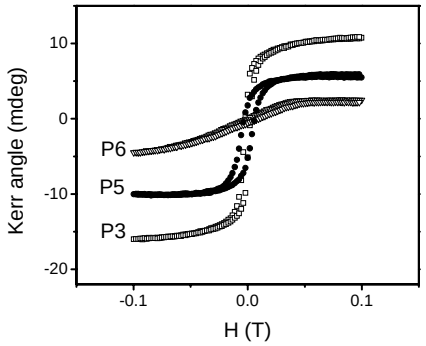

Fig. 22. Room temperature MOKE measurements on sample with increasing Co content.

The EDX spectra collected on the two samples have shown slightly increased oxygen content in the annealed sample as compared with the as prepared one, which will lead presumably to an increased partial oxidation of the Co particles in the annealed sample. The SEM images of the as deposited and the annealed P_5

films, presented in Fig. 23 (a and b), evidence clearly much larger grains induced by the thermal treatment.

HRTEM images of the as prepared and the annealed P_5 films are shown in Fig. 24 (a) and Fig. 24 (b), respectively. Electron diffraction patterns evidence that the structure with well arranged atomic planes belongs to metallic Co grains, which dimensions are much larger in the thermally annealed sample as compared with the as prepared one.

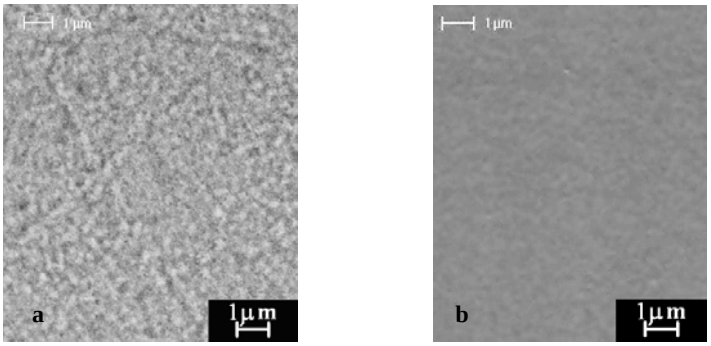

Fig. 23. SEM images of the as deposited (a) and annealed P5 sample (b).

In addition, the electron diffraction has proven the presence of cobalt oxide (the antiferromagnetic Co_3O_4) in both the as prepared and the annealed samples. The amount of the cobalt oxide is slightly larger in the annealed sample, in agreement with the EDS data proving increased oxygen content in this sample. The RT MOKE hysteresis loops of the as prepared and annealed P_5 films are presented in Fig. 25.

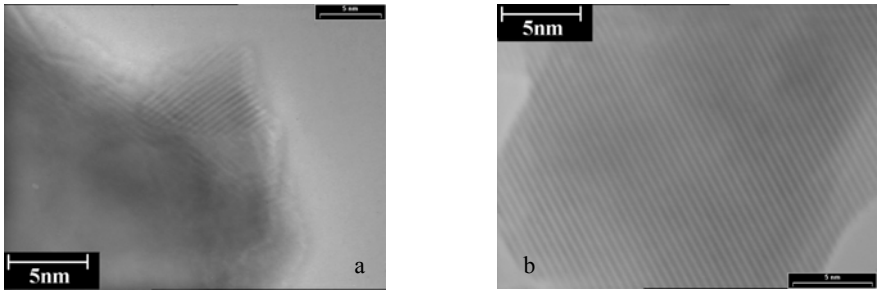

Fig. 24. TEM image of the as deposited (a) and annealed P5 sample (b).

One can see that the thermal treatment increases the saturation magnetization of the film as well as its coercive force. Based on this structural/morphologic picture of the two samples, we can interpret the corresponding RT MOKE curves as follows. In the as prepared sample, there are formed very fine Co grains (about

5 nm) with a thin magnetic dead layer of cobalt oxide, giving rise to a reduced magnetization of the sample (due to both defected spin structure and possible superparamagnetic behavior of the grains of lower dimensions). After the annealing treatment, the initial clusters agglomerate giving rise to much larger Co particles. In spite of a slightly thicker cobalt oxide layer on the surface, the Co core is significantly larger than in the case of the as prepared film, which leads finally to higher average magnetic moment per Co atom, due to both a less defected magnetic structure and reduced magnetic relaxation of the Co particles. Hence, a higher magnetization and coercive field is expected for the annealed sample.

The field dependent TMR curves obtained at RT on the two P_5 films (before and after annealing) are shown in Fig. 8. A much increased absolute value of the TMR effect has to be mentioned for the as prepared sample, in comparison with the annealed one. That is probably due to increased distances between the magnetic grains in the annealed samples (directly connected with formation of much larger magnetic grains), diminishing drastically the tunneling probability in this system. However, the thermal treatment appears to decrease the TMR coefficient in Co-MgO systems, opposite to the effect of similar treatments applied to nanoglobular GMR systems like Co-Cu or Fe-Cu [33].

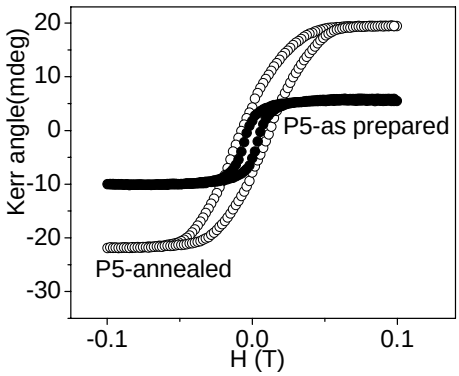

Fig. 25. Room temperature MOKE measurements of the as prepared and the annealed film.

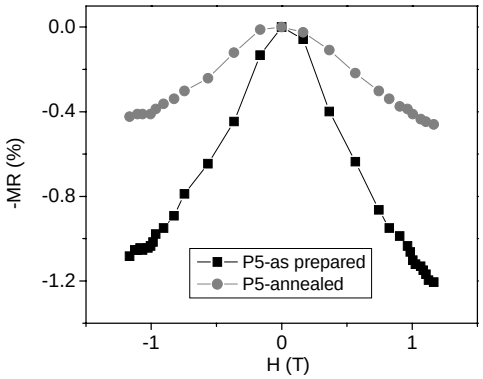

Fig. 26. TMR curves of the as deposited and annealed nanoglobular films.

The above observation can be also extended to the case of the MOKE and TMR data presented in Fig. 25 and Fig. 26, respectively. The continuous decrease of the magnetization in 0.1 T with the Co relative content in the films has to be explained by a reduced average size of the Co grains (and implicitly by an increased particle density) in films of higher Co content. That would explain the fast increase of the TMR effect when increasing the Co content in the film up to the optimal value of 26 at. %. However, by further increasing the Co content, the TMR effect starts to decrease, due to an enhanced magnetic disorder specific to the very

large surface area of very fine particles, connected also with a very weak magnetic response to the applied field.

5. Conclusions

Nanostructured films for applications as antifriction and magnetoresistive layers were prepared by the original method of thermionic vacuum arc (TVA) developed at the National Institute for Laser, Plasma and radiation Physics. The obtained results are summarized as follows:

Irregular and hemisphere type protuberances were formed on films surfaces. The surface roughness could be controlled by adjusting the process parameters such as the intensity of the filament heating current (the cathode temperature), the introduced electrical power and the anode cathode distance and the distance between the anodes and the substrate.

Metal concentration into the carbon matrix was controlled by the distance between the sample and the metal anode.

The XRD patterns of the prepared composite films show polycrystalline metal grains embedded into the amorphous carbon matrix.

In dry sliding the coefficient of friction depend on the metal concentration into the carbon matrix, having a minimum when the copper was of 71at% into the C-Cu composite layer and having a linear dependence in the C-Sn case with a minimum coefficient of friction when at 29 at % Sn into the C matrix.

Tribological performances of the carbon metal (metal: Cu, Sn) overlays were improved decreasing the coefficient of friction by 2–3 times compared with those of the substrate material.

Co-MgO thinn films with different Co contents were obtained by fixing film substrates at different distances from the Co and MgO sources.

A maximum TMR effect of about 1% was obtained at room temperature for a relative content of 25 at. %Co.

High resolution TEM and electron diffraction measurements reveal the presence of the Co grains as well as surrounding shells of cobalt oxide.

Post deposition thermal treatments of the Co-MgO films (one hour, 300ºC, 10^{-5} torr) increase substantially the average Co grain size and slightly the thickness of the cobalt oxide layers around nanograins. These structural results support the increased magnetization in the room temperature MOKE hysterezis loop in the annealed samples as well as the decreased TMR effect, due to increasing distances among Co nanograins.

References

[1] DEKEMPENEER E. H. A., MENEVE J., SMEETS J., Surf. Coat. Technol. **120-121** (1999) 692.
[2] LIU Y., ERDEMIR A., MELETIS E. I., Surf. Coat. Technol. **82** (1996) 48.

[3] JEONG G.-H, HWANG M.-S., JEONG B.-Y., KIM M.-H., LEE C., Surf. Coat. Technol. **124** (2000) 222.
[4] LEVOSKA J., LEPPÄVUORI S., Appl. Surf. Sci. **86** (1995) 180.
[5] YANG S., CAMINO D., JONES A. H. S, TEER D. G., Surf. Coat. Technol. **124** (2000) 110.
[6] VASIRAGHI C., FERRARI A.C., OHR R., CHU D., ROBERTSON R., Diam. Relat. Mater. **13** (2004) 1416–1421.
[7] SMIETANA M., SZMIDTA J., DUDEK M., NIEDZIELSKI P., Diam. Relat. Mater. **13** (2004) 954.
[8] REISEL A. D., SCHURER C., MULLER E., Diam. Relat. Mater. **13** (2004) 823–827.
[9] GRILL A., IBM J Res Develop., Vol. **43**, No. 1, 2, (1999) 147.
[10] CAREY J. D., SILVA S R. P., Phys. Rev. B **70**, (2004) 235417.
[11] MCKENZIE D. R., MULLER D. A., PAITHORPE B. A., Phys. Rev. Lett. **67** (1991) 773.
[12] LOSSY R., PAPPAS D.L., ROY R.A., CUOMA J.P., BRULEY J., J. Appl. Phys. **77** (1995) 4750.
[13] YI X. Z. Z., WU T. Z. X., WANG G., ZHANG H., Surf. Coat. Technol. **161** (2002) 120.
[14] LIFSHITZ Y., LEMPERT G. P., GROSSMAN E, Phys. Rev. Lett. **72** (1994) 2753.
[15] XIONG F., WANG Y.Y., LEPPERT V., CHANG R.P.H., L. Mater. Res. **8** (1993) 2265.
[16] KAUTEK W., PENTZIEN S., CONRADI A., KRÜGER J., BRZEZINKA K.-W., Appl. Surf. Sci. **106** (1996) 158.
[17] VOEVODIN A. A., DONLEY M. S., Surf. Coat. Technol. **82** (1996) 199.
[18] ZIEGEL H., SCHEIBE H. J., SCHULTRICH B., Surf. Coat. Technol. **97** (1997) 385.
[19] LOGOTHETIDIS S., GIOTI M., LIOUTAS CH., Carbon **36** (1998) 539.
[20] DEKKER M., Inc., *Dekker Encyclopedia of Nanoscience and Nanotechnology*, DOI: 10.1081/E-ENN, 120013606, (2004) 415.
[21] LUNGU C. P., MUSTATA I., MUSA G., ZAROSCHI V., LUNGU A. M., IWASAKI K., Vacuum, **76**, Issues 2-3, (2004) 127.
[22] LUNGU C. P., MUSTATA I., MUSA G., LUNGU A. M., ZAROSCHI V., IWASAKI K., TANAKA R., MATSUMURA Y., IWANAGA I., TANAKA H., OI T., FUJITA K., Surf and Coat. Techn, **200**, (2005) 399.
[23] LUNGU C. P., MUSTATA I., MUSA G., LUNGU A. M., BRINZA O., MOLDOVAN C., ROTARU C., IOSUB R., SAVA F., POPESCU M., VLADOIU R., CIUPINA V., PRODAN G., APETROAEI N., J. of Optoelectronics and Advanced Materials, Vol. **8**, No. 1, (2006) 74.
[24] LUNGU C. P., TUDOR A., BRESCIA R., LUNGU A. M., SURDU-BOB C. C., CHIRU P., POMPILIAN O., POROSNICU C., LAURIAN T., MUSTATA I., Special Issue of the International Journal of Surface Science and Engineering (IJSurfSE), in print.
[25] TUDOR A., VLASE M., Analele Universitatii din Galati, in print.
[26] LUNGU C. P., *Nanostructure influence on DLC-Ag tribological coatings*, Surf. and Coat. Techn. **200**, (2005) 192.
[27] XI L., J. Phys. D: Appl. Phys. **33** (2000) 621.
[28] MOODERA J. S., MESERVEY R. H., *Magnetoelectronics*, Ed M.Johnson, (Academic Press) 2004.
[29] JULLIERE M., Phys.Lett., **54 A** (1975) 225.
[30] TSYMBAL E. Y., MRYASOV O. N., LECLAIR P. R., J. Phys.: Condens. Matter **15** (2003) 109.
[31] KUNCSER V., MUSTATA I., LUNGU C. P., LUNGU A. M., ZAROSCHI V., KEUNE W., SAHOO B., STROMBERG F., WALTERFANG M., ION L., FILOTI G., Surf.& Coat. Techn. **1–4** (2005) 980.
[32] LUNGU C. P., MUSTATA I., MUSA G., LUNGU A. M., ZAROSCHI V., IWASAKI K., TANAKA R., MATSUMURA Y., IWANAGA I., TANAKA H., OI T., FUJITA K., Surf. and Coat. Techn. **200** (2005) 399.
[33] ANGHEL A., LUNGU C. P., MUSTATA I., ZAROSCHI V., LUNGU A. M., BARBU I., BADULESCU M., POMPILIAN O., SCHINTEIE G., PREDOI D., KUNCSER V., FILOTI G., APETROAEI N., Csech J.Phys. **56 B** (2006) 16.

Electrochemical Assisted Plasma Processing for Advanced Materials

V. A. ANDREI[1], C. DIACONU[1], G. ONCIOIU[1], M. FULGER[1], O. RUSU[1], E. COACA[1], C. DUCU[2], V. MALINOVSKI[2]

[1]Institute for Nuclear Research, Mioveni, Str. Campului no. 1,
E-mail: victor.andrei@nuclear.ro
[2]University of Pitesti

Abstract. Complex surface structures were developed on stainless steels used as structural nuclear materials, by various Plasma processing methods which include:

- Electrochemical assisted Plasma Processing (PE): the steel substrates were modified by nitruring and nitro-carburising plasma diffusion treatments;
- Carbonic films electrodeposition.

The processes and structures obtained in various experimental conditions were characterized by correlation of the results of the complementary techniques: XPS, "depth profiling", XRD, LAXRD and EIS.

The corrosion behaviour was studied by electrochemical techniques, and was correlated to the microstructure and the composition of the surface layers which are strongly depending of the electrical parameters.

An overall description of the processes involved in the surface properties improvement is presented.

1. Introduction

Electrochemical assisted Plasma Processing (PE) is a generic term which is used to describe a variety of high voltage electrochemical processes, which feature plasma-discharge phenomena occurring at an electrode-electrolyte interface. The plasma discharges occurs at the metal/electrolyte interface when the applied voltage exceeds a certain critical breakdown value (typically several hundreds of Volts). Discharge phenomena have been observed in both positive and negative biasing of a metal electrode and, depending on the electrode-electrolyte combination and polarisation parameters, can vary widely in appearance: from a steady uniform glow surrounding the electrode to discrete short-lived micro-discharges moving rapidly across its surface. Consequently, discharge characteristics – electrical, spatial and temporal, also vary significantly, providing different thermodynamic conditions at

the electrode surface. This critically determines the surface layer composition, structure and properties, which can be optimised for numerous surface engineering applications, if the discharge phenomena can be understood (and thus properly controlled) [1, 2].

Physical aspects of Electrochemical assisted Plasma Processing include mechanisms of discharge generation, its phenomenology (e.g. spatial, temporal and electrical characteristics of individual micro-discharge events, as well as their collective behaviour), and thermal impact produced to the surface layer of metal electrode. Knowledge on these aspects is extremely important to understand structure and phase formation in the surface layer.

Duplex treatments which include plasma electrolytic techniques are extremely useful where, in practical tribological situations, the application of a liquid lubricant is impossible and a thin top layer of a material with lubricious properties should be applied as part of a surface composite coating [1].

PE technology now represents a rapidly developing sector of surface engineering, however, major uncertainties remained concerning the process optimization, control and repeatability, which were mainly caused by the fact that the scientific understanding of key process fundamentals and discharge phenomena lagged well behind empirically based treatment trials. A first step towards closing these knowledge gap between fundamental process understanding and coating characteristics is the characterization of the non-homogeneous surface structures developed by plasma-assisted electrochemical processes.

In frame of the present study extensive trials were carried out in order to develop complex surface structures, on stainless steels used as structural nuclear materials, by various electrochemical treatments which include:

- anodically thermo-electrochemical treatments: the steel substrates were modified by nitriding and nitrocarburising plasma electrolytic diffusion treatments;
- carbonic films electro-deposition using a method for synthesis of DLC structures at atmospheric pressure and low temperature; a solution of acetylene in liquid ammonia was used as electrolyte [4].

2. Experimental

2.1. Thermo-electrochemical treatments

The model of the processes associated with thermo-electrochemical treatments of the steels is based on the mechanism of conductivity of the vapour-gas shell separating the anode from the solution [2]: the current carriers in the shell are anions of the electrolyte emitted from the solution under the action of a strong electric field.

The plasma discharges occurs at the metal/electrolyte interface when the applied voltage exceeds a certain critical breakdown value (typically several hundreds of Volts).

The critical value of the voltage is associated with the establishment of a stable three-phase system: metallic anode/ vapour-gas shell/ electrolyte solution.

The establishment of a stable three- phase system requires the transport by vapour-gas shell, of an electrical current enough great to generate the thermal flux necessary to assure the existence of a stable separation surface at the solution-vapour interface.

The critical value of the voltage is according to the critical value of the electric field necessary to assure the emission of the ions from electrolyte and the transport of the emitted ions, by vapour-gas shell to the anode.

The effects of the thermo-electrochemical processes are:

– anodic electrolytic heating: temperatures in the range 800–1200°C are established in 2–3 minutes;
– the diffusion of N and C species in the vapour-gas shell surrounding the anode and the interaction with metallic surface;
– the disconnecting of the voltage applied at anode/ solution interface results in the fast tempering of the steel-anode in the working solution, by fast condensation of the vapour-gas shell;
– after thermo-electrochemical treatment the nitrido-martensitic structure of the low carbon steels is changed.

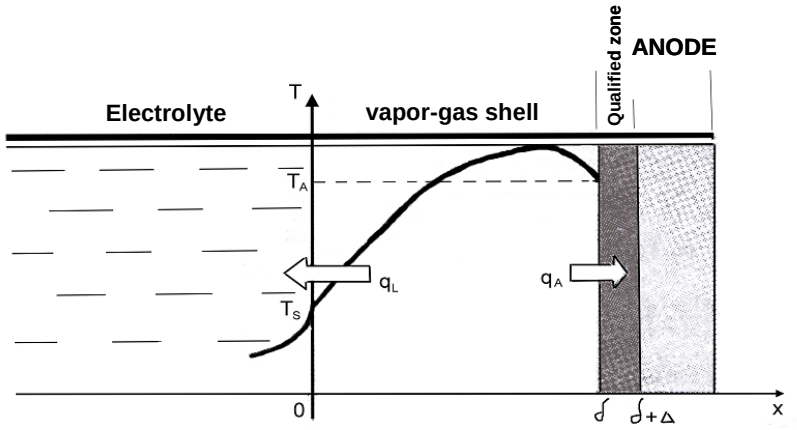

q_L – thermal flux at the interface steam-gaz coat/electrolyte;

q_A – thermal flux at the interface steam-gaz coat/anode;

T_A – anode temperature;

T_S – solution temperature.

Fig. 1. The three-phase system anode/ vapour-gas shell/ electrolyte solution.

Thermo-electrochemical treatments of carburizing and nitriding bath were applied using the equipment **TEC100 (SCINTI – Chisinau)** on carbon steel SA 106, austenitic steel 304 and martensitic steel 403. The experimental setup (Fig. 2.) was identically for carburizing (using glycerine solution as electrolyte) and nitriding (using NH_4OH solution as electrolyte) treatments. The parameters of the thermo-electrochemical treatments are presented in the Table 1.

Table 1. Thermoelectrochemical treatments (TE)

Material	TE	Sample code	Experimental parameters
Carbon steel SA 106	Carburising	106_C	U = 220 V, I = 6 A, t = 3 min
	Nitriding	106_N	U = 165 V, t = 3 min
Austenitic steel 304	Carburising	304_C	U = 220 V, I = 6 A, t = 3 min
	Nitriding	304_N	U = 165 V, t = 3 min
Martensitic steel 403	Carburising	403_C	U = 220 V, I = 6 A, t = 3 min
	Nitriding	403_N	U = 165 V, t = 3 min

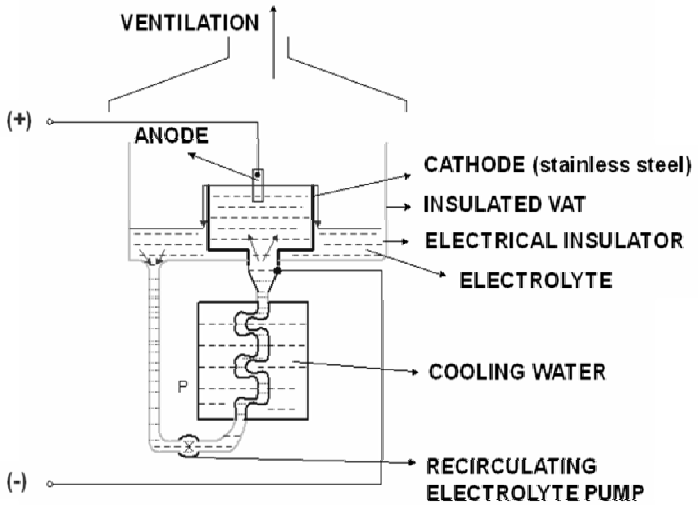

Fig. 2. Experimental set-up for thermo-electrochemical treatments.

2.2. Electrodeposition of carbonic films

A technique of carbonic films electro-deposition using a method for synthesis of DLC structures at atmospheric pressure and low temperature was developed; a solution of acetylene in liquid ammonia was used as starting electrolyte [3]. The acetylene was synthesized by calcium acetylide hydrolisis. The ammonia was obtained via distillation of NH_4OH. The working electrodes were stainless steel 304 samples treated by thermo-electrochemical carburising treatment. The evacuated

electrochemical cell was cooled in an acetone/dry ice bath while ammonia, anhydrous grade gas, was fed into the vessel and liquefied at ~ –60°C. Acetylene was then continuously bubbled through the vessel during the electrodeposition process.

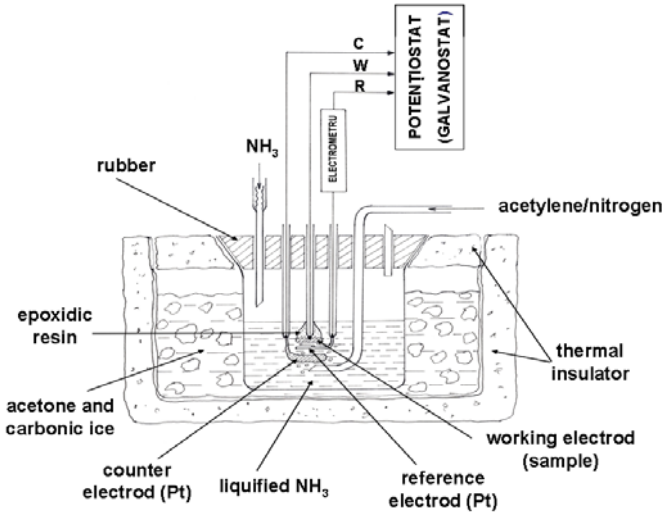

Fig. 3. Experimental set-up for electrodeposition of carbonic films.

The acetylene dissociates in NH_3, and the ions are discharged, by the reactions:

$$C_2H_2 \rightarrow C_2H^- + H^+$$

$$C_2H^- - 2e^- \rightarrow C_2 + H^+$$

A Princeton Applied Research 273 System (Potentiostat/ Galvanostat) was connected to the three electrodes and experiments were operated under potentiostatic control using anodic deposition, at a voltage in the range 1.4–6 V.

2.3. Characterization methods

The surfaces films developed by surface treatments were investigated by optical microscopy, ESCA, XRD and Electrochemical Impedance Spectroscopy. Corrosion behaviour was evaluated by electrochemical techniques [4].

Optical measurements were performed with NEOPHOT 2 optical microscope, and the microstructures of the treated materials were studied.

ESCA analyses (X-ray Photoelectron Spectroscopy – XPS) of the deposited films have been performed with an ESCALAB 250 (Thermo-Fisher Scientific) spectrometer. The residual pressure inside the measurement chamber was 10^{-10} Torr. The monochromatised X-ray Al K_α (E = 1486.6 eV) radiation was used and the calibration of the instrument was obtained taking as reference the silver line Ag $3d_{5/2}$ at 368.2 eV.

The **X-ray diffraction** data of austenitic steel 304 and martensitic steel 403 were collected at room temperature. Data acquisitions were made with a DRON UM1 diffractometer connected with PC. A horizontal powder goniometer in Bragg-Brentano focusing geometry with graphite monochromator was used. The incident Cu-Kα line, at 36 kV and 30 mA was used. The typical experimental conditions were: 10 s for each step, range angle 2θ = 25–120°, with a step of 0.05°. The patterns obtained in these conditions were used to make qualitative phase analysis. The range angle 2θ = 34–46° containing the 100% intensity peaks of Fe_3O_4, $Fe_{15}Cr_4Ni_2$, $(Cr, Fe)_7C_3$, CrN, FeO, CrC and CrFe were measured with a better statistics, 20 s for each step. In the same angular range the low angle incidence diffraction in order to determine the phase's presence in the surface films [3] from 1.0 to 8.0° incidence angle was performed.

Electrochemical impedance spectroscopy (EIS) measurements were performed using an PAR 273 System (Potentiostat/ Galvanostat), with Model 5210 Lock-in Amplifier. EIS measurements were performed at the open circuit potential, which correspond of the very small current into oxide layer, and the thickness of this oxide is not modified. The solution used in tests was the boric acid/ borax because that is a chemical inert environment for the superficial films developed on the samples.

3. Results

The results about the microstructures of treated samples and about corrosion rates (determined by Polarization Resistance Method) are presented in the Table 2.

Table 2. Microstructure of the films and corrosion rate

Sample	Surface film structure	Corrosion rate (mm/y)
106_C	Surface film – 10 μ	1.9×10^{-6}
106_N	Stratification surface structure: Compound layer – 100 μ Diffusion layer – 100 μ	2×10^{-6}
SA 106 as received		2.03×10^{-6}
304_C	Surface film – 50 μ	0.07×10^{-6}
304_N	Surface film – 10 μ	1.14×10^{-6}
304 as received		2×10^{-6}
403-C	Surface film – 400 μ	0.3×10^{-6}
403-N	Surface film – 150 μ	0.6×10^{-6}
403 as received		2.2×10^{-6}

EIS method provides qualitative information about surface thin films from Bode and Nyquist plots analysis. In the case of carburized and nitrating 304 samples the highest impedance values are closed to 10^5 Ω. The angle phases are smaller than 90° that signifies that films are not fully capacitive. For carburized 304 sample the angle phase has a greater value (63°) than nitrating 304 sample (48°) so, the films obtained by carburization are less porous. Smaller values of the capacitances correspond to a slow growth of the layers indicating a stability of this passive layer. The very high values of electrical resistances demonstrate a good corrosion resistance. The following values $C_{layer} = 6.244\times10^{-5}$ F/cm^2 and $R_{layer} = 1.9\times10^4$ Ωcm^2 for carburized 304 and $C_{layer} = 1.065\times10^{-4}$ F/cm^2, $R_{layer} = 5.836\times10^4$ Ωcm^2 for nitrating 304 denote that the layer obtained by carburization is thicker, corrosion resistant and protective. The value of polarization resistance for carburized sample is 70 000 Ωcm^2 and for nitrating sample 33 000 Ω cm^2; a greater polarization resistance indicate a smaller corrosion rate. The impedance value of carburized 403 is greater than the impedance value of the nitrating 403 so the film obtained by cementation has better properties. In both cases the angle phases have values smaller than 90º so the films are not fully capacitive that signify a porosity of films or a roughness of metal surfaces. The angle phase of carburized 403 is greater than the angle phase of nitrating 403 sample so the oxide layer developed by *carburizing TE* is less porous. Polarization resistance for carburized 403 is 450 000 Ωcm^2 comparatively with 20 000 Ωcm^2 of nitrating sample so, a very small corrosion rate for *carburized* sample. In the case of *carburized* sample the film capacitor act like a constant phase element (is a non-ideal capacitor because of the non-homogeneous surface). The value of the film capacitance in the case of nitrating sample is two magnitude orders greater than carburized sample. A smaller value of coating capacitance signifies an adherent film so, by *TE – carburizing* treatment can obtain thicker oxide layers.

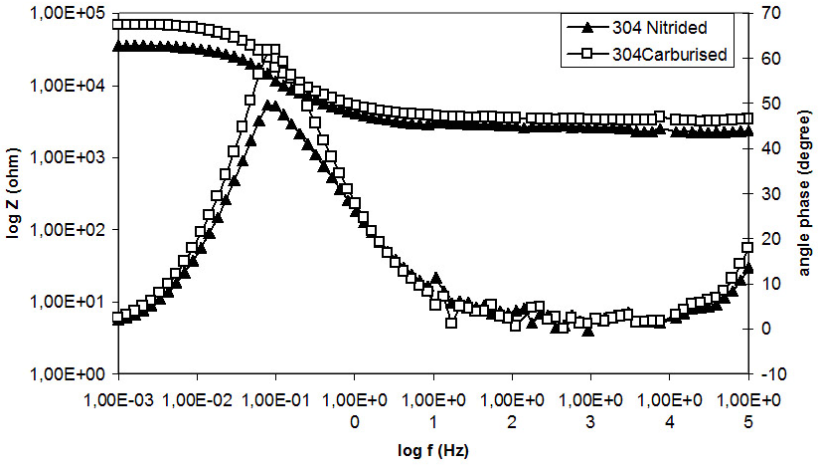

Fig. 4. Comparative Bode and angle phase plots for 304 carburised and 304 nitrided samples.

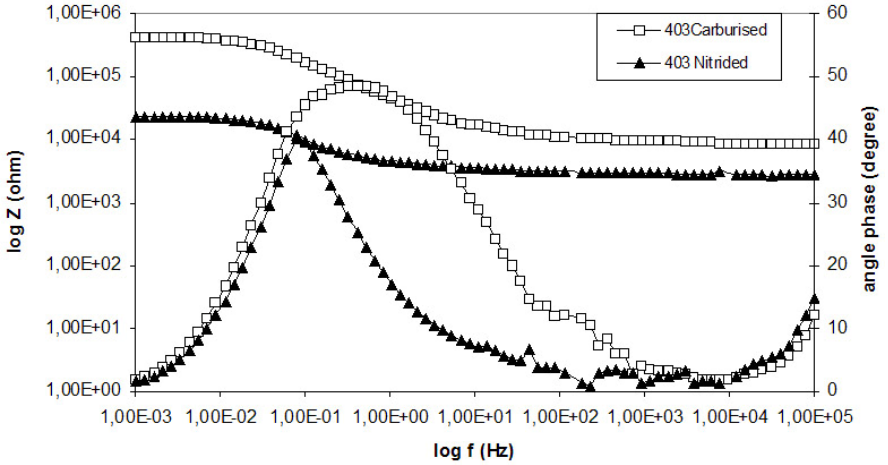

Fig. 5. Comparative Bode and angle phase plots for 403 carburised and nitrited samples.

Figures 6 and 7 show the XRD patterns of the austenitic steel 304 respectively martensitic steel 403 measured at room temperature, in three metallurgical states: as-received, after carburizing and after nitrating treatments.

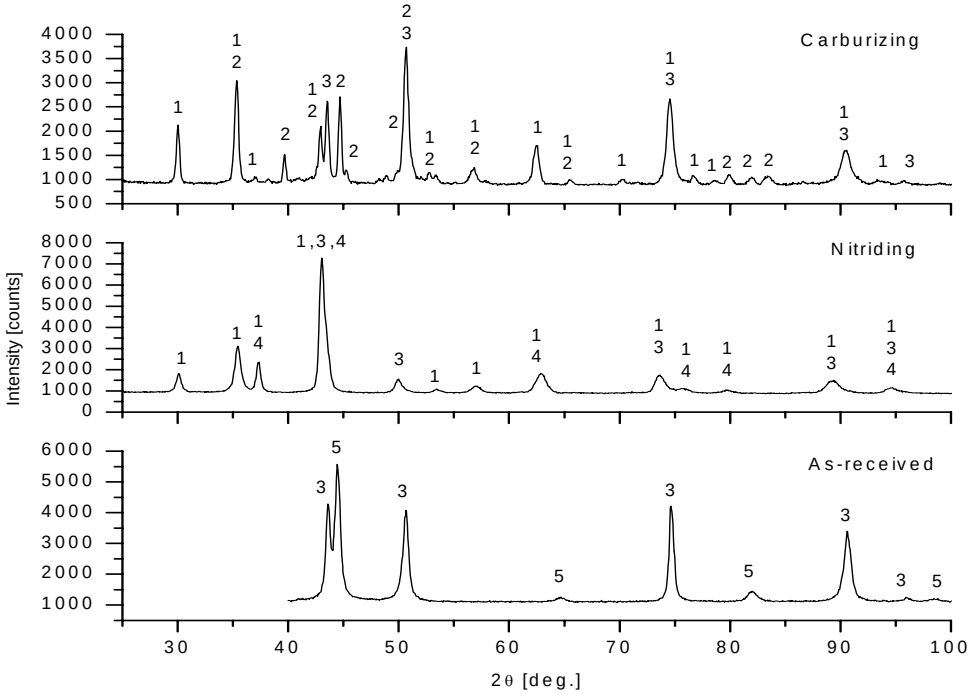

Fig. 6. XRD patterns of austenitic steel;
1 = Fe_3O_4, 2 = $(Cr,Fe)_7C_3$, 3 = $Fe_{15}Cr_4Ni_2$, 4 = CrN, 5 = CrFe.

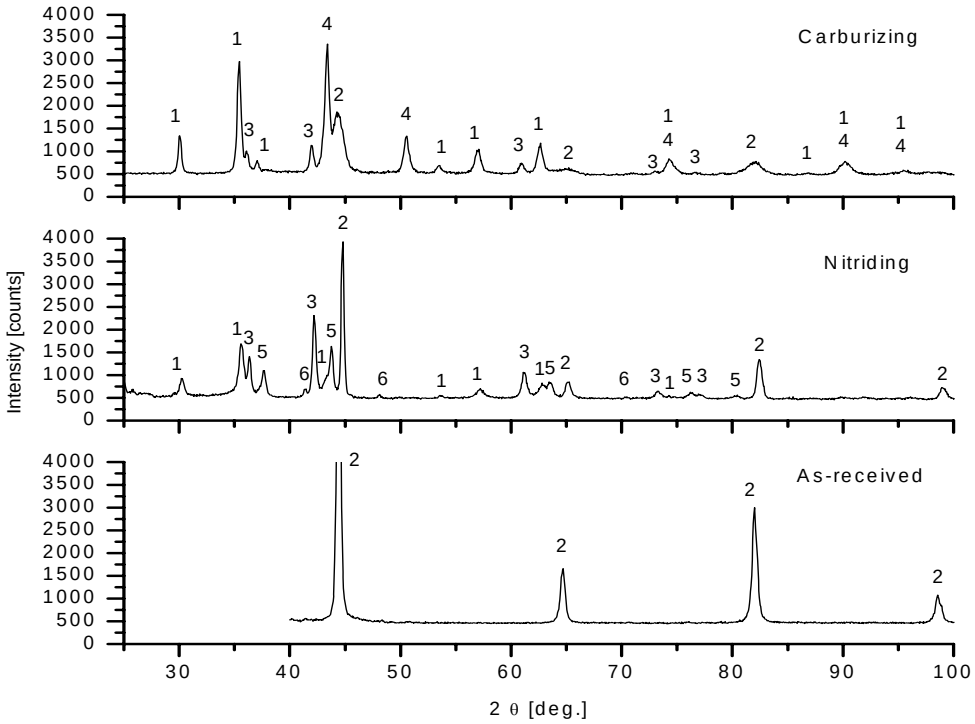

Fig. 7. XRD patterns of martensitic steel;
1=Fe_3O_4, 2=CrFe, 3=FeO, 4=CrC, 5=CrN, 6=γFe_4N.

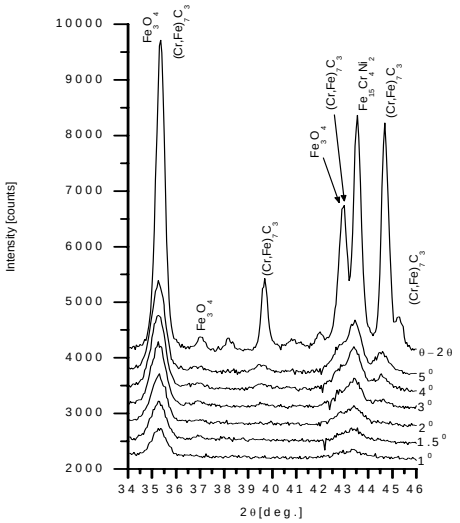

Fig. 8. LAXRD patterns of austenitic steel 304 after carburizing treatment.

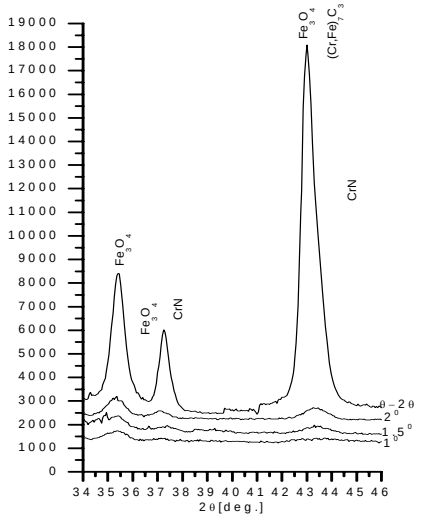

Fig. 9. LAXRD patterns of austenitic steel 304 after nitriding treatment.

Figures 8, 9, 10, 11 show the low angle X-ray diffraction patterns of austenitic and martensitic steel after carburizing and nitrating treatments, acquired between 1° and 8° incidence diffraction angles. The line profile analyses were applied in order to determine the mean crystallite size and the micro-strains of the surface layer, the results are presented in [3].

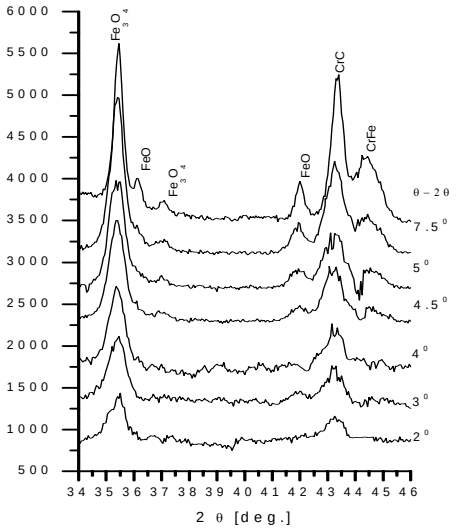

Fig. 10. LAXRD patterns of martensitic steel 403 after carburizing treatment.

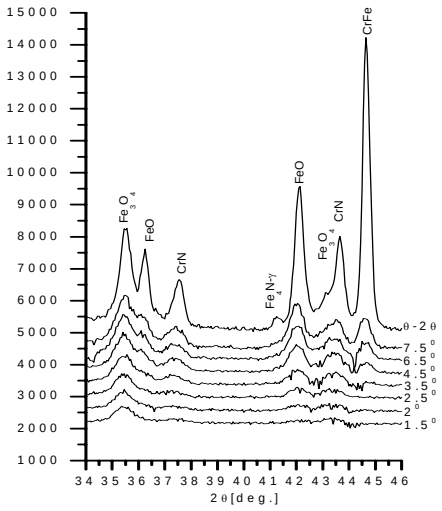

Fig. 11. LAXRD patterns of austenitic steel 403 after nitriding treatment.

A survey XPS spectrum (Fig. 12) on the austenitic steel 304 and martensitic steel 403 after carburizing and nitriding treatment was recorded and the data quantification was performed [5]. The surface elemental composition (atomic %) are presented in the Table 3.

Table 3. The surface elemental composition (atomic %)

	304-C	**304-N**	**403-C**	**403-N**
C1S	82.08	68.14	87.58	63.17
FE2P3	1.12	1.8	1.75	0.7
O1S	7.01	7.01	3.84	20.96
NI2P3	0	1.25	0.38	0.16
CR2P	9.79	16.59	6.45	8.61
N1S		5.2		6.4

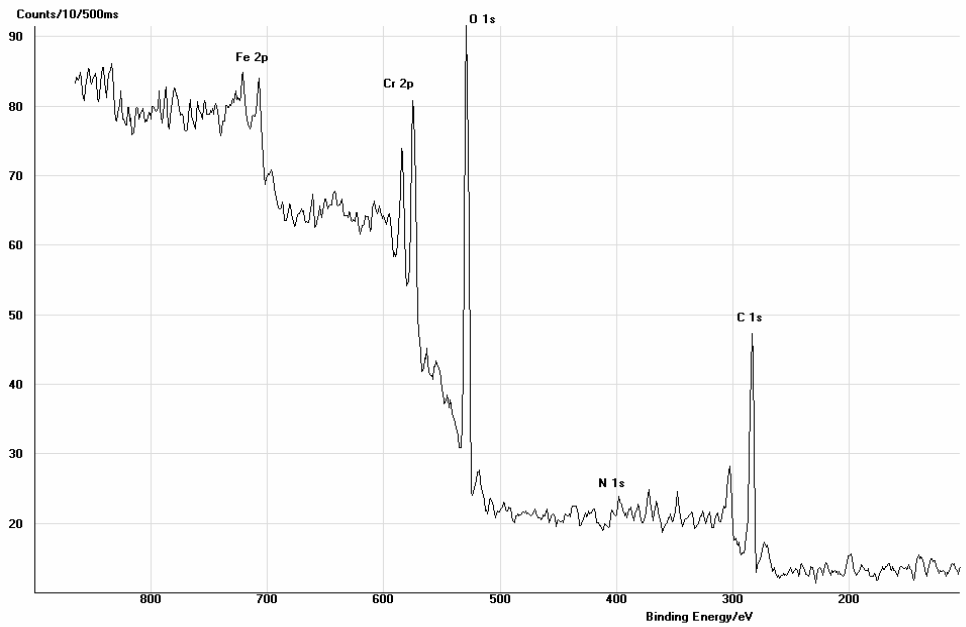

Fig. 12. Survey XPS spectrum on 304_C sample.

The analysis of the Fe2p3/2 component of the Fe2p doublet, using a deconvolution procedure (Fig. 13) confirm the presence of Fe_3O_4 identified by XRD and shows the presence of some spinelic oxide on the surface of austenitic and martensitic steels after thermo-electrochemical treatment.

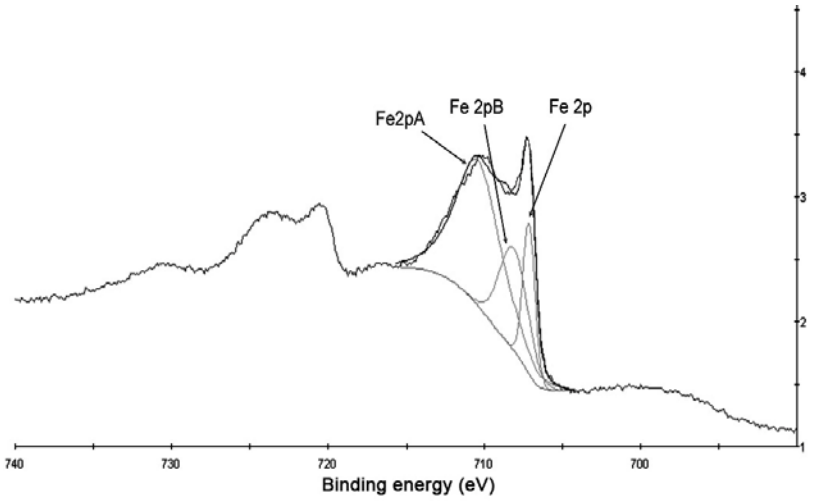

Fig. 13. Analysis of Fe 2p peak in XPS spectrum on carburised 304 austenitic steel.

Fe 2p component	Chemical bond	Binding Energy	At. %
Fe2p	(FeCr)	707.2	17.10
Fe 2p A	(FeCrO) Fe_3O_4	710.8	54.06
Fe 2p B	Fe_3C	708.6	28.84

Work in progress

An electrochemical method was developed for carbonic thin films deposition on selected steels substrate modified by PE treatments (electrodeposition of DLC films from a solution of acetylene in liquid ammonia at low temperature and low potential); preliminary XPS analysis indicate DLC structure of deposited films (Fig. 14).

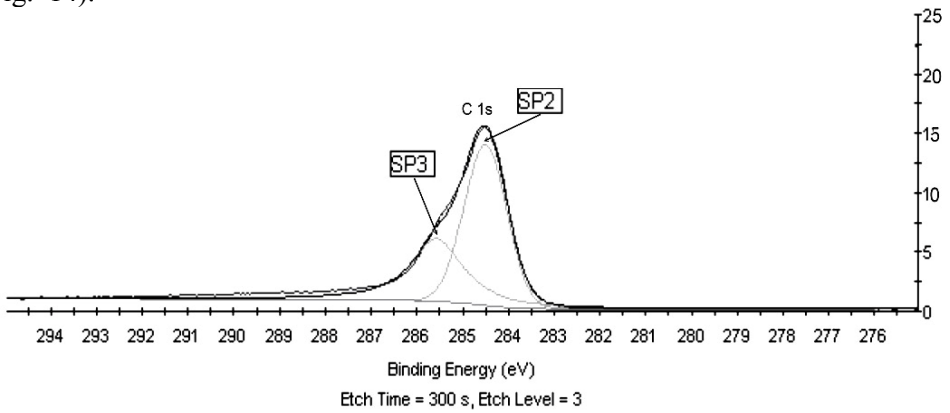

Fig. 14. XPS analysis of the electrodeposited carbonic layer.

The XPS analysis of the interface carbon layer/ substrate proves the 43%–55% sp^3 carbon bonds in the carbonic deposited layer.

Further developments related to the improvement of the duplex treatments are required to increase the sp^3 bonds concentration in the carbonic layer.

The electrodeposition method for DLC films deposition has a number of potential advantages over other methods: simplicity of apparatus, simplicity of film doping and film modification, favorable condition for growing new metastable forms of carbon because of the low temperature and the fact that the process is not in equilibrium.

4. Conclusions

The carbon steel SA 106, the austenitic steel 304 and the martensitic steel 403 have a very good corrosion behavior, after thermo-electrochemical treatments. The

protective oxide layer of Fe_3O_4 is growth on austenitic and martensitic steels by thermo electrochemical treatments of carburizing and nitrating. By LAXRD we found that Fe_3O_4 appear as external layer both on austenitic and martensitic steel. On to the martensitic steel the surface layer contains also CrC and CrN for carburizing respectively nitrating treatment.

The surface layer microstructures do not differ too much for austenitic and martensitic steel after carburizing treatments. By nitrating treatments, the microstructures of martensitic steel layer is different of austenitic steel surface layer.

For carburizing treatments, the thickness of oxide surface layer on martensitic steel ($\alpha_{lim} \approx 4.5°$) is greater than on austenitic steel ($\alpha_{lim} \approx 1.5°$). For nitrating treatments, these thicknesses are the same for both steel types ($\alpha_{lim} \approx 1.5°$).

An electrochemical method was developed for carbonic thin films deposition on selected steels substrate modified by PE treatments (electrodeposition of DLC films from a solution of acetylene in liquid ammonia at low temperature and low potential); the XPS analysis of the interface carbon layer/ substrate proves the 43% – 55% sp^3 carbon bonds in the carbonic deposited layer.

References

[1] MATTHEWS A., LEYLAND A., YEROKHIN A., PILKINGTON T., IGR Report:EPSRC Grant No.GR/ R15696.
[2] GANCHAR V. I., ZGARDAN I. M., DIKUSAR A. I., Surface Engineering and Applied Electrochemistry, **5**, 13–19, 199.
[3] NOVIKOV V. P., DYMONT V. P., Appl. Phys. Lett. **70**(2),1997.
[4] DUCU C., MALINOVSCHI V., ANDREI V., *Microstructures Characterization of Protective Surface on Electrochemical Treated Nuclear Steels*, EMRS, 2007.
[5] BRIGGS D., SEAH M. P. (eds.), *Practical Surface Analysis*, 2nd ed. Vol.I, *Auger and X-ray Photoelectron Spectroscopy*, Wiley, New York, 1990.

Organic-Inorganic Hybrid Composites

M. OLARU[1], T. BURUIANA[1], R. CRISTESCU[2], I. MIHAILESCU[2]

[1]*Petru Poni* Institute of Macromolecular Chemistry,
41A Gr. Ghica Voda Alley, 700487 Iaşi, Romania
[2]National Institute for Lasers, Plasma and Radiation Physics,
409 Atomistilor, RO-077125, Bucharest-Magurele, Romania
E-mail: olaruma@icmpp.ro

Abstract. The aim of this study was to synthesize and characterize new poly(ethylene glycol)s (PEGs) hybrid composites with or without a basic drug content, e.g., 2-[4-(2-methylpropyl)phenyl]propanoic acid (ibuprofen), obtained at different pH values. Through sol-gel approach of the polymeric matrix chloro-propyltriethoxysilane with a PEG precursor that contains a fluorescent dye (lissamine rhodamine-B sulphonyl chloride), new kind of hybrid materials were obtained in which silica aggregates were dispersed in the form of domains with typical sizes in the micrometer range, while the formation of quasi-spherical particles of nanometer dimensions was connected with PEG cladded and PEG-connected silica structures. The incorporation of ibuprofen within sol-gel derived matrix is expected to lead to compounds that allow a controlled and reproducible release of the drug. At the same time, in order to provide quality films highly required in the controlled released drug systems and to study the influence of the derivative group on both film structure and morphology, thin films of novel PEG derivatives with carboxyl and amine functional groups through matrix-assisted pulsed laser evaporation technique (MAPLE) were obtained.

1. Introduction

Among the various techniques used so far for the preparation of hybrid composites, sol–gel is one of the most versatile and widely used methods. The advantages of the process include low processing temperature methods that starts from homogeneous solution, thus giving a better control over structure and properties of the matrix. Therefore, such organic–inorganic hybrid materials offer endless opportunities for tailoring by design chemical, physical [1], biochemical [2,3], optical [4,5], sensing properties. [6] and separation in chromatography [7]. The hybrids having combined characteristics of organic and inorganic substances promise new materials of high performance/functionality to fully exploit this approach with benefits of the understanding of the two “worlds” (polymers and ceramics).

Poly(ethylene glycol)s (PEGs) are macromolecules representing a hydroxy-terminated polymeric chains of ethylene oxide repeating units, whose terminal hydroxyl groups are primarily responsible for the enhanced polarity of PEG molecules [8]. In the last years, considerable effort has been focused on the preparation of different types of block-copolymers containing PEG sequences to improve the hydrophilicity and physico-mechanical and biological properties of some polymers, especially polyesters. Among these structures, poly(ethylene glycol)-poly(L-lactic acid) (PEG/PLLA) is recognized for its ability to form more interesting nanoarchitectures with unique properties, such as temperature-dependent swelling, optical transmittance, and superior mechanical characteristics and so on [9]. Other examples include PEG–poly(propylene glycol)-PEG tribloc copolymers [10] obtained through "grafting to" process. On the other hand, PEG being a water- and organic-soluble polymer is often subjected to chemical modification and attachment to other molecules and surfaces in order to modulate the solubility and increases the size of the included molecules [11]. As result, a wide range of applications of PEG can be categorized as follows: purification of proteins, nucleic acids and biological materials, surface modification for retarding protein adsorption, platelet adhesion and thrombogenicity, drug conjugation and drug release [12].

Through sol-gel approach, PEG was utilised to protect the colloidal particles or to encapsulate biologic components with applications in biochemistry, separation technology, diagnostics and obtaining optical biosensors [13]. Many papers have been published on the use of PEG (or PEG-based block-copolymers) as structuring agents during the preparation of silica. It was evidenced the complexity of these reactions and that the phase separations are very sensitive for relatively small changes in reaction conditions. On the other hand, the rich structural and morphological transformations are due to the delicate hydrophilic/hydrophobic balance in the self-organization of the system [14]. One property that was not mentioned in most studies is the ability of PEG to operate as a flocculation agent. For instance, addition of a small amount of flocculant to a sol of silica particles leads to flocculation of only a portion of the colloidal particles, and if more is added, increasing amounts are precipitated. If sufficient flocculant is added to cover the surface of the particles, however, the sol is stabilized again with repulsive or nonattracting polymer-clad particles.

Within this context, MAPLE is evolving into a powerful technique for the controlled deposition of biopolymers. The method relies on the finding that the biopolymers dissolved within a frozen, absorbing solvent can, upon laser irradiation, eject in the gas phase in functional form [15, 16]. The process has several advantages over current techniques (dry, solvent-less technique that can be conducted under sterile conditions), being a fast process with run-times on the order of minutes. A variety of coating materials can be used, making it possible thus to produce films from various materials with a high biocompatibility. The performed studies have clearly demonstrated [17–22] the potential of MAPLE for the deposition of a wide range of organic

macromolecules (*e.g.* carbohydrates [23], nanotubes), polymers/biopolymers *(e.g.*, PEG) or even of larger biological structures (*e.g.*, viruses, proteins, cells, tissue components). Recently, thin films of polysaccharides [18, 24, 25], blood and proteins [19–21], collagen [22][22] were successfully produced for drug delivery and diagnostic applications. Thus, this method provides the possibility for the fabrication of micro/nano arrays of biomaterials [26–28] with applications in biosensing, chemical sensing, biochemical/microbiological analysis and even for therapeutic purposes (drug delivery systems, implant/ prosthetic fabrication).

The general objective of this study is to synthesize and characterize new PEG-doped hybrid composites in order to evaluate them as platforms for controlled drug delivery. The drug release rate from a silica xerogel matrix can be controlled by adding water soluble polymers such as PEG and its derivatives, affecting the formation of silica particles at the colloidal level during polycondensation by forming hydrogen bonds with residual silanol moieties in the silica network. Taking into account that the physicochemical characteristics of the drug molecule significantly control the release rate, a basic drug (ability of releasing in a controlled manner), *e.g.*, 2-[4-(2-methylpropyl)phenyl]propanoic acid (ibuprofen), was used. The selected materials thus have unique combination of three different components namely silicon-alkoxy groups, as well as hydroxyl and carboxyl functionality. The hydrolysable silicon alkoxide can be condensed to form inorganic Si-O-Si network and subsequent polycondensation yields highly crosslinked dense networked structure. For monitoring the drug delivery, a fluorescent dye (lissamine rhodamine-B sulphonyl chloride) was incorporated into the materials during the early stage of the sol-gel process. Previously, our studies have evidenced the effect of different polymeric fluorophores on the polymer properties and their applications [29]. Also, in this paper we attempt to recognize the different roles of PEG as structure-directing agent, flocculating agent, and in phase separation.

At the same time, in order to provide quality films highly required in the controlled released drug systems and to study the influence of the derivative group on both film structure and morphology, firstly, we obtained thin films of PEG derivatives with carboxyl and amine functional groups through matrix-assisted pulsed laser evaporation technique (MAPLE). The compositions determined by Fourier transforms infrared spectroscopy were similar to the starting materials, thus suggesting that the functionality within thin films is preserved. This technique will be further extended on the hybrid composites above mentioned.

2. Experimental part

2.1. Synthesis of hybrid composites with PEG sequences

Starting from a PEG precuror that contains a fluorescent dye (lissamine rhodamine-B sulphonyl chloride, 20% w/w), two new type of hybrid composites

(PEG-SO_2R-1 – without drug content, PEG-SO_2R-2 – with ibuprofen) were obtained through sol-gel approach. As follows, the synthesis for PEG-SO_2R-1 was performed involving the PEG precursor (PEG-SO_2R), chloro-propyltriethoxysilane and a stoichiometrical amount of water, at pH = 3, while PEG-SO_2R-2 was attained at pH = 5, in the presence of the same reactants as described previously and ibuprofen.

2.2. Measurements

The structures of PEG precursor and hybrid composites were verified by ^{1}H-NMR and FTIR spectroscopy by using a Bruker 400 MHz spectrometer and a Specord M80 spectrophotometer, respectively. The SEM micrographs were obtained by using a Carl Zeiss-950 scanning probe microscope, Heidenheim, Germany, the specimens being sputter-coated with gold. MAPLE depositions of PEG derivatives with carboxyl and amine functional groups were performed using a pulsed excimer KrF laser (λ = 248 nm, τ_{FWHM} = 7 ns, pulse repetition rate = 2 Hz). The incident angle of the laser beam was placed at an angle of 45° with respect to the normal of the target surface. The target-substrate distance was maintained at 3 cm. Prior to deposition, ~5 ml of the solvated fluid was dropwise added into the target holder and frozen by immersing in liquid nitrogen (LN). The copper target holder was placed on a homemade cryogenic rotating assembly, which was maintained at a temperature of ~ 173 K using a copper holder connected to a LN reservoir. The target was rotated at a rate of 0.4 Hz during film deposition to avoid heating and possible drilling by the pulsed laser beam. After preliminary tests, we set the incident laser energy at a value within the range (32–60) mJ. The laser spot area was (7–8) mm^2. The number of subsequent laser pulses applied for the deposition of one film was 15,000. In all experiments both sides polished Si<111> substrates were used. A control set of films were prepared by drop-casting in order to provide comparison data. The overall MAPLE deposition conditions of PEG 1 and PEG 2 thin films are collected in Table 1. The resulting PEG derivative thin films were characterized by FTIR spectra recorded with a Jasco 6200 apparatus (8 cm^{-1} resolution) with a specular reflectance device with VeeMax II variable angle (measurements performed at 50°), as well as AFM micrographs, made with an Integrated Platform SPM - NTegra model Prima in semicontact mode, error mode and phase contrast.

Table 1. MAPLE depositions conditions for polyethylene glycol derivatives with carboxyl (PEG-1) and amine groups (PEG -2)

Symbol	Energy/pulse [mJ]	Fluence [mJ/cm^2]	Spot area [mm^2]	Roughness [nm]
PEG 1 a	32	400	8	120
PEG 1 b	40	500	8	107
PEG 1 c	49	700	7	128
PEG 2 a	35	500	7	100
PEG 2 b	48	600	8	147
PEG 2 c	60	750	8	170

3. Results and discussion

Through sol-gel reaction of chloro-propyltriethoxysilane with or without the presence of a non-steroidal anti-inflammatory drug insoluble in water (e.g., ibuprofen), new hybrid composites were obtained. The incorporation of ibuprofen within sol-gel derived matrix is expected to lead to the obtaining of compounds that permit a controlled and reproducible release of the active agent. In a first step, the synthesis of a precursor starting from PEG and lissamine rhodamine B (20% w/w) was established, process followed by the sol gel reaction of chloropropyltriethoxysilane with PEG precursor, in the presence or absence of ibuprofen, at pH = 5 and pH = 3, respectively. The succession of reactions in the case of precursor is presented in Scheme 1, while the structures of the new formed products are given in Scheme 2.

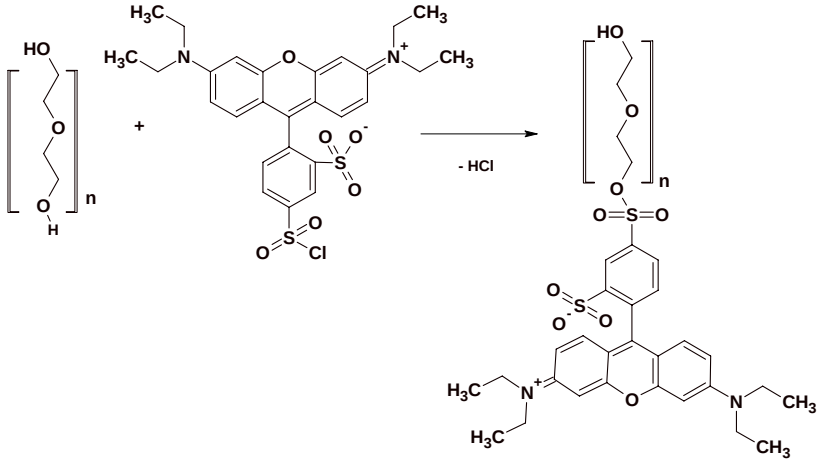

Scheme 1. Synthesis of PEG precursor.

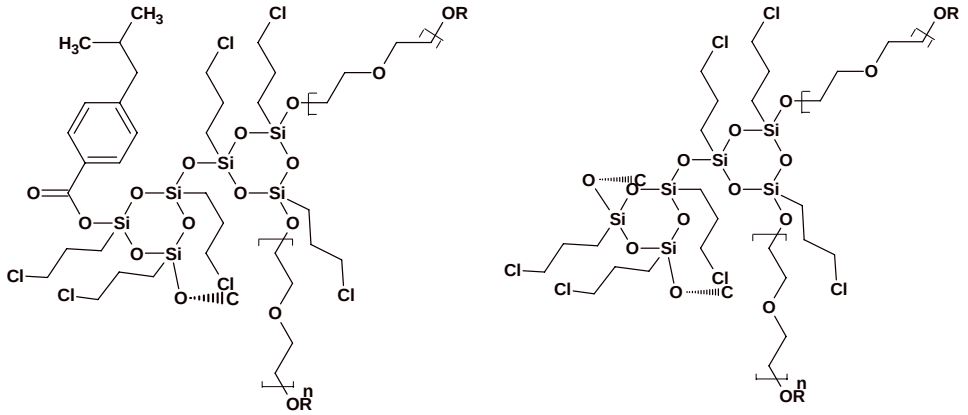

Scheme 2. Structures of the hybrid composites with PEG sequences.

The FTIR spectra of the PEG derivatives are shown in Fig. 1. A characteristic broad band appeared between 3443–3470 cm^{-1} corresponding to O–H stretching vibrations of the hydroxyl groups due the strong hydrogen bond of intra(inter) molecular type [30]. Hydrogen bonds play a crucial role in such conformational arrangements, creating hydrophilic associated domains [31]. Only in the case of PEG-SO_2R-1 hybrid compound, one peak at around 3750–cm^{-1} (the „fingerprint" of the isolated silanol vibration) can be distinguished, while the vicinal ones and the physical adsorbed water are characterized by adsorption bands in the range 3000–3800 cm^{-1}. Moreover, this small peak is supporting Sommer's hypothesis that silane bonds are converted to silanol bonds during gelation [32]. The C-H alkyl stretching band can be also observed around 2870–2954 cm^{-1}. A typical absorption band for both PEG-SO_2R and PEG-SO_2R-1 compounds is located at 1708 cm^{-1} and is attributed to the deformation mode of adsorbed molecular water in the generated pores [33]. For PEG-SO_2R-2 sample, one absorption peak at 1732 cm^{-1} belongs to the carbonyl group from ibuprofen. The shift of this band from 1705 cm^{-1} (corresponding to the "free ibuprofen") towards a higher wavenumber region (1732 cm^{-1}) is caused by the H-bond formed between the carbonyl groups from ibuprofen and the OH units from PEG and silica matrix.

The vibrational spectra of the silicates can be divided into two regions. The first region covers the frequency range 4000–1600 cm^{-1}, where stretching and bending vibrations of water molecules appear. The second region (below 1300 cm^{-1}) includes the vibrations due to the silicate layers. In general, the γ_{as}(Si-O-Si) modes appear in the region 1200–1000 cm^{-1}, whereas γ_s(Si-O-Si) become observable in the region 700–400 cm^{-1}. The bands assigned to Si-O-Si symmetric vibrations (1118 and 1114 cm^{-1} for PEG-SO_2R-1,2) are a result of the condensation reaction between hydrolyzed silanol Si-OH groups. At the same time, the presence of γ_{as}(Si-O-C) at 1023 and 1034 cm^{-1}, as well as the γ_s(Si-O-C) at 863 and 843 cm^{-1} for PEG-SO_2R-1 and PEG-SO_2R-2, respectively may be originated from the condensation reaction between Si-OH groups from hydrolyzed chloropropyltriethoxysilane and C-OH groups from PEG. Hence, the presence of Si-O-C and Si-O-Si bonds confirmed the existence of covalent linkages between the organic groups and silica, which led to a better compatibility and crosslinking network between organic and inorganic components. The peak positions of the Si-O-Si and Si-O-C modes are shifted to a higher wavenumber than that of the composite without drug (PEG-SO_2R-1). This frequency shift in the FTIR spectra can be related to changes in the bonding characteristics, such as the bonding structure and the bond length. For both hybrids, the peaks at 949 and 951 cm^{-1} are associated with the Si-OH vibrational mode owing to incomplete condensation of the Si-OH bonds.

The ^{1}H-RMN spectrum, together with the assignments of the observed resonances, revealed for the synthesized compounds the presence of the signals attributed to methylene protons from the α-position to the Si atom at 0.1 ppm and the methylene protons in the β-position to the Si atom at 1.7–1.8 ppm.

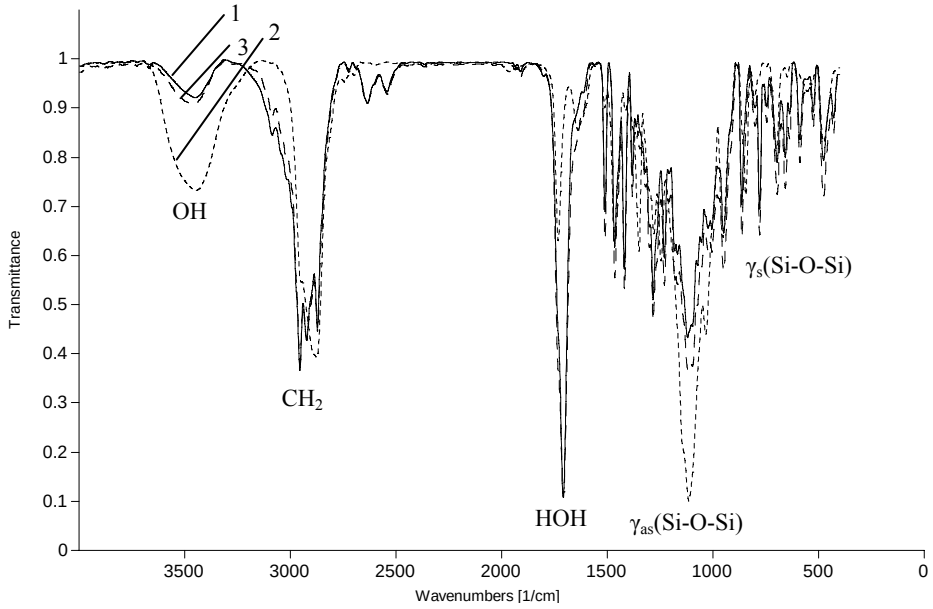

Fig. 1. FTIR spectra of PEG precursor modified with lissamine rhodamine B (1) and the hybrid composites with (2) or without ibuprofen (3).

Silica has a complex morphology that spans nanometer to micron size-scale and manipulation of the morphology at each structural level determines the properties of the product. The physical properties of silica essentially depend on the synthesis procedure, the most important ones being represented by the specific surface, the dimensions of the primary particles and aggregates, as well as the porosity. The differences between these physical characteristics are correlated with the organization form of the silica particles (aggregates or agglomerates). In the silica structure three types of particles organization can be distinguished. At the smallest size-scale, quasi-spherical primary particles are found ranging from 3–500 nm in diameter, these ones controlling the specific surface area of the powder. Under the effect of colloidal forces, the primary particles are clustered to form disordered aggregates at the 0.1 μm size-scale. Typically aggregates are further linked to form agglomerates that extend up to hundreds of μm in size. The dimension of the primary particles, the density and the aggregation and agglomeration degree influence the porosity and the specific surface of the silica. SEM characterization was conducted in order to evaluate the morphology of such hybrid composites. SEM analysis showed the existence of silica aggregates with well-defined micrometric dimensions (7.93–8.54 μm); due to its flocculation abilities, PEG is present only at the surface of the silica spheres, forming PEG-cladded and PEG-connected silica of nanometric dimensions (between 300–800 nm). This behavior of PEG of 2000 molecular weight is different of other values (e.g., for M = 600, super-aggregates), as was

values (e.g., for M = 600, super-aggregates), as was evidenced by other authors [34]. In Figure 2 are displayed the SEM micrographs at different resolutions for PEG-SO_2R-1 compound.

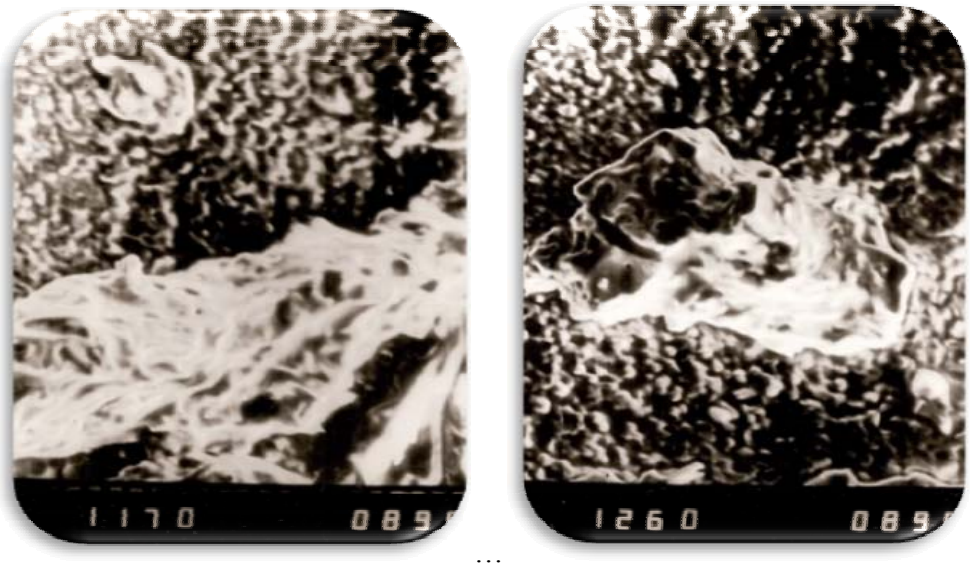

…

Fig. 2. SEM micrographs for PEG-SO_2R-1 compound at different resolutions.

A complimentary study on PEG derivatives consists in using MAPLE technique to obtain micro(nano) structured films for biomedical applications. Figure 3 contains the AFM micrographs for PEG 1 thin films obtained by MAPLE at a fluence of 400 mJ/cm^2 (a), 500 mJ/cm^2 (b), and 700 mJ/cm^2 (c). The surface morphology strongly depends on the laser fluence and at a value of 400 mJ/cm^2 (Fig. 3, a), macromolecules are aligned as statistic coils embedded in the DMSO solvent and then frozen. The laser beam removes the solvent by a sublimation process and a part of the statistic coils are mechanically rejected toward the substrate. Some of these statistic coils are splashed and spreaded on the substrate surface due to mechanical deformation, these ones having a disc-like shape with a diameter of 2–3 μm. At a fluence of 500 mJ/cm^2 (Fig. 3, b), a phase transition generates structures transformed by recrystallization. Therefore, there is a sufficient kinetic energy in order to extend macromolecules in bundles of macromolecule chains. Increasing the fluence, a local melting/crystallization process is noticed [35, 36], in which the crystallized macromolecules are organized in plate-like structures. At higher fluences (700 mJ/cm^2, Fig. 3, c), an agglomeration tendency of crystallized macromolecules organized in plate-like structures, typical for a global melting/crystallization process followed by solidification was evidenced too.

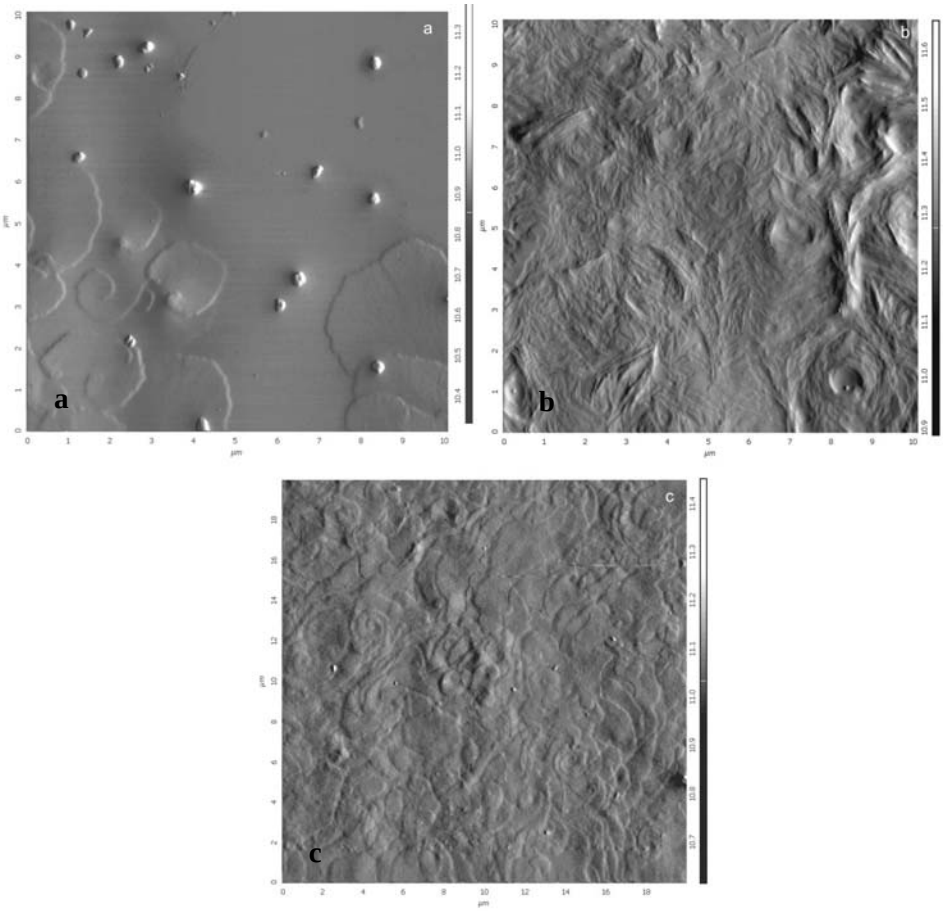

Fig. 3. AFM micrographs of PEG derivatives with carboxyl groups (PEG 1) thin films obtained by MAPLE at a fluence of 400 mJ/cm^2 (a), 500 mJ/cm^2 (b), and 700 mJ/cm^2 (c).

In Fig. 4 we give the AFM micrographs of polyethylene glycol derivatives with amine groups (PEG 2) thin films obtained by MAPLE at a fluence of 500 mJ/cm^2 (a), 600 mJ/cm^2 (b), and at 750 mJ/cm^2 (c). At a fluence of 500 mJ/cm^2 (Fig. 4, a) the macromolecules were aligned as statistic coils with a regular crystallized dendrite-like shape, while at 600 mJ/cm^2 (Fig. 4, b) the registered phase transition is responsible of the formation of layered platelet-like domains in spiral shape transformed by recrystallization.

Upon increasing the fluence up to 750 mJ/cm^2 (Fig. 4, c) it was noticed a similar behavior to that of the PEG 1 compound, e.g., the formation of the well-defined platelet-like structures, typical for a global melting/crystallization, process followed by solidification. A possible explanation could be done by the polyelectrolyte character due to the supplementary charge of the amine chains.

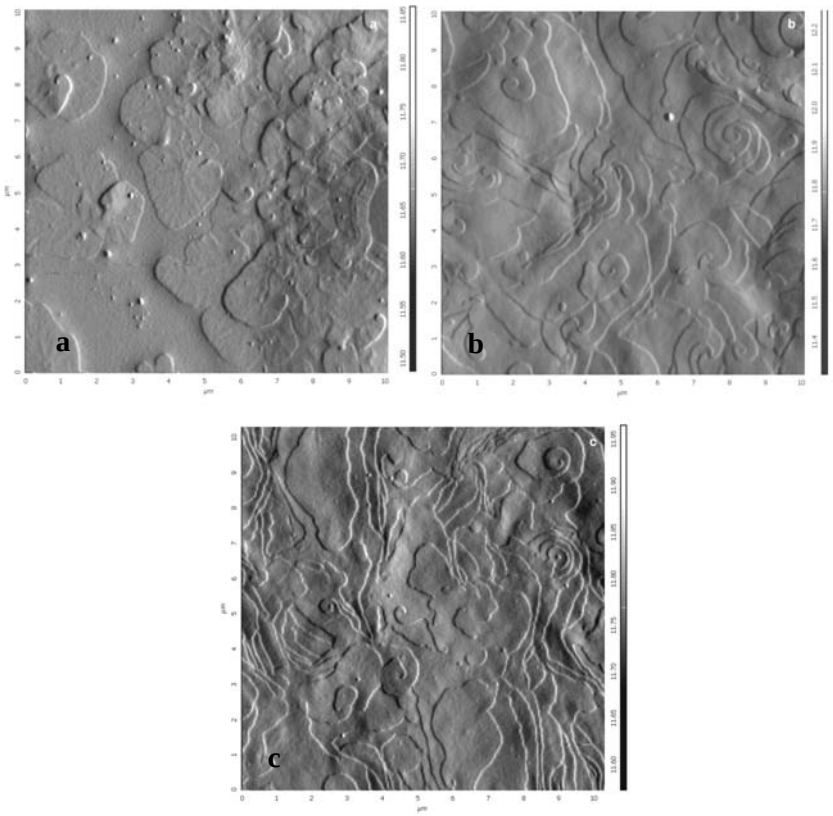

Fig. 4. AFM micrographs of PEG derivatives with amine groups (PEG 2) thin films obtained by MAPLE at a fluence of 500 mJ/cm^2 (a), 600 mJ/cm^2 (b), and 750 mJ/cm^2 (c).

4. Conclusions

The technique based on sol-gel polymerization described in this paper represented a versatile synthetic approach to obtain hybrid composites with tailor-made composition of both the organic core and the silica or organo-silica shell, as well as a good control on morphology, size and phase structure in the nano/micro range. Thus, were obtained silica aggregates with typical sizes in micrometer range, as well as quasi-spherical nanoparticles based on PEG-cladded and PEG connected silica structures. Due to rhodamine content, these compounds represent good models that allow a controlled and reproducible release of the drug.

At the same time, we demonstrated that MAPLE was suitable for producing novel PEG derivatives with carboxyl and amine functional groups, respectively thin films by MAPLE technique with very close similarity to the starting structures obtained by dropcast. AFM investigations showed that the surface morphology

depends equally both on the laser fluence and the type of the derivative group. Increasing the fluence for MAPLE-deposited thin films of PEG derivative with carboxyl functional groups, the surface morphology evolved from aligned macromolecules having a disc-like shape to plate-like structures that further have an agglomeration tendency, typical for a global melting/crystallization process followed by solidification. In case of PEG derivative with amine groups, the transition from regular crystallized dendrite-like shape to layered platelet-like domains in spiral shape and further to the formation of platelet-like structures was registered also. We concluded that MAPLE provided an improved approach for growing quality of the thin films based on PEG derivatives required in the controlled released drug systems.

References

[1] ROTTMAN C., GRADER G. S., DE HAZAN Y., AVNIR D., Langmuir **12**, 5505 (1996).
[2] BRAUN S., RAPPOPORT S., ZUSMAN R., AVNIR D., OTTOLENGHI M., Mater. Lett. **10**, 1 (1990).
[3] LI B., TAKAHASHI H., Biotechnol. Lett. **22**, 1953 (2004).
[4] CHIU W.-M., YANG C.-F., ZHANG Y.-S., Polym. Plast. Technol. Eng. 46, 767 (2007).
[5] QIU F. X., LI P. P., YANG D. Y., Polym. Lett. **1**, 150 (2007).
[6] WANG B., LI B., DENG Q., DONG S., Anal. Chem. **70**, 3170 (1998).
[7] KIM T. Y., ALHOOSHANI K., KABIR A., FRIES D. P., MALIK A., J. Chromatogr., A **1047**, 165 (2004).
[8] SUN D.Z., CHEN J., LU W.M., ZHENG X.M., Thermochim. Acta **351**, 1 (2000).
[9] HUH K. M., BAE, Y. H., Polymer **40**, 6147 (1999).
[10] HAMLEY I. W., CONNELL S. D., COLLINS S., Macromolecules **37**, 5337 (2004).
[11] CATALTARLA E., MCCARTHY J. T., Polym. Prepr. **44**, 897 (2003).
[12] TZIAMPAZIS E., KOHN J., MAGHE P. V., Biomaterials **21**, 511 (2000).
[13] GILL I., Chem. Mater. **13**, 3404 (2001).
[14] SMARSLY B.; POLARZ S.; ANTONIETTI M. J., Phys. Chem. B **105**, 10473-10483 (2001).
[15] TOFTMANN B., RODRIGO K., SCHOU J., ROMAN P., Appl. Surf. Sci. **247**, 211 (2005).
[16] RODRIGO K., TOFTMAN B., SCHOU J., PEDRYS R., J. Low Temp. Phys. **139**, 683 (2005).
[17] WU P. K., RINGEISEN B. R., KRIZMAN D. B., FRONDOZA C. G., BROOKS M., BUBB D. M., AUYEUNG R. C. Y., PIQUÉ A., SPARGO B., MCGILL R. A., CHRISEY D. B., Rev. Sci. Instrum. **74**, 2546 (2003).
[18] CRISTESCU R., DORCIOMAN G., RISTOSCU C., AXENTE E., GRIGORESCU S., MOLDOVAN A., MIHAILESCU I. N., KOCOUREK T., JELINEK M., ALBULESCU M., BURUIANA T., MIHAIESCU D., STAMATIN I., CHRISEY D. B., Appl. Surf. Sci. **252**, 4647 (2006).
[19] DORAISWAMY A., NARAYAN R. J., CRISTESCU R., MIHAILESCU I. N., CHRISEY D. B., Mat. Sci. Eng. C **27**, 409 (2007).
[20] CRISTESCU R., KOCOUREK T., MOLDOVAN A., STAMATIN L., MIHAIESCU D., JELINEK M., STAMATIN I., MIHAILESCU I. N., CHRISEY D. B., Appl. Surf. Sci. **252**, 4652 (2006).
[21] CRISTESCU R., PATZ T., NARAYAN R. J., MENEGAZZO N., MIZAIKOFF B., MIHAIESCU D. E., MESSERSMITH P. B., STAMATIN I., MIHAILESCU I. N., CHRISEY D. B., Appl. Surf. Sci. **247**, 217 (2005).

[22] CRISTESCU R., MIHAIESCU D., SOCOL G., STAMATIN I., MIHAILESCU I. N., CHRISEY D. B., App. Phys. A **79**, 1023 (2004).
[23] PIQUÉ A., MCGILL R. A., CHRISEY D. B., LEONHARDT D., MSLNA T. E., SPARGO B. J., CALLAHAN J. H., VACHET R. W., CHUNG R., BUCARO M. A., Thin Solid Films **536**, 355-356 (1999).
[24] CRISTESCU R., JELINEK M., KOCOUREK T., AXENTE E., GRIGORESCU S., MOLDOVAN A., MIHAIESCU D.E., ALBULESCU M., BURUIANA T., DYBAL J., STAMATIN I., MIHAILESCU I. N., CHRISEY D.B., J. of Phys.: Conference Series **59**, 144-149 (2007).
[25] CRISTESCU R., DORAISWAMY A., SOCOL G., GRIGORESCU S., AXENTE E., SIMA F., NARAYAN R. J., MIHAIESCU D., MOLDOVAN A., STAMATIN I., MIHAILESCU I. N., CHISHOLM B. J., CHRISEY D. B., Appl. Surf. Sci. **253**, 6476-6479 (2007).
[26] PATZ T. M., DORAISWAMY A., NARAYAN R. J., HE W., ZHONG Y., BELLAMKONDA R., MODI R., CHRISEY D. B., J. Biom. Mat. Res. B-Appl. Biomat. **78B**, 124 (2006).
[27] DORAISWAMY A., NARAYAN R. J., LIPPERT T., URECH L., WOKAUN A., NAGEL M., HOPP B., DINESCU M., MODI R., AUYEUNG R. C. Y., CHRISEY D. B., Appl. Surf. Sci. **252**, 4743 (2006).
[28] ZERGIOTI I., KARAISKOU A., PAPAZOGLOU D. G., FOTAKIS C., KAPSETAKI M., KAFETZOPOULOS D., Appl. Phys. Lett. **86**, 163902 (2005).
[29] BURUIANA E.C., BURUIANA T., POHOATA V., J. Photochem. Photobiol. A: Chem. **180,** 150 (2006).
[30] ANDRADE G., BARBOSA-STANCIOLI E.F., PISCITELLI MANSUR A.A., VASCONCELOS W.L., MANSUR H.S., Biomed. Mater. **1**, 221–234 (2006).
[31] *Plastics microstructure and engineering applications*, 2nd ed., Mills NJ (Ed), London: Edward Arnold Publishers, 1993.
[32] SOMMER L. H., *Stereochemistry, mechanism and silicon; an introduction to the dynamic stereochemistry and reaction mechanisms of silicon centers*, McGraw-Hill (Ed), New York, 1965.
[33] MANSUR H. S., OR´EFICE R. L., VASCONCELOS W. L., LOBATO Z. P., MACHADO L. J., J. Mater. Sci.: Mater. Med. **16**, 333–340 (2005).
[34] SUN Q., BEELEN T. P. M., VAN SANTEN R. A., HAZELAAR S., VRIELING E. G., GIESKES W. W. C., J. Phys. Chem. B **106**, 11539-11548 (2002).
[35] MAGONOV S. N., WHANGBO M.-H., *Surface Analysis with STM and AFM*, VCH, Weinheim, 1996, p.323.
[36] WHANGBO M.-H., MAGONOV S. N., BENGEL H., Probe Microscopy **1**, 23 (1997).

Investigation on Semiconductor Nanoparticles Prepared in Polymeric Matrices

S. PERETZ[1], E. TEODOR[2], M. ELISA[3], B. SAVU[4]

[1]Institute of Physical Chemistry *I. Murgulescu*, Department of Colloids,
202 Spl. Independentei, 060021, Bucharest, Romania
E-mail: peretz@icf.ro

[2]National Institute of Research and Development for Biological Sciences,
Centre of Bioanalysis, 296 Spl. Independentei, 060031, Bucharest, Romania

[3]National Institute of Research and Development Optoelectronics - INOE 2000,
1 Atomistilor St., 77125, Magurele, Romania

[4]Center for Microscopy-Microanalysis and Information Processing,
University *Politehnica* Bucharest,
313 Spl. Independentei, 060032, Bucharest, Romania

Abstract. The effect of some polymers like chitosan, alginate, carragennan, polyvinyl pyrrolidone or copolymer maleic anhydride/styrene, upon physico-chemical properties of nanoparticles generated in the polymeric phase was investigated. The size of nanoparticles was determined by fitting the absorbance data with some specific equations from quantum dots' literature. The fluorescence properties of the nanoparticles depend on the nature of capping polymer. The synthesized nanoparticles were dispersed in polymeric matrix and then were applied on glass support to form films. The properties of the prepared nanoparticles and also the deposited films were investigated by using confocal laser scanning microscopy, UV-Vis spectroscopy and fluorescence spectroscopy. The nanoparticles coated with polymers present low toxicity against cultured with Vero cells for a determined period of time. The toxicity diminishes up to 10 times by covering the semiconductor nanoparticles with polymers.

1. Introduction

Nanocrystalline semiconductor materials such a CdS and ZnS have attracted great interest due to their theoretical importance and significant potential applications. The nanometric size crystals can been prepared in the water-soluble polymers systems or hydrogels.

In the present study, the biocompatible polymers have been used due to their significant potential applications which admit the selective attachment of

ions from the enviroment. These represents the nucleation centers for the nanocrystals. The nanocrystals exhibit size dependent properties, size quantum effect such as a blue shift of absorption onset, a change of electrochemical potential band edge, and an enhancement of photocatalytic activities, with decreasing crystallite size [1].

The photochemical and photophysical properties of the nano-sized semiconductors on various preparation have been characterized, but few reports describe their application as florescent probes [2, 3].

Cadmium sulphide, a direct gap material with E_g of 2.42 eV at room temperature, can be used for photoelectronic devices [4]. For the semiconductor crystallite, its electronic properties start to change if the diameter approaches to the Bohr diameter; this is the so-called quantum size effect, which can be observed as a blue shift in the optical bandgap. By incorporation of small semiconductor clusters into solid matrices such as polymers and glasses the problems associated with colloidal solutions are solved [5]. In the case of CdS quantum size effect occurs as the crystallite diameter is comparable or below the exciton diameter of 5–6 nm. Many techniques have been explored to synthesize small clusters, mostly II-VI such as CdS, in the nanometer size regime in a variety of media, such micelles, polymers, glasses, solutions, thin films and zeolites.

Nanotechnology, in the form of nanoparticles with properties, which can be precisely tailored by chemical methods, is rapidly becoming an important new tool in the arsenal of the biotechnologist. Nanoscale materials become more and more the subject to intense investigation for use in cancer diagnosis and therapy. It was obtained novel quantum dot-hyaluronic acid (QD-HA) conjugates which could be successfully used for real-time bio-imaging of HA derivatives in nude mice [6]. The novel QD-HA conjugate will be further used to investigate the biological roles of hyaluronic acid with a different molecular weight in the body.

In this paper, we investigated the effect of some polymers and copolymers upon physico-chemical properties of nanoparticles synthesised in the polymeric phase. By dispersing the synthesized nanoparticles in a polymeric matrix some films have been prepared. The influence and the biocompatibility of CdS and ZnS nanoparticles coated with polymers were evaluated in relation with cultures of Vero cells. The biocompatibility of the suspension of nanocomposites was determined by MTT Cell Proliferation Assay, a quantitative, convenient method for evaluating a cell population's response to external factors, whether it is an increase in cell growth, no effect, or a decrease in growth due to necrosis or apoptosis [7]. We investigated the growth and morphology of the nanoparticles and characterized the absorption and florescence properties of deposited films by using confocal laser scanning microscopy, UV-Vis spectroscopy and fluorescence spectroscopy.

2. Experimental

2.1. Materials

The reactants, cadmium nitrate tetra hydrate $Cd(NO_3)_2 \times 4H_2O$ from Aldrich and sodium sulphide ($Na_2S \times 9H_2O$) from Fluka, were analytical grade purity. The polymers: sodium alginate from brown algae of low viscosity grade, chitosan low-viscous, and polyvinyl pyrrolidone K60 (PVP) were supplied by Fluka, and were used without further purification. The copolymer, maleic anhydride/styrene 1:1 with M = 60,500 (CoMAS) was prepared as laboratory samples at Macromolecular Chemistry Institute – Iaşi (Romania). The water used in the experiments was Micropore filtered.

2.2. Preparation of nanoparticles

Therefore two methods were used:

Method 1. A mixture formed by an aqueous solution of Na_2S with the concentration $2.4–5.0 \times 10^{-3}$ M and the polymer or copolymer in concentration of 0.2 % (w/w) was prepared. Afterwards, this blend was mixed under rapid stirring (300 rpm) with a second aqueous solution of $Cd(NO_3)_2 \times 4H_2O$ of concentration 1×10^{-3} M, and nitrogen gas was bubbled throughout system.

Method 2. The cadmium ions in the solution were obtained from the solubilization in the purified water of salt as cadmium nitrate, and were mixed with a solution of reducing agent such as sulphide ions (Na_2S). Colloidal cadmium sulphide particles were prepared by mixing quickly (at 300 rpm) the two solutions, and afterwards these were introduced in a 0.2% polymer solution; the system was purged with N_2 gas for 30 minutes to prevent the photocorrosion and the formation of the colloidal sulphur. The aqueous solutions containing $Cd(NO_3)_2$ and Na_2S were freshly prepared and were used over short period from their preparation. The used copolymer was dissolved in a solution alkalinized with NaOH 0.1 N and the pH of the Na_2S aqueous solution was in the range of 9.5–11. The chitosan solutions were prepared by dilution with acetic acid 0.1 N.

2.3. Preparation of the films

The films have been obtained by mixing CdS or ZnS colloidal solution with a polymer solution. The mixture was stirred for five minutes and then, the films have been obtained by the deposition of the above-mentioned mixture on a sodium-lime-silicate glass substrate, by means of an aluminium device having an inner hole and an aperture at the bottom, with a slope angle of 15°. The films have been dried at 105–120°C, for 5–10 min. After cooling the samples to the room temperature, the films have been protected with aluminium foil.

2.4. Cytotoxicity determinations

The cytotoxicity or the biocompatibility of the suspension of nanoparticles was determined by MTT Cell Proliferation Assay. The key component is (3-[4,5-dimethylthiazol-2-yl]-2,5-diphenyltetrazolium bromide) or MTT. Mitochondrial dehydrogenases of viable cells cleave the tetrazolium ring, yielding purple formazan crystals insoluble in aqueous solutions. The crystals are dissolved in acidified isopropanol. The resulting purple solution is measured spectrophotometrically. An increase or decrease in cell number results in a concomitant change in the amount of formazan produced, indicating the degree of cytotoxicity caused by the test material. MTT test was done after one and 2 days on Vero cells (from the *Vero* lineage derived from epithelial cells of kidney from African green monkey, 20–25 passage), cultured with different concentrations of nanostructured suspensions (0.01–10%). Cell suspension was obtained by subconfluent culture trypsinization and was seeded into 24-well plates; each well was seeded with 3×10^4 cell /mL. Cells were cultured 24 h in Dulbecco's modified Eagles medium/10% FBS (DMEM) and after standing overnight the culture medium was replaced with nanostructured suspensions. The supernatant was replaced after one and 2 days of exposure of cells to QD suspensions and the cells were washed with PBS, and then 500 μL MTT solution (0.25 mg/mL) was added to each well. The cells were washed after 3 h of incubation at 37°C, the formazan crystals formed in living cells solubilized with 1 mL isopropanol, and the absorbance measured at 570 nm with a Jasco UV-Vis spectrophotometer.

2.5. Methods – microscopy and spectrometry

The morphology of the prepared nanoparticles and also the deposited films were investigated by using confocal laser scanning microscopy. Because one of the main potential applications is in the field of bioimaging, we have investigated our quantum dots by means of a modern Leica TCS SP microscope. We have used the previously recorded optical absorption spectra in order to choose the proper excitation wavelength for the confocal study. The Leica TCS SP is the only broadband multiphoton confocal microscope with spectral capabilities, allowing us to record the fluorescence emission spectra with a 4 nm resolution. As one can tell, the biological laser scanning confocal microscopy relies heavily on the fluorescence techniques, as a method to obtain contrast with high degree of sensitivity coupled with the ability to specifically target structural components and/or dynamic processes in chemically fixed as well as in living cells and tissues. The excitation conditions in the confocal microscopy are several orders of magnitude more severe. Restrictions imposed by the characteristics of the traditional fluorophores and the efficiency of the microscope optical system become the dominating factors in determining the optimal excitation rate and the emission collection strategies.

The absorption spectra of the nanoparticles were made by using an UV-Vis spectrophotometer VARIAN Cary 100 Bio and the fluorescence spectra by a FluoroMax-4 HORIBA spectrofluorometer. The shape and the average diameter of nanoparticles were determined by using a JEX 200CX (JEOL) transmission electron microscope (TEM).

3. Results and discussion

The obtaining of CdS particles results from the reaction between the metal ions (Cd^{+2}) and sulphide ions (S^{2-}), as follows:

$$Cd(NO_3)_2 + Na_2S \rightarrow CdS + 2NaNO_3 \quad (1)$$

It has been experimentally documented that the precipitated uniform particles are typically polycrystalline and that their formation involves two distinct dynamical stages [8]. In the first process nanosize crystalline precursors, primary particles, are nucleated in supersaturated solution, while in the second process, these primary particles aggregate into larger colloids, secondary particles [9].

The formation mechanism of these particles was described by Towey and coworkers [10]. The reaction of CdS nanoparticles involved three steps: the chemical reaction step, the nucleation step and the particle growth step.

1. Formation of the CdS species:

$$Cd^{2+} + S^{2-} \rightarrow (CdS)_1 \quad (2)$$

2. Formation of aggregates with higher agglomeration numbers from reactions of small particles:

$$(CdS)_m + (CdS)_n \rightarrow (CdS)_{n+m}\ (m, n \geq 1) \quad (3)$$

3. Growing of particles by addition of Cd^{2+} and S^{2-} ions:

$$(CdS)_n + S^{2-} \rightarrow (Cd_n\ S_{n+1})^{2-} \quad (4)$$

$$(CdS)_n + Cd^{2+} \rightarrow (Cd_{n+1}\ S_n)^{2+} \quad (5)$$

The aggregate with charge is expected to react in the same way as 1:1 stoichiometric species indicated in 2nd step. The Ostwald ripening may also occur but this process involves dissolution of the solid.

Synthesis of ZnS nanoparticles in aqueous polymer solution in according to the following equation:

$$ZnCl_2 + Na_2S \rightarrow ZnS + 2NaCl_2 \quad (6)$$

The studies of Weller et coworkers [11] has tried to correlate the cadmium sulphide particle size with the absorption spectra. They showed the experimental correlation of threshold wavelength and the particle threshold diameter [12].

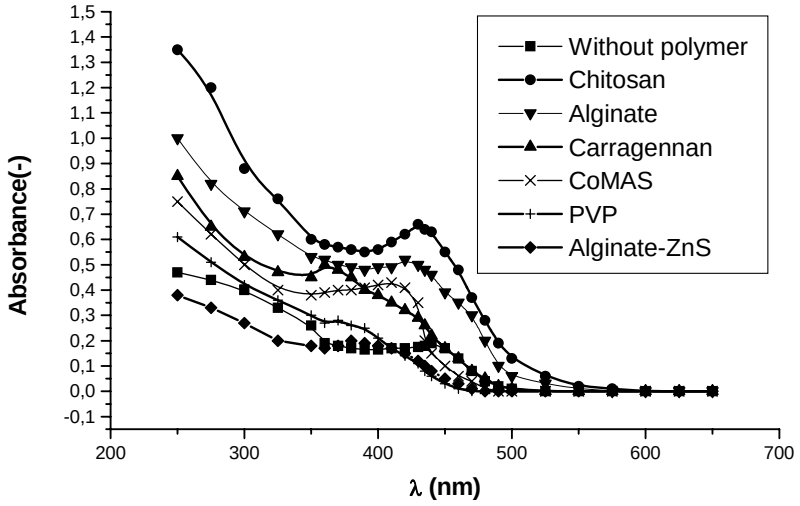

Fig. 1. UV-Vis absorption spectra of semiconductor nanoparticles coated with different polymers, $C_{[CdS\ or\ ZnS]} = 1\times10^{-4}$ M, 20 minutes after preparation.

For CdS the additivated samples present a displacement of the absorption peaks to the greatest wavelengths and an increasing of the absorption intensities for the coated particles. In the case of ZnS the coating of the particles have a little influence of the value of absorbance.

For the determination of the CdS particles size, some of their specific properties were used. In the case of semiconductor particle, there is a correlation between the absorption spectrum and the energy of the band gap (E_g). The determination of the energy of the direct band gap (E_g) is possible by fitting the absorbance data using the Wang equation [5]:

$$E_g = \frac{h\nu(A^2 - \sigma^2 h\nu)}{A^2}, \tag{7}$$

where σ is the molar absorption coefficient [$M^{-1}cm^{-1}$], A is a proportional coefficient, whose value varies according to each spectrum [$J^{1/2}M^{-1}cm^{-1}$], hν is the photon energy, and h is Planck's constant [$6.626\cdot10^{-34}$ J·s]. With the E_g determined one could calculate the diameter of CdS nanoparticles (d_p) using Brus' equation [13]:

$$E_g - E_{g,bulk} = \frac{h^2}{2d_p^2}\left(\frac{1}{m_e} + \frac{1}{m_h}\right) - \frac{3.6e^2}{4\pi\varepsilon d_p}, \tag{8}$$

where $E_{g,bulk}$ is the band gap of bulk semiconductor [J], m_e and m_h are the effective masses of electron and hole, respectively, e is the charge of an electron [1.602×10^{-19} C], and ε is the dielectric constant. The values of $m_e = 0.19\ m_e$, m_h =

= 0.8 m_e and $\varepsilon = 5.7\varepsilon_0$ were employed for CdS particles. Here, m_e is the electron rest mass [9.11×10^{-31} kg] and ε_0 is the dielectric constant of vacuum [8.854×10^{-12} $C^2J^{-1}m^{-1}$].

The data from absorption spectra presented in the Fig. 1, were fitted and estimated with equations 7 and 8, obtaining the average diameters of bulk and capping CdS particles, which ranges within 6.7 and 10.6 nm.

The sequence of the values of particle diameter (d_p), compared at 20 minutes from mixing two solutions was:

$$d_{pChitosan} > d_{p\ Alginate} > d_{p\ CoMAS} > d_{p\ Carragennan} > d_{p\ PVP} > d_{p\ \ without\ polymer} \quad (9)$$

It could be observed that both the presence of the polymer and their nature influence the particle size.

The kinetics of CdS particles in the growing step shown that the diameter of the cadmium sulphide particles have an fast increase in the first 30 minutes from the preparation, and after grow slightly in the next 40–120 minutes, and after the kinetics' curves flatten.

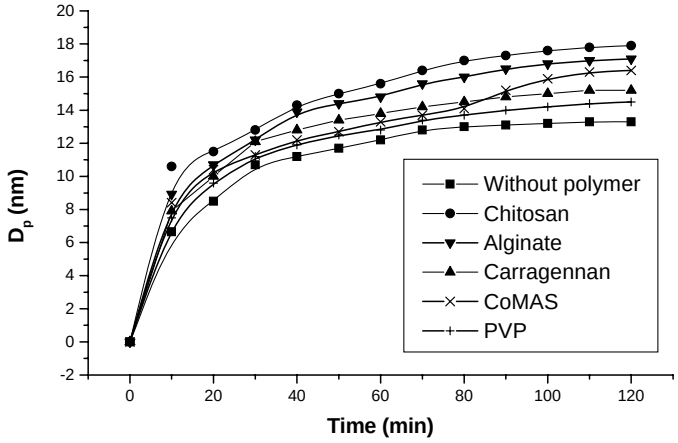

Fig. 2. Time dependence of the nanoparticle diameter, $C_{[CdS]} = 1\times10^{-4}$ M.

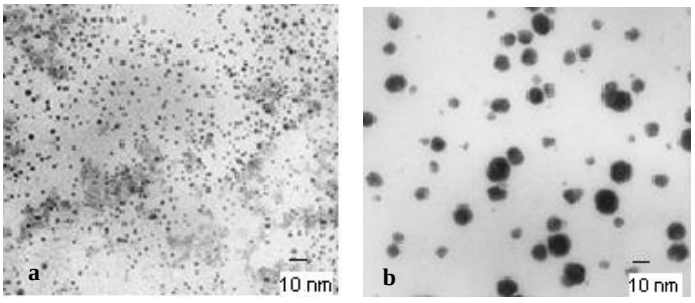

Fig. 3. TEM micrographs, a) CdS without polymer; b) almost spherical CdS particles synthesized in presence of chitosan.

From TEM measurements we observe that the average diameter increases for the coated nanoparticles, phenomenon that is more obvious in the presence of polymers like chitosan, than in absence of the added polymers (see Fig. 3).

The Figures 4 a to g presents the results of the transmission electron microscopy determinations, which give the information about the distribution of the crystals average size.

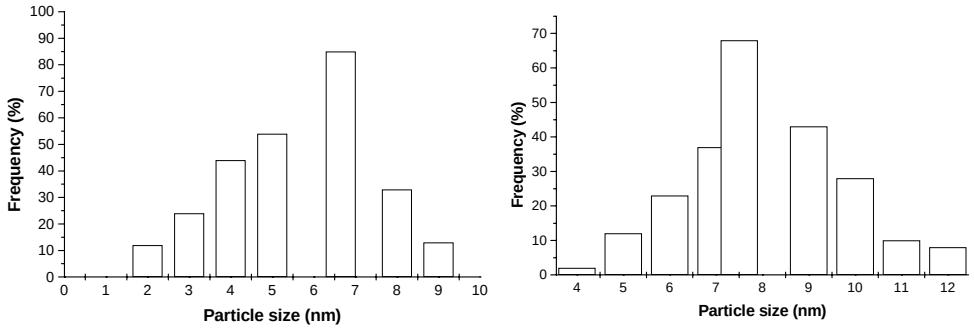

a)

b)

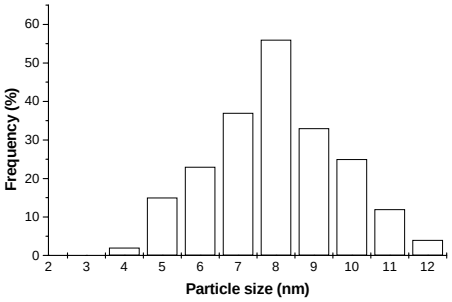

c)

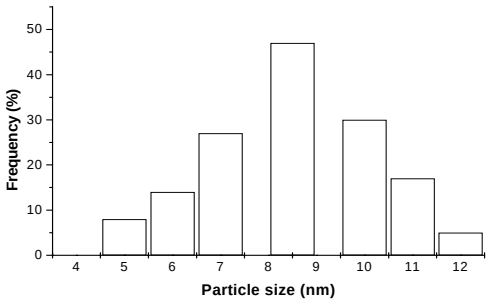

d)

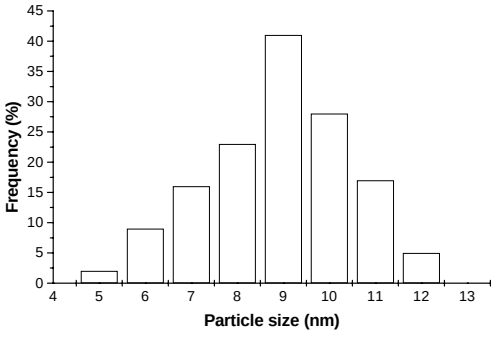

e)

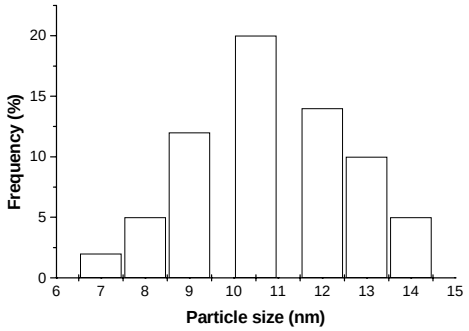

f)

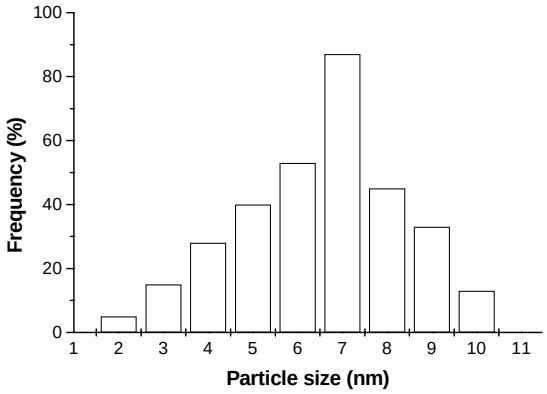

g)

Fig. 4. Size distribution of nanoparticles, a) CdS without polymer; b) CdS coated with PVP; c) CdS coated with carragennan; d) CdS coated with CoMAS; e) CdS coated with alginate; f) CdS coated with chitosan; g) ZnS coated with alginate.

The frequency of the majority particles in the size distribution depends on the nature of the polymer and decreases if we add polymers in the system. In the growing stage the size of coated crystals raise, the value of frequency decreases and the width of the distribution increases [9].

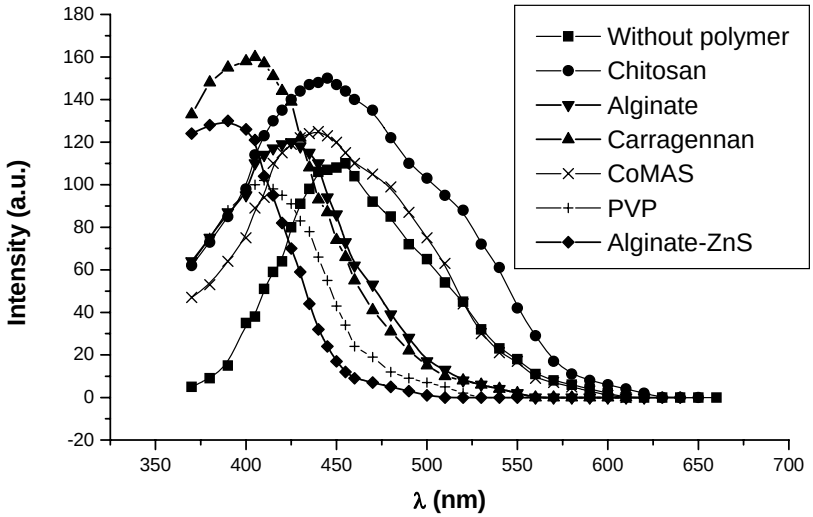

Fig. 5. Fluorescence of CdS particles coated with polymers, $C_{[CdS\ or\ ZnS]} = 1\times10^{-4}$ M.

Figure 5 shows fluorescent intensity of semiconductor nanoparticles single and coated with polymers. Fluorescence intensity of the CdS nanocrystals slightly increases for the additivated samples.

It is found that the samples of CdS coated nanoparticles exhibited different peaks function of capping polymer. The coating of CdS nanoparticles by polymers reduces effectively the local surface-trap states so that it can improve the photoluminescence properties of CdS nanoparticles [4]. Some authors believed that CdS nanoparticles showed the band edge photoluminescence peak centered at 450 nm [14]. For the coated nanoparticles the emission peak shifts due to the quantum confined effect.

In addition, the maximum wavelength of spectra shifts towards red with the increasing number of hydrocarbon [2]. The additive is known to interact with cadmium ions. It suggests that shorter carbon chain undergoes attraction for cadmium ions and forms the particle easily [15].

We considered that negative charges on CdS and positive charges on the polymers generate electrostatic interactions in the samples.

The modification of CdS nanoparticles by ethylene diamine reduces effectively the local surface-trap states so that it can improve the photoluminiscence properties of CdS nanoparticles [4].

For controlled passivation of cluster surfaces, several methods have been developed by using hydroxide ions, amines, ammonia and ZnS [16]. Typical semiconductor clusters as prepared contain surface defects. As a result, the initial photognerated electron-hole pairs (excitons) get trapped very rapidly. This is reflected in the photoluminescence spectrum, which usually shows a broad trap emission, red-shifted from the exciton absorption peak. As a result of these passivation procedures, new band-edge emissions can be observed in the photoluminescence spectra [5].

The synthesized nanoparticles were dispersed in polymeric matrix and then were applied on glass support to form films. The films are relatively homogeneous, have a nanostructured texture and a good adherence on support.

Figure 6 b shows a microscopic image of the surface of the deposited film made by confocal laser microscope, and cadmium sulphide can be observed as dispersed dots under a phase-contrast microscope, and some luminescence was detectable under fluorescence device (see Fig. 6 a).

The film of sample 55 CdS which contains the copolymer maleic anhydride/styrene, presents for the spectrum of emission a main maximum at 510 nm and some other picks at 523 nm and 533 nm (see Fig. 7 a).

The micrograph of polymeric film in the Fig. 7 b shows the existence of crystalline concentrations which contain the small particles relative spread in the polymeric matrices; it can be observed some clusters provided by the non-homogeneities of the film.

The recorded fluorescence spectra for the investigated samples have a full width at half maximum value of about 30 nm with a symmetric distribution around the central maximum and the spectral profile not skewed towards the longer wavelengths as one can tell by looking at the Fig. 8 a, typical for a quantum dot structure.

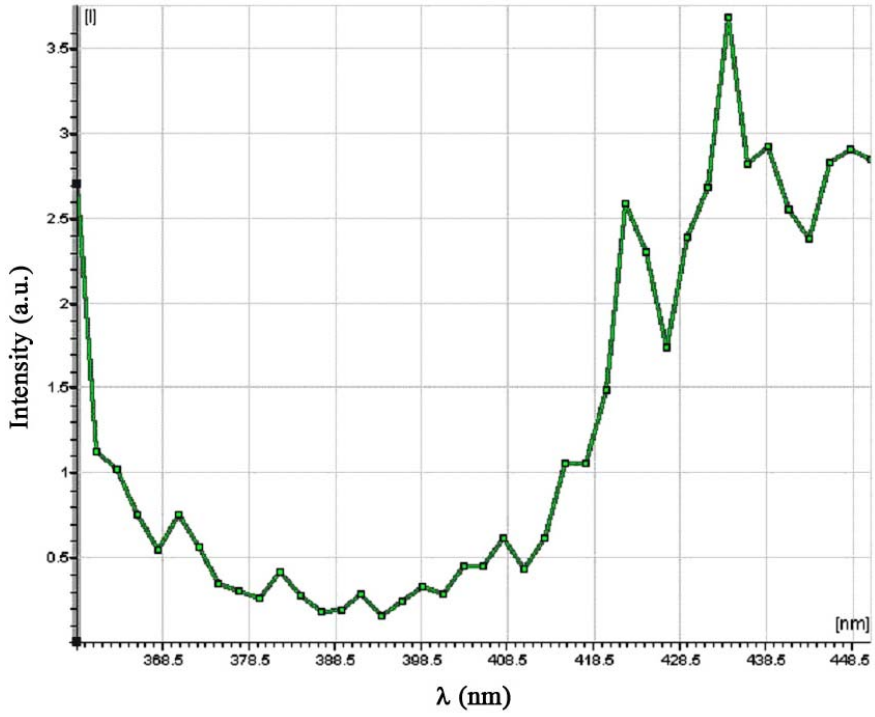

a)

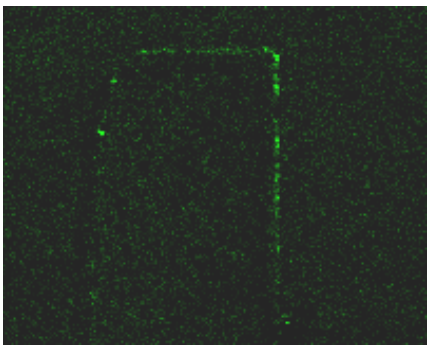

b)

Fig. 6. CdS nanoparticles in chitosan film,
a) the fluorescence; b) surface of CdS-chitosan film.

The extension of the spectral profile towards the longer wavelengths (having higher intensity "tails") and the photobleaching are the main problems concerning most organic fluorochromes. The narrow emission profile is the one that can enable several quantum dots conjugates to be simultaneously observed in multiple labeling

experiments. The ability to stimulate multiple quantum dot sizes in the same specimen with a single excitation wavelength, obtaining several different fluorescent signals with a good signal to noise ratio is the reason to consider these artificial structures as excellent candidates for the multiple labeling experiments.

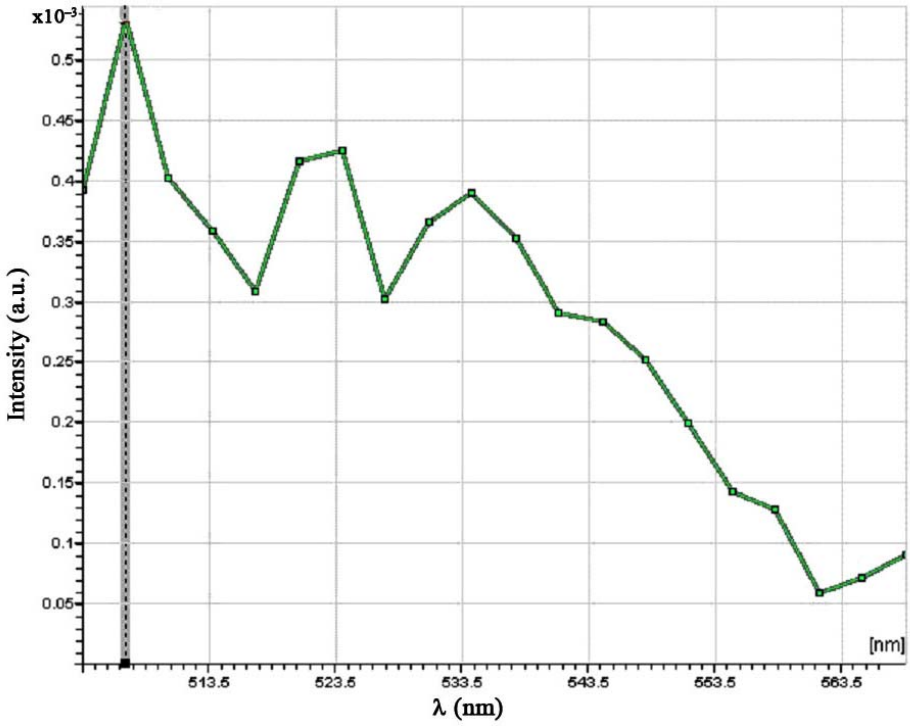

a)

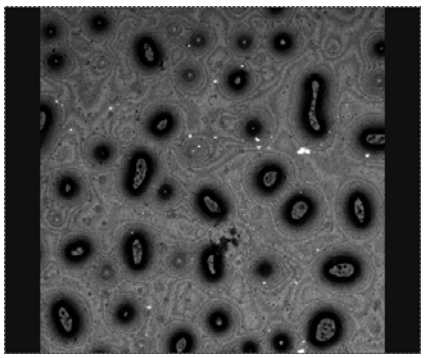

b)

Fig. 7. CdS nanoparticles CdS in CoMAS film,
a) the fluorescence; b) surface of CdS-CoMAS film.

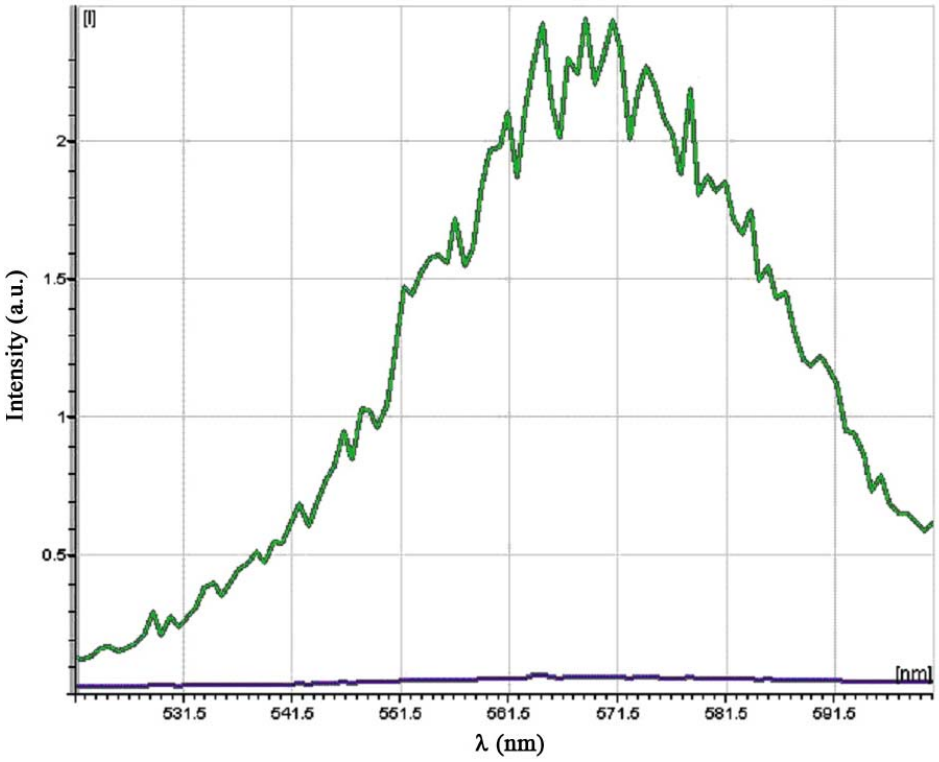

a)

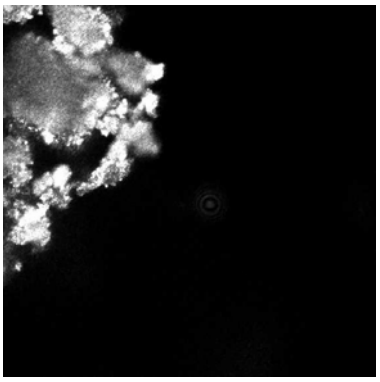

b)

Fig. 8. CdS powder in carragennan film, a) the fluorescence;
b) surface of CdS - carragennan film.

It was obtained a solid product by a new method, in the powder form of orange color. These CdS nanoparticles, in the powder form, have been used together

with carraghenan biopolymer of 2 % concentration to obtaining a nanocomposite in film form. This optimal composition was applied on glass support. By using confocal microscopy method (see the micrograph of Fig. 8 b) and by fluorescence determinations (Fig. 8 a), we can suppose as cadmium sulphide exist in the form of nanoparticles in this powder.

The cytotoxicity or the biocompatibility of the suspension of nanoparticles was determined by MTT Cell Proliferation Assay. The absorbance at 570 nm obtained for control was considered 100%. The results for the treated cells were expressed as percentage from the control, untreated culture. Cell viability was expressed as a percentage of control treated with different concentrations of quantum dots (QD) suspensions.

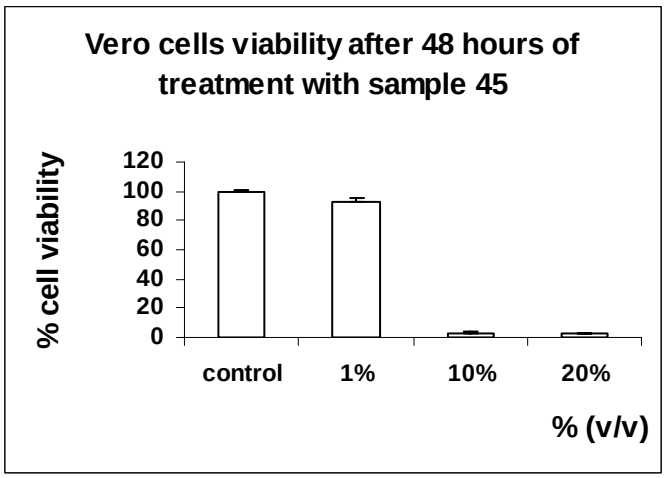

Fig. 9. Cytotoxicity induced by different concentrations of CdS-CoMAS (v/v) from initial 1×10^{-4} M.

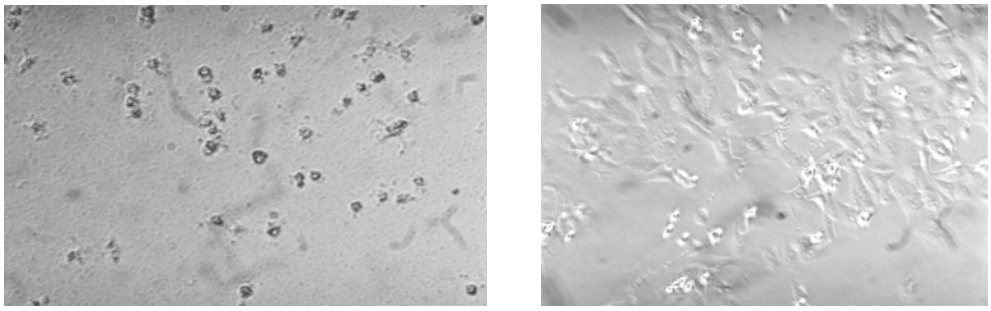

a) **b)**

Fig. 10. Micrographs of Vero cells after 48 hours of treatment with sample 45 (CdS-CoMAS), a) 1% v/v; b) 10% v/v.

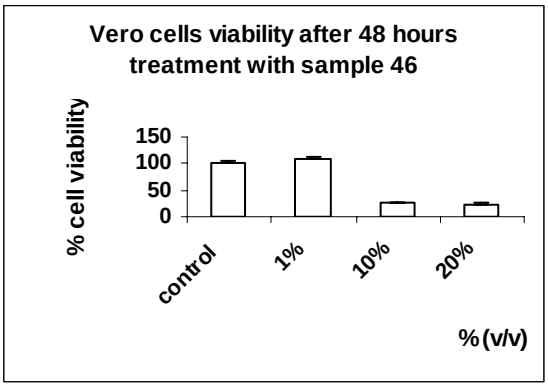

Fig. 11. Cytotoxicity induced by different concentrations of CdS-chitosan (v/v) from initial 1×10^{-4} M.

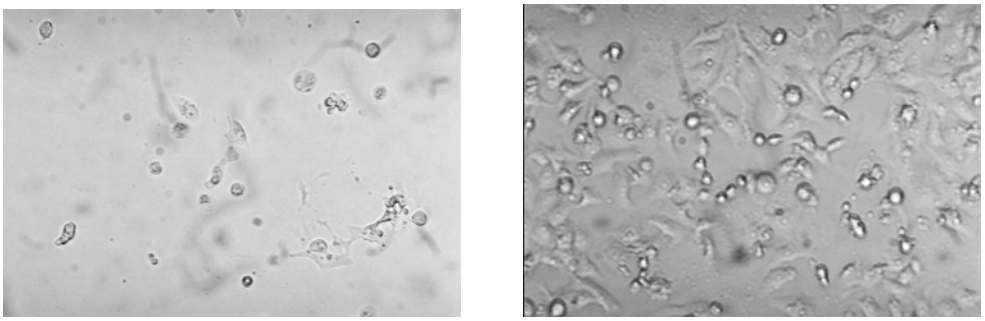

a) **b)**

Fig. 12. Micrographs of Vero cells after 48 hours of treatment with sample 46 (CdS-chitosan), a) 1% v/v; b) 10% v/v.

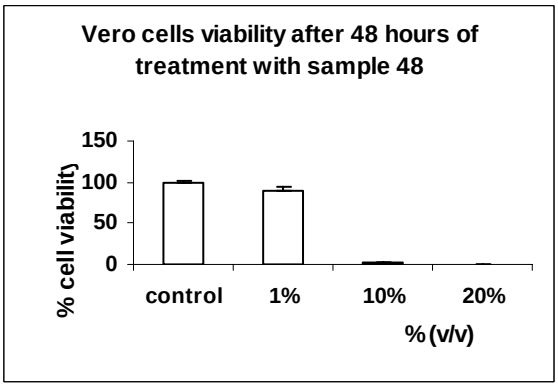

Fig. 13. Cytotoxicity induced by different concentrations of CdS-alginate (v/v) from initial 1×10^{-4} M.

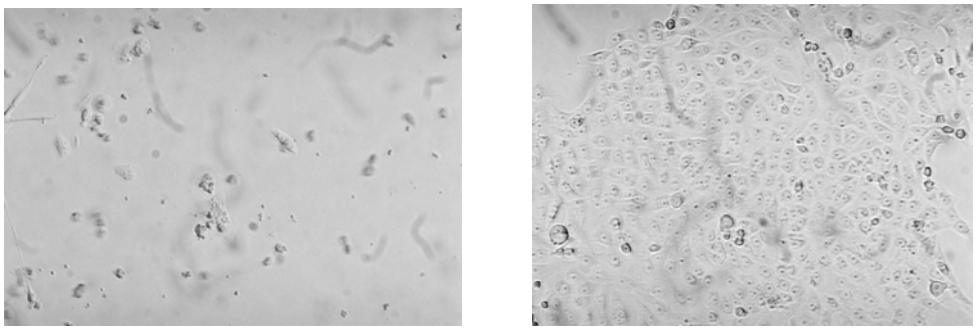

a) **b)**

Fig. 14. Micrographs of Vero cells after 48 hours of treatment with sample 48 (CdS-alginate), a) 1% v/v; b) 10% v/v.

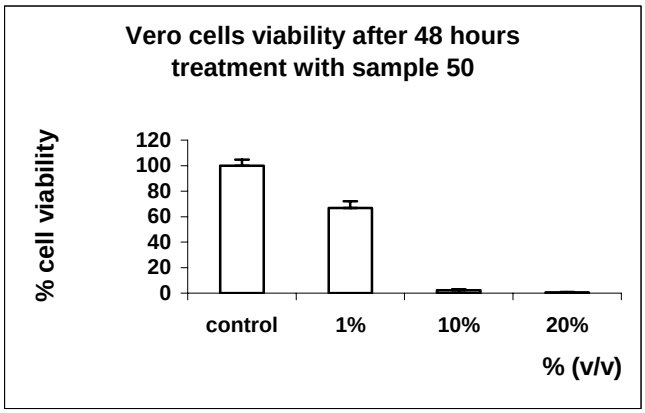

Fig. 15. Cytotoxicity induced by different concentrations of CdS-PVP (v/v) from initial 1×10^{-4} M.

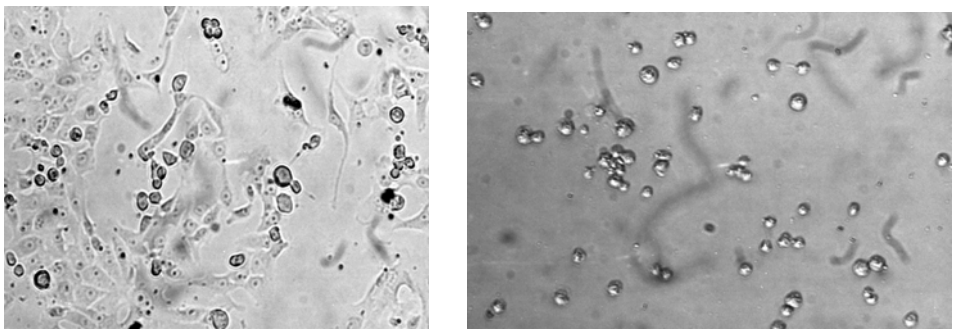

a) **b)**

Fig. 16. Micrographs of Vero cells after 48 hours of treatment with sample 50 (CdS-PVP), a) 1% v/v, b) 10% v/v.

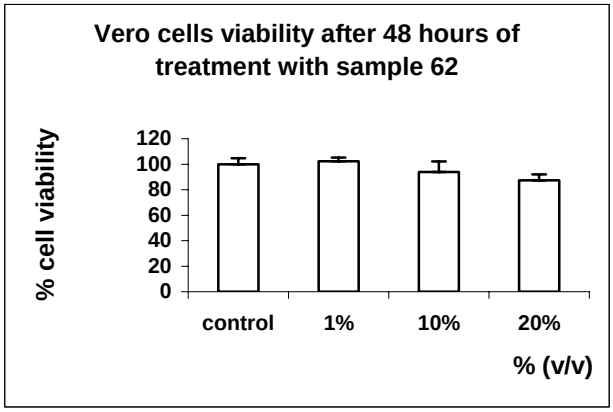

Fig. 17. Cytotoxicity induced by different concentrations of ZnS-Alginate (v/v) from initial 1×10^{-4} M.

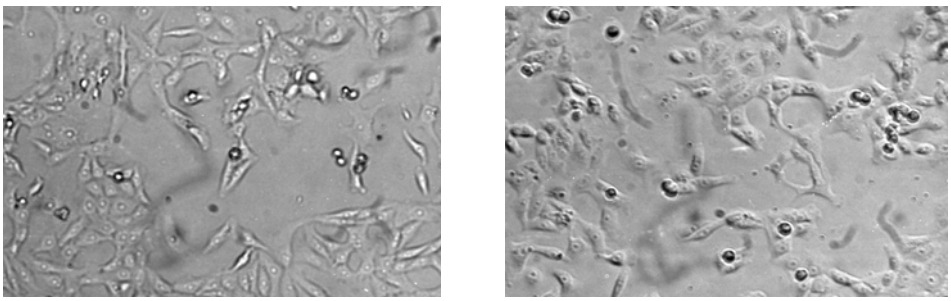

a) **b)**

Fig. 18. Micrographs of Vero cells after 48 hours of treatment with sample 62 (ZnS-Alginate), a) 1% v/v; b) 10% v/v.

The studies suggest that QD toxicity depends on multiple factors derived from both the physicochemical properties of quantum dots and environmental conditions [17]. Quantum dot composition, size, charge, concentration, outer coating bioactivity (capping material and functional groups), and mechanical stability are each factors that, individually or collectively, could determine QD toxicity. The most significant factors in assessing the risk of quantum dots toxicity are the functional coating and QD core composition and stability.

In vitro studies suggest certain quantum dots types may be cytotoxic. Lovric and coworkers [18] found that CdTe quantum dots coated with mercaptopropionic acid (MPA) and cysteamine were cytotoxic to rat pheochromocytoma cell (PC12) cultures at concentrations of 10 μg/mL. Uncoated CdTe quantum dots were cytotoxic at 1 μg/mL. Cell death was characterized as chromatin condensation and membrane blebbing, symptomatic for apoptosis. Cytotoxicity was more pro-

nounced with smaller positively charged quantum dots (2.2 ± 0.1 nm) than with larger equally charged quantum dots (5.2 ± 0.1 nm) at equal concentrations (cytotoxicity determined by MTT [3-(4,5-dimethylthiazol-2-yl)-2,5-diphenyltetrazolium bromide] assay). Quantum dot size was also observed to affect subcellular distribution, with smaller cationic quantum dots localizing to the nuclear compartment and larger cationic quantum dots localizing to the cytosol. The mechanisms involved in cell death were not known but were considered to be due to the presence of free Cd (QD core degradation), free radical formation, or interaction of quantum dots with intracellular components leading to loss of function. Cytotoxicity and the potential interference of qdot labelling with cellular processes are primary issues in any live-cell or animal experiment. These questions are complicated by the variety of protocols of quantum dot synthesis, solubilization or functionalization [19].

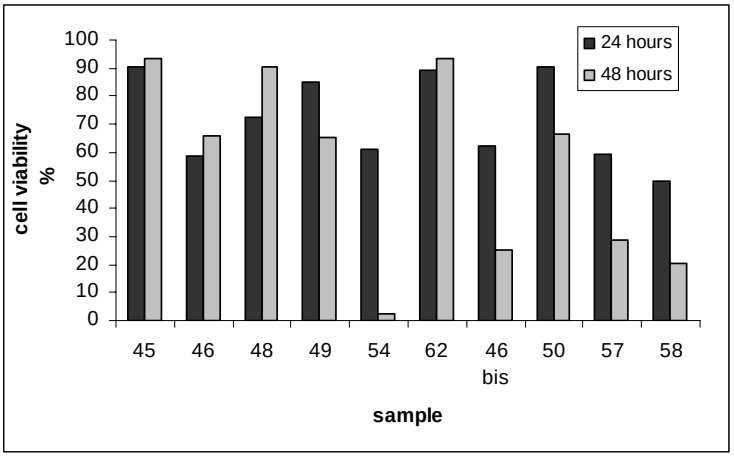

Fig. 19. Comparative cell viability or induced cytotoxicity of synthesised semiconductors coated with different polimers, after 24 and 48 hours of treatment with 1% sample.

Anyway, the polymer-coated nanoparticles synthesised by us present low toxicity after one day of cultivation with Vero cells (Fig. 19). After two days, the toxicity increase, but one day of viability it is enough for using the obtained nanostructures in imagistic studies.

4. Conclusions

We have elaborated a simple and efficient method for the obtaining semiconductor nanoparticles in polymers solution. The used polymers have an important role in the size control, the stability and like capping agent of the particles.

The nanoparticles can exist long time in polymers solution and they can be used for the obtaining of films on glass support. The size of nanoparticles was de-

termined by fitting the absorbance data with some specific equations from quantum dots' literature.The kinetics data from UV-Vis spectra show that the nanoparticles present an initial rapid formation, followed by a very slow growth process. The fluorescence properties depend on the nature of capping polymer.

The samples containing CdS-CoAMS, CdS-Alginate, CdS-PVP, and ZnS-Alginate have a better biocompatibility and a lower induced toxicity on cultured Vero cells.

The cytotoxicity of semiconductors diminishes up to 10 times by coating with polymers; the sample CdS-Alginate (concentrations 1×10^{-5} M) present no toxicity for cultured cells more after 24 hours, and sample 62 ZnS-Alginate is non-toxic even after 48 hours of cultivation with Vero cells, up to 20 μM concentration.

All these facts are a good premise to use the synthesized semiconductors for imagistic studies.

References

[1] MALEKI M., GHAMSARI M.S., MIRDAMADI S., GHASEMZADEH R., Semiconductor Physics, **10**, pp. 30–32 (2007).
[2] MATSUZAWA Y., SUZUKI J., J. Chem. Eng. Japan, **34**, pp. 700–702 (2001).
[3] BRUCHEZ M., MORONNE M., GIN P., WEISS S., ALIVISATOS A.P., Science, **281**, pp. 2013–2016 (1998).
[4] TANG H., YAN M., ZHANG H., XIA M., YANG D., Materials Letters, **59**, pp. 1024–1027 (2005).
[5] WANG Y., HERRON N., J. Phys. Chem., **95**, pp. 525–532 (1991).
[6] KIM J., PARK K., HAHN S. K., Int. J. Biol. Macromol, **42**, pp. 41–45 (2008).
[7] MOSMANN T., J. Immunol. Methods, **65**, pp. 55–63 (1983).
[8] LEE S. H., HER Y.S., MATIJEVIC E., J. Colloid Interface Sci., **186**, pp. 193–198 (1997).
[9] LIBERT S., GORSHKOV V., GOIA D., MATIJEVIC E., PRIVMAN V., Langmuir, **19**, pp. 10679–10683 (2003).
[10] TOWEY T.L., KHAN-LODHI A., ROBINSON B.H., J. Chem. Soc. Faraday Trans., **86**, pp. 3757–3762 (1990).
[11] WELLER H., SCHMIDT H. M., KOCH U., FOJITIK A., BARAL S., HENGLEIN A., KUNATH W., WEISS K., DIEMAN E., Chem.Phys Lett., **124**, pp. 557–560 (1986).
[12] SUZUKI K., HARADA M., SHIOI A., J. Chem. Eng.Japan, **29**, pp. 264–276 (1996).
[13] BRUS L.E., J. Chem.Phys, **80**, pp. 4403–4409 (1984).
[14] MOORE D.E., PATEL K., Langmuir, **17**, pp. 2541–2544 (2001).
[15] NOSAKA Y., YAMAGUCHI K., MIYAMA H., HAYASHI H., Chem. Lett., **4**, pp. 605–608 (1988).
[16] STEINGERWALD M.L., CARROLL P.J., BRUS L.E., J. Am. Chem. Soc., **112**, pp. 1327–1333 (1990).
[17] HRDMAN R., Environmental Healths Perspective, **114**, pp. 165–173 (2006).
[18] LOVRIC J., BAZZI H.S., CUIE Y., FORTIN G.R.A., WINNIK F.M., MAYSINGER D., J. Mol. Med., **83**, pp. 377–385 (2005).
[19] MICHALET X., PINAUD F. F., BENTOLILA L. A., TSAY J. M., DOOSE S., LI J. J., SUNDARESAN G., WU A. M., GAMBHIR S. S., WEISS S., Science, **307**, pp. 538–544 (2005).

The Study of Antibacterial Activity of Nanostructured TiO_2 Thin Films

M. ENACHE[1], C. VĂCĂROIU[1], G. POPESCU[1], L. DUMITRU[1], A. BREZEANU[1], M. GARTNER[2], M. ANASTASESCU[2]

[1]Institute of Biology Bucharest of the Romanian Academy
[2]Institute of Physical Chemistry *I. Murgulescu* of the Romanian Academy
E-mail : madalin.enache@ibiol.ro

Abstract. This paper deals with investigation of antibacterial activity of TiO_2 thin films with various concentration of PEG (0.01–0.1M) and iron (1.23 and 7%) in their composition or doped with nitrogen and followed by thermal treatment at different temperatures (500–1000°C). The results revealed that investigated thin films have antibacterial activity which is influenced by coatings compositions and temperature of thermal treatment. The optimum concentration of iron and PEG enhanced antibacterial activity and induced some change for the surface structure which became congruent with this antibacterial activity. The photocatalytic reaction is higher at low iron content. The investigated nanostructures doped with nitrogen and thermal treated at 600°C have a better antibacterial activity that structures treated at 500°C. On the other hand, this activity has been influenced by illumination time with white artificial light. The electron microscopy investigations revealed that main effect towards microbial cell are at the level of cell membrane and could be associated with cell degradation, minivesicles formation, strong plasmolize and intracellular vacuoles, cellular ghost and membrane fragments.

1. Introduction

Since the photochemical disinfection of *Escherichia coli* in the presence of TiO_2/Pt was reported by Matsunaga *et al.* [12], the technology of photocatalytic inactivation studies using TiO_2 under ultraviolet light irradiation has obtained much attention in the last years [11, 21, 23]. The antimicrobial activity of UV/TiO_2 has been assayed in several bacteria and viruses including *Escherichia coli, Lactobacillus acidophilus, Serratia marcescens, Pseudomonas aeruginosa, P. stutzeri, Bacillus pumilus, Streptococcus mutans, S. cricetus, S. sobrinus, Deinococcus radiophilus*, yeast as *Saccharomyces cerevisiae*, algae as *Chlorella vulgaris* and viruses such as phage MS2, *B. fragilis* bacteriophage, poliovirus [11, 14, 15]. It is widely

known that materials containing metals such as silver, copper, zink show antibacterial properties and activities. More specifically, metal ions penetrate in bacteria and inactivate their enzymes, or can generate hydrogen peroxide, thus killing bacteria [19, 20].

Transparent TiO_2 films, TiO_2 immobilized in acetylcellulose membranes [13] and entrapment of TiO_2 into sol–gel prepared pellets [18] have been tested and use of optical fibers or intermittent and variable irradiation have been also recommended to improve the applications. Municipal wastewaters have been also treated with relatively good efficiency [1, 21] and total and fecal coliforms and viruses present in secondary wastewater effluents have been successfully removed [21]. Also, the technology can even be applied to destroy bioaerosols in air. As TiO_2 photocatalysis can make use of the UV part of the solar spectrum, it becomes promising to potabilize the waters in some tropical countries with scarce hydric resources and high availability of solar irradiation [14].

Titania exists in a number of crystalline forms the most important of which are anatase and rutile. It is well known that TiO_2 absorbs UVA, resulting in the formation of paired electrons and holes [7]. Photogenerated holes are thought to be trapped, and absorbed on the surface of TiO_2 particles [18]. The photocatalytic activity of anatase-type TiO_2 was greater than that of rutile type, because the optical band gap of anatase-type TiO_2 (3.23 eV) is greater than that of rutile type (3.06 eV), thus UVA-irradiation of anatase type should generate electrons and holes more efficiently than in the case of rutile type. Upon excitation by light whose wavelength is less than 385 nm, the photon energy generates an electron hole pair on the TiO_2 surface. The hole in the valence band can react with H_2O or hydroxide ions adsorbed on the surface to produce hydroxyl radicals (OH), and the electron in the conduction band can reduce O_2 to produce superoxide ions (O_2^{-}). Both holes and OH·are extremely reactive with contacting organic compounds. Detection of other reactive oxygen species (ROS), such as hydrogen peroxide (H_2O_2) and singlet oxygen, has also been reported. Together with $^1O_2$ (singlet molecular oxygen) these radicals are a highly reactive oxygen species that may harm living systems by oxidizing critical cellular macromolecules, including lipids, nucleic acids [2] and proteins. It also promotes deleterious process, such as lipid peroxidation, membrane damage and cell death [4, 10].

When illuminated, TiO_2 particles act as a semiconductor, generating HO radicals and other reactive oxygen species by electrochemical reactions conducted at the surface of photocatalyst. Because of their high level of reactivity, they are also very short lived. When irradiated TiO_2 particles are in direct contact with or close to microorganisms, the microbial surface is the primary target of the initial oxidative attack. Phospholipids are an integral component of the bacteria cell membrane, and the susceptibility of these compounds to attack by reactive oxygen species has been well documented [9].

Despite many potential applications of these nanoparticles [17, 22], their use are currently limited to environments where insufficient UV lights can be made to be in contact with TiO_2 surface. Thus it has become an important goal in the development of these materials, to try to modify them such that lower energy, visible light such as conventional internal light sources, may also be used to stimulate both the photocatalytic activity and the superhydrophilicity that usually accompanies it [6]. By inclusion of specific dopants it should be possible to improve the efficiency of the photocatalytic behavior by creating new band structures or by suppressing the recombination of photogenerated electron-hole pairs to improve quantum efficiency [8]. Many authors have concluded that N-doping of TiO_2 leads to visible light photoactivity, but there is a difference in opinion as to how doping achieves this, as well as disagreements in many of the conclusions drawn from the results [24].

Even if exist a lot of data regarding photocatalytic activity there are no informations available about the role of thermal treatment of TiO_2 films towards antibacterial properties of such nanostructures. In this paper we have been investigated the antibacterial properties of N-doped TiO_2 films and the effect of thermal treatments of doped nanostructures on the viability and growth of an *E. coli* strain isolated from an wastewater treatment plant nearby to the Buzău city, and characterized in our laboratory. On the other hand, the effect of iron and PEG content of coatings on the antibacterial activity is described.

2. Materials and methods

Culture and media – The *E.coli* strain used in the present investigations has been procured from the Center of Microbiology, Institute of Biology Bucharest, as mentioned before. The strain was growth in nutritive broth, solidified with agar 20 g/l when necessary.

Investigated nanostructures – The investigated samples were represented by TiO_2 coatings having in composition iron and PEG in various concentrations as described in Table 1 or doped with nitrogen and thermal treated at different temperatures (Table 1).

The effect of Fe^{2+} and PEG on the bacterial growth – The samples represented by coatings on the glass (1-8) were immersed in flask with 22.5 ml of nutrient broth (pH 7.2) and inoculated with E. coli culture (2.5 ml) having O.D. at 660 nm around 0.16. The flasks were incubated without shacking at 37^0C. The effect of coatings composition has been evaluated following the differences in evolution of growth in the presence of each tested sample (O.D. at 660 nm was registered). After this test, the samples were transferred in 25 ml nutrient broth without bacterial inoculum in order to test if bacterial cells remain on the surface of coatings and which is the effect of coatings composition if bacterial concentration is lower.

Table 1. Details about investigated samples

Sample	Fe %	PEG_{600} (M)	Sample	Layer number	Thermal treatment (TT) temperature (^{0}C)	Atmos-phere of TT
1	1.23	0.06	9	5	500	O_2
2		0.029	10			NH_3
3		0.014	11		600	NH_3
4		0.11	12			O_2
5		0.00	13	3	400	NH_3
6	7	0.069	14		500	
7		0.017	15		800	
8	Glass support		16		1000	

The viability of E. coli strain at the doped films surface – In this case a volume of 200 µl of bacterial culture corresponding of 10^6 dilution series was spread on the surface of TiO_2 films and illuminated with white light (3.1×10^4 lux) from 20 cm for 0.17, 0.5, 1 and 4 hours, at room temperature. After each time period, the 200 µl bacterial culture illuminated was diluted with 800 µl sterile distilled water and transferred in melted solidified medium. The samples were incubated for 24 hours at 37°C and CFU was registered.

The effect of TiO_2(N) films on the bacterial cell – was observed by *electronic microscopy* following adapted method of Hayat [5]. Briefly, the cells growth in the presence of tested films were harvested by centrifugation at 9500 rpm and prefixed in 3% glutaraldehyde in Na-cacodylate – HCl buffer (0.2M), at 4°C, overnight. Before and after agar (2%) inclusion the cells were washed with same buffer (0.1M). After that the cells were fixed in OsO_4 1% at 4°C overnight. A dehydration step with alcohol and mixture propylene oxide: alcohol (1:1 v/v) and propylene oxide was performed. After dehydration the cells were embedded in epoxy resin EPON 812 (Fluka). After polymerization, thin sections were performed at the LKB ultramicrotome. The sections were contrasted by Raynolds method [16] using lead citrate and uranil acetate and then were visualized at the transmission electron microscopy at the electrons acceleration of 75 kV.

3. Results and discussion

The effect of Fe^{2+} and PEG on the bacterial growth – The results showed in Fig. 1 revealed the growth of bacterial cells in the presence of coatings but with

differences in culture evolution during to 72 hours of growth. The first answer after 24 hours of growth split the investigated samples in two groups. In the presence of samples 1, 5 and 7 was registered a low growth which could be associated with chemical composition of tested coatings. In opposite, the group of samples 2, 3, 4, 6 and 8 has a good growth. In this group was observed that sample 4 showed a good growth probably due to the presence of high concentration of PEG in the coating composition.

The results revealed that at iron content of 1.23% (samples 1–5) the inhibitory effect of coatings is influenced by PEG concentration from composition and decrease in the presence of high content of PEG. There was observed one exception for 0.06M PEG (sample 1) content. Also, some inhibitory effect was observed if PEG was no present in coating composition (sample 5) but at low intensity if compare with sample 1 (0.06M PEG). The inhibitory effect appear to increase when iron content increase at 7% (sample 7) and PEG content remain relatively constant around 0.01M (samples 3 and 7). On the other hand, if PEG content increases at 0.069M (sample 6) the inhibitory effect decrease (sample 6, iron content 7%). These results confirm that presence of PEG in coating composition conducted at modification of inhibitory activity of tested sample. Most probably high concentration of PEG conferee a high degree of porosity of the coatings and bacterial cell cover the pores and thus contribute at decrease of photocatalityc properties of the coatings. The results revealed that growth of bacterial cells is inhibited by tested thin films on the glass support and the intensity of inhibitory effect is correlated with chemical composition of coatings.

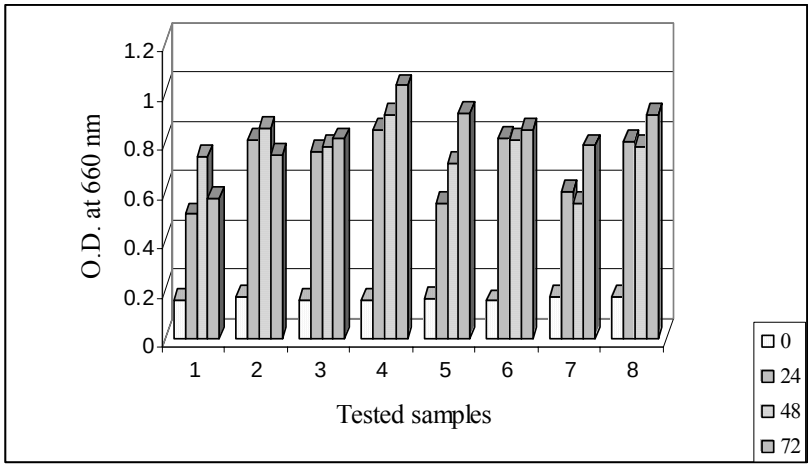

Fig. 1. The growth of E.coli strains in the presence of investigated samples.

After these investigations the samples were transferred in 25 ml nutrient broth without bacterial inoculum in order to test if bacterial cells remain at the sur-

face of coatings and which is the effect of coatings composition in the presence of low bacterial concentration. The results showed in Fig. 2 revealed that some bacterial cells are able to remain to the surface of coatings but the growth is lower that in first test. This experiment appears to be not suitable for the inhibitory effect highlighting but also revealed the influence of PEG towards this effect.

The registered data revealed that in the absence of PEG (sample 5) the cells appear to not remain to the surface of the coatings (Fig. 3). In this case, the porosity degree of the coating surface is reduced by comparison with coatings having PEG in composition in various concentrations [3] and these argued against adherence capacity of the cells to the coating surface. On the other hand, at 1.23% iron content and various PEG concentrations (sample 1–4) the investigated strain remain on the surface of the coatings and are able to grow (the best growth was in the presence of 0.06M PEG). In the presence of 7% iron in composition, the inhibitory effect of the coatings appears to be influenced by PEG in a similar way as in previously test (high concentration of PEG conducted at decreasing of inhibitory effect).

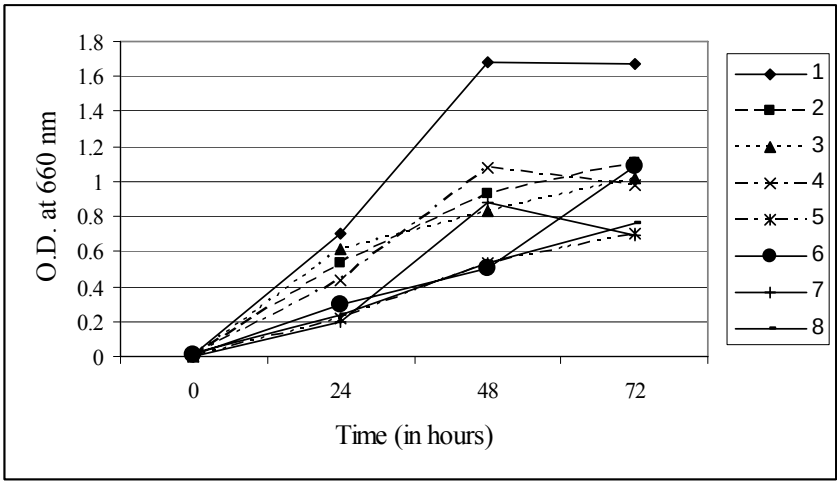

Fig. 2. The effect of coatings composition on the growth of low number of bacterial cells.

The viability of E. coli strain at the doped films surface – The registered data are showed in Figs. 4 and 5. The investigated samples both with three or five layers, showed antibacterial activity under illumination. The samples doped with nitrogen and thermal treated at 600°C appear to have a better activity than sample treated at 500°C (Fig. 4, samples 10 and 11). A similar behavior towards thermal treatment has been observed for the undoped samples (Fig. 4, samples 9 and 12). The results obtained showed that antibacterial activity of the samples treated in NH_3 atmosphere has been better that of the samples treated in oxygen atmosphere (Fig. 4). In all experimental condition was observed that antibacterial activity is

correlated with illumination time and increase with it. The results registered at 0.5 hours of illumination for the sample 9 and 10 (Fig. 4) could be due to growth of the microbial cells to the surface of coatings as a consequence of heat resulted from illumination lamp. On the other hand, the microbial cells most probably have some protective mechanisms for adaptation to the stress due to reactive oxygen species generated at the surface of the coatings following the iradiation.

By increase temperature of thermal treatment at 600°C (samples 11 and 12, Fig. 4) some modification of photocatalytic properties of the coatings appear and conducted to a better antibacterial activity. The obtained results showed that treatment in nitrogen atmosphere help for this activity.

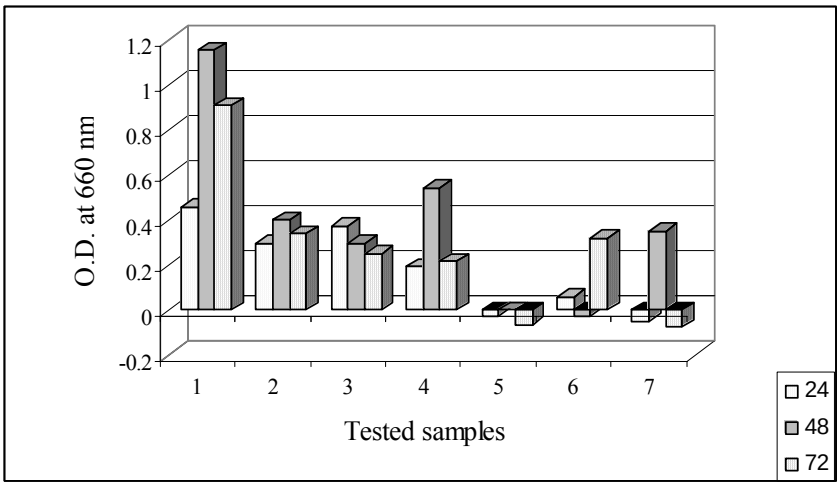

Fig. 3. The effect of porosity degree of the coatings surface on the growth of bacterial cells.

A similar behavior was observed also for the samples with three layers, increasing temperature of thermal treatment determine increasing of antibacterial activity respectively (Fig. 5). By opposite with five layers there was observed that treatment in nitrogen atmosphere don't influenced antibacterial activity but this effect could be eliminated by increasing temperature of thermal treatment (Fig. 5, samples 15 and 16). The intensity of antibacterial activity was correlated with illumination time in a similar way as five layers investigated samples. The samples 13 and 14 appear to have a lower antibacterial activity if compare with samples 15 and 16. The samples are characterized by different thermal treatment temperatures (Table 1) and antibacterial activity could be correlated with this treatment.

The results of electron microscopy showed some modification of cell shape and structures. Both three and five layers investigated films induced transformation from rod to circle form. This effect appears to be more significant for the cells growth in the presence of three layers films (Fig. 6). Most probably the free radi-

cals generated at the surface of photocatalysts attack the membrane phospholipids of bacterial cells and thus induce destruction of the cell. The results from figure 6 showed that presence of investigated films induced some modification in membrane permeability which promotes destruction of cell content.

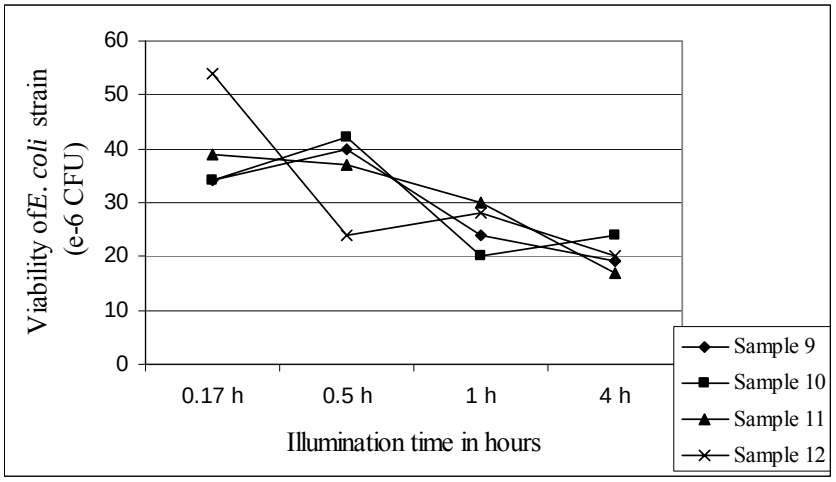

Fig. 4. Antibacterial activity of five layers investigated titania N doped.

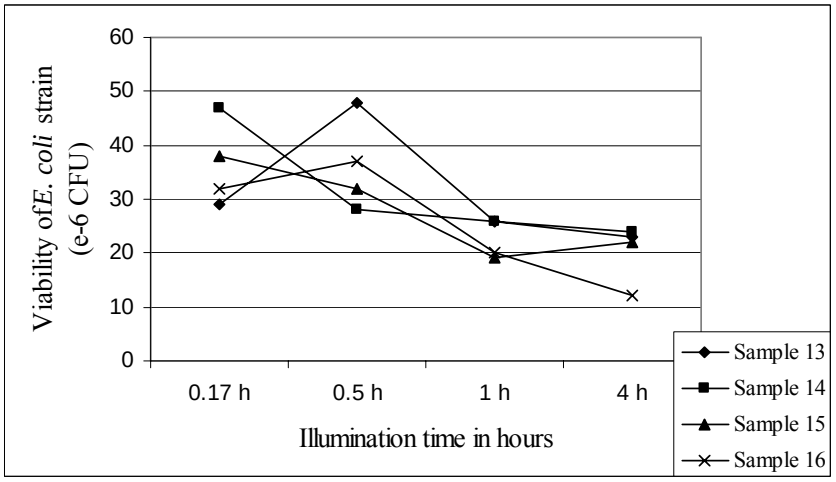

Fig. 5. Antibacterial activity of three layers investigated titania N doped.

The investigation revealed a number of cellular ghost and membrane fragment following to complete destruction of the microbial cell. On the other hand, was observed some minivesicle, cells with strong plasmolize and intracellular vacuoles. These data revealed a possible antibacterial effect of nanostructured TiO_2 films.

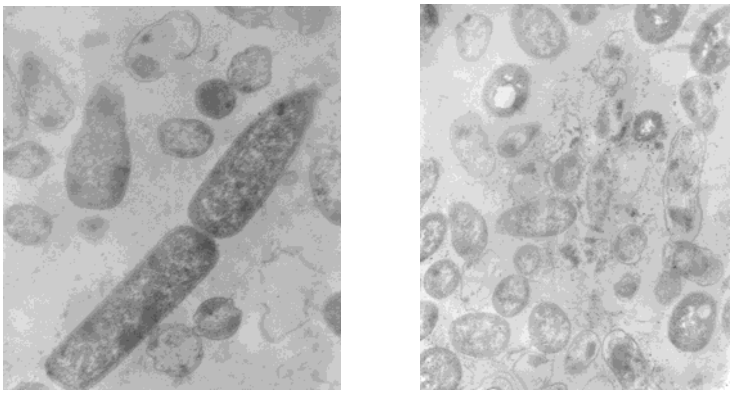

a) **b)**

Fig. 6. The effect of investigated films on the microbial cells observed at electronic microscope: a – microbial cells growth in absence of TiO_2 nanostructures film; b – microbial cells growth in the presence of three layer N-doped TiO_2 (sample 15).

4. Conclusions

The antibacterial activity of coatings having in composition Fe^{2+} and PEG, enhanced at the optimum content both of iron and PEG. The activity of tested samples crystallized in anatase phase appears to be optimum at low iron content. The results revealed that investigated films both with three or five layers showed antibacterial activity. This activity appears to be influenced by thermal treatment temperatures which increase densification of the investigated photocatalysts. By increasing temperature of the treatment also increase the antibacterial activity. The investigated films with three layers appear to have a better activity than five layers nanostructures and this activity increase by illumination with visible light being correlated with time of illumination.

The registered data supported future investigations for development of technologies for decontamination in various fields like wastewater treatment, hospitals, pharmaceutical or food industry.

References

[1] AGUSTINA T.E., ANG H.M., VAREEK V.K., *A review of synergistic effect of photocatalysis and ozonation of wastewater treatment*, J. Photochem. Photobiol. C: Photochem. Rev., **6**, pp. 264–273 (2006).

[2] ASHIKAGA T., WADA M., KOBAYASHI H., MORI M., KATSUMURA Y., FUKUI H., KATO S., YAMAGUCHI M., TAKAMATSU T., *Effect of the photocatalytic activity of* TiO_2 *on plasmid DNA*, Mutat. Res., **466**, pp. 1–7 (2000).

[3] GARTNER M., TRAPALIS ROVA N., GIANNAKOPOULOU T., DOBRESCU G., ANASTASESCU M., OSICEANU P., GHITA A., ENACHE M., DUMITRU L., STOICA T.,

ZAHARESCU M., BAE J.Y., SUH, S.-H., *Doped sol-gel* TiO_2 *films for biological applications,* Bull. Korean Chem. Soc., **29**, pp. 1038–1042 (2008).

[4] HALLIWELL B., GUTTERIDGE J.M.C., *Free Radicals in Biology and Medicine*, Oxford Press, Oxford, UK., 1999.

[5] HAYAT M. A., Basic Electron Microscopy Technique, Van Nostrand Reinhold Company, New York, USA, 1972.

[6] HU S., WILLEY R. J., NOTARI B., *An investigation on the catalytic properties of titania–silica materials*, J. Catal., **220**, pp. 240–248 (2003).

[7] JUDIN V. S. P., *The lighter side of* TiO_2, Chemistry in Britain, 1993, pp. 503–505.

[8] JUSTICIA I., ORDEJÓN P., CANTO G., MOZOS J. L., FRAXEDAS J., BATTISTON G. A., GERBASI R., FIGUERAS A., *Designed self-doped titanium oxide thin films for efficient visible-light photocatalysis,* Adv. Mater., **14**, pp. 1399–1402 (2002).

[9] KAPPUS H., *Lipid peroxidation: mechanisms, analysis, enzymology and biological relevance*. In H. Sies (ed.), Oxidative stress, pp. 273–310. Academic Press Inc. New York. USA, 1985.

[10] KIM S. Y., KIM E. J., PARK J. W., *Control of singlet oxygen-induced oxidative damage in Escherichia coli*, J. Biochem. Mol. Biol., **35**, pp. 353–357 (2002).

[11] MANNES P. C., SMOLINSKI S., BLAKE D. M., HUANG Z., WOLFRUM E., JACOBY W. A., *Bactericidal activity of photocatalytic* TiO_2 *reaction: toward an understanding of its killing mechanisms,* Appl. Environ. Microbiol., **65**, pp. 4094–4098 (1999).

[12] MATSUNAGA T., NAMBA Y., NAKAJIMA T., *Electrochemical sterilization of microbial cells*, Bioelectrochemistry and Bioenergetics, **13**, pp. 393–400 (1984).

[13] MATSUNAGA T., TOMODA R., NAKAJIMA T., MAKAMURA N., KOMINE T., *Continuous sterilization system that uses photosemiconductor powders*, Appl. Environ. Microbiol., **54**, pp. 1330–1333 (1988).

[14] OLLIS D. F., PELIZZETTI E., SERPONE N., *Destruction of water contaminants*, Environ. Sci. Technol., **25**, pp. 1523–1529 (1991).

[15] PASPALTSIS I., KOTTA K., LAGOUDAKI R., GRIGORIADIS N., POULIOS I., SKLAVIADIS T., *Titanium dioxide photocatalytic inactivation of prions*, J. Gen. Virol., **87**, pp. 3125–3130, (2006).

[16] RAYNOLDS R. S., *The use of lead citrate at high ph as an electron-opaque stain in electron microscopy*, J. Cell Biol., **17**, pp. 208–212 (1963).

[17] SALATA O. V., *Application of nanoparticles in biology and medicine*, J. Nanobiotechnology **2**:3 (2004).

[18] SJOGREN J. C., SIERKA R. A., *Inactivation of phage MS2 by iron-aided titanium dioxide photocatalysis*, Appl. Environ. Microbiol., **60**, pp. 344–347 (1994).

[19] TRAPALIS C. C., KOKKORIS M., PERDIKAKIS G., KORDAS G., *Study of antibacterial composite* Cu/SiO_2 *thin coatings*, J. Sol-Gel Sci. Techn., **26**, pp. 1–6 (2003a).

[20] TRAPALIS C. C., KEIVANIDIS P., KORDAS G., ZAHARESCU M., CRISAN M., SZATVANYI A., GARTNER M., $TiO_2(Fe^{3+})$ *nanostructured thin films with antibacterial properties*, Thin Solid Films, **433**, pp. 186–190 (2003b).

[21] WATTS R. J., KONG S., ORR M. P., MILLER G. C., HENRY B. E., *Photocatalytic inactivation of coliform bacteria and viruses in secondary wastewater effluent*, Water Sci., **29**, pp. 95–100 (1995).

[22] WHITESIDES G. M., *The "right" size in nanobiotechnology*, Nature Biotechnology, **21**, pp. 1161–1165 (2003).

[23] WONG M. S., CHU W. C., SUN D. S., HUANG H. S., CHEN J. H., TSAI P. J., LIN N. T., YU M. S., HSU S. F., WANG S. L. CHANG H. H., *Visible-light-induced bactericidal activity of a nitrogen-doped titanium photocatalyst against human pathogens*, Appl. Environ. Microbiol., **72**, pp. 6111–6116 (2006).

[24] YATES H. M., NOLAN M. G., SHELL D. W., PEMBLE M. E., *The role of nitrogen doping on the development of visible light-induced photocatalytic activity in thin* TiO_2 *films grown on glass by chemical vapour deposition*, J. Photochem. Photobiol. A, **179**, pp. 213–223 (2003).

The TiO_2-Pt Nanoparticles Effect on the Ultrastructural Features of the *Allium Sativum Sagitatum* Callus

G. C.CORNEANU[1], M. CORNEANU[2], C. CRĂCIUN[3], C. LAZĂU[4], I. GROZESCU[4]

[1]University of Craiova, Biology-Genetics Dept., 200585-Craiova, Romania;
[2]University of Agronomical Sciences and Veterinary Medicine of Banat, Genetic Engineering Dept., 300645-Timisoara, Romania;
[3]*Babes-Bolyai* University, Electron Microscopy Center, 400006 - Cluj-Napoca, Romania;
[4]I.N.C.-D.E.M.C. 300860-Timisoara, Romania.
E-mail: gabicorneanu@yahoo.com

Abstract. An *in vitro* callus culture of *Allium sativum sagitatum* was treated, or has not, with a fine powder of TiO_2-Pt nanoparticles for five days. The treated or untreated callus culture, was maintained at a light regime of 16 h light per day, in a growth chamber, at 24°±2°C. The ultrastructural features of the callus were analyzed at a TEM JEOL JEM1010 apparatus (Electron Microscopy Center, *Babes-Bolyai* University, Cluj-Napoca, Romania). Because the treatment with TiO_2-Pt nanoparticles was performed by spraying, the effect of the TiO_2-Pt nanoparticles effect was dependent on the cell position in the callus tissue. In the cells situated near the callus surface, the TiO_2-Pt nanoparticles presented a toxic effect, while in the cells from the middle of the callus, the TiO_2-Pt nanoparticles increased the metabolic processes, the cells being in an intense metabolic activity.

1. Introduction

Titanium dioxide was initially considered as being biologically inactive [1, 2]. The researches performed with ultrafine particles of TiO_2 (under 20 nm in diameter), established a strong inflammatory effect in lung with rats, in comparison with the large particles (250 nm in diameter [3]). Titanium interacts with biological fluids, through the stable layer of titanium dioxide, with role in the biocompatibility. The UV rays induce the formation of some pyrimidine dimmers in the DNA molecule, with a subsequent evolution influenced by different factors. The effect is depending on the TiO_2 molecule reactivity. TiO_2 can induce lesions in the DNA molecule, by the action of the free radicals resulted from photochemical reactions [4].

Doped with other elements, the TiO_2 nanoparticles enhanced their photocatalytic reactivity [5]. There were numerous researches by which some bimetallic nanoparticles were obtained [6]. The investigations of the TiO_2 nanoparticle effect on the vegetal cell were rare, being noted the ultrastructural modifications [7, 8], as well as the nanoparticles effect on the chromosome integrity [9].

2. Material and methods

Titanium dioxide was doped with platinum ions and it was synthetized by the sol-gel method. The precursor for titanium was titanium tetrachloride and for platinum, acid hexachloroplatinate hydrate (1% Pt from titanium quantity) was used. The obtained material was characterized through X-ray diffraction (XRD) and scanning electron microscopy (SEM). From the diffractogram analysis (Fig. 1), it result that the *anatase* crystallization form was obtained [8]. The nanoparticles powder was analyzed at a scanning electron microscope of the JEOL JSM 5510 LV type (Electron Microscopy Center in *Babes-Bolyai* University of Cluj-Napoca). The particles' size was of about 30 nm, their shape being presented in Fig. 2.

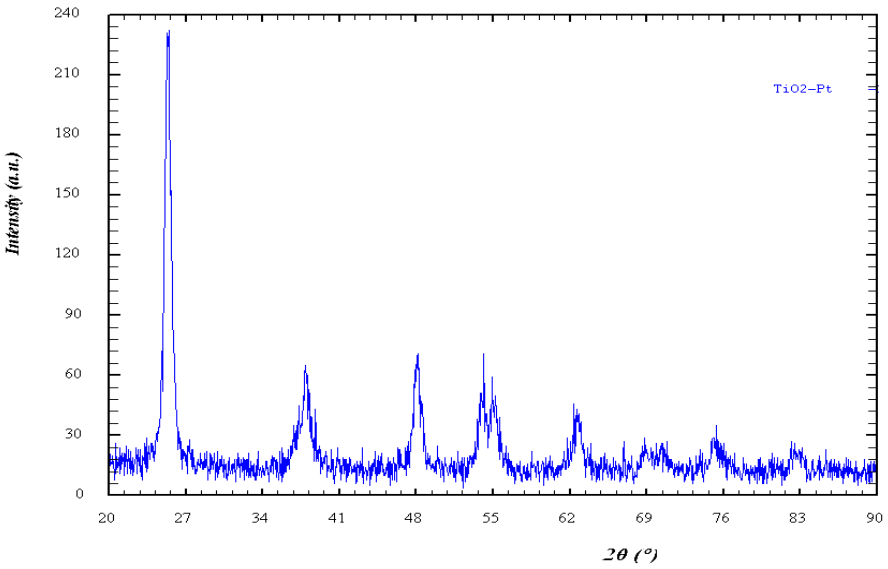

Fig. 1. X-ray diffraction spectrum for TiO_2 doped with Pt – 1%.

The experiment was performed upon an *in vitro* callus culture of *Allium sativum sagitatum*, developed on a basal **MS** culture medium without hormonal supplement. Half of the callus culture was treated with a powder of TiO_2-Pt and half of it was not treated.

The treatment of the callus was performed through dusting, by using 5 mg of TiO_2-Pt nanoparticles deposited on a callus surface of about 1 cm^3. The dusted callus has been maintained for 5 days on the medium culture surface, at a light regime of 16 h light per day and a temperature of 24°±2°C. In the two callus type (treated or untreated), the ultrastructural features were analyzed, both at the surface of the callus (in direct contact with the TiO_2-Pt nanoparticles), and inside it. For ultrastructural investigations, callus fragments of about 1 mm^3 were prefixed in a 2.5% glutaraldehyde solution (2.5 h), postfixes in a 1% Millonig solution (1.5 h), and then included in vestopal W. The seriated sections of about 90 nm thickness, were contrasted with uranyl acetate and lead citrate and then analyzed at a TEM JEOL-JEM 1010 microscope (Electron Microscopy Center, *Babes-Bolyai* University of Cluj-Napoca, Romania).

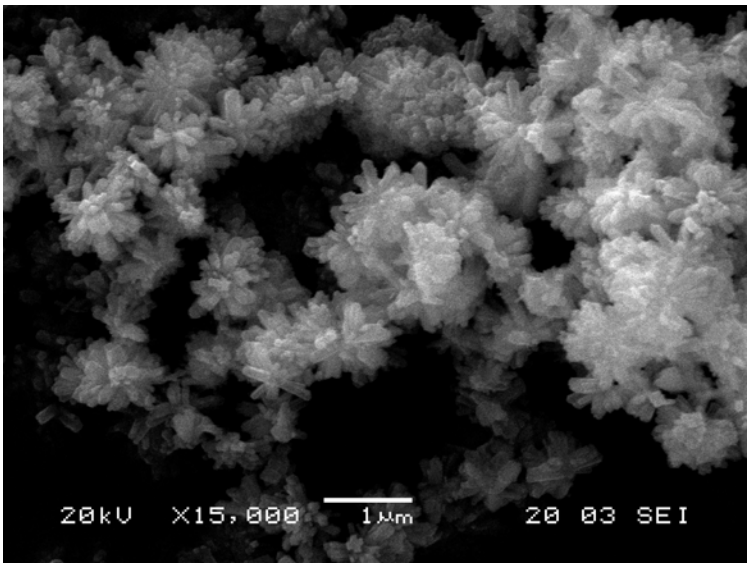

Fig. 2. The TiO_2-Pt nanoparticles shape at SEM.

3. Results and discussions

3.1. The ultrastructural features of the callus in Control

In Control, the cells present a normal structure. The parenchymatic cells present a regulate shape, with slightly round edges. The amount of cytoplasm and of cellular organelles is different, depending on the cell metabolic activity. In the cells with an intense metabolic activity, there are numerous ribosomes and mitochondria, a rich endoplasmic reticulum, proplastids usually having only thylakoids undisposed in grana (Fig. 3).

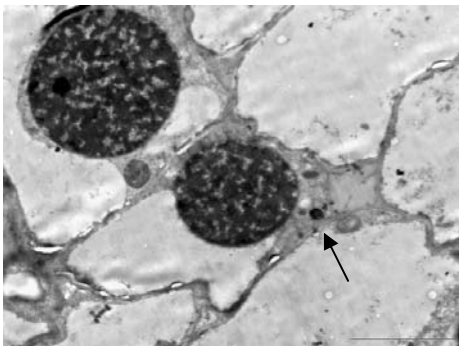

Fig. 3. Parenchymatic cell with proplastid.

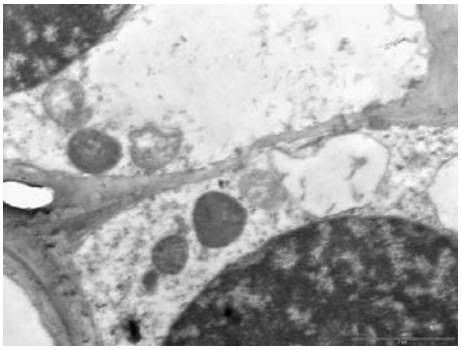

Fig. 4. Mitochondria with different structure.

The mitochondria ultrastructure can be normal or slightly altered. The normal mitochondria present a structured matrix and vesicular cristas, while the altered mitochondria present small lysis focuses in matrix (Fig. 4). As an adaptation to the intense metabolism, there are peroxisomes in some cells (Fig. 5). The nucleus with central disposition, presents blocks of heterochromatin inside, the nucleus feature being similar to those of a nucleus in the S and G2 stages of the interphase (Figs. 3, 5). Around the nucleus, there are cytoplasm with mytochondria, ribosomes and endoplasmic reticulum. In some areas of the callus, there are binucleate cells, probably as a result of the amitotic divisions, the two nuclei being adjacent and separated through a fine wall, which divides the mother cell in two sectors (Fig. 6).

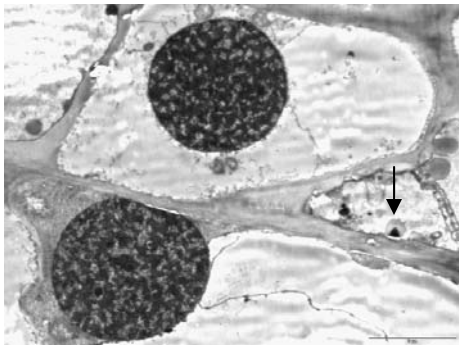

Fig. 5. A peroxisome in a cell.

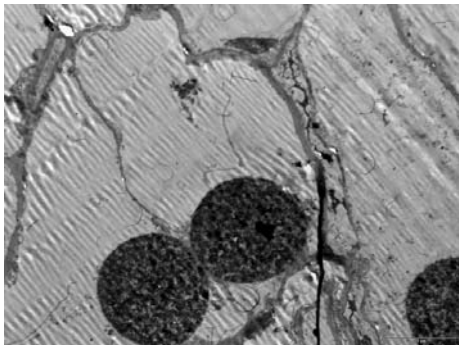

Fig. 6. Binucleate cell.

In the parenchymatic cells of the callus, there are drops of a synthetized substance, probably of a lipidic nature, as well as an amorphous matter (Fig. 7). A granular matter is present in vacuoles and in the cytoplasm. Between adjacent cells, there are communication jonctions (Fig. 8), which allow a selective diffusion of the molecules between adjacent cells and facilitate the direct communication between cells.

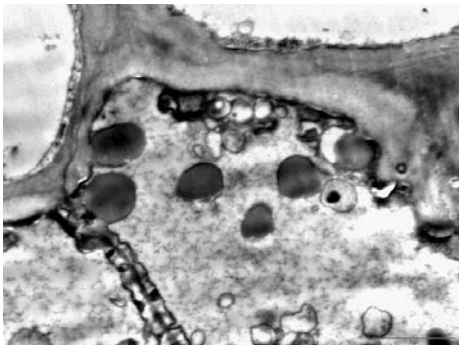

Fig. 7. Vacuole with a different matter.

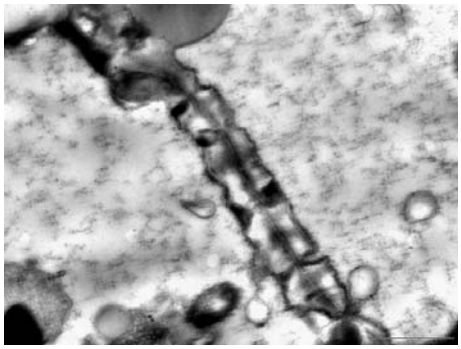

Fig. 8. Communication jonction.

3. 2. The ultrastructural features of the callus under treatment wityh TiO_2-Pt

As the callus treatment with TiO_2-Pt was performed by spraying, the TiO_2-Pt effect depended on the cell position in the callus tissue. Thus a cytotoxic effect was noticed in the cells situated at the callus periphery (in direct contact with TiO_2-Pt powder) and a stimulatory effect on the cell metabolism, in the cells situated in the middle of the callus.

Cytotoxic effect. As the cells at the callus periphery were in direct contact with the TiO_2-Pt powder, the ultrastructural features of the cells were altered. These cells present a small cellular content, having a pelicular cytoplasm with few cellular organelles (Fig. 9). The nucleus having a round shape present heterochromatin disposed in rows inside. Sometimes there are areas with rarefied chromatin (Figs. 9, 10). There is a small amount of cytoplasm and cytoplasmic organelles around the nucleus, in comparison with the cells situated inside the callus. There are areas with rarefied cytoplasm in the cell (Fig. 10). The tonoplast is brocken and deached from the plasmalemma, due to a plasmolysis process (Fig. 10). On the two parts of the tonoplast surface, some aggregates of TiO_2-Pt particles were noticed. The TiO_2-Pt nanoparticles, single or aggregated, are spread inside the cell (Fig. 12). A finely granular amorphous substance, free (Fig. 10) or in vacuoles (Fig. 11), is also present inside the cell. In some cells there are myelinic structures (Figs. 11, 12), as a result of some cellular organelles degradation (mitochondria, proplastids and endoplasmic reticulum). These structures were reported also in the animal cells, induced by TiO_2 nanoparticles [10].

Stimulatory effect. The cells situated in the middle of the callus are in an intense metabolic activity and present a normal ultrastructure. The cells present a rich cytoplasm and cellular organelles. The tonoplast is intact. In the nucleus, the heterochromatin is disposed in rows and has no areas with rarfefied chromatin, some of them being in the $\mathbf{G_1}$ phase of the mitotic cellular cycle (Fig. 13) and others in the **S** phase (Fig. 14). Around of the nuclei are present a big amount of cytoplasm with cellular organelles (Fig. 13). Mitochondria present a normally structured ma-

trix and vesiculous cristas. Some of the mitochondria are in division (Figs. 13, 15). There are TiO_2-Pt nanoparticles in cells, usually aggregated. The presence of some aggregates of TiO_2-Pt nanoparticles in the cell is due to platinum properties. The platinum being an expensive material [11], some of the properties of these nanoparticles can be modified in the cell; as a consequence, platinum particles adhere to one another. There is also an amorphous material in the cell, finely dispersed in the vacuoles, on the inner membrane or in the cytoplasm (Fig. 16).

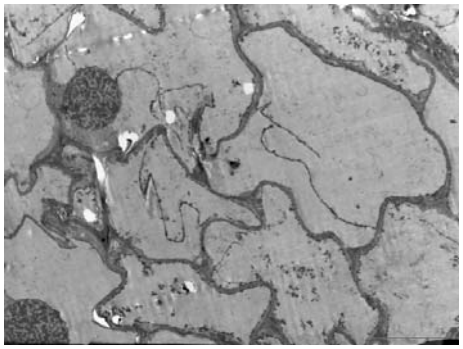

Fig. 9. Cytotoxic effect of TiO_2-Pt.

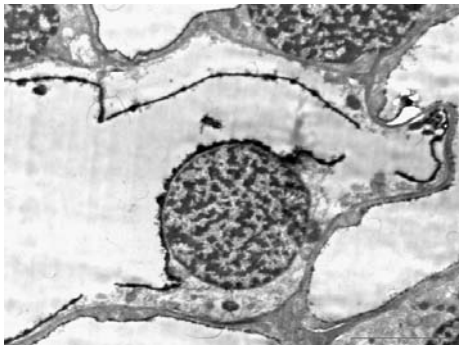

Fig. 10. Lysis area in cytoplasm and in nucleus.

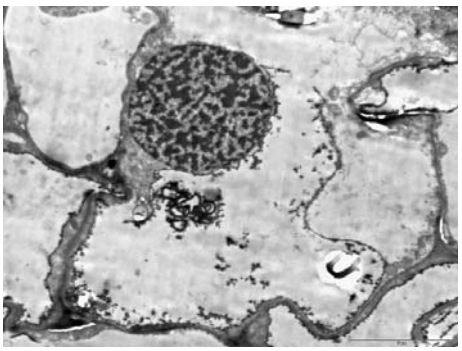

Fig. 11. Vacuole with amorphous matter.

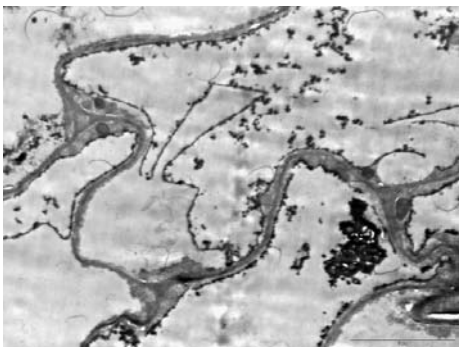

Fig. 12. Myelinic structure.

3.3. Interaction of the TiO_2-Pt nanoparticles with eukaryote (vegetal) cell

In the scientific references, there is little information on this subject. In experiments performed in *Mus musculus*, intraperitoneally injected with TiO_2-Pt nanoparticles and then exposed or not at a stress factor (X-irradiation of the whole animal body), the effect induced at the liver level, as well as the nanoparticle interaction with the cellular organelles, were investigated [8]. In liver, the exces of nanoparticles are extracted from the general circulation and accumulated in the Kupffer cells. The TiO_2-Pt nanoparticles are present only in the cells with macro-

phagic activity (Kupffer cells), especially near the endoplasmic reticulum, in cytoplasm and in vacuoles, as well as in the circulatory system (sinusoid capillaries).

In experiment performed with ferrofluids (Fe_3O_4) in plant, the magnetite particles interaction with the vegetal cell was also studied [12]. The *Mammillaria duwei* plant were *in vitro* cultivated on media supplied with magnetic fluid with water as carrier liquid, under different experimental conditions. The magnetite particles were identifyied in the euchromatic regions of the nucleus, in the chloroplast (near grana or in stroma thylakoids), in mitochondria (on crista surface), as well as on the tonoplast or inner plasmalemma surface.

In this experiment, the interaction of TiO_2-Pt nanoparticles with the parenchymatic cells from *Allium sativum sagitatum* callus, was analyzed. The nanoparticles penetrate the callus on its surface, they being administered through dusting. In the cells at the callus peryphery, the TiO2-Pt nanoparticles induced lesions. They induced the tonoplast and plasmalemma breakage (Figs. 9–12), single or aggregated nanoparticles being present on the two surfaces of the tonoplast, on the inner surface of the plasmalemma, as well as in vacuole and in the cytoplasm. Some of TiO_2-Pt aggregated nanoparticles are accumulated at the mielinic corpuscles (Figs. 11, 12), being eliminated from the cell.

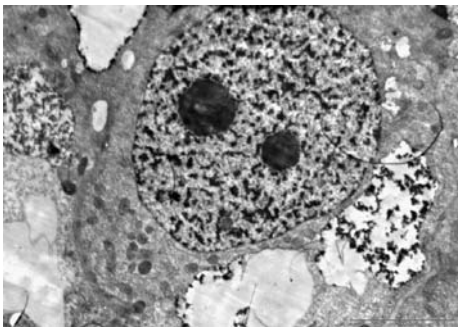

Fig. 13. A nucleus in G_1 stage.

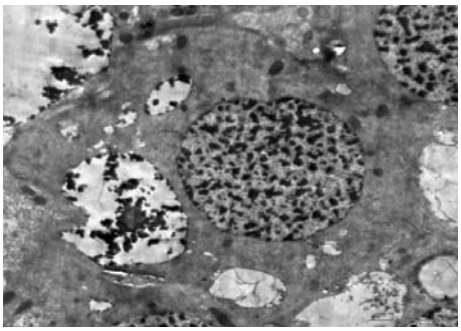

Fig. 14. TiO_2-Pt in vacuole accumulation.

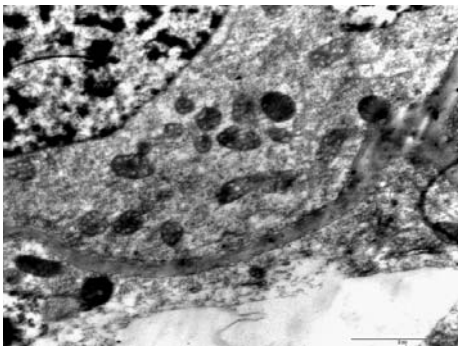

Fig. 15. Mitochondria in division.

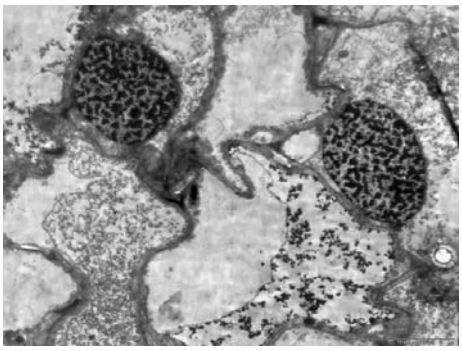

Fig. 16. TiO_2 accumulation in cytoplasm.

In the inner region of the callus, the TiO_2-Pt nanoparticles (single or usually aggregated), are accumulated in vacuoles (Fig. 13), or in the cytoplasm, especially near mitochondria (Fig. 15). They are also present on the inner surface of the plasmalemma (Figs. 13, 15), or on the tonoplast surface (Fig. 16). Also, they are accumulated in some vacuoles, while they are practically absent from other vacuoles (Fig. 14).

4. Conclusions

The treatment of the *Allium sativum sagitatum* callus by spraying with a TiO_2-Pt powder has different effects depending on the cell position relative to the TiO_2-Pt nanoparticles. In the cells from the inner callus, which are not in direct contact with the titanium dioxide powder, an intensification of the metabolic processes of the cells was noticed: increase in the cytoplasm amount and in the number of cellular organelles (mitochondria, ribosomes, endoplasmic reticulum), mitochondria divisions, as well as an intense synthesis activity, exemplified by increase in the number of ribosomes and the presence of the synthetized substances.

The cytotoxic effect was present in the cells at the callus periphery, which were in direct contact with the TiO_2-Pt nanoparticles. A plasmolysis process, the tonoplast breakage and its release from plasmalemma, myelinic structures resulted from altered organelles (chloroplasts, mitochondria, endoplasmic reticulum) were noticed.

The TiO2-Pt nanoparticles, single or aggregated, are present in the cytoplasm (especially in the proximity of mitochondria) and in the vacuole, on the inner surface of the plasmalemma and on both surfaces of the tonoplast. In the cells at the periphery of the callus, the aggregates of TiO_2-Pt are accumulated at the myelinic corpuscle level and they can be eliminated from the cell.

Acknowdledgements. These researches were sponsored by the NUSA/CEEX grant 18/2005.

References

[1] FERRIN J., OBERDÖRSTER G., *Biological effects and toxicity assessment of titanium dioxides: anatase and rutile*, Am. Ind. Hyg. Assoc., **46** (2), pp. 57–68 (1985).

[2] LEE K. P., TROCHIMOWICZ J. H., REIHARDT C. F., *Pulmonary response of rats exposed to titanium dioxide* (TiO_2) *by inhalation for two years*. Toxicol. Appl. Pharmacol., **79**,pp. 179–192 (1985).

[3] LI X. Y., GILMOUR P. S. DONALDSON K., MacNEE W., *Free-radical activity and pro-inflammatory effects of particulate air pollution (PM10) in vivo and in vitro*, Thorax. **51**, pp. 1216–1222 (1996).

[4] SERPONE N., SALINARO A., EMELINE A., *Deleterious effects of sunscreen titanium dioxide nanoparticles on DNA: efforts to limits DNA damage by particle surface modification*, Prof. SPIE, June, 4258, pp. 86–98 (2001).

[5] SCHIERTERT C. W., YAGHOUBI S., GERBER N. C., McSHERRY J. J., McCUE J. P., *Dietary titanium and infant growth*, Biol. Trace Elem. Res., **83**, pp. 149–167 (2001).
[6] DANIEL M.-C, ASTRUC D., *Gold nanoparticles: assembly, supramolecular chemistry, quantum-size-related properties, and applications toward biology, catalysis, and nanotechnology*, Chem Rev., **104**, pp. 293–346 (2004).
[7] CORNEANU C. G., CRĂCIUN C., CORNEANU M., LAZĂU C., GROZESCU I., SILOSI I., ROGOZ S., PRODAN G. C., BARBU-TUDORAN L., MIHALI C., ŞTEFĂNESCU I., CORNEANU L.-M., *The* TiO_2-Pt *nanoparticles implication in the immune response and their interaction with the animal cell*, in *Progress in Nanoscience and Nanotechnologies*, **11** (Eds. I. Kleps, A. Catrinel Ion, D. Dascălu), pp. 183–192. Edit. Academiei Române, Bucureşti (2007).
[8] WOLOSCHAK G., PAUNESCU T., THURN K., MASERE J., LAI B., *Intracellular localization of titanium dioxide-DNA nanocomposites*, Cornel University, ERL Workshop (2006).
[9] CORNEANU C. G., CORNEANU M., LAZĂU C., *The* TiO_2 *action on the eukaryote chromosomes*, Buletin SNBC, **36**, pp. 115. Edit. Risoprint, Cluj-Napoca (2008).
[10] SINGH S., *Toxicological effects of nanoparticles in vitro studies with titanium dioxide*, Doctoral Thesis, Heinrich Heine University, Düsseldorf (2005).
[11] GEERLINGS H., DAVID K., *Engagement and translation: perspective of a natural scientist*, in *What Can Nanotechnology Learn from Biotechnology?* (K. David and P.B. Thompson, eds), Academic Press/Elsevier, Burlington, London, San Diego, pp. 189–219 (2008).
[12] CORNEANU C. G., CRĂCIUN C., CORNEANU M., CRĂCIUN V., BICA D., *The vegetal eukaryotic cell interaction with magnetite particles, at in vitro culture*, in 9^{th} *International Conference on Magnetic Fluids*, Zarm Bremen, 2 pp. (2001).

Temperature Impact on Properties of Fe_xO_y-PPy Nanocomposites

Dragoş-Viorel BREZOI[1], Rodica-Mariana ION[1,2]

[1]Valahia University, Materials Science Department, Targoviste, Romania
E-mail: dragosh_brezoi@yahoo.com
[2]ICECHIM, Analytical Department, Bucharest, Romania
E-mail: rodica_ion2000@yahoo.co.uk

Abstract. The transition behavior for various iron oxide–polypyrrole compositions was investigated with the help of differential scanning calorimeter. Two distinct thermal transitions have been observed on iron oxide–polypyrrole nanocomposites prepared by simultaneous gelation and polymerization process: a transition from magnetic phase (γ-Fe_2O_3) to nonmagnetic phase (α-Fe_2O_3) of iron oxides in the temperatures' range 410–450°C and polypyrrole degradation at 373°C. The iron oxide–polypyrrole nanocomposites annealed at different temperatures were found to be magnetic with the magnetization values decreasing with increasing annealing temperature.

1. Introduction

In the last few years, the effect of nanoscale size on physical properties and their potential in nanomaterials engineering has attracted attention of researchers throughout the world [1]. Due to very small particle size, nanoparticles with size in the range of 10–50 nm, have bigger surface area and high porosity in sol form.

Nanostructured materials that are modulated on length scale have shown to possess properties different from and often superior to those of conventional materials having grain structures on microsize scale [2]. Decreased the particle size increased number of atoms close or linked to the surface and interfacial regions, will affect the electronic structure of surface and interface and magnetic properties, too.

The ability to control the particle size and morphology of nanoparticles is very important for advanced industry of high-tech applications of nanostructured metal oxide material devices such as dye-sensitized solar cells [3], displays and smart windows [4], chemical [5], gas [6] and biosensors [7], and supercapacitors [8].

Nanocomposites with metal oxides exhibit unique properties as they combine the good properties of the ingredients. Such materials have applications in electronic, optical, magnetic, and sensing devices [9].

The properties of the nanocomposite between conducting polymers and metallic oxides depend on their preparation methods, polymer concentration, and the size of oxides nanoparticles. Nanocomposites of iron oxide–polypyrrole have shown good humidity and gas sensing properties and magnetic support [9].

Conducting polymers, such as polypyrrole (PPy) (Fig. 1), have been used as the active layers of gas sensors [10–12].

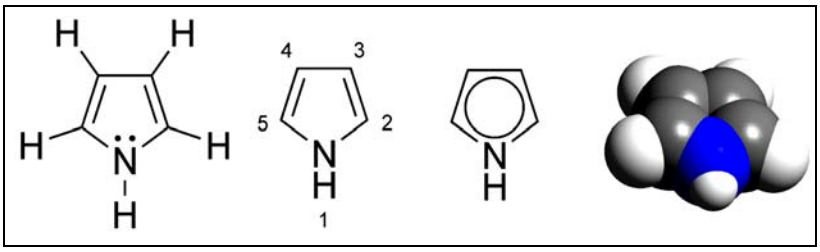

Fig. 1. Pyrrole chemical formula.

By comparison with many commercially available sensors, metal oxides-based and prepared at high temperatures, the sensors with conducting polymers have many improved characteristics. They have high sensitivities and short response time; especially, these feathers are ensured at room temperature.

The iron oxides exist in three forms: FeO, Fe_2O_3 (γ-Fe_2O_3 and α-Fe_2O_3) and Fe_3O_4. Fe_2O_3 has polymorphic transformations depend temperature, and certain structure at low temperature and another structure at high temperature: γ-Fe_2O_3 (cubic, inverse spinel) $\rightarrow$ α-Fe_2O_3 (hexagonal, corundum) at ~ 410°C. Transformation from one form to other is possible by oxidation or reduction mechanisms, at different temperatures: FeO $\leftrightarrow$ Fe_3O_4 $\leftrightarrow$ Fe_2O_3 [13].

The purpose of the thermal analysis techniques (TGA and DSC) is to study the thermal stability and decomposition, solid-state transition, melting point, purity, crystallinity and aging behavior of different materials. These thermal studies on iron oxides help in understanding the transition behavior of iron oxide into polypyrrole shell [14–17].

In our previous papers, we have reported preparation the nanocomposites of iron oxide–polypyrrole by simultaneous gelation and polymerization process [9] which resulted in production of magnetic phase of iron oxide; we have reported phase change induced by polypyrrole in polypyrrole–iron oxide nanocomposites having different pyrrole concentration, too [9]. These nanocomposites showed remarkable changes in magnetic and electrical properties with different concentrations of pyrrole [9, 18, 19].

In this paper we report the thermal studies performed on nanocomposites of polypyrrole–iron oxide to explain in detail the degradation of polypyrrole and to understand the phase change induced by polypyrrole in these nanocomposites.

2. Experimental

2.1. Synthesis

Nanocomposites of iron oxide and polypyrrole were prepared by simultaneous gelation and polymerization processes (Fig. 2), using $Fe(NO_3)_3 \cdot 9H_2O$ as precursor and 2-methoxy ethanol as solvent [3]. To 80 ml of the above solution, different amounts of pyrrole (5, 10, 15, 20 and 25%) were added and the solution was initially heated at 60°C with continuous stirring to form the gel (Table 1).

During the gelation with 15% amount of pyrrole, magnetite is generating into nanocomposite structure [9, 18, 19].

Table 1. Experimental conditions for nanocompozites Fe_xO_y-PPy obtaining process

Sample	Vol. of Fe^{3+} solution [ml]	Vol. Py [ml]	Py [% vol.]	Total volume [ml]	T [°C]
1P1	80	4,21	5	84,21	60
1P2	80	8,88	10	88,88	60
1P3	80	14,11	15	94,11	60
1P4	80	20	20	100	60
1P5	80	26,66	25	106,66	60

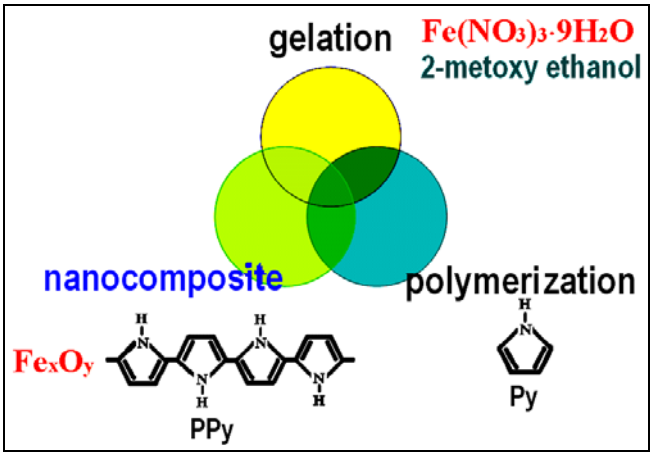

Fig. 2. Obtaining the Fe_xO_y–PPy nanocomposites by simultaneous gelation and polymerization processes.

Resulted samples were annealed at different temperature (see in Table 2) at p = 270 bar, in inert atmosphere of Ar, for further investigation of their properties. The powders were compressed using a hydraulic press.

Table 2. The samples of Fe_xO_y-PPy nanocomposite and abbreviations significant

Sample	**1P1T$_{350}$**	**1P2T$_{350}$**	**1P3T$_{350}$**	**1P4T$_{350}$**	**1P5T$_{350}$**			
Source	1P1	1P2	1P3	1P4	1P5			
T_t [°C]	350	350	350	350	350			
Sample	**1P3T$_{100}$**	**1P3T$_{150}$**	**1P3T$_{200}$**	**1P3T$_{250}$**	**1P3T$_{300}$**	**1P3T$_{400}$**	**1P3T$_{450}$**	**1P3T$_{600}$**
Source	1P3	1P3	1P3	1P3	1P3	1P3	1P3	1P3
T_t [°C]	100	150	200	250	300	400	450	600

2.2. Apparatus

X-ray diffraction was performed using Philips PW-1050 X–Ray diffractometer with CuKα radiation (λ = 1.5418 Å at 35 kV).

Thermogravimetric analysis of these compounds was carried out simultaneously on a Du Pont TG -DTA analyzer. A sample of 12 mg was used initially, and thermal analysis was carried out from room temperature to 800°C at a heating rate of 5°C / minute. The atmosphere of oxygen gas with open sample holder and small platinum boat was used.

Infrared (FTIR) spectra were recorded using KBr pellets presses under vacuum, using a FTIR Perkin-Elmer 2000 spectrophotometer over the 4000–400 cm^{-1} range at a rate of 0.5 cm/s. Two milligrams of each sample together with 200 mg KBr (FTIR grade) were first homogenized in an agate grinding mortar.

Fig. 3. NanoR-AFM by Pacific Nanotechnology with NanoFeel 300 manipulator and X'Pert Software.

Microscopy imaging was performed using NanoR-AFM by Pacific Nanotechnology with NanoFeel 300 manipulator and X'Pert Software (Fig. 3). Magnetization was measured with Lakeshore VSM 7304.

3. Results and discussions

The electrical, magnetic, and structural properties of Fe_xO_y–PPy nanocomposites with different compositions have been reported [9, 18, 19]. Even all the nanocomposites were found to be magnetic, the sample with 15% polypyrrole (PPy) was found to be more magnetic as compared to others.

3.1. X-ray diffraction

The X-ray diffraction indicated a single phase of iron oxide (Fe_3O_4) for nanocomposite with 15% PPy, whereas the nanocomposites with lower concentrations of PPy show the presence of mixed phases, magnetic (Fe_3O_4) and nonmagnetic (α-Fe_2O_3), with the grain size varying with the annealing temperature from 10–30 nm.

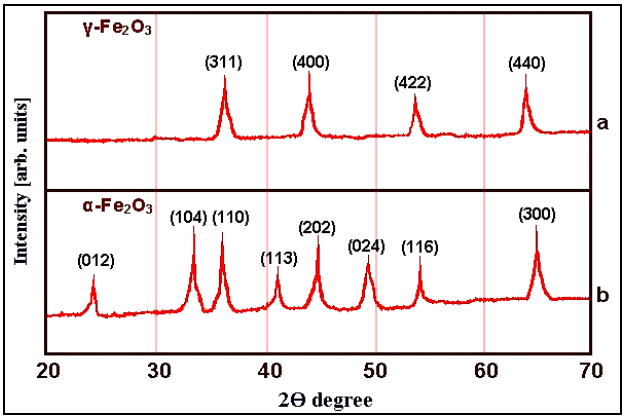

Fig. 4. XRD patterns of magnetically separated parts of the nanocomposite with 10 % PPy: (a) magnetic part and (b) nonmagnetic part.

The separation of magnetic phase was performed from the nanocomposite powder with 10% PPy (with mixture of phases) by a permanent magnet. X-ray diffraction studies were carried out on these magnetically separated components.

3.2. FTIR transmission spectra

FTIR spectroscopy has proven to be a valuable tool for the characterization of different compounds. Infrared spectra illustrate the plot of absorbed infrared radiation dependent on the wave-numbers (wavelengths) caused by the interaction of the infrared radiation with matter.

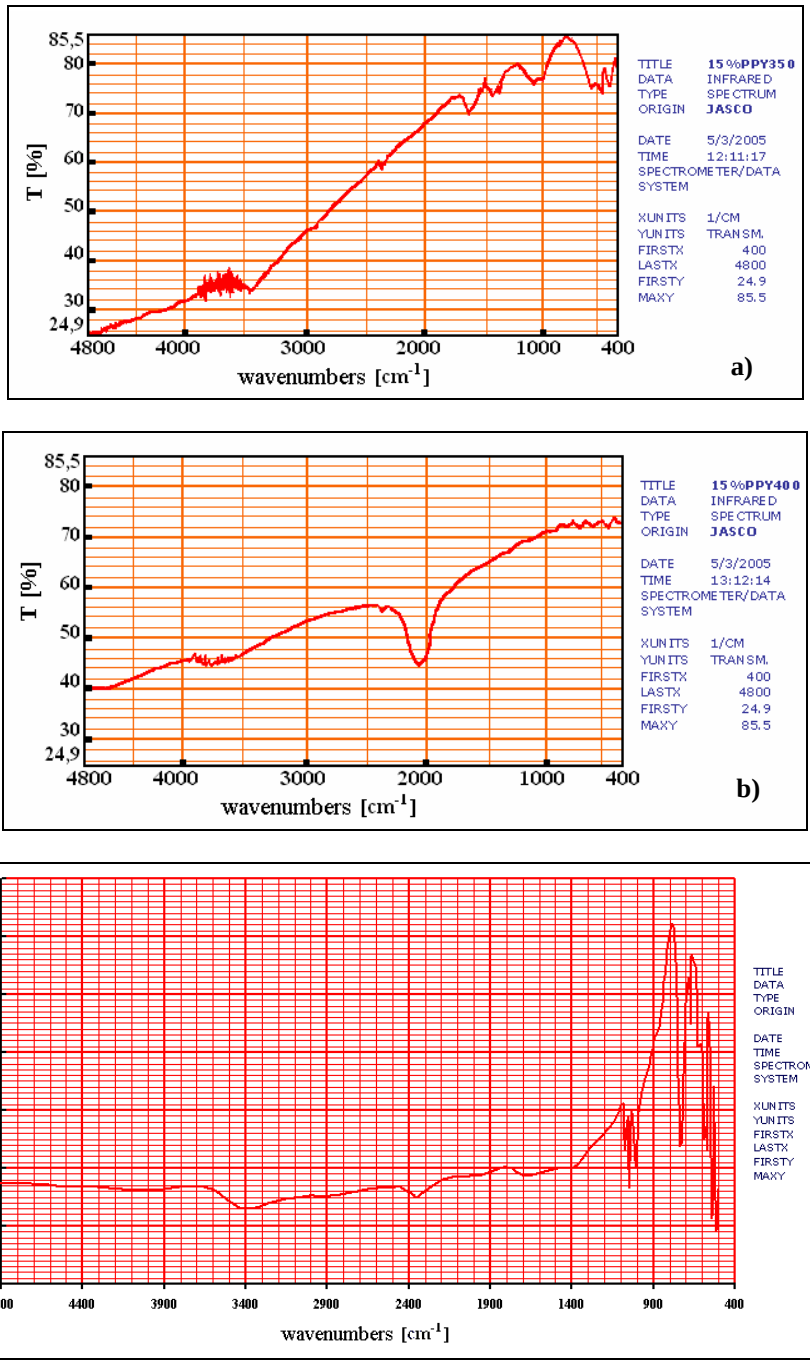

Fig. 5. FTIR spectra of the nanocomposite powder annealed at (a) 350°C, (b) 400°C and (c) unannealed.

FTIR spectra (Fig. 5) shows that the main characteristic absorption bands for PPy into the composites are shifted to higher frequencies as compared to those of pure PPy. In the composite nanostructures with Fe_3O_4, the absorption bands ascribed to pyrrole ring vibrations shift to higher frequencies, indicating the existence of an interaction between PPy backbone and magnetic nanoparticles.

The FTIR transmission spectra of the nanocomposite powders with 15% PPy unannealed and annealed at 350 and 400°C were recorded to confirm the polymerization of pyrrole (Fig. 5).

In the spectra for nanocomposite annealed at 350°C (Fig. 5a), some bands were observed at 782, 1088 and 3402 cm^{-1} attributed to the presence of PPy. The characteristic Fe–O vibrations have been detected in the region between 400 and 1000 cm^{-1}. The sample annealed at 400°C (Fig. 5b) didn't exhibit any of the PPy bands.

3.3. Thermal analysis

Thermal analytical techniques are routinely used to study mass variation during desorption, adsorption, or decompositionof materials.

Figure 6 a–d shows DSC thermograms for the nanocomposite sample with 15% PPy annealed at different temperatures.

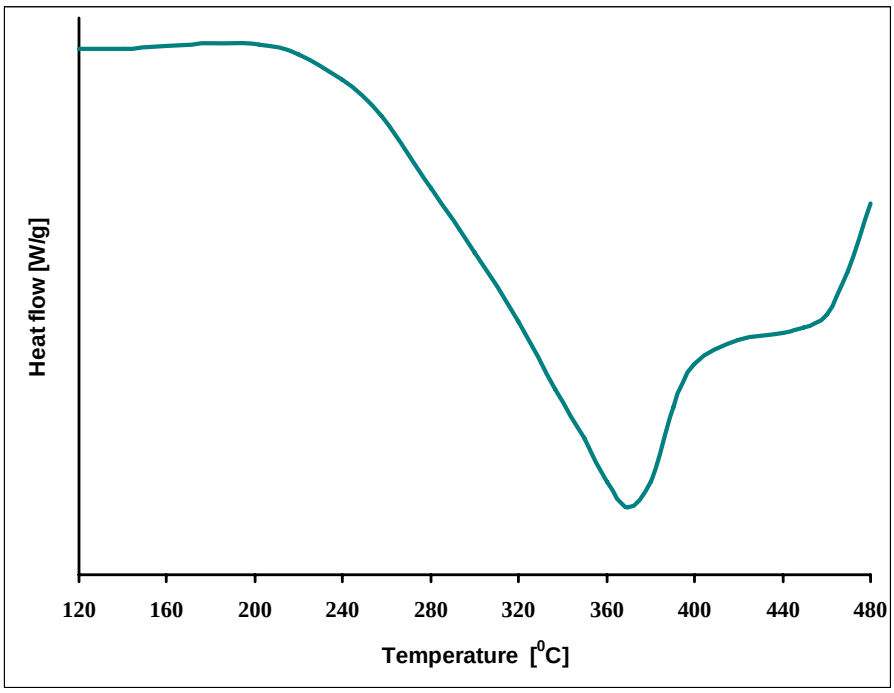

a)

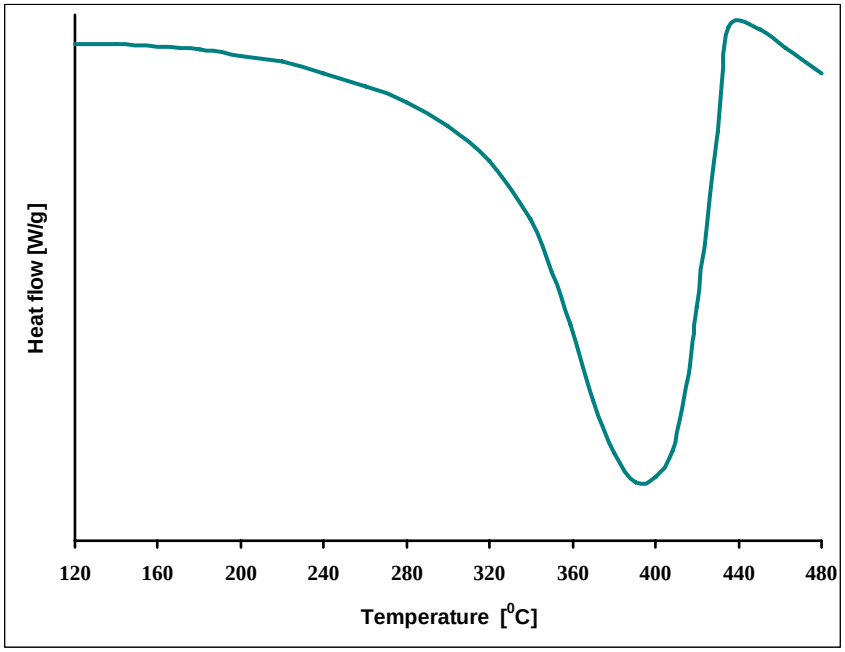
Heat flow [W/g]
120
160
200
240
280
320
360
400
440
480
Temperature [^{0}C]

b)

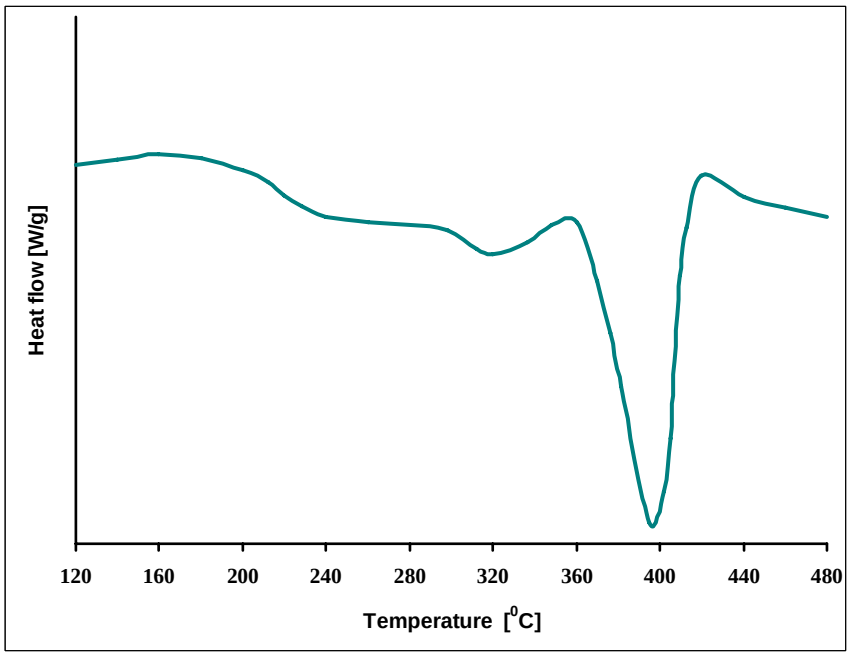
Heat flow [W/g]
120
160
200
240
280
320
360
400
440
480
Temperature [^{0}C]

c)

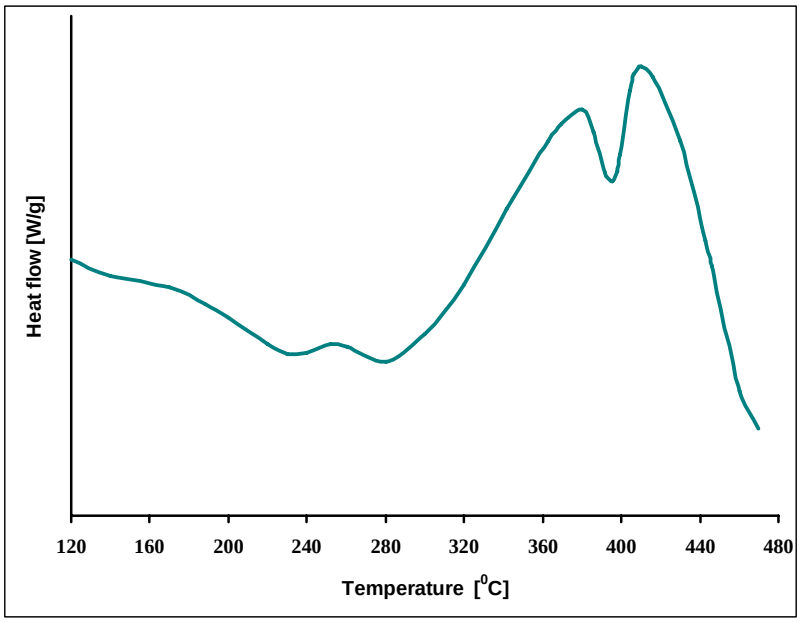

d)

Fig. 6. DSC thermograms for the nanocomposite sample with 15% PPy annealed at different temperatures: (a) unannealed, (b) 150°C, (c) 200°C and (d) 300°C.

The thermograms of the unannealed sample and the sample annealed at 150°C exhibited a deviation at lower temperatures ranging from 120 to 200°C indicating degradation of PPy in this temperature range.

Two exothermic peaks were observed for samples annealed at 200 and 300°C. The exothermic peak which appears at lower temperature is attributed to degradation of PPy [20].

In the case of samples annealed at 200 and 300°C this same peak is shifted to 360 and 380°C respectively. The shift in degradation temperature could be attributed to increasing of conjugation length progressively with annealing temperature increasing, making PPy more stable. This is also in good agreement with our earlier results where conductivity was found to be direct dependent of annealing temperature for nanocomposite with 15% PPy [18].

The second exothermic peak observed in the range 410–435°C is attributed to a transition from magnetic γ-Fe_2O_3 phase to nonmagnetic α-Fe_2O_3 phase of iron oxide and simultaneous recrystallization process, that is reported by J. Morales *et al.* [15].

For the unannealed sample this transition peak was not observed up to 460°C. The samples annealed at 150, 200 and 300°C, will induce some transition peaks at lower temperatures: 435, 420 and 410°C. It is likely that the particles in the nano-

composite annealed at higher temperatures have already crystallized, identified by narrowing of recrystallization peak.

Thus two simultaneous processes of transition from magnetic to nonmagnetic and recrystallization process cause a downward shift in transition peak from 435 to 410°C. This could be probably explained to single domain nature in smaller particles.

Figure 7 show the DSC thermograms for nanocomposite with 15% and 25% of PPy annealed at 200°C.

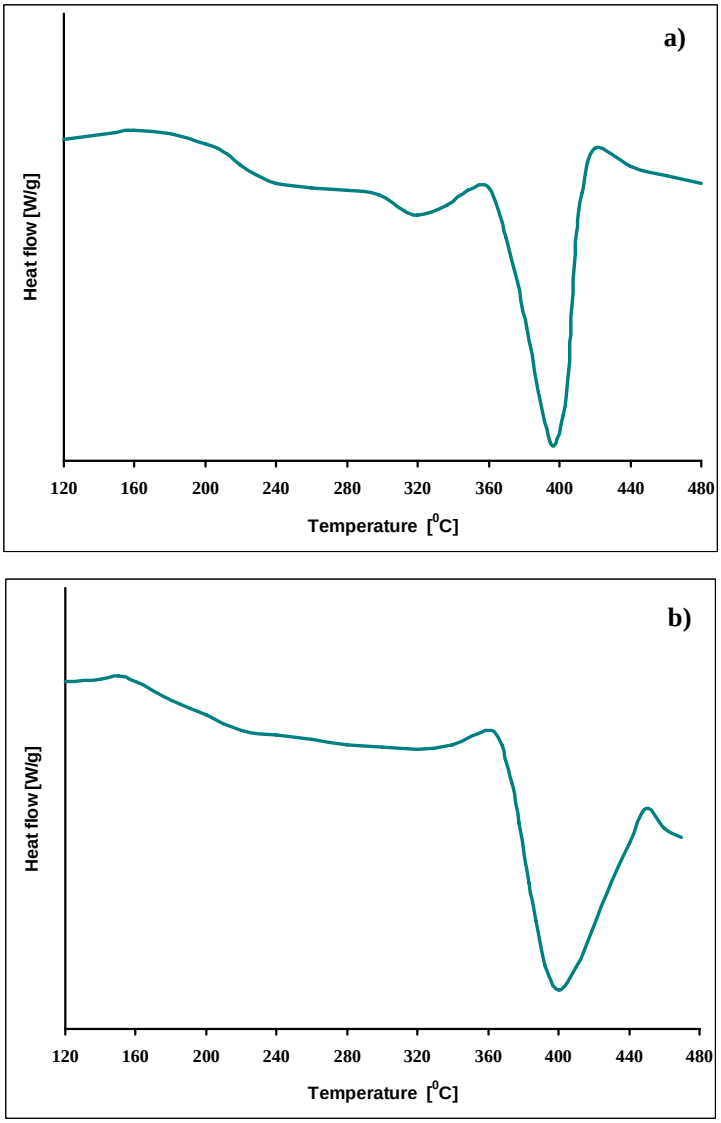

Fig. 7. DSC thermograms for nanocomposite with 15% and 25% of PPy annealed at 200°C.

The thermograms exhibited two exothermic peaks: the first exothermic peak was observed around 360°C and corresponds to degradation of PPy and the second exothermic peak was observed in the range 410–450°C and is attributed to transition from magnetic γ-Fe_2O_3 phase to nonmagnetic α-Fe_2O_3 phase of iron oxide.

Increasing the PPy concentration, a new peak at higher temperatures is observed, which could be attributed to a phase transition.

Thermal degradation techniques, such as thermogravimetry (TG) and differential thermal analysis (DTA) have been used for many years to elucidate structural features of decayed natural heterogeneous organic matter, providing important information on the chemical characteristics of the sample. Thermal analysis has the advantage that it is simple, fast, and reproducible; it can be performed on the whole sample without requiring pre-treatment. Thermal methods are based on programmed heating of the samples in a controlled atmosphere. Different components in the sample, which undergo transformations at different temperatures, produce a graph whose shape reflects the chemical composition and structure of the sample.

Differential temperatures can also arise between two inert samples when their response to the applied heat–treatment is not identical. DTA can therefore be used to study thermal properties and phase changes which do not lead to a change in enthalpy. The baseline of the DTA curve should then exhibit discontinuities at the transition temperatures and the slope of the curve at any point will depend on the microstructural constitution at that temperature.

The TG-DTA was performed on nanocomposite with 15% PPy. From Fig. 8 one can see that the degradation process for this composite proceeds in five stages. The first decomposition stage between 20 and 194.71°C corresponds to water loss. According to the Fig. 8, a strong degradation starts at about 412.02°C, the temperature at which the weight loss exceeds 58.69%.

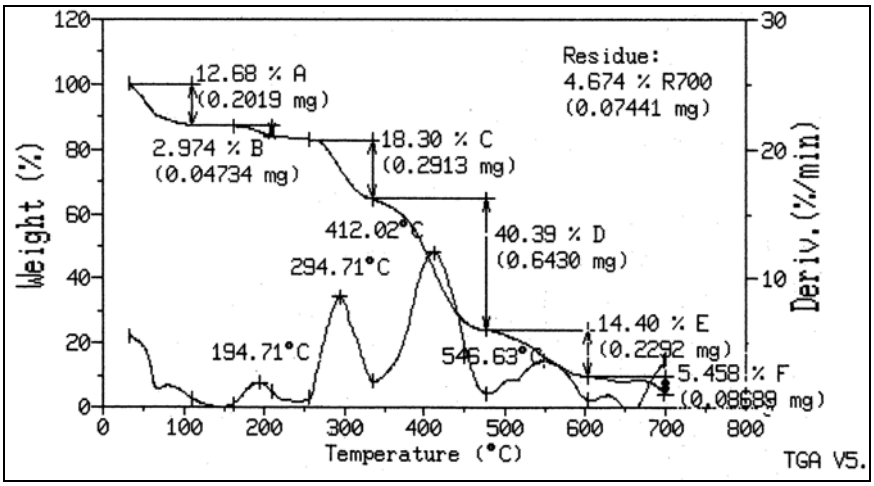

Fig. 8. TG-DTA on nanocomposite Fe_3O_4-Ppy.

Dehydration becomes complete during the second stage which occurs in the range 90.79–194.71°C.

Carbon monoxide and the hydrogen molecules are evolved in the IIIrd and IVth stages, which is observed to take place in 194.71–412.02°C, yielding iron oxide and carbon.

Next step in the decomposition curve (the Vth stage), which is complete at 546.63°C, resulted in the formation and the liberation of NO_x. The observed and calculated mass losses in the present case are 14.4.

The residual mass percent was calculated to be 4.647 (0.07441 mg).

Result of the thermogravimetric analysis shows a six-stage decomposition process (Table 3).

Table 3. Thermal behavior of Fe3O4-PPy composite (where T_i = initial decomposition temperature; T_m = temperature of maximum rate of weight loss; T_f = final decomposition temperature; w = weight loss)

Stage	T_i (°C)	T_f (°C)	Molecules evolved	w (%)
I	20	90.79	H_2O	12.68
II	90.79	194.71	H_2O	2.974
III	194.71	294.71	$CO+H_2+NO_x$	18.30
IV	294.71	412.02	$CO+H_2+NO_x$	40.39
V	412.02	546.63	NO_x	14.4
VI	546.63	800	CO	5.458

Under heating, the studied compound undergoes three main processes: dehydration, thermal degradation, and residue formation. Hence, it was shown that under an oxidative atmosphere, the rupture of the metal–ligand bonds (an endothermic process) is followed by the combustion of the organic moiety (a very exothermic process).

The bimodal dehydration occurs in the temperature range 20–194.71°C and extends well beyond the initiation of denitration step. The denitration step occurs in the temperature range 194.71–546.63°C and contains three substages with various extent of NO_x release.

The multi-step dehydration and denitration indicate the crystallographic inequivalence and can be explained by the different hydrogen bonding schemes and Fe–O bond distances.

The TG weight loss profile was mathematically deconvoluted into six substages and each substage could be properly assigned to dehydration, concomitant dehydration, and denitration, decarbonilation, followed by denitration and decomposition of residual compound.

DTA involves heating or cooling a test sample and an inert reference under identical conditions, while recording any temperature difference between the sample and reference. This differential temperature is then plotted against time, or against temperature. Changes in the sample which lead to the absorption or evolution of heat can be detected relative to the inert reference.

3.4. Atomic Force Microscopy

With an AFM it is possible to measure more than physical dimensions of a surface. This is because there is a "physical" interaction of the probe with a surface. An example is that by lightly pushing against a surface with the probe, it is possible to measure how hard the surface is. Also the availability of the probe to glide across a surface is a measure of the surface "friction".

The sample surface in ambient conditions will have a thin contamination layer composed of water and other contaminants from the environment. It is not possible to eliminate completely this layer but we have been keeping the samples in a dry place.

Imaging mode can be classified as contact or vibrating (non-contact) depending on the net forces between the probe and the sample. As the probe is brought close to the sample, it is first attracted to the sample surface.

A variety of long range attractive forces, such as Van der Waals forces are at work. As the probe gets very close to the surface, the electron orbital on the surface of the probe and the sample start to repel each other. As the gap decreases, these repulsive forces neutralize the attractive forces, which then become dominant. With X'Pert Software it has been measured the average size of nanoparticles and we selected the representative topographic images of the samples (Fig. 9).

The cantilever specifications used in this work were: material silicon nitride (125 μm length, 4 μm thick and 30 μm width) with a nominal frequency resonance 330 kHz, and force constant 42 N/m. AFM tip specification used in this work were: material silicon, geometry triangular pyramid (with 3 and 6 μm base and 10 and 20 μm length), aspect ratio 3:1 and tip radius < 20 nm.

The AFM samples were prepared by deposing a powder on a glass (1.5 cm length, 1.5 mm thick and 1 cm width). We have used vibrating mode technique because the deposed thin films are fragile.

AFM imaging (Fig. 9) was realised only on the samples with 15% PPy, annealed at 200°C (a), 350°C (b) and 450°C, respectively: (a) 1P3T200AFM, (b) 1P3T350AFM, (c) 1P3T450AFM.

All the images from Fig. 9 show spherical-shape particles, with aleatory position on surface. Average size of the particles of the samples annealed at 200 and 350°C (Fig. 9a, b) is in the range 20–50 nm.

The agglomeration tendence was increased with annealing temperature and was resulted clusters with average size up to 100 nm for sthe sample annealed at 350°C (Fig. 9b) and 200 nm for sthe sample annealed at 450°C (Fig. 9c).

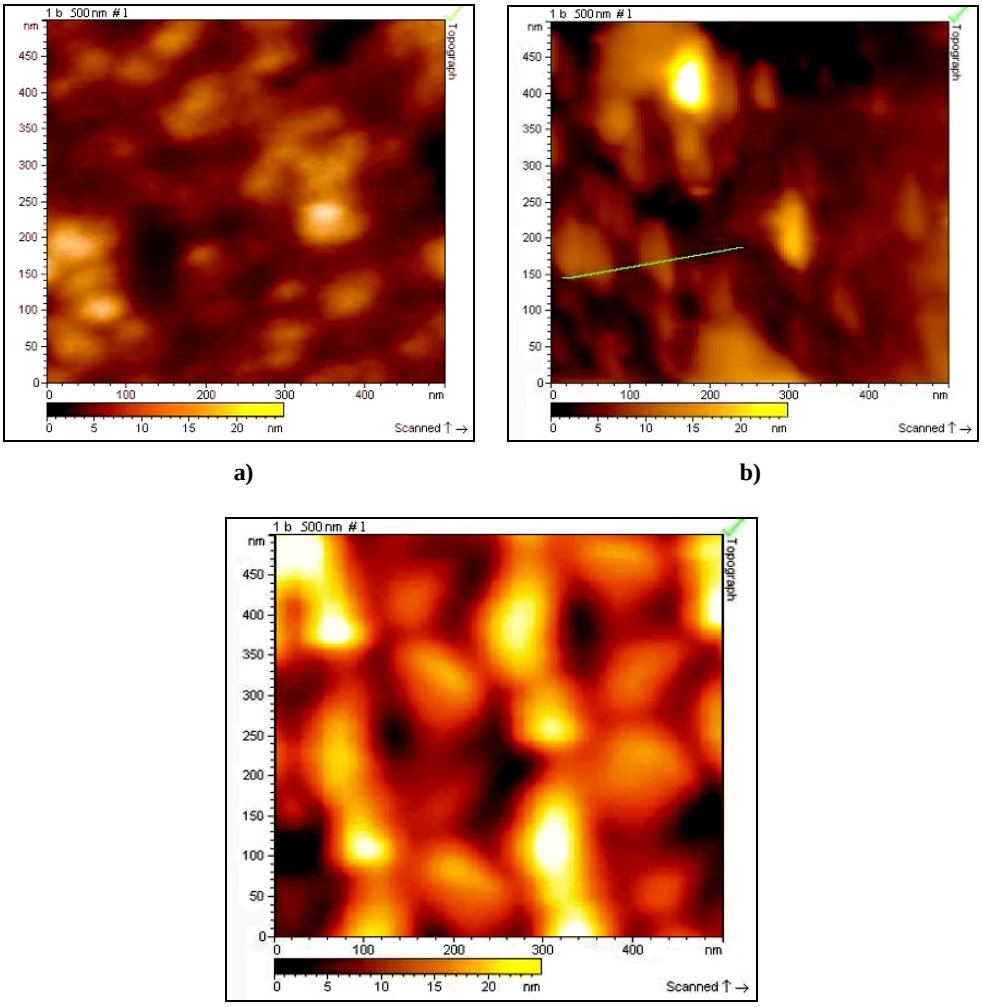

Fig. 9. Topographic AFM images, 500×500 nm, "vibrating mode" of the samples with 15% PPy, annealed at 200°C (a), 350°C (b) and 450°C (c).

3.5. Influence of annealing temperature on magnetization

Preliminary observation on the magnetic behavior show that the nanocomposites with 15% PPy is comporting a magnetic response. The magnetization M was measured at room temperature in a field of 10 kOe, with vibrating sample magnetometer (VSM).

The magnetization values for the samples annealed at 100, 150, 250, 350, 400, 450 and 650°C are showed in the Fig. 10.

The low value of magnetization at higher annealing temperature (400, 450 and 650°C) is due to the transformation of magnetic phases of iron oxides to α-Fe_2O_3 phase which is very weak magnetic.

It is well-known that magnetization is influenced by crystallinity, type of phase of iron oxides and particle size. In comparison with earlier reported values, the low values of magnetization is due to the reduced particle size.

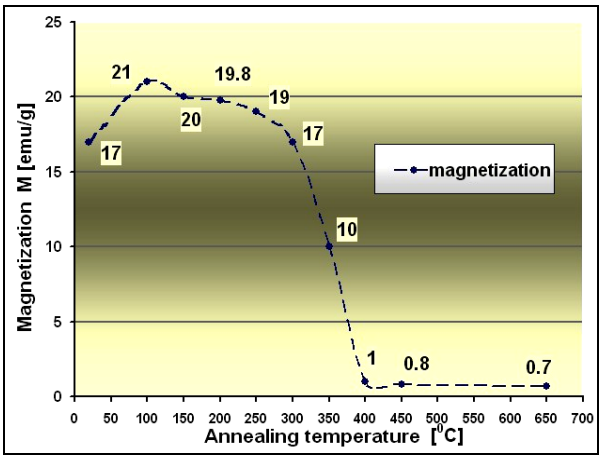

Fig. 10. Influence of annealing temperature on magnetization.

4. Conclusions

Due annealing at different temperatures into the nanocomposites of iron oxides and PPy, two phenomena was observed: a magnetic to nonmagnetic transition of iron oxides and PPy degradation. These phenomena were investigated with the help of differential scanning calorimeter. The samples showed a transition in the range 410–450°C, after dissociation of PPy, and all the peaks from this temperatures' range were an indication of magnetic transition corresponding to γ-Fe_2O_3 phase of iron oxide to a nonmagnetic α-Fe_2O_3 phase of iron oxide into these nanocomposites. This transition was not observed in nanocomposites with lower contains of PPy.

Increasing the annealing temperature was determined decreasing transition temperature. For low values of transformation temperatures, the degradation temperature of PPy is shifted in the same manner with the treatment temperature of nanocomposite powders. The iron oxide–polypyrrole nanocomposites annealed at different temperatures were found to be magnetic with the magnetization values decreasing with increasing annealing temperature.

From TG-DTA, we concluded that iron oxide-polypyrrole nanocomposite sample undergoes three main processes: dehydration, thermal degradation, and

residue formation. Hence, it was shown that under an oxidative atmosphere, the rupture of the metal–ligand bonds (an endothermic process) is followed by the combustion of the organic moiety (a very exothermic process).

The bimodal dehydration occurs in the temperature range 20–194.71°C and extends well beyond the initiation of denitration step. The denitration step occurs in the temperature range 194.71–546.63°C and contains three substages with various extent of NO_x release.

The multi-step dehydration and denitration indicate the crystallographic inequivalence and can be explained by the different hydrogen bonding schemes and Fe–O bond distances.

References

[1] MORIARTY P., Rep. Prog. Phys. **64**, p. 297 (2001).
[2] HADJIPANAYIS G. C., PRINZ G. A., *Science and Technology of Nanostructured Materials*, Plenum Press, New York (1991).
[3] HAGFELDT A., GRATZEL M., Chem. Rev., **95**, p. 49 (1995).
[4] GRANQVIST C. G., *Handbook of Inorganic Electrochromic Materials*, Elsevier Science, Amsterdam (1995).
[5] JANATA J., JOSOWICZ M., VANYSEK P., DEVANEY D. M., Anal. Chem**., 70(12)**, 179R (1998).
[6] *Semiconductor Sensors in Physico-Chemical Studies: Handbook of Sensors and Actuators 4* (L.Y. Kupriyanov, ed.), Elsevier, Amsterdam (1996); *Gas Sensors: Principles, Operation, and Developments* (G. Sberveglieri, ed.), Kluwer, Dordrecht (1992).
[7] *Handbook of Biosensors and Electronic Noses* (E. Kress-Rogers, ed.), CRC, Boca Raton, FL (1997).
[8] SARANGAPANI S., TILAK B. V., CHEN C. P., J. Electrochem. Soc., **143(11)**, p. 3791 (1996).
[9] BREZOI D. V., ION R. M., Sensors and Actuators B: Chemicals, **109**, 1, p. 171 (2005).
[10] DUBBE A., Sens. Actuators B, **88**, pp. 138–148, (2003).
[11] ZAKRZEWSKA K., Thin Solid Films, **391**, pp. 229–238, (2001).
[12] TIMMER B., OLTHUIS W., VAN DEN BERG A., Sens. Actuators B, **107**, pp. 666–677, (2005).
[13] MACAROVICI C. GHE., MACAROVICI D., *Chimia oxizilor dubli,* Academy Ed., Bucharest (1975).
[14] SUN B., SCHWEINSBERG D.P., Synth. Met. **68**, p. 49, (1994).
[15] MORALES J., TIRADO J. L., VALERA C., J. Am. Ceram. Soc. **72**, p. 1244, (1989).
[16] VENKATRAMAN A., HIREMATH V.A., DATE S. K., KULKARNI S. D., Bull. Mater. Sci. **24**, p. 617, (2001).
[17] TSUTSUMI N., ISHIDA S., KIYOTSUKURI T., J. Appl. Polym. Sci. B:Polym. Phys. **32**, p. 1899, (1994).
[18] BREZOI D. V., ION R. M., *Proc. ROMAT*, Ed. Printech, Politehnica University, Bucharest, Romania, p. 235, (2004).
[19] BREZOI D. V., ION R. M., *Proc. "Symp. Photonics Technologies for 7th Framework Programm - Opera 2015"*, Wroclaw, Poland, p. 542, (2006).
[20] MOHAMMAD F., CALVERT P. D., BILLINGHAM N. C., Bull. Mater. Sci. **18**, p. 225, (1995).
[21] ION R. M., BREZOI D. V., J.Optoel. Adv. Mat., **9(4)**, pp. 936–939, (2007).

New Results Regarding the Micro/Nano/Bioapplications of Some Natural or Synthetic Polymers

G. C. CHITANU, G. MOCANU,
E. C. BURUIANA, L. SACARESCU

Institutul de Chimie Macromoleculara *Petru Poni*,
Al. Grigore Ghica Voda 41A 700487 Iasi, Romania
E-mail: chita@icmpp.ro

Abstract. Recent results concerning the use of new synthetic or functionalized natural polymers for nano/bio/applications are presented. The first chapter presents novel polysaccharide microparticles obtained from pullulan and carboxymethylpullulan by using a new crosslinking agent – [3-(glycidoxypropyl) trimethoxysilane]. They presented interesting properties of interaction with biologically active substances, which recommend them as supports for controlled release drug systems. The second chapter gathers the newest results on the synthesis of NLO-molecules build on polysilane structures enclosing various electro-active groups. The structural influence of the Si-H functionality on the low temperature restructuration processes is discussed in relation with the electronic spectrum profile and fluorescence properties. Further, new polysilane-metal complexes structures were obtained by the polycondensation reaction of α,ω-bis(chloromethyl)-polymethylphenylsilane with the Ni (II) complex of bis(salicylidene)ethylenediamine. The chloro-functionalized polysilane was obtained by a modified Wurtz coupling procedure at low temperatures. To obtain the polymer-metal complex the resulted macroligand was complexed with metal cations. This structure is characterized by a highly localized electro-activity in the redox moiety combined with a specific σ conjugative effect in the polysilane chain. UV-VIS and FL spectral analyses as were used to investigate the optical properties of the polysilanes in relation with their chemical structure.

The paper present also results regarding the biomedical applications of maleic copolymers and polyacrylates with photosensitive groups, that outline new applications fields for the polymers in nanotechnology.

1. Introduction

Nanoscience is a recent scientific area which concerns itself with the study of materials that have very, very small dimensions – from hundreds to tens of nanometers in size. Nanotechnology is a field of applied science focused on the design, synthesis, characterization and application of materials and devices on the nano-

scale. Nanoengineering is the practice of engineering on the nanoscale. Nanobiotechnology (or bionanotechnology, or biomolecular nanotechnology) is a new wing in nanoscience and nanotechnology, developed last years at the crossroad of biology, biotechnology, medicine and nanoscience. It is based on the principles and chemical pathways of living organisms, ranging from genetic-engineered microbes to custom-made organic molecules. It encompasses the study, creation, and illumination of the connections between structural molecular biology and molecular nanotechnology, since the development of nano-machinery might be guided by studying the structure and function of the natural nano-machines found in living cells [1–4].

The current uses of polymers consist mainly in: plastics, elastomers, natural, artificial and synthetic fibres/yarns, coatings, paintings and foams, sealants or gaskets, functional polymers (reactive polymers, linear or cross-linked polyelectrolytes, additives for paper, textiles or leather industry), thermal or electric insulators. Besides these traditional fields, new advanced applications of polymers are developing: optoelectronics and photonics, fuel cells and battery technology, aircraft and automobile industry, membrane-based technologies, thin coatings and protections, food and cosmetics, environment monitoring and protection, biomedical purposes.

Polymers are a frequent partner in the nanoworld. We could define a polymer nanoscience, dedicated to theoretical and fundamental aspects, and the polymer nanotechnology, which deals with nanomaterials and nano-objects based on polymers. There is a huge amount and a great variety of research and results in this field. A tentative of clustering the nano-objects could be done as follows, according to the number of nanodimensions: nano 3D objects, such as nanoparticles, nanospheres, nanocapsules, dendrimers; nano 2D objects, such as biopolymers, nanofibres, nanowires; and nano 1D objects, such as very thin films, multilayers, etc. A constant increase of the contribution of natural or synthetic polymers to the realization of nanoentities, nanostructures or nanodevices could be observed. A similar trend can be identifyied in the functionalization with polymers of other nanomaterials based on carbon or inorganic compounds. These two tendencies have as a main result the diversification of nanoproducts and their successful application in nanotechnology or bionanotechnology/medicine. In our contribution we will report recent results concerning the use of new synthetic or functionalized natural polymers for nano/bio/applications.

2. New polysaccharide-based microparticles crosslinked with siloxanic units

Many papers have been devoted in last years to the study of polymer hydrophilic gels – macromolecular networks crosslinked through chemical or physical methods, possessing interesting properties which recommend them for various biomedical, bio-technological, pharmaceutical applications. In this last field, one

can mention the use of polysaccharide-based gels as delivery systems for peptides, oligonucleotides [5] and protein drugs [6]; many dextran hydrogels were prepared by Hennink et al. and their interaction with proteins (lysozyme, IgG) was studied [7–10]. In this chapter is presented a new method of obtaining microparticles of pullulan (P) and carboxymethylpullulan (CMP) by using 3-(glycidoxypropyl)-trimethoxysilane (TMS), which forms crosslinks through grafting with epoxy end on polysaccharide OH and through hydrolysis and condensation of the methoxy silane groups at the other end (Scheme 1).

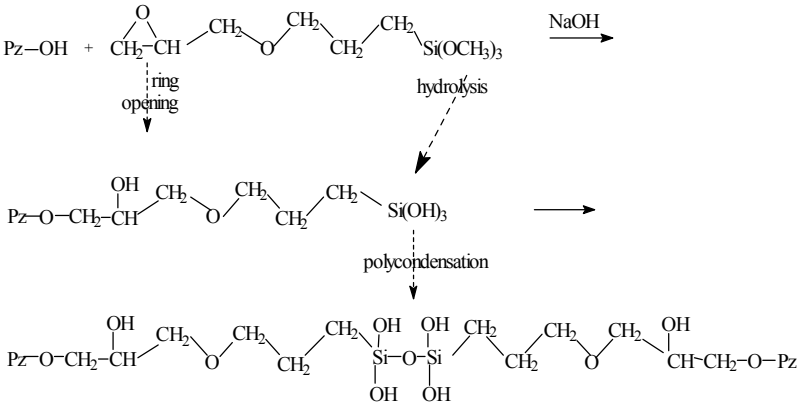

Scheme 1.

The microparticles were prepared by dispersion of an alkaline polysaccharide solution in an organic suspension medium, in the presence of a stabilizer and of crosslinking agent (TMS) (Tables 1 and 2). The new microparticles were characterized and their interaction with biologically active substances was investigated. In Figure 1 are given the images of dry or swollen microparticles, having 40–120 μm diameters. Other characteristics are also presented in Tables 1 and 2.

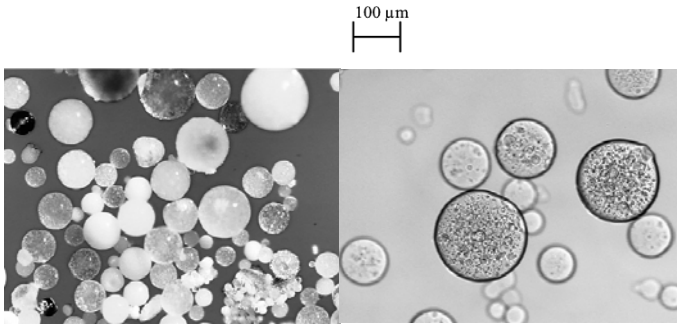

Fig. 1. Microparticles of carboxymethylpullulan crosslinked with TMS dry (left) and swollen in water (right).

From SEM images one can see that the surface of the microparticles presents either wider or narrower holes, as a function of the amount of crosslinking agent (Fig. 2).

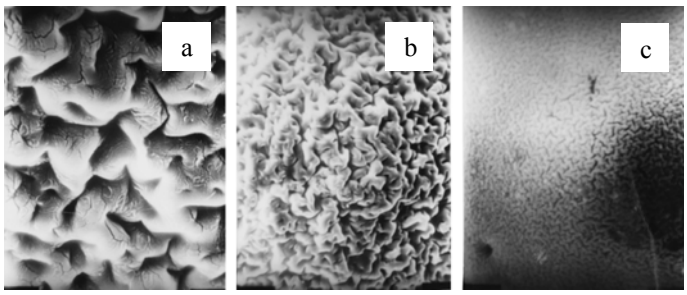

Fig. 2. SEM of CMP microparticles crosslinked with various amounts of TMS (samples: CMP: 0.38 (a); CMP: 0.58 (b) and CMP: 0.38_{NaCl} (c) from Table 2).

Table 1. Reaction conditions and physico-chemical characteristics of pullulan microparticles

Sample	Molar ratio TMS/ GU	Si content g%	Specific density g/mL	Water swelling g/g
PR-0.14	0.14/ 1	2.40	1.10	2.34
PR-0.24	0.24/ 1	3.30	1.088	2.22
PR-0.41	0.41/ 1	3.80	1.05	2.14

Table 2. Reaction conditions and physico-chemical characteristics of CMP microparticles

Sample	Molar ratio TMS/ GU	Si content g%	Specific density g/mL	Water swelling g/g
CMP: 0.77	0.77/ 1	4.02	1.166	10.50
CMP: 0.58	0.58/ 1	3.75	1.158	14.70
CMP: 0.38	0.38/ 1	2.38	1.140	25.10
CMP: 0.38_{NaCl} *)	0.38/ 1	2.30	1.118	8.50
CMP: 0.19	0.19/ 1	0.87	0.89	36.50

*) Solution in presence of NaCl

The microparticles obtained from anionic carboxymethyl pullulan are more hydrophilic than those obtained from the neutral polysaccharide pullulan (as can be seen from the water swelling values from Tables 1 and 2). By using of a higher amount of crosslinking agent, the obtained microparticles have a higher specific density and a lower water swelling. The differences in porosity of the synthesized microparticles were evidenced from determinations of the different molecular weights PEG retention.

As can be seen from Fig. 3, microparticles of P crosslinked with TMS retain various amounts of PEG 600 and 1000, as a function of their initial amount of crosslinking agent. PEG 4000 being retained in very small amounts, it may be considered as the molecular weight (MW)-limit of exclusion (hydrodynamic radius R_H 2.5 nm). The CMP crosslinked microparticles (more hydrophilic) retain PEG with higher MW, in amounts depending on the initial ratio of crosslinking agent. Thus, the PEG with MW 35000, which is retained in very small amounts on all CMP supports, can be considered as their exclusion limit (R_H 10 nm) (Fig. 4). Moreover, the presence of NaCl in the initial CMP solution influences the PEG retention properties of the microparticles by diminishing the exclusion limit for PEG retention at 13500 (R_H 6 nm).

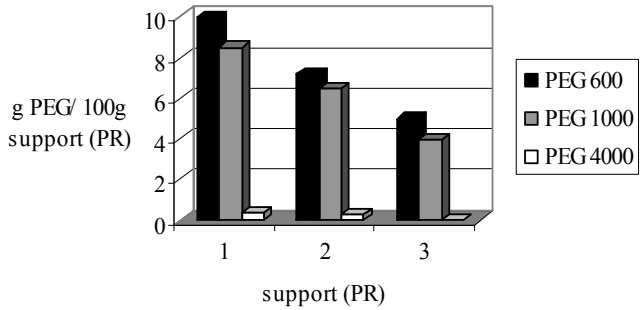

Fig. 3. Retention of PEG with various MW on PR microparticles.

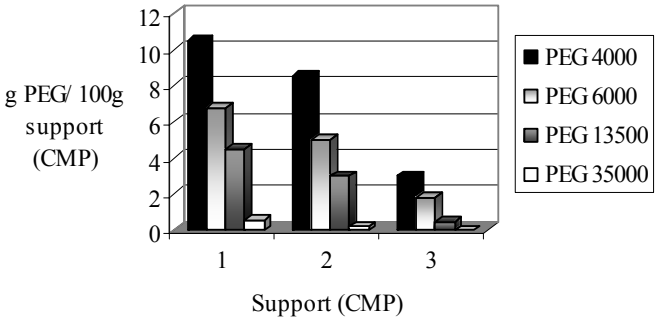

Fig. 4. Retention of PEG with various MW on CMP microparticles.

The interaction of the new microparticles with biological active substances (drugs) was investigated in order to appreciate their performances as controlled release drug systems. The CMP microparticles with siloxanic hydrophobic residues can interact with biomolecules through both electrostatic and hydrophobic forces. Some data on the retention of basic drugs such as propranolol and quinidine are presented in Table 3.

Table 3. Propranolol and quinidine retention on CMP crosslinked supports

Support	Drug	Retained drug	
		g/ g support	meq drug/ g support
CMP: 0.38	quinidine	1.0	3.06
CMP: 0.58	quinidine	0.97	2.97
CMP: 0.77	quinidine	0.83	2.54
CMP: 0.38	propranolol	0.82	3.16
CMP: 0.58	propranolol	0.73	2.81
CMP: 0.77	propranolol	0.70	2.70

Quinidine is retained in relatively higher amounts on these supports, probably due to its higher basicity (pK_a 10, compared to that of propranolol 9.5). The amount of drug retained on the supports decreases with the increase of the crosslinking degree. This fact can be correlated with the more hindered access of the drugs into the more crosslinked network and with a synergistic hydrophobic effect of uncrosslinked alkylsilane units in less crosslinked supports. Accordingly, the release rate of the drugs from their conjugates with CMP supports increases with the decrease of their crosslinking degree, due to the more rapid access of the external fluid to the reactive sites (Figs. 5 and 6).

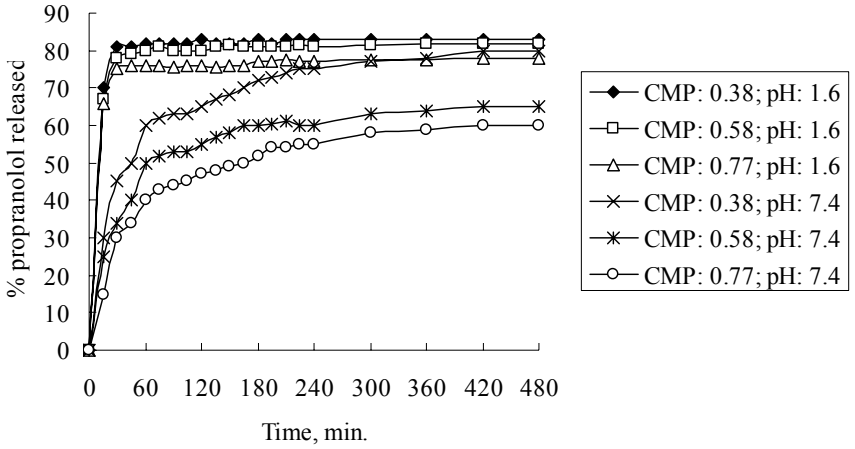

Fig. 5. In vitro release of propranolol from its conjugates with CMP supports.

The *in vitro* release of the propranolol (Fig. 5) and quinidine (Fig. 6) was faster for drugs in acidic (pH 1.6) than in buffered (pH 7.4) solutions. The propranol is more quickly released, due probably to its lower basicity. In acidic pH, the release occurs with a "burst" effect on all supports, the rate depending on the crosslinking degree.

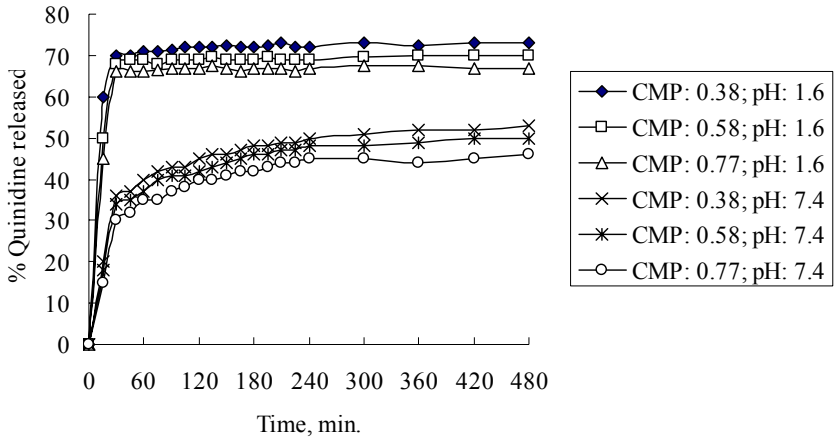

Fig. 6. In vitro release of quinidine from its conjugates with CMP supports.

In order to change the release profile especially in acidic pH, the microparticle-quinidine complexes were covered with an enteric soluble polymer – cellulose acetate phthalate (CAP) using a technique of solvent evaporation [11]. The *in vitro* release curves proved that microparticles' covering with cellulose acetate phthalate film (CAP) induces a delayed release in both acidic and buffered solutions (Fig. 7). Thus the performances of the support/drug polymeric system for controlled release of drugs may be improved.

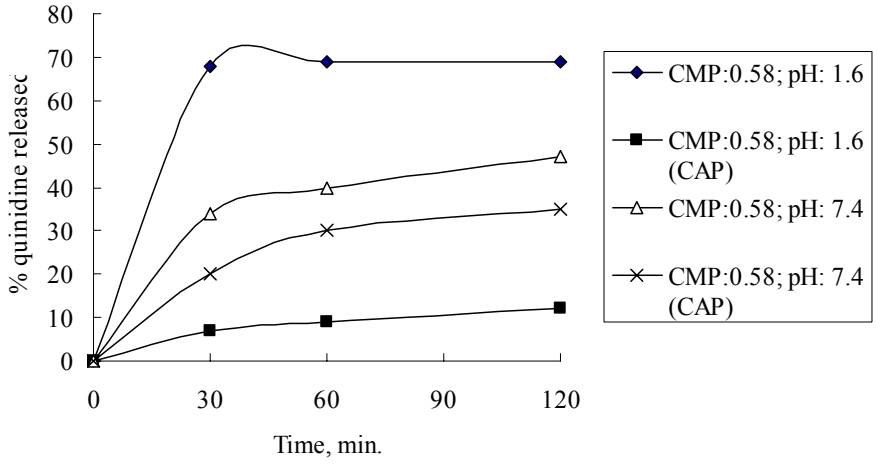

Fig. 7. Comparative release curves of quinidine from coated with CAP or uncoated complexes drug-microparticles.

In conclusion, novel polysaccharide microparticles were obtained from pullulan and carboxymethylpullulan by using a new crosslinking agent – [3-(glycidoxy-

propyl) trimethoxysilane]. They presented interesting properties of interaction with biologically active substances, which recommend them as supports for controlled release drug systems.

3. Synthesis of modified polysilanes with nonlinear optic properties

It is known that nonlinear optics (NLO) deal with the interaction of electromagnetic field (light) with matter to generate new electromagnetic fields, altered with respect to phase, frequency, amplitude or other propagation characteristics from the incident field. One of the intensively studied nonlinear optical phenomena is second harmonic generation or frequency doubling. In the case of second-order nonlinear optical processes, the macroscopic nonlinearity of the material (bulk susceptibility) is derived from the microscopic molecular nonlinearity and the geometrical arrangement of the NLO-chromophores. Organic molecules that exhibit second-order NLO properties usually consist of a delocalized π-system, enclosing either a donor or acceptor substituent or both. One approach to achieve this property is balancing the electro-active properties of the donor and acceptor substituents [12] and another one is the synthesis of molecules with a (σ–π)-conjugated frame. This chapter gathers the newest results on the synthesis of NLO-molecules build on polysilane structures enclosing various electro-active groups.

The intriguing NLO properties of polysilanes originate from the σ–conjugative character of the polysilane chain combined with the electronic influence of the various organic substituents [13]. Through this study new polysilane-metal complex structures were investigated in order to show the influence of the metal-complex segments onto the σ-electrons delocalization along the main chain. One of our aims is the understanding of the electronic transitions and the extent of (σ–π)-conjugation occurring in these polymeric systems and to investigate the interaction between donor and acceptor substituents through the conjugated frame. To this end, we have studied the absorption and emission properties of these compounds by UV and steady state fluorescence spectroscopy.

For this purpose a poly[diphenylsilane-co-methyl(H)silane] (PSHDF) was synthesized first by homogeneous coupling reaction using 15C5 crown ether complex with Na [14]. The next step was to modify the main silicon chain by insertion of ligands and subsequent complexation with the appropriate metal cations.

The chloromethyl-functional polysilane was obtained by a modified Wurtz coupling technique in THF. For this purpose methylphenyldichlorosilane was polymerised in the presence of chloromethyldimethylchlorosilane on sodium wire in anhydrous/inert medium. The polysilane-metal complex was then prepared through the polycondensation reaction of the chloromethyl functional polysilane with the Ni-salen diphenol complex with triethylamine as proton acceptor [15, 16] (Scheme 2).

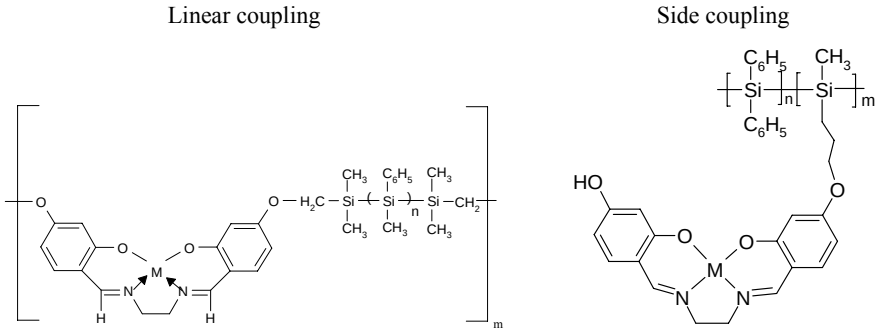

Scheme 2. Polydiphenyl-bis(salicyliden)ethylenediamine-metal complex (M=Ni, Cu).

Optical properties of polysilanes To understand the electro-optical properties of the polysilane-metal complexes it was necessary first to investigate the polyhydrosilane backbone. It is known that the UV spectrum of a polymethylphenylsilane homopolymer shows an absorption band at 280 nm indicating the presence of σ–π transitions due to the phenyl substituent and another one at 340 nm corresponding to the σ–σ* transitions of the conjugated silicon chain [17]. When two aryl groups are attached to the polysilane chain, like in PSHDF, the interaction between the π–orbitals of the phenyls and the σ conjugated silicon chain lead to a decreased optical band gap, causing the absorption maximum to shift to around 350 nm [18].

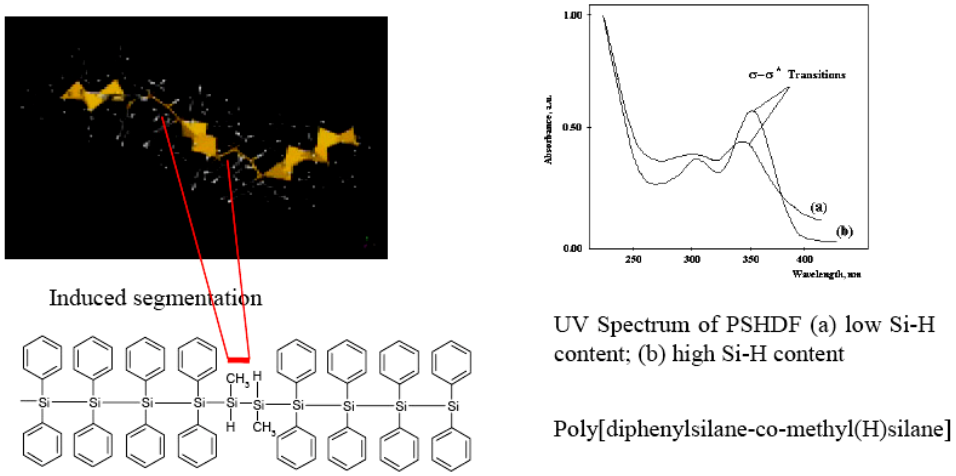

Fig. 8. UV spectrum of polyhydrosilanes.

PSHDF structures were investigated further by steady state fluorescence (FL) measurements and compared with a polymethylphenylsilane hompolymeric structure (PSMF). The mirror image relationship and the bandwidth between absorption and emission give information concerning the regularity of the main chain spatial

conformation [19]. The FL spectral profile of PSMF with full width at half maximum *fwhm* = 25 nm is very different from the mirror image of the absorption band at 340 nm indicating that the stiff helical chain conformation of PSMF has frequent irregularities generated by the chiral inversions or twisting from P to M motifs (Figure 8) [19]. In contrast, PSHDF showed relatively narrow UV absorptions with *fwhm* = 15 nm and the FL spectral profile closer to the mirror image of the 350 nm absorption band. This is somehow surprising because the small methyl(H)silyl fragments which create bending and fractures of the main silicon chain, should produce a UV absorption maximum shift to lower wavelengths, widening of the bands and strong irregularities in the FL spectra.

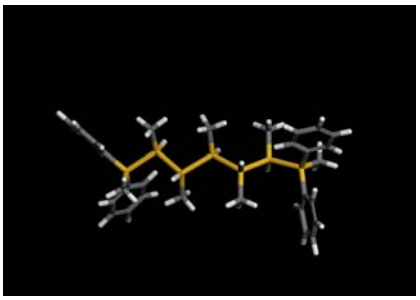

Methylhydrosilyl transplanar segment.

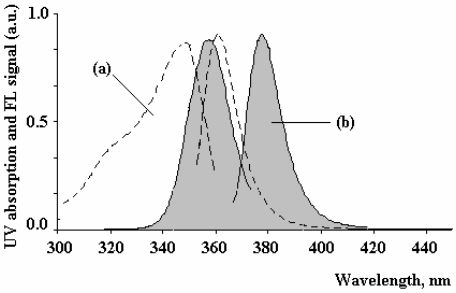

FL Spectra of PSMF (a) and PSHDF (b) in $CHCl_3$ at room temperature.

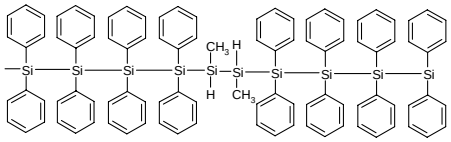

Helicoidal diphenylsilyl-segment.

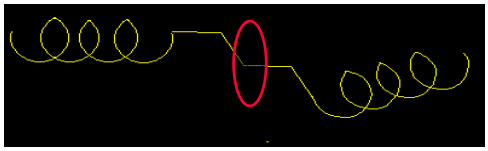

Dynamic relaxation of polyhydrosilane chain.

Fig. 9. Fluorescence spectra of polyhydrosilanes.

The absence of such effects indicates that the long diphenylsilyl segments with a stiff and regular helical global conformation [20] are coupled through transplanar small fragments which eliminate the internal conformational tensions allowing a free rotation of the chain around the –Si-Si-Si-Si- dihedral angle of the methyl(H)silyl (Fig. 9). Therefore, the σ–electron delocalization within the polydiphenylsilane blocks is not affected by the low temperature restructuring of the small methylhydrosilyl fragments.

The electronic properties of the synthesized polysilane-metal complex structures were evaluated through UV-VIS spectral analysis for both linear and pendant architectures. Thus it was observed that both electronic spectra profiles display the specific σ–σ* at 320 nm. In addition, the absorption bands corresponding to the

metal complex transitions could be noticed at 380–460 nm and 400–480 nm, respectively. The UV spectrum of the linear structure shows broad absorption bands and lower intensities than the starting building segments (Fig. 10). This suggests that the interferences between the σ electrons delocalized over the polysilane skeleton and the π electrons of the metal complex affect the conduction mechanism through increasing of the bandgap. The lower intensities of the absorption bands result probably from the altering of the local conformation within distances shorter than 10 silicon atoms.

The UV spectrum of the pendant structure shows higher intensities for the σ–σ*transitions in polysilane at 340 nm (Fig. 11). Also, the values of the wavelength remain almost unchanged comparing with the starting compounds. Therefore, we concluded that the pendant polysilane-metal complex is appropriate for a hybrid conduction mechanism study because in this case there seem to be no conjugative bridging with the metal complex moiety. The electronic properties of both segments remained unaltered by the coupling procedure and behave like separate entities, separating the electrono-donor character of the metal complex units from the main polymeric frame.

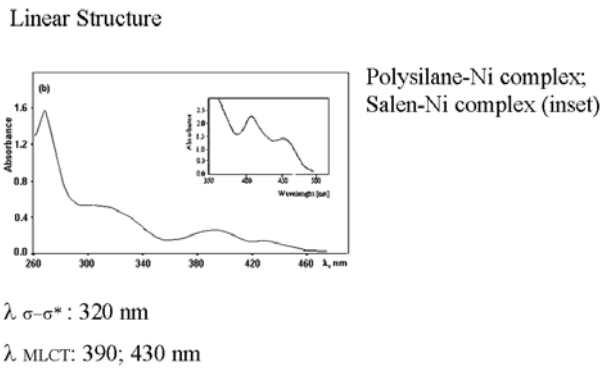

Fig. 10. UV absorption spectrum of the linear polysilane-metal complex.

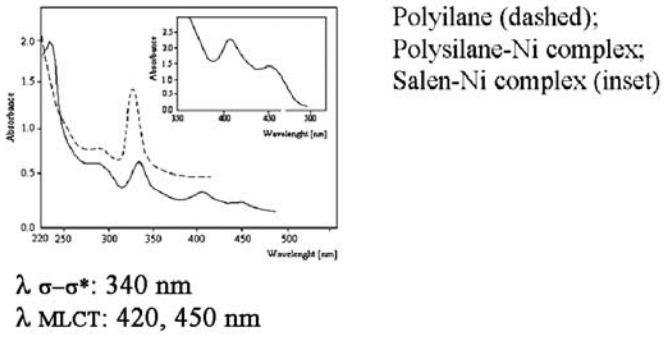

Fig. 11. UV spectrum of the pendant polysilane-metal complex.

In conclusion, the optical and electronic properties of polyhydrosilanes and polysilanes-metal complexes support their application as NLO materials for opto-electronics. The electronic spectra of polyhydrosilanes revealed the presence of the σ–chromophore units as in polymethylphenylsilane, a NLO material which is already in exploitation. New polysilane structures were created by enclosing of electrono-donating metal complex fragments and formation of a DσA structure.

4. Photopolymers for laser ablation at 308 nm

One of the main challenges in surface chemistry and materials science is the discovery and application of novel materials in biophysics, optoelectronics, and nanotechnology. Among them, the design of photosensible polymers occupies a central place in the development of functional devices for specialized applications like photoresponsive systems, medical applications, optical data storage [21]. In relation to polymers intended for photolithographic processes, the literature studies have been primarily focused on microstructuring through UV/laser irradiation of standard polymers (polyimides, polymethacrylates, polycarbonates) or doped systems (polymers/rodhamine, pyrene, benzophenone) [22], but often, the quality of the ablated zones is relatively poor. Although the first reports of laser ablation of polymers were issued by Y. Kawamura and R. Srinivasan as a possible alternative to conventional photolitography, many questions are still open [23]. Polymer ablation, further reviewed by Lippert et al [24], is typically described in terms of thermal, photothermal or photochemicals models, sometimes viewed as combined processes. Therefore, the current research on polymer ablation is divided in two main areas: (i) applications of laser ablation, developing new materials and techniques and (ii), studies concerning ablation mechanisms. Significantly, probing ablation mechanisms and improving ablation parameters (i.e. ablation rate and quality) need new photopolymers designed for an irradiation wavelength at 308 nm. Contextually, some triazene polymers have been intensively investigated [25] to be exploited in microlithography and photoresist technique owing to the intrinsic qualities of triazene chromophore (-N=N-N<). The dominating aspects that can succeed the performance of photoresist systems are the dimensions, resolution and sensitivity of systems during the irradiation process. As a consequence, the promising candidates to accomplish these particular conditions are those that can be structured by the dry development of structuring techniques such as excimer laser lithography. Such “dry–etching” capability has the advantage that no additional wet-developing steps are necessary after irradiation, making this technique attractive for industrial applications.

On this line, we reported previously data on various polyurethanes with triazene and bistriazene groups in their structure, whose ablation properties depend on the polymer and chromophore structure [26]. In order to achieve a better understanding of the effect of the triazene chromophore on the polymer properties, the

ablation behavior of triazene polyacrylates irradiated at 308 nm is presented in the following. Figure 12 shows the structure of the synthesized triazene polyacrylates which were exposed to laser irradiation (XeCl excimer laser) to evaluate the influence of laser beam on polymer surface.

The polymers were studied at low fluences (between 10 and 400 $mJ \cdot cm^{-2}$), when the influence of structural parameters on the ablation rate can be observed. The ablation parameters, F_{th} (threshold fluence) and α_{eff} (effective absorption coefficient) indicated that p-methoxi triazene copolymer PA-1 had a threshold fluence of 211 $mJ \cdot cm^{-2}$, while F_{th} of the second copolymer was much lower (F_{th} = 112 $mJ \cdot cm^{-2}$). Therefore, the high stability of the PA-2 to UV irradiation could be encouraging for laser structuring applications where no modification of the polymer under ambient conditions is preferred. The morphology of the polymeric films after laser ablation was visualized by scanning electron microscopy (SEM). In Fig. 13 the photographs of the PA-1 (left) and PA-2 (right) structures are shown as examples, both the ablation spots being made after 10 pulses at 420 $mJ \cdot cm^{-2}$ fluence.

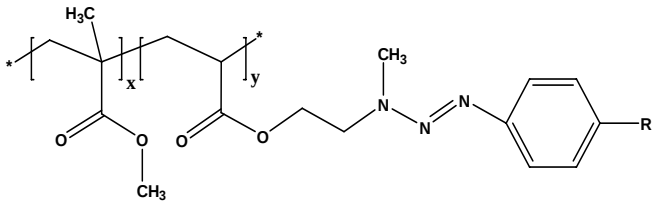

When R = OCH_3 (PA1)
R = Cl (PA2)

Fig. 12. Structure of the triazene polyacrylates.

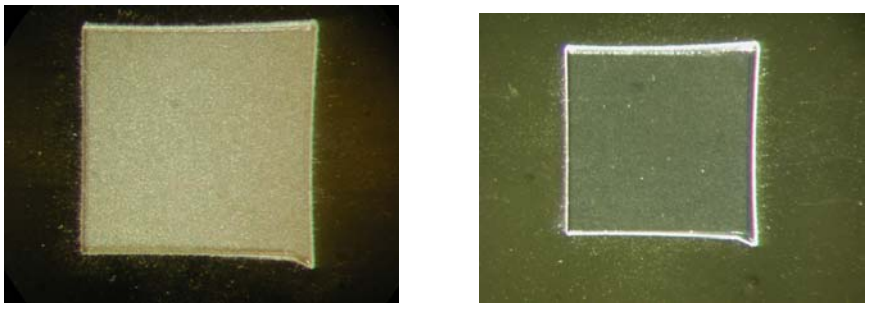

Fig. 13. SEM micrographs of the ablated craters (308 nm) for PA-1 (left) and PA-2 (right).

These photoimages confirm a well defined structuring process due to the decomposition of triazene moieties in the investigated polyacrylates, for which a clean surface is very important for the application of laser ablation in lithography. As expected, from the size of the microridges, the resolution is, in the micrometer or even submicrometer domain.

In conclusion, the experiments performed with the excimer laser irradiation (308 nm) demonstrated that the designed copolymers could be used for the fabrication of microstructures with adequate accuracy. Moreover, the generated microridges illustrate the absence of any amount of redeposited material and the achieving of a flat and smooth surface.

5. Conjugates of maleic anhydride copolymers with disinfectant compounds

The use of maleic anhydride (MA) copolymers in medicine and pharmacy is a topic in which fascinating results were already obtained, including the current applications [27, 28]. So can be mentioned the SMANCS (neocarzinostatin conjugate with n-butyl monoester of MA–styrene copolymer) and the DIVEMA (MA–divinyl ether copolymer), promoted after laborious and long time lasted research efforts. Three main directions could be evidenced from the literature data: MA copolymers possessing *per se* bioactivity; conjugates of MA copolymers with various drugs; drug formulations as solid dispersions based on MA copolymers. Another promising application is the engineering of biosurfaces on which thin polymer coatings were deposited and chemically modified. MA copolymers are also used for medical analysis kits, dental materials, components of biomaterials (for example, with hydroxyapatite), functionalization of dialysis membranes, immobilization of bioactive molecules for tissue engineering. In this chapter are gathered some of our results regarding the synthesis and characterization of new derivatives of maleic anhydride copolymers with disinfecting agents or with menthol, aiming the use in dentistry.

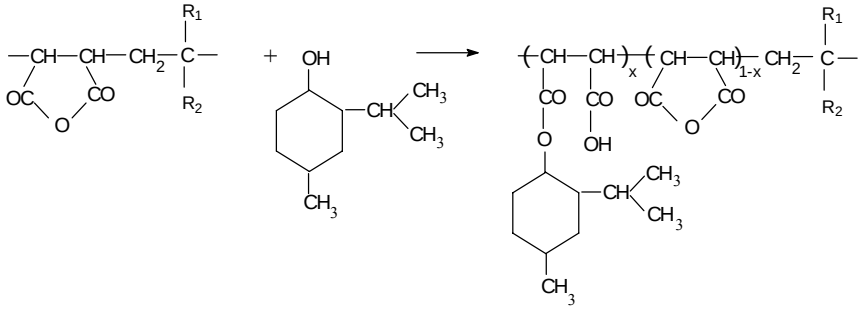

Scheme 3. Chemical reaction between MA copolymers and menthol.

The esterification of MA copolymers with the OH functions of menthol is illustrated in Scheme 3. The same reaction was carried out with thymol and eugenol. Generally the reaction takes place in dipolar aprotic solvents, preferably N-methylpyrrolidone, without catalysts, at temperatures below 80°C. The conversion was estimated by conductometric titration in acetone-water mixture, being between

25 and 50% referred to the maleic anhydride moieties. The new derivatives with thymol or eugenol were characterized by IR spectra and TG analysis and their antimicrobial activity was tested on various species of bacteria by evaluation of the phenol coefficient. The sample having the poly(maleic anhydride-alt-styrene) as parent copolymer and the eugenol as disinfecting species was demonstrated as satisfactory active against *Staphylococcus aureus*, having the phenolic coefficient as high as 5.83 [29].

Another type of conjugates which we have synthesized starting from MA copolymers was the derivatives with menthol [30]. These new products could be used in dental prosthesis, as macromolecular systems which release the odorant, being a remedy against fetid breath. In this case conversions of 0.2 up to 0.35 were attained, depending on the chemical structure of the parent copolymer. The compatibility between poly(methyl methacrylate) – PMMA –, one of the typical polymeric materials used in dentistry, and the menthol derivative of MA-MMA copolymer (MMh) was checked by viscometric measurements in solution (Fig. 14). At low concentrations the intrinsic viscosity values of the mixture are higher than the calculated ones (curve 4, Fig. 14), suggesting a relatively strong interaction between the two polymers.

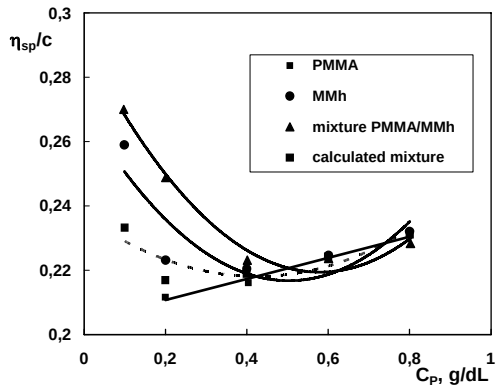

Fig. 14. Reduced specific viscosity of poly(methyl methacrylate) (PMMA) (1), MA-MAM derivative (MMh) (2) and PMMA/MMh mixture (3) in acetone at 30°C.

In conclusion, our attempts directed on some still "free" windows, such as the synthesis of new derivatives with disinfecting agents or with menthol, were up to now successful. The new derivatives were carefully purified and characterized from point of view of composition/conversion and behaviour in aqueous medium, involving the biocide or compatibility properties, and the results were promising.

Acknowlwdgement. The financial support of Romanian National Authority for Scientific Research, CEEX project no. 42/2005-2008 is gratefully acknowledged.

References

[1] *Societal implications of nanoscience and nanotechnology*, Nanoscale Science Engineering and Technology (NSET) Workshop, Sept. 2000, Report ed. by M.C. Roco, W.S. Bainbridge, Arlington, National Science Foundation, 2001.
[2] ROSENTHAL A. M., *Chem. Mater.*, **20** (4), p. 9 (2002).
[3] NIEMEYER C. M., MIRKIN C. A., eds., *Nanobiotechnology: concepts, applications and perspectives*, Weinheim, Wiley-VCH, 2004.
[4] *Nanoscience and nanotechnologies: opportunities and uncertainties*, RS Policy Document 19/2004, www.royalsoc.ac.uk.
[5] JANES K. A., CALVO P., ALONSO M. J., *Adv. Drug Delivery* **47**, p. 83 (2001).
[6] CHEN J., SEONGBONG J. O., PARK K., *Carbohydr. Polym*. **28**, p. 69 (1995).
[7] HENNINK W. E., FRASEN O., VAN DIJK-WOLTHUIS W. N. E., TALSMA H., *J. Control. Release* **48**, p. 107 (1997).
[8] JONG S. J., SMEDT S. C., WAHLS M. W. C., DEMEESTER J., KETTENES-VAN DEN BOSH J. J., HENNINK W. E., *Macromolecules* **10**, p. 3680 (2000).
[9] FRASEN O.,. STENEKES R. J. H,. HENNINK W. E, *J. Control. Release* **60**, p. 211 (1999).
[10] FRASEN O., VANDERVENNET L., RODERS P., HENNINK W. E., *J. Control. Release* **71**, p. 261 (2001).
[11] FUNDUEANU G., CONSTANTIN M., ESPOSITO E., CORTES R., NASTRUZZI C., MENEGATTI E., *Biomaterials* **26**, p. 4337 (2000).
[12] (a) SOULA G., MIGNANI G., FR 2,630,442, 1989; (b) MIGNANI G., KRÄMER A., PUCCETTI G., LEDOUX I., SOULA G., ZYSS J., MEYRUEIX R., *Organometallics* **9**, p. 264 (1990).
[13] HASEGAWA T., IWASA Y., SUNAMURA H., KODA T., TACHIBANA H., MATSUMOTO M., ABE S., *Phys. Rev. Lett.*, **69**, p. 668 (1992); ABE S., SCHREIBER M., SU W. P., YU J., *Phys. Rev. B* **45**, p. 9432 (1992).
[14] a) G. SACARESCU, L. SACARESCU, R. ARDELEANU, P. KURCOK, Z. JEDLIŃSKI, *Macromol. Rapid Comm.* 22, 405 (2001); b) G. ZIEGLER, J. HEINRICH, G. WOTTING, *J. Mater. Sci.* 22, 3041 (1987).
[15] SACARESCU G., ARDELANU R., SACARESCU L., SIMIONESCU M., *J. Organomet. Chem.* **685**, p. 202 (2003).
[16] SACARESCU L., ARDELEANU R., SACARESCU G., SIMIONESCU M., *Polym. Bull.* **54**, p 29 (2005).
[17] (a) GILMAN H., ATWELL W. H., SCHWEBKE G. L., *J. Organomet. Chem.* **2**, p. 369 (1964); (b) BOBERSKI G., ALLRED A.L., *J. Organomet. Chem.* **80**, p. 6 (1968); (c) BOBERSKI W. G., ALLRED A. L., *J. Organomet. Chem.* **88**, p. 65 (1975).
[18] SACARESCU L., SIKOU A., ARDELEANU R., SACARESCU G., SIMIONESCU M., *Macromol. Rapid Commun*. **27**, p. 1054 (2006).
[19] FUJIKI M., *J. Am. Chem. Soc.* **116**, p. 6017 (1994).
[20] FUJIKI M., KOE J. R., TERAO K., SATO T., TERAMOTO A.,. WATANABE J, *Polym. J.* **35**, p. 297 (2003).
[21] MORIGAKI K., SCHÖNHERR H., FRANK C. W., KNOLL W., *Langmuir* **19**, p. 6994 (2003); ROUZER C. A., SABOURIN M., SKINNER T. L., THOMPSON E. J., WOOD T. O., CHMURNY G. N., KLOSE J. R., ROMAN J. M., SMITH R. H., MICHEJDA C. J., *Chem. Res. Toxicol*. **9**, p. 172 (1996); NATANSOHN A., ROCHON P., *Chem. Rev*. **102**, p. 4139 (2002).
[22] KUNZ T.,. STEBANI J, IHLEMANN J., WOKAUN A., *Appl. Phys.* A **67**, p. 347 (1998); DAVIS C., SNYDER R. W., EGITTO F. D., D'COUTO G. C., BABU S. V., *J. Appl. Phys.* **76**, p. 3049 (1994).
[23] KAWAMURA Y., TOYODA K., NAMBA S., *Appl. Phys. Lett*. **40**, p. 374 (1982); SRINIVASAN R., MAYNE-BANTON S., *Appl. Phys. Lett*. **41**, p. 576 (1982).

[24] LIPPERT T., DICKINSON J. TH., *Chem Rev.* **103**, p. 453 (2003).
[25] LIPPERT T., YABE A., WOKAUN A., *Adv. Mater*. **9**, p. 105 (1997).
[26] BURUIANA E. C., MELINTE V., BURUIANA T., LIPPERT T., YOSHIKAWA H., MASHUHARA H., *J. Photochem. Photobiol. A: Chem.* **171**, p. 261 (2005); BURUIANA E. C., MELINTE V., BURUIANA T., SIMIONESCU B. C., LIPPERT T., URECH L., *J. Photochem. Photobiol. A: Chem.* **186**, p. 270 (2007).
[27] CULBERTSON B.M., *Maleic and Fumaric Polymers*, in: *Encycl. Polym. Sci. Eng.*, 2nd edn., J. Kroschwitz, Ed.; J. Wiley and Sons, New York, 1987; vol. **9**, pp. 225–294.
[28] BRESLOW D. S., *Pure Appl. Chem.*, **46**, p. 103 (1976).
[29] CHITANU G. C., ANGHELESCU-DOGARU A. G., POIATA A., BUMBU G. G., VASILE C., RINAUDO M., CARPOV A., *Rev. Roum. Chim*., **47**, p. 1205 (2002).
[30] POPESCU I., CHITANU G. C.,. POPA M. I, CARPOV A., *Polymeric conjugates of menthol with maleic anhydride copolymers for dentistry*, *Proceedings, IUPAC World Polymer Congress, 40-th International Symposium on Macromolecules, MACRO 2004*, Paris, Frace, July 4-9 2004, [http://www.e-polymers.org/paris/data/L3387.pdf].

Integated Microsensors for Nitric Oxides Detection for Biomedical and Environmental Applications

Carmen MOLDOVAN[1], Rodica IOSUB[1], Cristian BOSCORNEA[2], Lavinia HINESCU[3], Victor VOICU[3], Mihai HINESCU[3], Monica ROBU[2], Mihai NISULESCU[1], Marian ION[1]

[1]National Institute for R&D in Microtechnologies,
PO Box 38-160, 72225 Bucharest, Romania
E-mail: cmoldovan@imt.ro

[2]*Politehnica* University Bucharest, Faculty of Industrial Chemistry,
44 Calea Victoriei Street, Bucharest, Romania

[3]Army Center for Medical Research,
37, C.A. Rossetti Street, Bucharest, Romania
E-mail: mhinescu@yahoo.com

Abstract. The paper presents the layout and the technological steps for an interdigitally integrated capacitor used for gases detection. Silicon micromachining technology is applied for manufacturing the sensor substrate.

The sensitive layer used is phthalocyanine (Pc) deposed by EDL (evaporated dyes layers technique). Many solutions were found as phthalocyanine derivatives deposition technique. Considering the different sensitivities of phthalocyanines derivatives, we obtained different gas sensors. The copper phthalocyanine (Cu Pc) and nickel phthalocyanine (Ni Pc) have been investigated for NO_x detection. The measurement of sensors for NO_x and NH_3 detection will be presented as concentration versus impedance.

The microsensors testing structures deposited with phthalocyanines were investigated by impedance measurements in a vacuum chamber controlled by a gas analyzer.

The measurements were made at room temperature but a medium temperature is applied (<200°C) after measurement, for cleaning the material in order to reuse the sensor. The sensor is integrated, MOS compatible, cheap, easy to be used and has a low power consumption.

1. Introduction

The gas sensors are commonly used for pollution control measuring low concentrations of pollutant gases in air, generated by motor vehicle or industrial emissions.

The main factor to be considered in selection of NO, NO_x, or NO_2 sensors for measurements in ambient environments or in biomedical field is the sensitivity.

Nitrogen dioxide (NO_2), nitrogen monoxide (NO) and carbon monoxide (CO) represent a significant health hazard for every one of us; the first alarm threshold limit is set at concentration of 200 $\mu g/m^3$ (106 ppb) for NO_2 and 15 mg/m^3 (13 ppm) for CO/1/.

The operating principle of the gas sensors is based on the change in conductivity due to the chemisorption of gas molecules at the sensitive layer surface. The integration of standard CMOS technology with conducting sensitive layer as phthalocyanine (Pc) deposited by EDL technique was one of the goal of our research. We deposited three types of layers phtalocyanine based: copper phthalocyanine (CuPc), nichel phthalocyanine (NiPc) or iron phthalocyanine (FePc) films to be used as gas sensitive layers for the detection of NO_x, and NO_2 in ambient air.

The layout and the technological steps of a gas sensor based on an interdigitated capacitor integrated with a polysilicon heater, micromachined on a silicon membrane, CMOS compatible, and the test measurements for NO_x andNO_2 are presented.

The microsensors deposited with phthalocyanines were investigated by impedance measurements in a vacuum box controlled by a gas analyzer.Small quantities of these gases can be detected by measuring the resistance of a Pc film.The gas sensors were tested in a box at a constant temperature and their resistance was determined function of NO_x and NO_2 concentration and in presence of an inert gas N_2. The integrated heating element consists of a polysilicon layer underneath the active area. A temperature sensitive resistor will enable precisely temperature control. The sensor is integrated in CMOS technology adding special micromachining processes.

It comes out that these sensors prove stability and sensitivity in polluted air.

2. Sensor Design and Fabrication

The schematic drawing of the sensor chip is presented in Fig. 1. The scheme present the layout and the cross – section of the sensor chip presenting information about technological steps and sensor design. The layout is a simplified version, the interdigitated electrodes having a higher number of fingers/2/. The real structure of the sensor will be presented by SEM pictures. The fabrication process starts with thermal oxidation of the silicon wafers and patterned before the selective ion implantation. High dose boron ($9 \cdot 10^{15}$ cm^{-2}, 100 KeV) is implanted and diffused followed by a boron doping from solid source + diffusion (1050°C, 4 hours). In this wayit was realized the p-n junction, 12 μm depth, for anisotropical stop etch, in two steps, for obtaining the requested depth. After boron diffusion the thickness of the oxide grown on the silicon surface is X_{ox} = 8000 Å. The masking layer for the anisotropic etching on the backside of the wafer and for isolation is obtained by the deposition and configuration of a 2000 Å Si_3N_4 layer. The next step is the deposi-

tion and the configuration of a 4000 Å boron doped polysilicon layer. After polysilicon configuration, the resistor serving as heating element is obtained. A simplified version could be to use the silicon membrane high doped with boron as heater, without polysilicon resistor. A CVD oxide is deposed such as dielectric layer and the contacts at polysilicon layer are open. Cr-Au deposition and configuration follow. Then the interdigitated electrodes, the resistor for monitoring the chip temperature and the necessary bond pads are defined by photolithography above the insulated heater element. The gold (Cr-Au) was used as electrode material to achieve a good contact with the Pc film. The utilisation of Al as electrode material give us, also, very good results.

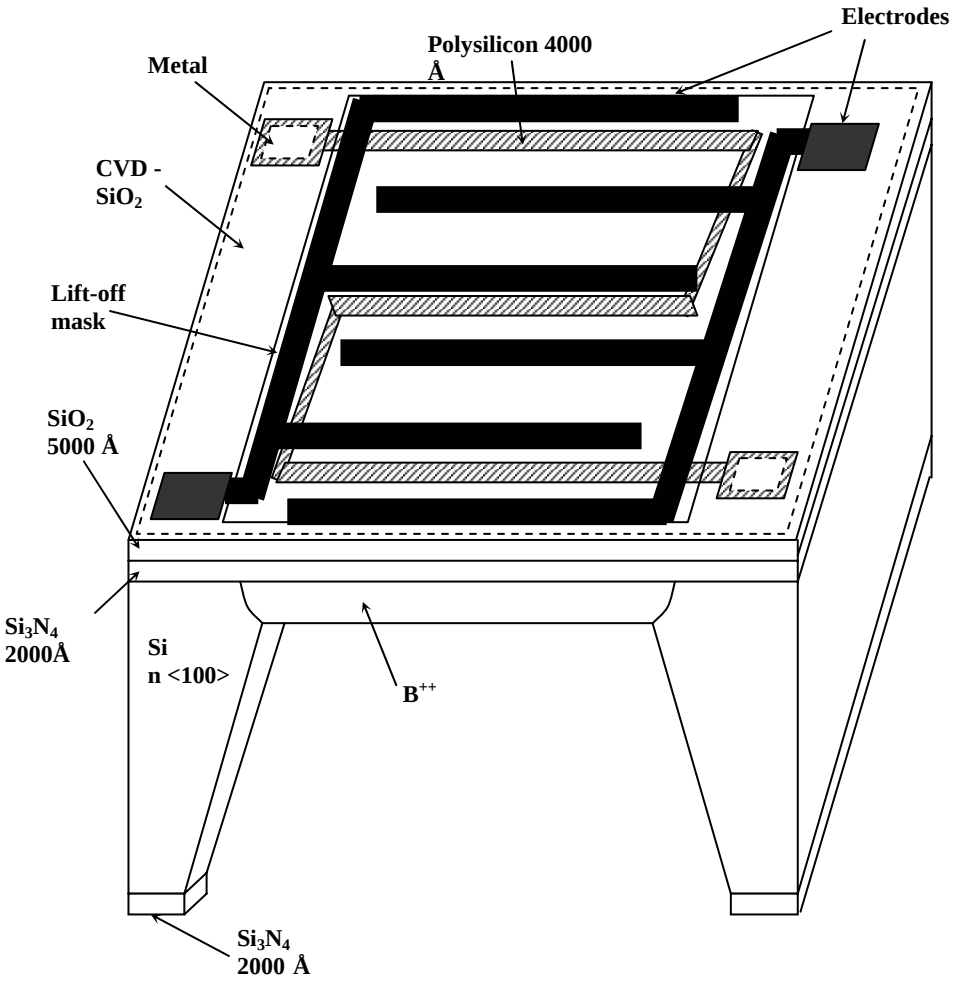

Fig. 1. Scheme of the sensor chip.

The following step was the deposition and the configuration by double side alignment of 2 μm borophosphosilicate glass (BPSG), as mask material for the anisotropic etching, which has a low temperature deposition (<400°C) and can be used after metallization.

BPSG layer can be easily removed and the contact and the pad windows are opened. The etching is stoppedat B^{++} doped regions where the etching rate is very slow and the thickness of the membrane is also, defined. In the caseof silicon anisotropic etching in EDP type F (ethylenediamine: pyrocathecol: water: 1000 ml: 160ml: 160ml), BPSG can be replaced by densified CVD/3/. The utilisation of BPSG, densified CVD as mask materials and EDP as etching solution allow us to obtain the compatibility of the anisotropic etching with the I.C. technology.

Phthalocyanines films of various thickness (40 nm for CuPc and NiPc; 20 nm for FePc) were vacuum evaporated onto the substrates of the interdigitated electrodes in order to analyse their sheet resistivities. The phthalocyanine film temperature could be very accurately controlled by the integrated heating element and thermoresistor. For an accurately deposition of Pcs in the active area of the device, the lift off technique will be used.

The SEM picture of the encapsulated sensor, covered with phthalocyanine is presented in Fig. 2.

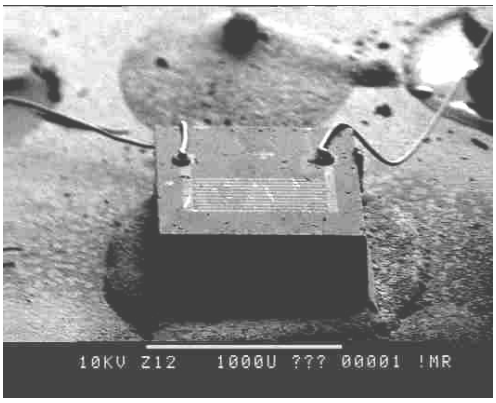

Fig. 2. SEM picture of the sensor chip.

The active area of the sensor contains the metal electrodes. The thickness of the metal layer (Cr-Au) is 400 nm. It is important to study the uniformity of the covering with Pc in order to prevent degradation by clustering of the contact metal.

On a substrate with electrodes on top, Pc film forms not a continuous film over the edge of the electrode strips because during the evaporation of the film the incident angle of the Pc molecules is not exactly normal to the substrate and on one side the strip edge forms a kind of shadow /4/. The film thickness at his point is probably smaller than the average thickness. The electrode strips are much higher

that the Pc film deposited on top. We expect a relative bad covering of the strips and a relative high number of cracks caused by the edges of capacitor strips. Pcs films deposited on electrodes had high resistance measurement values: 10 MΩ for CuPc, 15 MΩ for NiPc, 30 MΩ for FePc. The cracks can be observed in Fig. 3 and 4. For a better integrity of Pcs layer we will act for design and technology changes in order to obtain the planarization ofthe substrate.

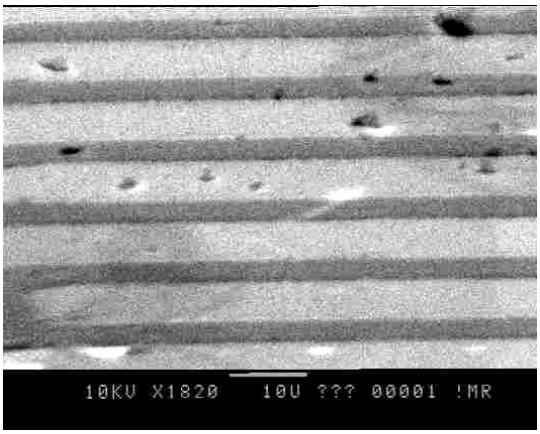

Fig. 3. SEM picture of the electrodes covered with 40 nm CuPc area.

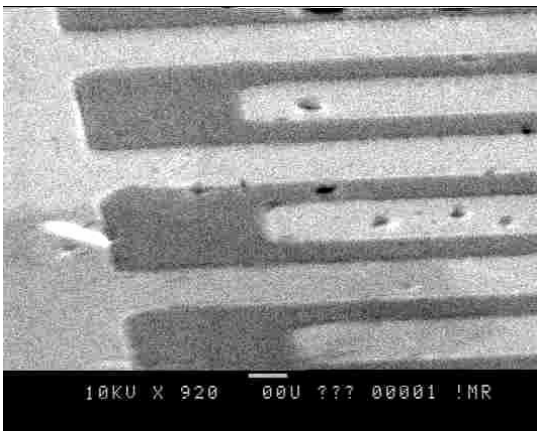

Fig. 4. SEM picture of the electrodes covered with 20 nm FePc area.

3. Experiments

Thin sensitive phthalocyanines films were deposed by evaporation /5/ to obtain gas sensors. The sensors have been tested in a plexiglass box at a constant temperature and the resistance was determinated function of NO_2 and NO_x.

For the NO_2 analyse, 2ml of concentrated HNO_3 allowed to evaporate in a Petri dish inside the Plexiglas box and the responses were measured after every 20 seconds. The entire experiment was done in an automatic manner and the electronic circuit was entirely enclosed in a plexiglass box to avoid electrical interferences.

Sensitivity of NO_x and NO_2 has been tested with a gas analyser; calibrations of each gas have been repeated at least 5 times, typical reproducibility of the sensor response were at 1–3mV.

The method used for Pc deposition wasEDL, as evaporated Pcs at 200÷400°C under high vacuum (~10^{-5}Torr) forms a film of 40–50 nm for CuPc or NiPc and 20 nm for FePc onto the chip with interdigitated electrodes for conductance measurements. The thickness and the speed (10^{-4}÷1 nm/s) of deposition of the metal phthalocyanine film was controlled with a quartz balance.

It comes out that these metal phthalocyanines films are very stable and sensitive in very aggressive environments. The measurements were made at room temperature but a medium temperature is applied (< 200°C) after measurement, for cleaning the material in order to reuse the sensor; in our case the temperature applied was 150°C for one hour.

The Figures 5, 6 show the sensor characteristics for 40 nm CuPc film in NO_2 and NO_x.

Metal phthalocyanines exhibit changes of conductance in presence of very small (ppb) concentration of oxidizing/reducing gases; their bulk conductance ranges from 10^{-6} to 10^{2} ohm^{-1} cm^{-1}.

4. Results and Discussions

The measurements indicate us the decreasing of the resistance with the increasing of the concentration for NO_2 and NO_x gases and for all types of phtalocyanines and sensors (Figs. 5–10).

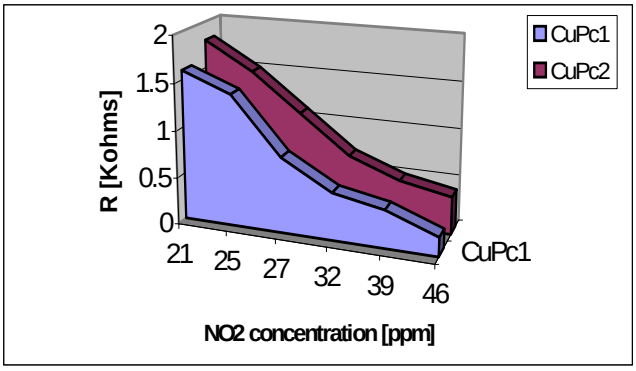

Fig. 5. Resistance versus NO_2 concentration for CuPc.

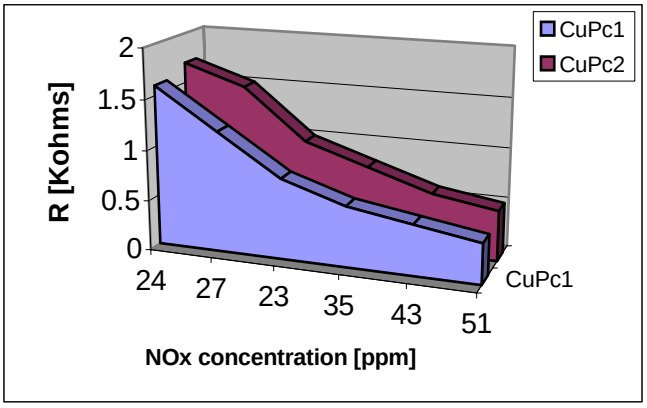

Fig. 6. Resistance versus NO_x concentration for CuPc.

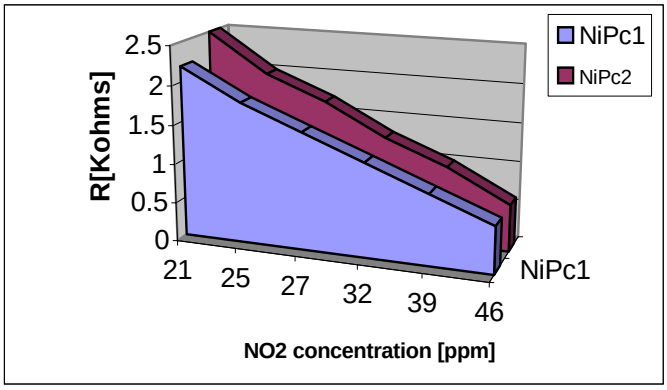

Fig. 7. Resistance versus NO_2 concentration for NiPc.

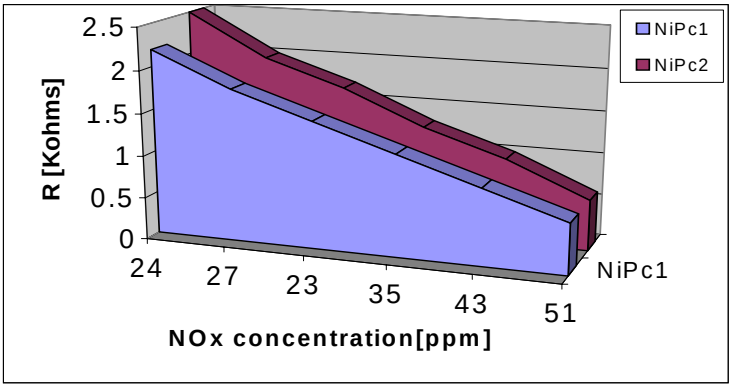

Fig. 8. Resistance versus NO_x concentration for NiPc.

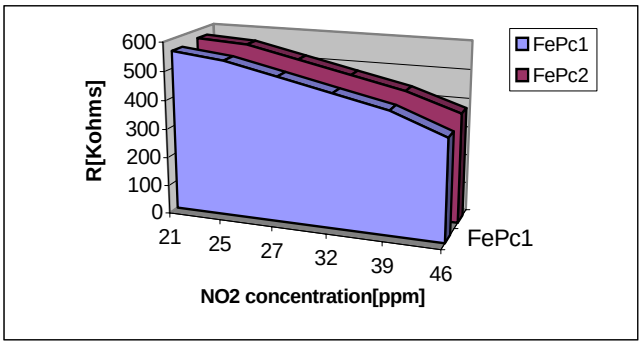

Fig. 9. Resistance versus NO_2 concentration for FePc.

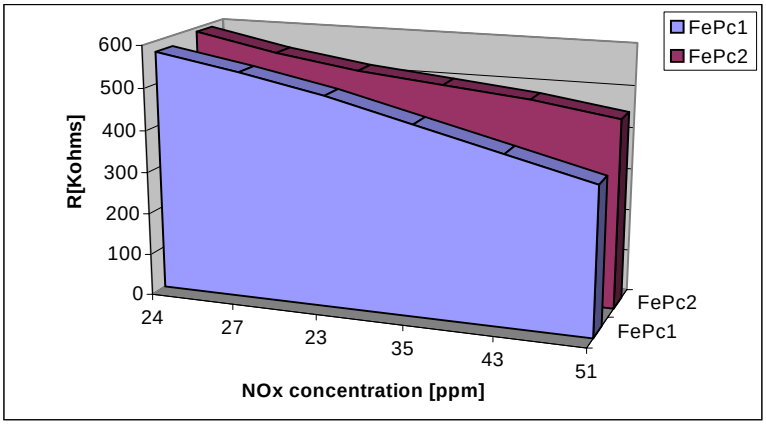

Fig. 10. Resistance versus NO_x concentration for FePc.

Two different area are used for sensors in order to study the sensitivity function of layout. Different read out values has been obtained, showing the influence of the sensors dimensions in response. The reproducibility of the silicon technology will allow us to obtain identical and reproducible sensors.

Phthalocyanine structure is a large planar molecule with a delocalized electron system, which can easily be ionized. A phthalocyanine molecule is a good electron donor. The ring of N atoms around the central metal forms a potential well, which is responsible for the semiconducting properties. Metal phthalocyanines are very stable from chemical and thermal point of view, as a result of their intrinsic structural characteristics. The operating principle of the sensors is based on the change in conductivity due to the chemisorption of gas molecules at the semiconductor surface. Depending on whether the reaction is oxidizing or reducing, acceptors or donors will be produced at the film surface leading to the formation of a space-charge layer and modification of the free carrier density.

The differences in sensitivity for Cu, Ni, FePcs can be explained by the electronic configuration of metals coming in Pcs composition. The simple Pcs conductivity is usually low (approximately $10^{-14}\Omega^{-1}cm^{-1}$). The transitional metals help the conduction due to electron transport through redox system. The metal is much more efficient if it forms plan complexes with conjugate ligands (Pc). An excellent example is CuPc which has the highest mobility between of all organic compounds (75 cm^2/v.s). Here "dz^2" orbitals of copper superpose with "3d" orbitals of azomethane of adjacent molecules with 0.388 nm interplanare distance.

When air alone was exposed to the Pc film, the signal change was insignificant compared with that on exposure of the air and nitrous oxide mixture. When the exposure time of gas was longer than 5 minutes, there was no further current increase recorded showing that the Pc film has been saturated.

5. Conclusions

Three main types of thin phthalocyanines films have been studied from point of view of NO_x and NO_2 sensitivity: CuPc, NiPc, FePc. They exhibit changes of conductance in presence of small concentration of nitrogen oxides gases. Resistance measurements have been done without contact problems for Pcs films deposited on interdigitated electrodes.

The sensitivity and stability of the sensor are sufficient for applications during the measurements made at room temperature of polluted air and even aggressive environments such as the NO_2 steams from HNO_3 100%. The temperature of 150°C was applied for one hour, for cleaning the material (metal phthalocyanines films) in order to reuse the sensor.

The sensor in entirely integrated, MOS compatible, cheap, easy to be used and has a low power consumption.

References

[1] LEGIN A., RUDNITSKAYA A., SELEZNEV B., VLASOV Y., *Taste Ouantification Using the Electronic Tongue; Electronic Noses and Olfaction*, 2000 Proceedings, pp. 13–16.
[2] MOLDOVAN C., IOSUB R., MODREANU M., Sensors and Actuators A, **3277** (2002) pp. 1–8.
[3] COBIANU C., IORGULESCU R., SAVANIU C., DIMA A., DASCALU D., SICILIANO P., CAPONE S., RELLA R., QUARANTA F., VASANELLI L., Proceedings DTM Paris, 1999, pp. 1151–1158.
[4] SCHUTZE U., WEBER J., ZACHEJA J., KOHL D., MOKWA I., ROSPERT M., WERNO J., Sensors and Actuators A, **37–38** (1993) pp. 751–755.
[5] BOSCORNEA C, TOMAS S., GHINESCU L, TARABASANU C., Journal of Materials Processing Technology **119** (2001) pp. 344–347.

SU-8 Microfluidic Channels for Bio-Chemo Applications

Raluca MÜLLER, Irina CODREANU, Laura EFTIME,
Alexandru HERGHELEGIU, Loredana DRAGHICIU, Marian POPESCU

National Institute for Research and Development in Microtechnologies (IMT Bucharest)
E-mail: raluca.muller@imt.ro

Abstract. The paper presents the realization and microphysical characterization of rectangular and y–shape micro-channels, manufactured using a polymeric material: SU8. The fluid flow in both configurations was simulated with COMSOL Multiphysics software. The micro-channels were intended to be used in microfluidic applications for chemo-bio investigations.

1. Introduction

Microchannels are used in microtechnologies for platform as "Lab on Chip". They are usually integrated with micro-valves, pumps, reaction chambers and can be integrated with electronic chips [1] or optical parts as waveguides and detection elements like photodiodes [2].

SU-8 polymer is a biocompatible material which can be successfully used in the manufacturing of integrated microfluidic platforms for a wide range of bio-chemo applications, using low cost integrated technologies, in order to develop miniaturize microsystems for portable use, sensitive and reliable.

We present in this paper the fabrication of different configuration of micro-channels to be used in microfluidic applications, obtained by SU-8 and the simulation of fluid flow, using COMSOL Multiphysics software. We obtained rectangular and y-shaped fluid microchannels, which were investigated using scanning electron microscopy.

2. Fabrication/Characterization Results

There are different techniques used for manufacturing micofluidic microchannels: etching of silicon wafers using wet or dry micromachining techniques, glass micro channels fabrication, which allows the optical observation of the fluid, or polymeric based microchannels using photolithographic techniques (SU-8 or PMMA). The use of polymeric materials represents a flexible and in the same time chip method.

SU8 is a negative photoresist, an epoxidic resin, initialy used for the manufacturing of high aspect ration of 3D micromechanical structuresis. It has remarcable properties as: chemical inert, mechanical stable, very good adhesion on SiO_2 and Si_3N_4, transparent for the electromagnetic radiation for 500–850 nm range, hidrofob, so far recomaded for an economic alternative for the microfluidic channel manufacturing [3, 4].

As substrate we used silicon <111> wafers. For a good adesion, the substrate was clean (H_2SO_4:H_2O_2=1:3) and dryed before the polymer deposition. We used SU-8 negativ photoresist (SU-8 2005, MicroChem Corp., MA) which was spin-coated for a thickness of 6 μm, at 1000 rmp for 40 s. The layer was pre-baked for 1 min at 65°C, 2 min at 95°C and 1 min at 65°C, in order to evaporate the solvent and to densify the film. This process of upgrading the temperature is necessary for a good polymerization of the resist., and to obtain a low stress film. To obtained the desired thickness of the microfluidic channels (12 μm) we repeated two times the process. The layers were exposed by UV radiation. After the exposure, a thermal treatment at 95°C for 4 min was performed for the resulted of SU-8 layer in order to selectively cross-link the exposed portion of the film, developed with Micro-Chem SU-8 Developer for 3 min. A 10 min hard-bake process was finally performed at a temperature of 150°C to improve the mechanical resistance (hardness) by a further cross-link of the final resist pattern. The structures were then analyzed by scanning electron microscopy (SEM). The final measured thickness of the microfluidic microchannels were about 11 μm.

We defined 2 different confugurations by standard litographic technique: rectangular and y –shaped The resulted dimensions were the following: 10–11 μm depth; 12–22 μm width and length between 5 and 10 mm.

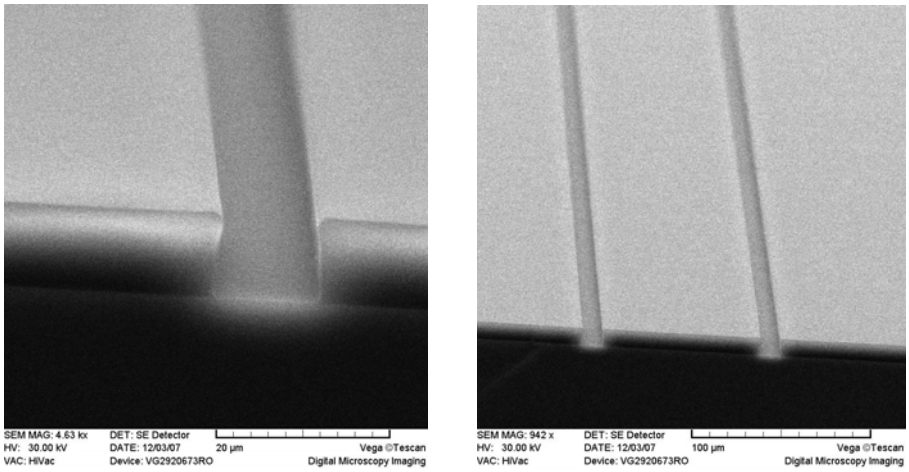

a) **b)**

Fig. 1 a, b. SEM photos of rectangular microchannels etched in SU8 polimer.

As one can see in Figs. 1 and 2, the investigations of scanning electron microscopy (SEM) show very high aspect ration walls and a very good uniformity for relatively long channels (mm).

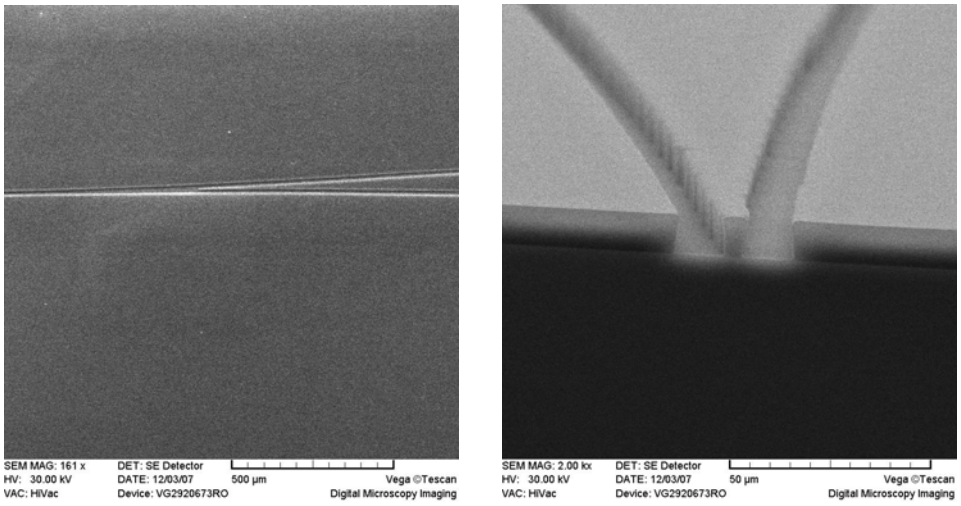

a) **b)**

Fig. 2 a, b. SEM photos of y-shaped microchannels etched in SU8 polimer.

3. Simulation

The simulation of a fluid flow in the microchannels has been performed using COMSOL Multiphysics software. The flow was considered to be an incompressible laminar flow and was simulated using the incompressible Navier-Stokes application mode. First there has been simulated the flow in a simple rectangular channel. Figure 3 presents the layout of this channel.

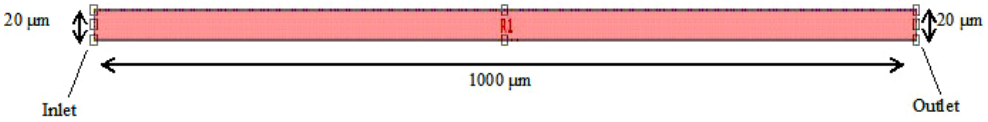

Fig. 3. Layout of the rectangular channel.

The geometrical dimensions are the following: channel length 1000 µm, channel width is 20 µm and the channel height is 10 µm.

Figure 4 presents the result of the simulation: the velocity field of the fluid in the channel. The fluid is water, and it has been considered a 10 Pa pressure at the inlet of the channel, and the slip condition on the walls of the channel: lateral and bottom.

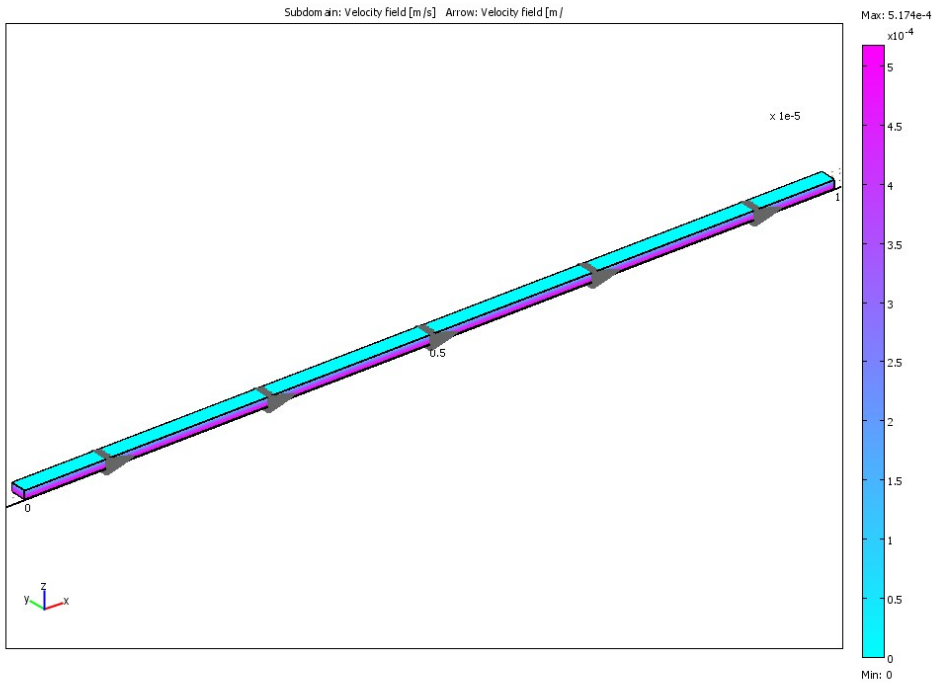

Fig. 4. Velocity field of fluid flow in a rectangular channel.

A simulation for a y shaped channel has also been performed. Figure 5 presents the layout of the y-shaped channel. The total length of this channel is 1000 µm. The width of the initial channel and of the two secondary channels that form the y arms is 20 µm and the height of the channel is 10 µm. The angle formed by the two secondary channels that form the y arms is 2°. The fluid that flows through this channel is also water. The pressure at the inlet is 10 Pa, and the pressure at the outlets is 0.

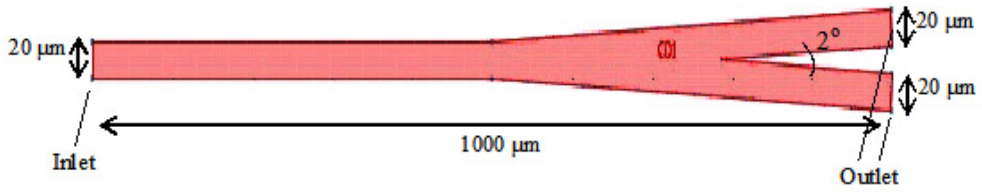

Fig. 5. Layout of the y-shaped channel.

The result of the simulation show the velocity field (Fig. 6) of the water flow in the y-shaped microchannel. It can be seen that the velocity decreases in the two secondary channels and the flow keeps it laminar incompressible nature.

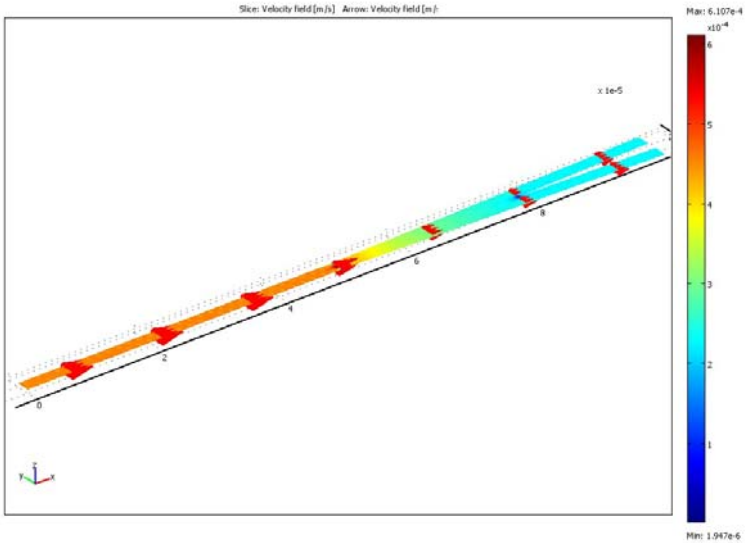

Fig. 6. Velocity field of the fluid flow in a y-shaped channel.

4. Conclusions

We manufactured high aspect ration fluidic microchannel using SU-8 polymeric material. The velocity of the fluid flow was simulated in the two types of configurations: rectangular and y-shaped, using COMOSOL Multiphysics software.

The developed microfluidic channels are chip, easy and fast to fabricate and can be utilized for chemo-bio investigations, using small quantities of biological materials, being an alternative to silicon techniques. Further work has to be done to integrate driving electrodes and other system components with the fluidic microchannels, in order to control the movement of charged bio-samples.

References

[1] SON S. U., CHOI Y. H., LEE S. S., *On-Chip Integation of Microfluid and Cell Detector for Micro Cell Counter*, Key Engineering Materials Vols. **270–27**, 200, pp. 1083–1088.

[2] WHEELLER A. R. *et. al.*, *Microfluidic Device for Single-Cell Analysis*, Anal. Chem., **75**, 2003, p. 3249.

[3] HONG G.,. HOLMES A. S, HEATON M. E., *SU8 Resist Plasma Etching and Its Optimization*, DTIP 2003, France, p. 268–271.

[4] GADRE A., KASTANTIN M., LI S., GHODSSI R., *An Integhgrated Bio-MEMS Fabrication Technology*, Int. Semiconductor Device Sympos. (ISDRS), Washington D.C., Dec 2001, pp. 186–189.

Thin Films for Solar Cell Applications Obtained from Complex Targets by Magnetron Sputtering on New Substrates

Lucica BOROICA[1], Victor Rares MEDIANU[2], Sanziana Ioana BOROICA[3]

[1]National Glass Institute, Th. Pallady 47, Bucharest 032258, Romania
E-mail: boroica_lucica@yahoo.com
[2]National Institute for Laser, Plasma and Radiation Physics, Bucharest, Romania
[3]University of Bucharest, Romania

Abstract. In order to reach the world target of 4% share of electricity production by 2030 worldwide, the major issues in the solar cell domain are to lower the costs of modules from around 3 €/Wp to below 0.5 €/Wp, to have products with a maximum capacity for building integration like roofing elements or walls panels, and to find processes leading to the fabrication of environmentally friendly PV products.

For these purposes our team proposes to make complex targets ($CuInS_2$) with different amount of Ga and to make films deposition on new substrates like composite glasses, kapton and metal sheets (Ti foil and stainless steel foil).

1. Introduction

Solar cells/integrated photovoltaic elements are semi-conducting multi-layer devices that produce electric energy, by photo-voltaic effect. Materials used as substrates are usually Si, GaAs, CdTe [1] but recent researches were based especially on replacing the Si and glass, with metallic foils (Ti, Mo). The photo-voltaic elements based on multi-layer structures using as active element $CuInSe_2/S_2$ have at this moment the best quantum efficiency [2–3]. Reports on CdSe film junctions with CIGS [4] and CdTe are also available. The investigation of chalcopyrite materials such as $CuInSe_2$ or $CuInS_2$ at the interface with semiconductors from group II-IV were recently researched [5]. The study of the In_2S_3-Cu_2S-CuS system has shown the existence of a solid solution range with In_2S_3 vacancy in spinel crystal structure [6]. These solid solutions have been synthesized in the form of powders and single crystals by solid state and chemical vapor transport reactions. The cell parameters for $CuInS_2$, which exhibits the chalcopyrite structure, are: bc-tetragonal $I\,42d$ (122), $a=b=0.5523$, $c = 1.1133$, $c/2a = 1.0079$ [7].

InSe layered semiconductors are new class of materials for solar energy conversion application [8]. The transport properties of InSe along the layers and method of obtaining have been widely investigated [9–15].

The methods to prepare less toxic $CuInS_2$ are varied. The starting materials are In metallic as powders and S_2 in excess [16]. From metallic indium melt were grown various single and multiphase samples of chosen compositions. Were identified three Cu-In phases, the In-S phase In_6S_7, and the ternary phases $CuIn_5S_8$ and $CuInS_2$ by means of their PAC signals [17].

$CuInS_2$ and $CuInSe_2$ with different morphologie shapes were also obtained by similar hydrothermal and solvothermal synthesis, crystal growth from melt in the ternary system. Single crystalline (112)-oriented $CuInS_2$ surfaces can be obtained using a lamellar eutectic growth mechanism, with crystallizing of $CuInS_2$ melt by horizontal gradient freeze in a temperature gradient ranging from 5–15°C/cm, under elevated argon pressure of ~20 bar [18–22].

2. Experiments

Were obtained complex targets (I), for film deposition was selected magnetron sputtering method (II), and some materials were studied for Si replacing (III). In towards to Si replacing we propose to use: kapton and metal sheets (Ti foil and stainless steel foil).

Experiments were made in three directions: designing the succession of multi-layers, preparing of complex targets ($CuInS_2$), and selecting new substrates.

The deposition method was selected magnetron sputtering using in a VARIAN ER 3119 unit. In this case are necessary targets with the following dimensions: Ø = 100 mm ± 1 mm and h = 4 mm – 6 mm [23–29].

Was proposed the following succession of layers presented in Fig. 1.

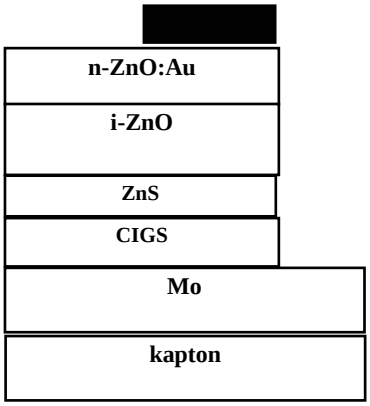

Fig. 1. The proposed multilayer composition.

2.1. Preparing of complex targets

Were obtained complex targets by using powders Cu-S_2-In and Cu-S_2-In_2S_3 as starting materials, and then doping with 8% Ga.

The starting materials and their characteristics are presented in Table 1.

Table 1. Characteristics of used materials

No experiment	Starting materials	Characteristics	
		Density [g·cm^{-3}]	Melting point [°C]
1	In (white metal)	7.31	156.60
	Cu (red powder)	8.96	1084.62
	S_2 (yellow powder)	2.07	112.8
2	In_2S_3 (red metal	4.90	1050
	Cu (red powder)	8.96	1084.62
	S_2 (yellow powder)	2.07	112.8

The powders were dry mixed for 30 minutes in ceramic crucibles, than thermal treated in an electric furnace with superkanthal elements type LHT 02/16 (Nabertherm Germany) in N_2 atmosphere. The thermal treatment was: heating from 20°C up to 1000°C; duration 5 h, at 1000°C; cooling duration was 10 h. The temperature was kept by using a controller that programs the heating regime. N_2 gas flow was kept at constant pressure of 5 bar.

In Fig. 2 are presented the results of the experiments (a) using In metallic – an exothermic reaction took place at about 150°C, and b) using In_2S_3).

a) **b)**

Fig. 2. Aspect of complex targets: a) using In metallic; b) using In2S3.

The obtained materials were structural characterized by X-ray diffraction, using an X-ray diffractometer (Bruker-AXS type D8 ADVANCE) having Cu anode, filter k_β de Ni.

2.2. I Doping

The obtained target $CuInS_2$ was doped by volume diffusion with Ga in H_2S atmosphere. This method leads to obtain $CuInS_2$ and $CuGaS_2$.

The sequences of the process to obtain complex materials $CuInS_2$ doped with 99.99% metallic Ga may be described as:

1. First from Cu_2S and In_2S_3 was obtained the phase $Cu_{11}In_9$;
2. Sulphating and formation of the ternary compound $CuInS_2$ chalcopyrite;
3. Diffusion in the chalcopyrite of Ga;
4. Re-crystallization of phase $CuInS_2$ and $CuGaS_2$ that leads to formation of quaternary $CuInGaS_2$.

2.3. Film deposition

Thin films can be obtained by several techniques such as: pulsed laser deposition, molecular beam epitaxy (MBE), magnetron sputtering (**RF)** ion layer gas reaction, and so on [30]. $CuInS_2$ thin films were prepared by ion layer gas reaction using C_2H_5OH as a solvent, CuCl and $InCl_3$ as reagents and H_2S gas as suphuration source.

Epitaxial and polycrystalline films were grown by a co-vaporization process in a vacuum chamber containing sulphure vapors [31]. Thin films of $CuInS_2$ can be deposited on substrates at temperatures as low as 300°C [32].

By RF magnetron sputtering deposition are made layers of: Mo (700 nm–1000 nm.); CIGS (1500 nm–2000 nm); ZnS (50 nm–100 nm); i-ZnO (500 nm–1000 nm) and n-ZnO: Al (800 nm–1200 nm) [33–39].

2.4. Substrate selection

As substrate we propose to use materials such as: composite glasses, kapton and metal sheets (Ti foil and stainless steel foil), which are common and not expensive.

On a transparent plastic foil substrate a semiconductor CdS film for a photonic application was realized using pulsed-laser deposition [40]. Although plastic is not considered to be a favorable substrate material for semiconductor thin-film formation, the deposited CdS film possesses good adhesion, with a polycrystalline texture, flat surface (roughness/thickness = 0.003), and room-temperature photosensitivity with a blue-shifted peak at 2.54 eV.

In order to use kapton as substrate the materials was analyzed by DTA (differential thermal analyze) and mechanical properties (stress, Young modulus and elongation after water treatments).

Results are presented in Figs. 3–5.

The advantage of using as substrates metallic foils or plastics despite Si are the following: the solar cells made will be more thin and lighter then the classic

ones. Also the obtained devices are easy to use being able to be used in stationary and mobile applications (automobile, in space, mobile telephones).

Problems may appear, such as technological ones, but also about the compatibility between the substrate and the semi conducting materials used as energy generators.

From technological point of view, the first problem that occurs is that the solar cells are subjected to mechanic efforts during the fabrication process that may lead to bending. This fact has more consequences:

– changing of shape and dimensions of device;
– due to difference in the elastic modulus and the chemical composition between the substrates may appear cracks in the layers and as a consequence to reduce the efficiency of the solar cell.

A special problem that may appears during the process of solar cell fabrication with polymeric (polyimide type) substrate is that concerning the adhesion of thin film to substrate.

In this paper we select as substrate two types of polyimide foils noted Kapton HN and Kapton VN to study the behavior of such substrate after covering it with a thin film.

Each foil has 125 μm thickness.

Kapton is a polyimide that has unique properties and that recommends it to be one of the most suitable substrates and support for applications in electronics.

Kapton has the ability to maintain physical properties (mechanical and electrical) in a wide temperature domain and so it is suitable to be used as substrate to flexible solar cells.

Kapton is obtained by polymerization of an aromatic anhydride with a dyamine.

After the tests made on sample Kapton HN and Kapton VN used in this paper was demonstrated that it is not soluble in organic solvents being chemical resistant.

On the Kapton HN and Kapton VN foils were performed the following tests: degassing tests, water stability tests, mechanical properties test and thermal properties tests.

In order to establish the behavior to degassing of Kapton was made the following experiment:

– samples were put in place and the pressure was reduced up to 10^{-6} torr;
– samples were than heated up to 450°C.

Due to fact that the polyamide and Kapton are obtained after a polycondensation reaction their properties are affected by long treatment in water.

In order to establish the water stability, the Kapton substrate was boiled in water for 1000 h.

The mechanical properties (Young modulus, tensile strength and elongation) of Kapton foils were measured in a Single Column Testing Machines 1-5 KN test device, from Lloyd Instruments.

Thermal gravimetric properties were measured using a TGA 92 from SETARAM. Samples were heated up to 550°C with 10°C/min. and then kept at 550°C for 30 minutes.

3. Results

3.1. Degassing tests

In Fig. 3 (a, b) are presented the curves obtained after degassing tests for sample Kapton HN and Kapton VN. It can be observed that the amount of gas obtained after degassing process for both samples, at different temperatures and pressures are in the accepted values.

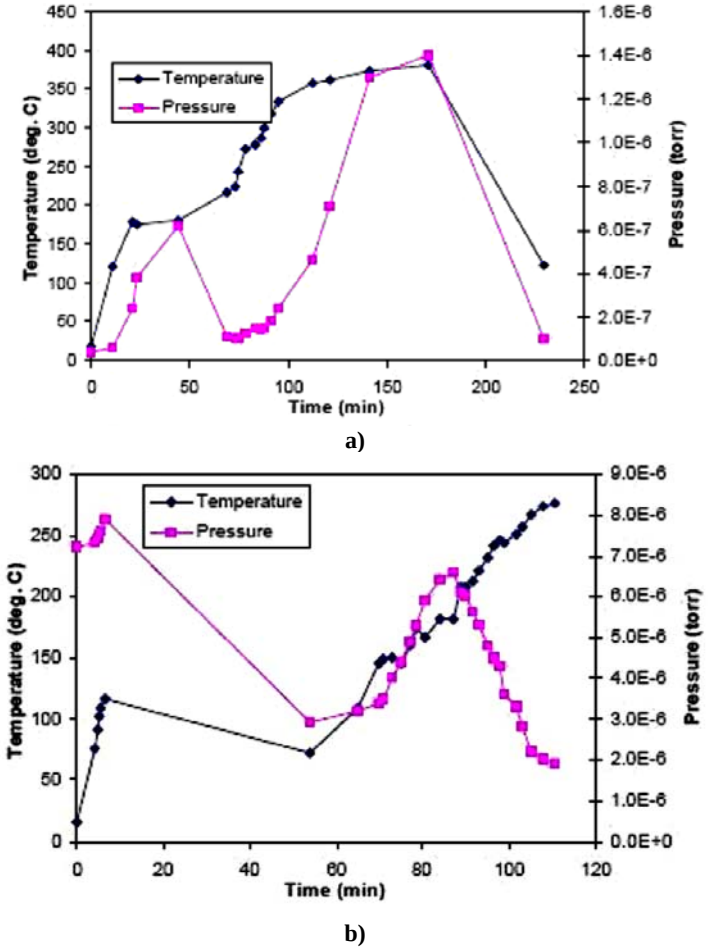

Fig. 3. Degassing curves for samples Kapton HN (a) and Kapton VN (b).

3.2. Water stability tests

In Figs. 4 and 5 are presented the results obtained after boiling in water, at 100°C, for a Kapton HN sample of 125 μm thickness, for 1000 h.

It can be observed that, even when the sample was boiled for long time, its mechanical properties decreases, but very low.

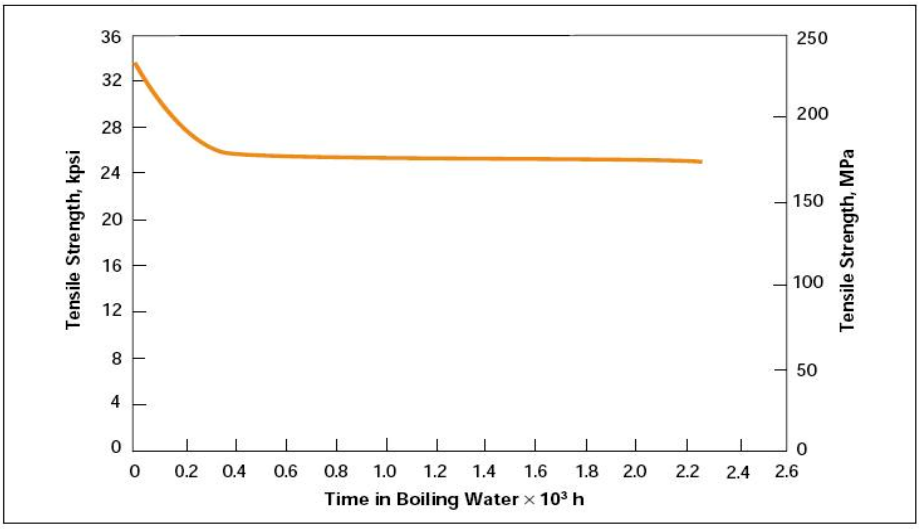

Fig. 4. Variation of tensile after boiling in water of a Kapton HN foil (thickness 125 μm).

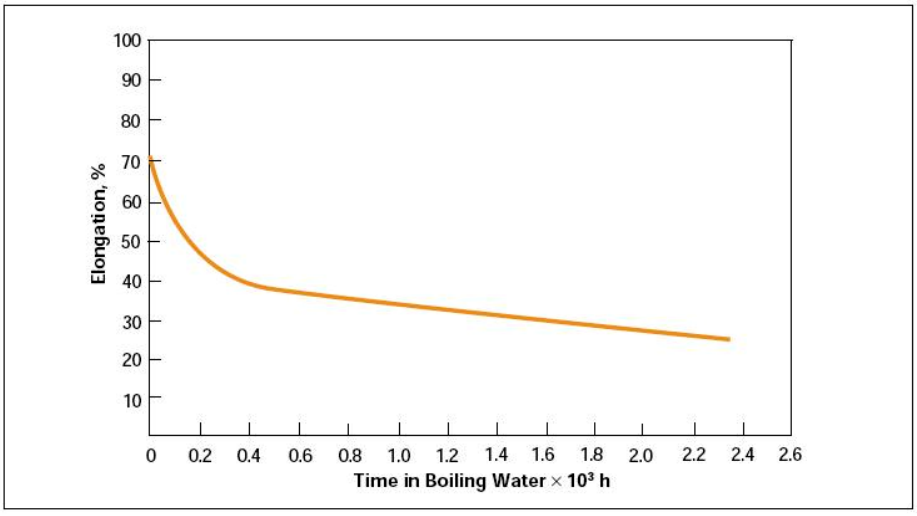

Fig. 5. Elongation after water treatments of Kapton HN substrate (thickness 125 μm).

3.3. The mechanical properties tests

Tensile strength (Fig. 4) and elongation (Fig. 5) are at good parameters. By decreasing the temperature and water content the mechanical properties of Kapton increased. By increasing the temperature and water content the mechanical properties decreased but remain in acceptable parameters to be used as substrates for flexible solar cells.

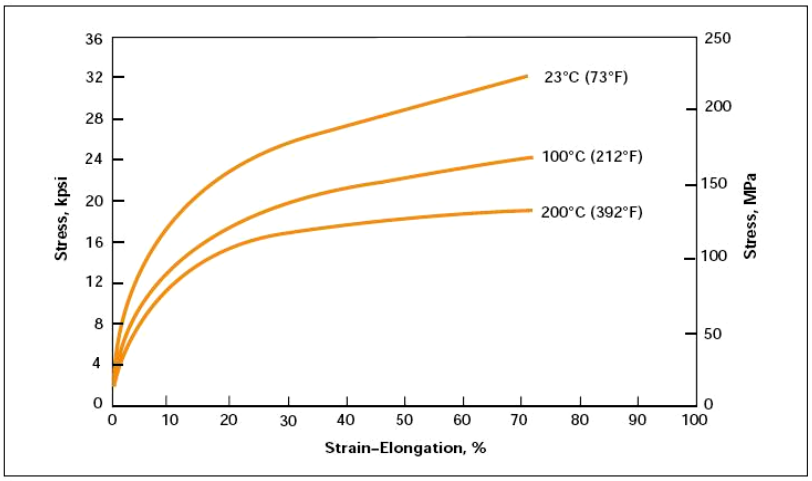

Fig. 6. Stress and Young modulus of Kapton HN substrate (thickness 125 μm).

From the curves in Fig. 6 it appears that stresses decrease by increasing the temperature.

3.4. Thermal properties tests

The thermo-gravimetric analyze of a Kapton HN foil (thickness 125 μm), is given in Fig. 7 and shows that the weight loss is 0.

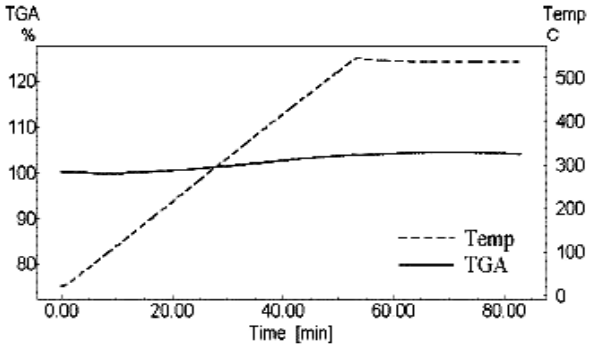

Fig. 7. DTA of Kapton HN substrate (thickness 125 μm).

It may be concluded that in the condition of a thermal treatment at 550°C the sample is stable. But it can be observed that, if the temperature increases, the color of sample changes and it is less flexible.

The prepared complex $CuInS_2$ targets were used to obtain thin films by R.F magnetron sputtering deposition, in a VARIAN ER 3119 unit.

Result of X-ray diffraction made to the obtained targets is presented in Fig. 8. It showed out that, at surface, the S_2 is in low concentration.

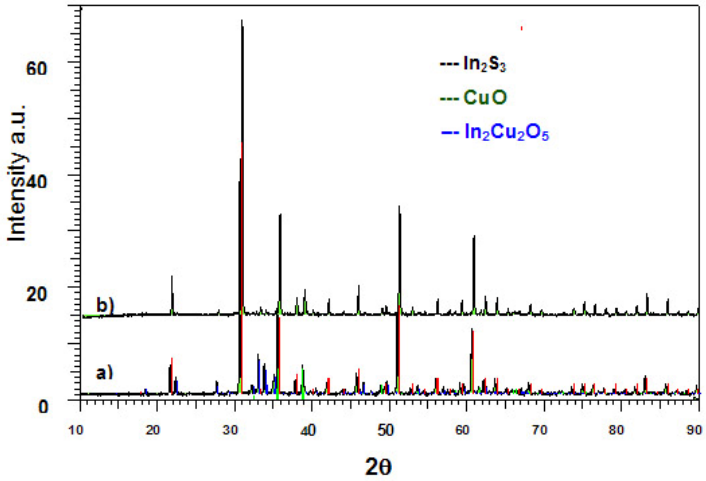

Fig. 8. X-ray diffraction pattern of a) the bulk sample and b) surface sample.

The deposition of multilayer structures was achieved in neutral atmosphere of N_2 or Ar, at partial pressures in the range 5×10^{-4}–5×10^{-3} torr. The deposition rates are optimized to be in the range 0.1–1 Å/s and the thickness of the thin films is in the range 20 nm–2000 nm in order to preserve the stoichiometry. The multilayer structures were analyzed as regards the surface morphology, using atomic force microscopy. Results are presented in Fig. 9.

4. Conclusions

Using powders such as Cu-S_2-In_2S_3 and Cu_2S-In_2S_3 were obtained complex targets that were used to deposit thin films for solar cell fabrication. By testing at thermal treatment the kapton sample was stable until 550°C.

Elongation increased with temperature, having a maxim at 300°C, but the sample was stable. By increasing the temperature and the amount of water the sample remains in parameters to be used as substrate for solar cells.

By using magnetron sputtering (**RF)** deposition method thin films were obtained on different substrates, kapton, inox and Ti foils**.**

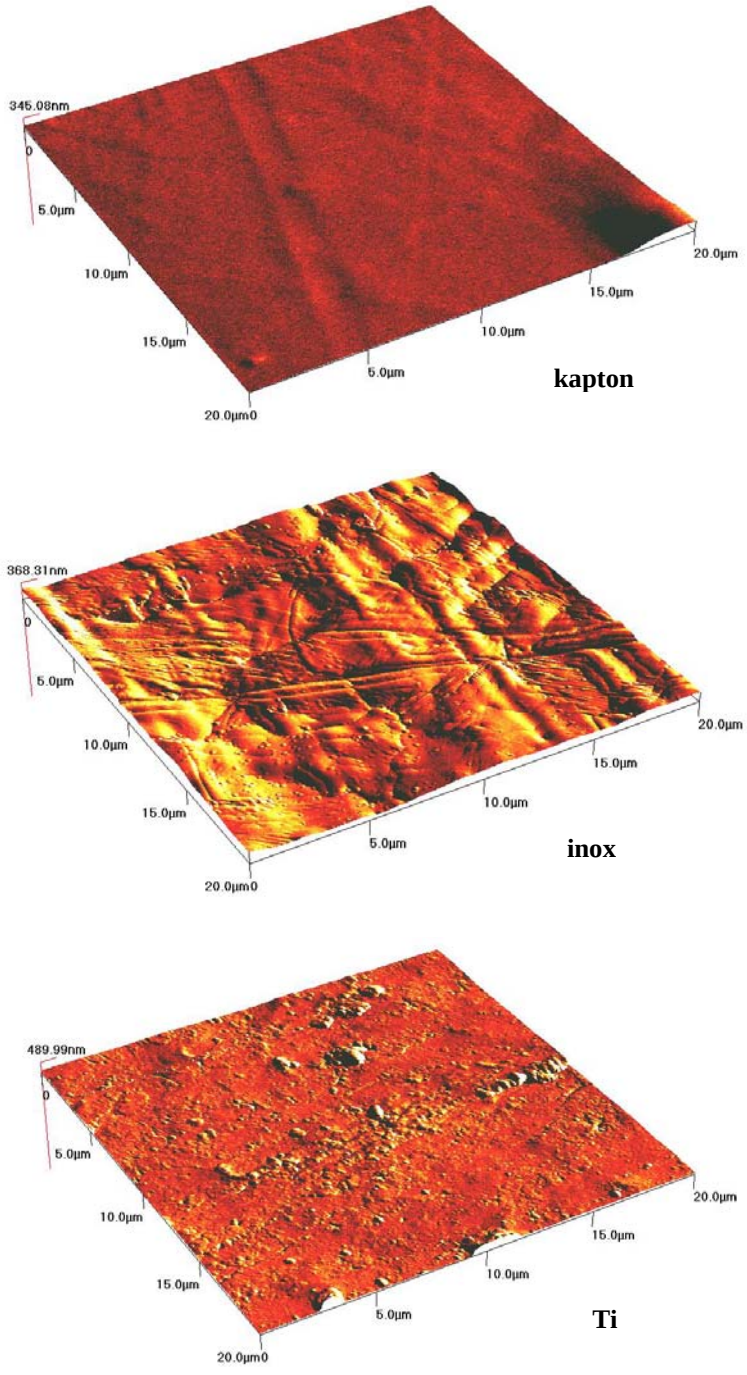

Fig. 9. AFM of the films deposited on different substrates: kapton, inox and Ti foil.

Kapton has the ability to maintain physical properties, in a large temperature domain, that is suitable for flexible solar cells fabrication, as substrate. Developing and studying technological skills of advanced nano-materials, with special emphasis on quaternary composite nano-layers for PV cells, are the main goal of the work. RF magnetron sputtering techniques is the physical process to be used to manufacture PV devices. Si substrates were replaced with good technological results by kapton.

Acknowledgement. The paper was financed by project CEEX 279/ 2006.

References

[1] BORAH M. N., CHALIHA S., SARMAH P. C., RAHMAN A., Journal of Optoelectronics and Advanced Materials, Vol. **10**, No. 6, 2008, pp. 1333–1339.
[2] WIENKE J.A., GORIS M. J. A. A., GEYER V., DAM VAN R., SCHUH N., CdS *layer optimization for* CuInS2 *solar cells based on coated glass beads*, 21st European Photovoltaic Solar Energy Conference and Exhibition, Dresden, Germany, 04.09.2006.
[3] VILELA M. F., ANSELM K. A., SOORIAR N., JOHNSON J. L., LIN C. H., BROWN G. J., MAHALINGAM K., SAXLER A., SZMULOWICZ F., Journal of Electronic Materials, Vol. **30**, No. 7, 2001, p. 798.
[4] KLEIN A, SÄNBERLICH F., LIU G., TIEFENBACHER S., JAEGERMAN W., in *Abstract Quantsol, Surface Science Division*, 2003.
[5] CONTRERAS M. A., EGAAS B., RAMANATHAN K., HASOON F., NOUFI R., Prog. Photovolt. Res. Appl. **7**, p. 311, 1999.
[6] MAHAWALA P., VAKKALANKA S., JEEDIGUNTA S., FEREKIDES C. S., MOREL D. L., Thin Solid Films **480–481**, p. 466 (2005).
[7] SCHLEUSSNER S., Cu(InGa)Se_2 *thin film solar cells with* ZrN *as back contact*, Diplomarbeit, Universitat von Uppsala / Schweden, 2003.
[8] BINSMA J M, GILING L J, BLOEM J., J. Cryst. Growth, **50**, pp. 429–436, 1980.
[9] RUDIGIER E., *Phase Transformations and Crystalline Quality of* $CuInS_2$ *Thin Films*, 2004, Digitale Bibliothek der Universität Marburg.
[10] PY F., OLIVIER-FOURCADE J., JUMASA J.-C., Journal of Solid State Chemistry, Vol. **99**, 2, pp. 319–328, 1992.
[11] GÜRBULAK B., KUNDAKÇI M., ATEŞ A., YILDIRIM M., Phys. Scr. **75**, pp. 424–430, 2007.
[12] TAGIEV B. G., NIFTIEV G. M., AIDAEV F. S., Phys. Status Solidi A, **89**, p. 639, 1985.
[13] SEGURE A., MARI B., MARTINEZ-PASTOR J., CHEVY A., Phys. Rev. B, **43**, p. 4953, 1991.
[14] RIERA J., SEGURE A., CHEVY A., Phys. Status Solidi A, **136**, p. K47, 1993.
[15] CAMASSEL J., MERLE P., MATHIE H., CHEVY A., Phys. Rev. B, **17**, p. 4718, 1978.
[16] ABD EL- MOIZ A. B., Physica B, **191,** p. 293, 1993.
[17] IMAI K., SUZUKI K., HAGA T., HASEGAWA Y., ABE Y., J. Cryst. Growth, **54**, p. 501, 1981.
[18] DE BLASI C., MICOCCI G., MONGELLI S., TEPORE A., J. Cryst. Growth, **57**, p. 482, 1982.
[19] BRÜSSLER M., METZNER H., HUSEMANN K.-D., LEWERENZ H. J., Hyperfine Interactions, Springer Netherlands, Vol. **60**, 1–4, pp. 805–808, 1990.
[20] METZNER H., BRÜSSLER M., HUSEMANN K.-D., LEWERENZ H. J., Phys. Rev. B, **44**, pp. 11614–11623, 1991.
[21] GOU X., CHENG F., SHI Y., ZHANG L., PENG S., CHEN J., SHEN P. J., Am. Chem. Soc., **128**(22), pp. 7222–7229, 2006.
[22] ZHBANKOV O. YE., OLEKSEYUK I. D., YURCHENKO O. M., PANKEVICH V. Z., Cryst. Res. Technol., **41**, p. 843, 2006.

[23] ALVAREZ GARCÍA J., *Characterisation of* CuInS2 *Films for Solar Cell Applications by Raman Spectroscopy*, Tesis, B.12089-2003/84-688-1186-6, 2002.
[24] KRUNKS M., BIJAKINA O., MIKLI V., VAREMA T., *Formation and recrystallization of* $CuInS_2$ *films in spray pyrolytic process*, J. Therm. Anal., to be published.
[25] BOROICA L., BOROICA I., ROTIU E., SAVA B. A., MEDIANU R., TIMUS C., HÜLSENBERG D., *Intl. Conference Proc. of. SPIE*, vol. **6785**, p. 24-2, 2007.
[26] BOROICA L., MEDIANU R., DINESCU M., BOROICA I., Applied Surface Science, Elsevier, Vol. **248**, p. 381, 2005.
[27] BOROICA L., MEDIANU R., DINESCU M., BOROICA I., HÜLSENBERG D., Proc. 50. Internationales Kolloquium Technische Universität Ilmenau, 2005, 65.
[28] MEDIANU V. R., TIMUS C., BOROICA L., CuInGa*Se_2/S_2 *thin films for solar cells with high quantum efficiency*, Conference on Trends in Optoelectronics, June 17–19, 2007, Munich, Germany.
[29] JINWEN Q., ZHENGGUO J., JIJUN Q., ZHIFENG L., Journal of the Chinese Ceramic Society, Vol. **34**, No. 8, pp. 937–940, 2006.
[30] HARRIS J.D. *et al.*, IEEE Photovoltaic Specialists Conference, pp. 563–566, 2000.
[31] BANGER K. K. *et al.*, Chem. Mater., Vol. **13**, pp. 3827–3829, 2001.
[32] KAISER I., EMST K., FISCHER C. H., J. Sol. Energy Mater. Solar Cells, **67**, pp. 89–96, 2001.
[33] NANU M., REIJNEN L., MEESTER B., J.Thin Solid Films, **431–432**, pp. 492–496, 2003.
[34] BRAUNGER D., HARISKOS D., WALTER T., J. Sol. Energy Mater. Solar Cells, **40**, pp. 97–102, 1996.
[35] BANDYOPAHYAY S., CHAUDHURII S., PAL A. K., J. Sol. Energy Mater. Solar Cells, **60**, pp. 323–339, 2000.
[36] KURANOUCHI I. S., NAKAZAWA T., J. Sol. Energy Mater. Solar Cells, **50**, pp. 31–36, 1998.
[37] SIHAM M., ABDEL-HAMID E., J. Fizika A, **4**, pp. 171–179, 1997.
[38] HOLLINGSWORTH J. A., BAMGER K. K., JIN M. H., J. Thin Solid Films, **431–432**, pp. 63–67, 2003.
[39] LINDOOS S., ARNOLD A., LESKELA M., J .Appl. Surf. Sci., **158**, pp. 75–80, 2000.
[40] ACHARYA K. P., SKUZA J. R., LUKASZEW R. A., LIYANAGE C., ULLRICH B., J. Phys. Condens. Matter., **19**, pp. 196–221, 2007.

Hybride Nanocomposite Nafion/Porous Silicon Structures – Fabrication and Characterization

Adina BRAGARU, Mihaela MIU, Florin CRACIUNOIU,
Irina KLEPS, Monica SIMION, Teodora IGNAT,
Veronica SCHIOPU, Adrian DINESCU

National Institute for Research and Development in Microtechnologies (IMT),
Bucharest, 077190, Romania

Abstract. The objective of this work is to demonstrate the potential of the nanoporous silicon and corresponding hybrid materials based on it as proton conductors in general, with a specific focus on its potential applications in fuel cells. Hybrid inorganic/organic structures were fabricated and analysed in the view of further applications in miniaturized fuel cells technology. Taking into account the advantages obtained by nanotructuration, nanostructured porous silicon was used as matrix for both protonic polymer (Nafion) impregnation and catalyst (Pt) deposition.

1. Introduction.

The design of energy sources, power portable devices like cellular phones, laptop computers or sensors networks, is a challenge. These devices are presently powered with batteries that limit their autonomy and require human intervention and electrical energy sources to recharge. Moreover, they generate wastes incompatible with their proliferation. The international technology roadmap for semiconductors predicts a decrease of the voltage required to power the working of microcircuits toward 0.6 V in the next 10 years [1].

Fuel cell technology has been generally recognized as a key twenty-first century energy source, with growing importance for preserving the environment as it produces environmentally benign energy [2, 3]. The use of miniature fuel cells (μFCs) appears an attractive way to power portable electronics with a clean and refillable energy source. This is one of the reasons to explain the intense activity presently occurring in the FC research field. Among all kinds of FC, only two are really suitable for miniaturization. The limitation principally comes from the working temperature required to be lower than 100°C. One of them is the proton ex-

change membrane (PEM)-FC. A key element of a PEMFC is the membrane that must have high conductivity for protons and be impermeable to all other present species (H_2, O_2, water, any other fuel, etc). The operation principle of the standard PEMFC is presented in Fig. 1 [3]:

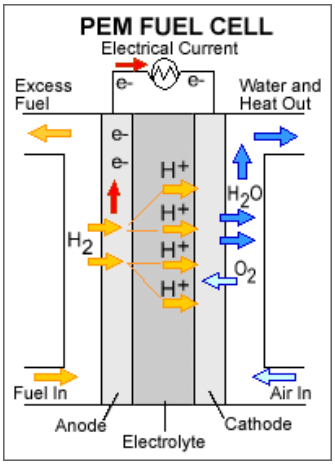

Fig. 1. Operation of Polymer Electrolyte Membrane Fuel Cell – PEMFC [3].

The schematic presentation shows a basic design of a fuel cell which consists on two electrodes on either side of an electrolyte (polymer). While the hydrogen fuel is supplied to the anode and oxygen is supplied to the cathode of the fuel cell, the charge carrier is the hydrogen ion (proton) obtained in the course of a chemical reaction where the hydrogen is split into an electron and a proton; furthermore, electricity, heat and water are produced.

The micro direct methanol fuel cell (μDMFC) is considered as the most promising type of fuel cell for small power-supply units because of its advantage of ambient condition operation, which is most essential for portable application [4–9]. Similar reactions take place in this particular type of cell, as it is presented in Fig. 2 [10]:

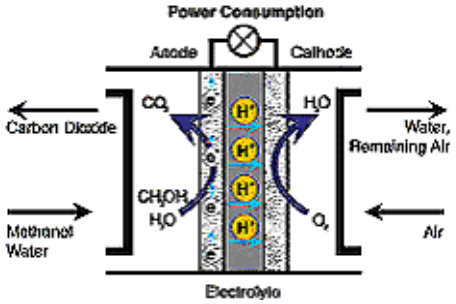

Fig. 2. Schematic view of a direct methanol fuel cell [10].

However, the liquid methanol (CH_3OH) is oxidized in the presence of water at the anode generating CO_2, hydrogen ions and the electrons that travel through the external circuit as the electric output of the fuel cell. The hydrogen ions travel through the electrolyte and react with oxygen from the air and the electrons from the external circuit to form water at the anode completing the circuit.

$$\text{Anode Reaction: } CH_3OH + H_2O \Rightarrow CO_2 + 6H^+ + 6e^-$$

$$\text{Cathode Reaction: } 3/2\ O_2 + 6\ H^+ + 6e^- \Rightarrow 3\ H_2O$$

$$\text{Overall Cell Reaction: } CH_3OH + 3/2\ O_2 \Rightarrow CO_2 + 2\ H_2O$$

There are two major drawbacks with the direct methanol fuel cell (DMFC): a relatively lower anode electrocatalytic activity and methanol crossover, and the low efficiency of fuel consumption and methanol poisoning at the cathode. Active research effort has recently been focused on DMFC proton exchange membranes, especially with respect to methanol crossover [11–16].

State-of-the-art miniature FC technology [17–22] generally use ionomer films to conduct protons from the anode, where hydrogen is consumed, to the cathode producing, with the reduction of oxygen, water, electrical current and heat. At the present time, the best conductivity (0.08 $S \cdot cm^{-1}$) is reached by the polymeric Nafion perfluorosulfonated membranes. However the high cost and the geometric instability during hydration are only some of the severe constraints of such polymers.

On the other hand, silicon micromachining processes are employed for fabrication of a broad spectrum of miniaturized micro-electro-mechanical-systems (MEMSs), and represents a suitable approach for development of μDMFC, because they allow to micropattern the substrate with desired 3D features. For example, Maynard and Meyers [23] proposed a conceptual design for a miniaturized proton exchange membrane methanol-based fuel cell based on silicon technology, achieving 0.5–20 W recorded power. Most recently, Yu *et al.* [24] fabricated a miniature twin-fuel-cell connected in series by sandwiching two membrane-electrode assemblies between two silicon micro-machined plates. Pavio *et al.* [25] has been investigated the low-temperature co-fired ceramic (LTCC) material as an alternative for the bipolar plates of micro fuel cell systems, and they have reported a DMFC prototype.

In portable fuel cells, water and gas management represents a critical issue to enhancement of cell performance and sustained cell operation for an extended period of time. Blum *et al.* [26] discussed overall water balance between the cell's net production rate and water loss through an air-breathing cathode. It was recognized that a water-neutral condition occurs when the water molecules lost per molecule of methanol consumed by the cell reaction approaches two, a stoichiometric value of the net water production per mole of methanol. Under this water-neutral condition, there is neither need to carry water in the fuel tank of such a micro DMFC, nor dry out of the cell. Recently, Lu and Wang [27] presented a photographic study

of bubble dynamics on the anode side and liquid water flooding on the cathode side, thereby providing a basic understanding of gas and water management requirements in DMFC and hence aiding a judicious selection of suitable materials for anode and cathode backing layers.

2. Experimental processes

To be fully compatible with microelectronics processes and standard microfabrication techniques the FC is integrated on silicon substrates. *The objective of this work* is to demonstrate the potential of the nanoporous silicon and corresponding hybrid materials based on it to act as proton conductors in general, with a specific focus on its potential applications in fuel cells. Porous silicon (PS) has been an intensively studied material, primarily due to its unique optical properties, but recently, novel applications have been developed using other interesting characteristics [28]. It is formed by anodic etching in hydrofluoric acid based solutions; a wide range of porous layer thicknesses, porosities, surface areas and morphologies can be obtained depending on the anodization conditions [29]. The nanoscale pores may provide efficient channels for proton transport.

An easy method to obtain nanocomposite materials consists on introducing/ impregnation the matrix material with the second one; the main advantage is that the resulting material exhibits both constituents' properties. Taking into account these characteristics, we have studied an organic/inorganic nanocomposite material based on Nafion – known as the best polymeric element – and porous silicon – nanostructured Si matrix – in order to obtain a new *proton exchange membrane (PEM)* which can be subjected to specific MEMS processes for fuel cell application.

(i) The first stage is realization of the silicon membrane, with 50 μm thickness, by a standard wet etching process in a 40% KOH solution at 80°C. A photolithographic positive process was used to define on both silicon wafer sides the mask which contains a simple design with 3×3 mm squares. A schematic view of the proposed design is presented in Fig. 3:

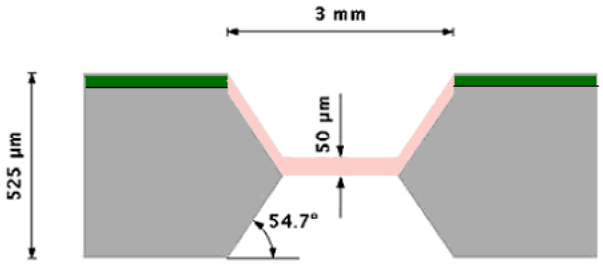

Fig. 3. Schematic cross-section view of the porous silicon membrane;
silicon is in grey, porous silicon is in pink, and the oxide layer is in green.

A thick – 1.5–2 μm – thermal oxide layer is required to resist as mask for the long silicon etching process (about 4 hours).

(ii) The electrochemical etching for membrane nanostructuration was performed using the AMMT GmbH equipment controlled by a computer in oder to realize the porozification process. As it is well known the porosity and the pores geometry are depending on the anodization parameters, like current density, electrolyte solution, and process time [29, 30]. In order to obtain the optimum PS morphology as well as the electrical characteristics, two types of pore geometries has been studied: (i) a branched structures of pores/ fibrils with tens of nanometers dimensions; (ii) columnar pores with 1–2 microns diameters. For fabrication, two types of silicon were studied, as following:

- *n-type* silicon wafers, with (111) crystallographic orientation, having 525 +/−25 μm thickness and a low resistivity 1–5 mΩ·cm, see the SEM images in Fig. 4;
- *n-type* silicon wafers, with (100) crystallographic orientation, having 525 +/−25 μm thickness and a resistivity of 0.01–0.02 Ω·cm, see the SEM images in Fig. 5.

The solution used as electrolyte is a mixture of ethanol and hydrofluoric acid (C_2H_5OH: HF = 1:1) and the anodization parameters were modified in order to obtain a 50% porosity, corresponding to 20 nm pores size, in the first case, and 500 nm pores size, in the second case.

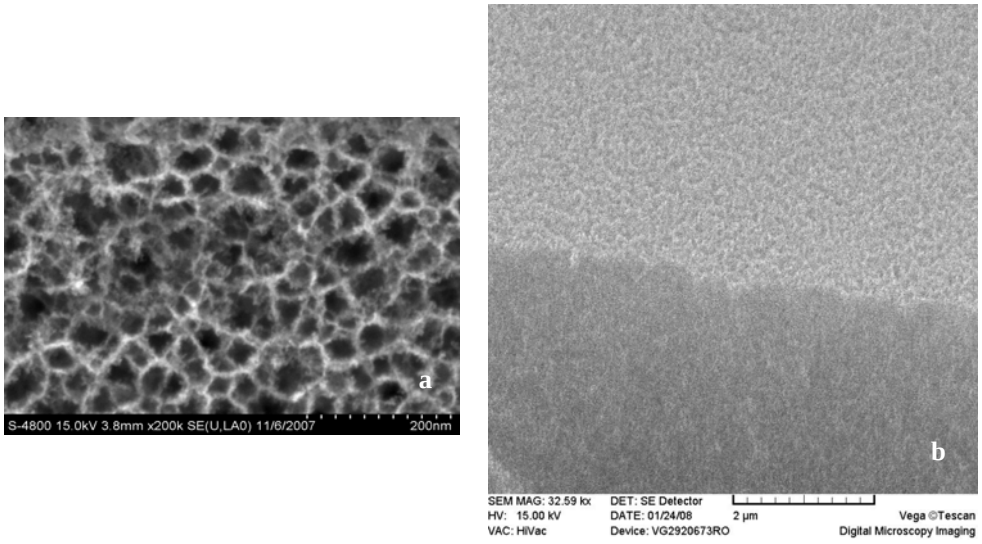

Fig. 4. SEM images of the porous silicon – 20 nm pores size, plan view (a) and (b) cross section.

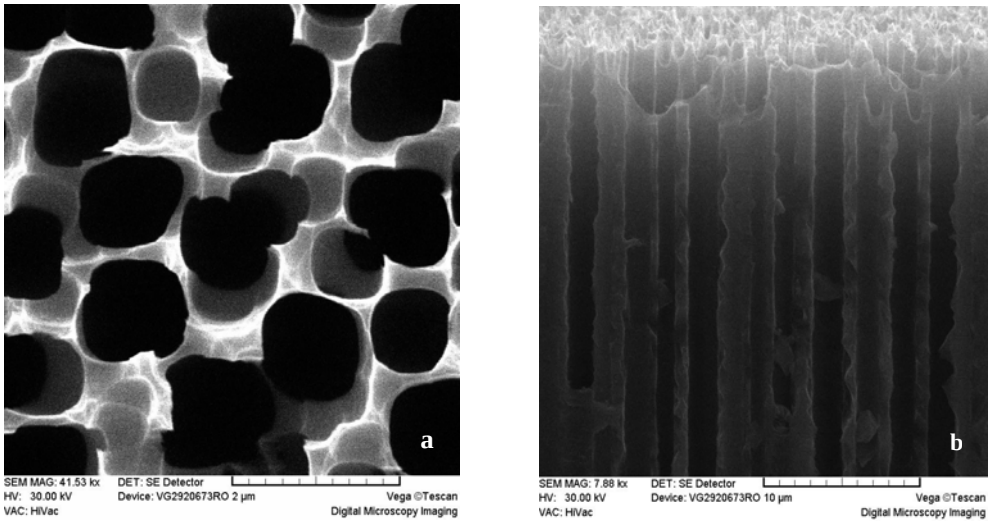

Fig. 5. SEM images of the porous silicon – 500 nm pores size, plan view (a) and (b) cross section.

(iii) Nanoporous silicon membranes were filled with a Nafion 117 solution (purchased from Fluka GmbH- Sigma Aldrich).

Nafion is a sulfonated tetrafluorethylene copolymer [31]. It is the first of a class of synthetic polymers with ionic properties which are called ionomers. The ionic properties of Nafion were created by adding sulfonic acid groups. Nafion combines the physical and chemical properties of its teflon base material with ionic characteristics that give to the final material the following properties: extremely resistance to chemical attack; relatively high working temperatures compared to many polymers (up to 190°C); highly ion-conductivity (it functions as a cation exchange polymer); super-acid catalytic properties; selectively and high permeability to water. Nafion has received a considerable attention as a proton conductor for proton exchange membrane (PEM) fuel cells, known as polymer electrolyte membrane because of its excellent thermal and mechanical stability.

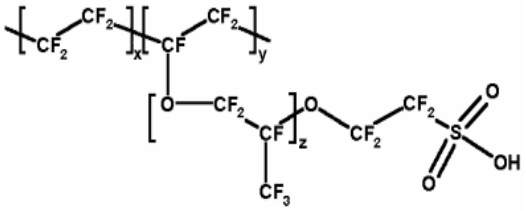

Fig. 6. Nafion chemical structure.

A 5% Nafion solution in aliphatic alcohols and water was applied on nanoporous silicon structures and after solvent evaporation, a nanocomposite

membrane was obtained, Nafion- porous silicon, a membrane with the advantages of the Nafion for proton conduction compatible with an integrated silicon mass production technology.

A first step consists in making porous silicon surface hydrophilic in order to improve the pores filling process. The porous silicon samples are immersed for 10 minutes in boiling Piranha solution, consisting in a mixture of an 80% of pure sulfuric acid and 20% of a 33% aqueous solution of hydrogen peroxide. After making hydrophilic the porous silicon surface, the samples are immersed in a 5% Nafion solution 117 in low aliphatic acids and water, from Fluka GmbH (Sigma-Aldrich group), for 2 hours.

The volume of Nafion solution filled in the porous membrane was calculated according to the estimated volume of the pores. For a membrane surface of 9 mm^2 with 50% porosity, corresponding to 20 nm pores size, the necessary volume is about 4 µl.

The final structure is a nanocomposite nafion- porous silicon membrane, which is characterized using Scanning Electrochemical Microscopy (SEM), in Fig. 7.

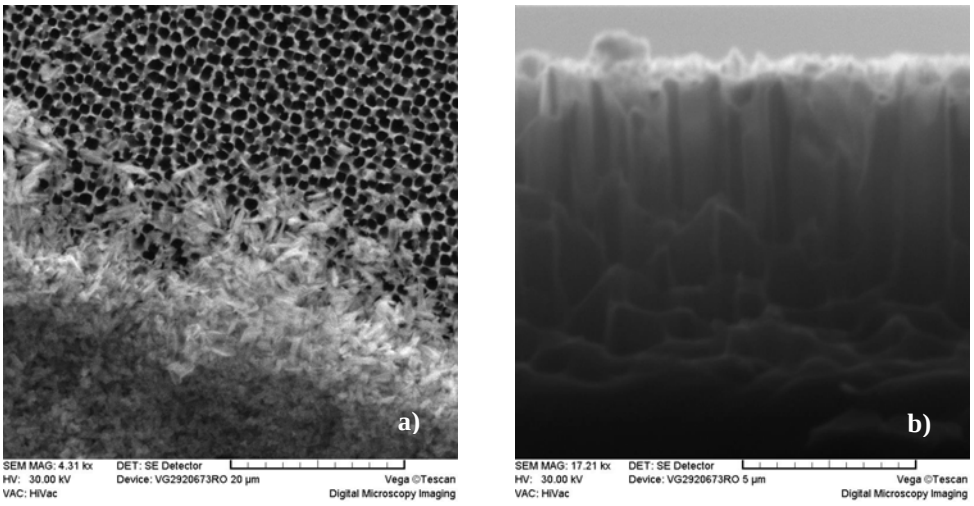

Fig. 7. SEM images of the porous silicon after adding Nafion, plan view (a) and (b) cross section.

Compositional characterization of the Nafion- porous silicon nanocomposite membrane was performed by a Spectrometer IR with Fourier Transformation: FTIR (Fourier – Transform Infrared Spectroscopy), from Tensor 27, produced by the Bruker Optics having the spectral range: 4000–400 cm^{-1} and the resolution: 0.5 cm^{-1}.

In the case of the porous silicon spectra: the presence of the silanol groups is indicated by the wide band centered at the 3500 cm^{-1} (stretching of hydrogen bonded silanol and adsorbed water [32]). The band at 648 cm^{-1} is specific to Si-Si

bond and 893 cm^{-1} can be related to the O_3-SiH, lattice vibration. The 1053.5 cm^{-1} and 843 cm^{-1} wavenumbers are specific to Si-O-Si stretching bond and the band at 2150.4 cm^{-1} is specific to Si-O-H bending.

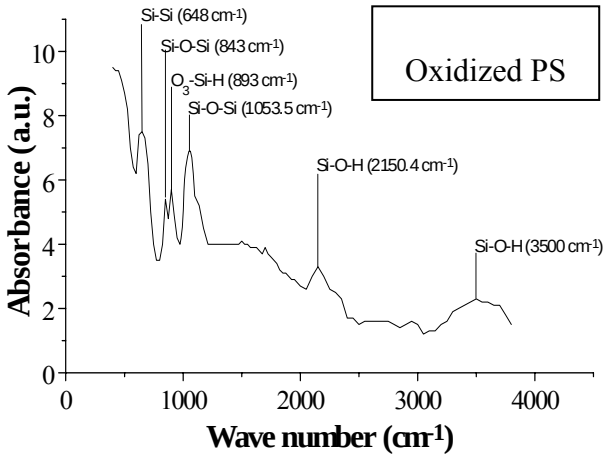

Fig. 8. IR spectra of the porous silicon.

In the case of the 5% Nafion solution spectra, Fig. 9: the band at 1057 cm^{-1} is corresponding to SO_3H group, the bands at 1380 cm^{-1}, 1154 cm^{-1} are correponding to C-F bond, and 959 cm^{-1} is ascribed to characteristic functional groups in plain Nafion [33], especially to C-O-C bond. Also, the bands at 1604 cm^{-1} and 3350 cm^{-1} are specific to OH groups and the 2970 cm^{-1} band is for C-H bond from aliphatic compounds.

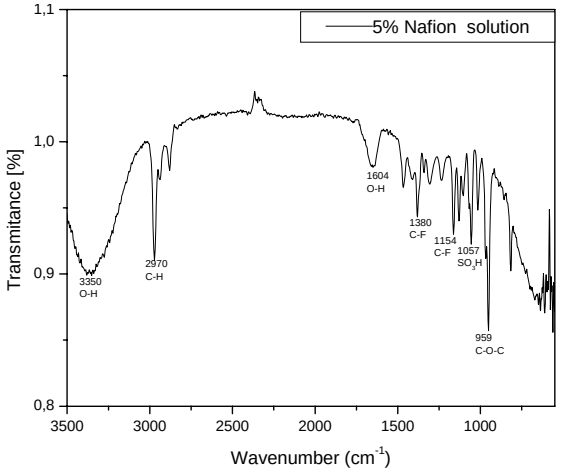

Fig. 9. IR spectra of the 5% Nafion solution.

A comparison between the IR spectra of the two types of Nafion- porous silicon membranes is presented in figure 10. The both IR spectra are similar presenting the specific bands for the Nafion solution (1215 cm^{-1} and 1147 cm^{-1} for C- F bond, 1057 cm^{-1} for the SO_3H group, 970 cm^{-1} for the CO-C bond), and also, the specific bands for porous silicon (1053cm^{-1} and 835 cm^{-1} wavenumbers are specific to Si-O-Si stretching bond, 650 cm^{-1} for Si- Si bond).

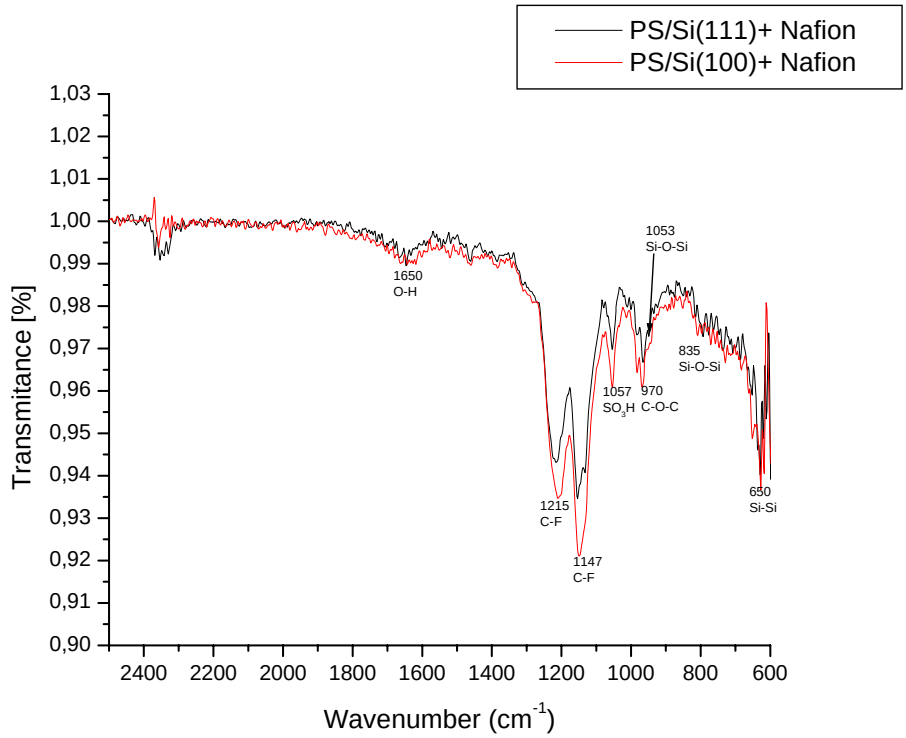

Fig. 10. IR spectra of the two Nafion – porous silicon membranes.

The metallic (Pt) nanoparticles are deposited onto the nafion- porous silicon membranes, using H2PtCl6 (3.5 mM) precursor solution, by chemical impregnation or by electrochemical deposition Pt nanoparticles with about 100 nm sizes have been obtained.

SEM images of the platinum nanoparticles deposited on the nanostructurated surface are presented in Fig. 11.

The SEM images reveals Pt particles with about 100 nm sizes and a porous structure. Due to this structure, these particles are increasing the internal area of the membrane.

The presence of the platinum particles in the nanocomposite membrane increases also, the proton conductivity of the membrane, due to the generation of the water molecules on the Pt particles by the recombination of permeated hydrogen

and oxygen. The platinum deposited on the nanocomposite Nafion-porous silicon membrane acts as catalyst for the electrochemical reactions specific in fuel cell.

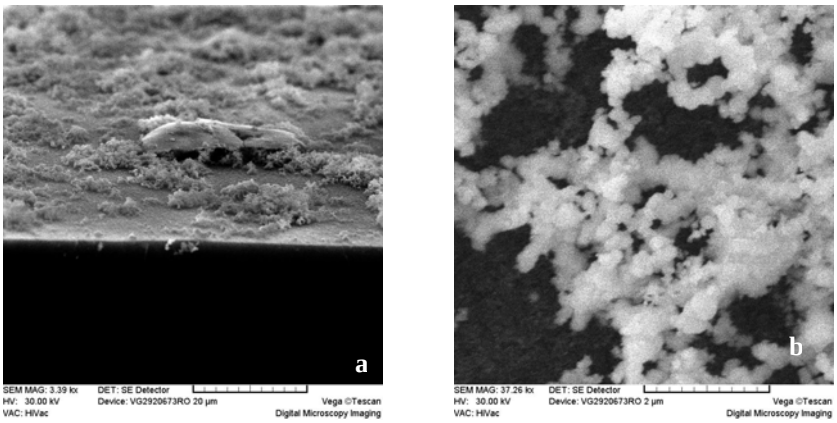

Fig. 11. SEM images of the platinum nanoparticles deposited on the nanostructurated surface, (a) plan and (b) detail view.

3. Conclusions

The technological conditions to obtain a nanocomposite Nafion- porous silicon membrane impregnated with platinum nanoparticles on two *n* types silicon (111) and (100) were described.

The membrane morphology investigated by SEM and structural characterization performed by FTIR reveals that the experimental structures are suitable for using as *proton exchange membrane* (PEM).

It was demonstrated a new way of making porous silicon membrane filled with a Nafion-117 solution for fuel cell applications.

Its main advantage is the compatibility with the silicon micromaching techniques which allows cell miniaturization.

Acknowledgements. The authors gratefully acknowledge the support of the Romanian Ministry of Education and Research through the contract no. 11-024 (PN II Program) and respectively, through the contract no. 883 (CNCSIS Program).

References

[1] *International Roadmap for Semiconductors*, executive summary, Technical report, SIA, Retrieved from http://public.itrs.net/, 2003, 57.

[2] CHEN C. Y. *et al.*, *Performance of an air-breathing direct methanol fuel cell*, J. Power Sources, **123**, 2003, pp. 37–42; *Hydrogen*, Fuel Cells & Infrastructure Technologies Program Multi-Year Research, Development and Demonstration Plan, U.S. Department of Energy, October 2007.

[3] SHAH K. *et al.*, *Novel microfabrication approaches for directly patterning PEM fuel cell membranes*, J. Power Sources, **123**, 2003, pp. 172–181.
[4] PICHONAT T. *et al.*, *Development of porous silicon-based miniature fuel cells*, J. Micromech. Microeng., **15**, 2005, S179–84.
[5] GOLD S. *et al.*, *Acid loaded porous silicon as a proton exchange membrane for micro-fuel cells*, *J. Power Sources,* 135, 2004, 198–204.
[6] YAMAZAKI Y., *Application of MEMS technology to micro fuel cells*, Electrochim. Acta 50, 2004, 663–6.
[7] SHAH K. *et al.*, *A PDMS micro proton exchange membrane fuel cell by conventional and non-conventional microfabrication techniques*, Sensors Actuators B, **97**, 2004, pp. 157–67.
[8] CHANG H. *et al.*, *Materials and processes for small fuel cells*, Solid State Ion., 2002, **148**, p. 601.
[9] CHAN S. H. *et al.*, *Development of a polymeric micro fuel cell containing laser-micromachined flow channels*, J. Micromech. Microeng., 2005, **15**, 231–6.
[10] ARICÓ A. S., SRINIVASAN S., ANTONUCCI V., 2001, *DMFCs: From Fundamental Aspects to Technology Development*, Fuel Cells, **1–2**, pp. 133–161.
[11] SHIMIZU T. *et al.*, *Design and fabrication of pumpless small direct methanol fuel cells for portable applications*, J. Power Sources, **137**, 2004, pp. 277–83.
[12] HAN J. *et al.*, *Direct methanol fuel-cell combined with a small back-up battery*, J. Power Sources, **112**, 2002, p. 477.
[13] BLUM A. *et al.*, *Water-neutral micro direct-methanol fuel cell (DMFC) for portable applications*, J. Power Sources, 2003, **117**, pp. 22–5.
[14] YEN T. J. *et al.*, *A micro methanol fuel cell operating at near room temperature*, Appl. Phys. Lett., 2003, **83**, pp. 4056–8.
[15] WOZNIAK K. *et al.*, *A micro direct methanol fuel cell demonstrator*, J. Micromech. Microeng., 2004, **14**, pp. S59–S63.
[16] LU G. Q. *et al*., *Development of micro direct methanol fuel cells for high power applications*, J. Power Sources, 2005, **144**, pp. 141–5.
[17] HEBLING C., *Portable Fuel Cell Systems*, Fuel Cell Bulletin, **46** (7), 2002, pp. 8–12.
[18] LU G. Q., WANG C. Y., YEN T. J., ZHANG X., *Development and Characterization of A Silicon-Based Micro Direct Methanol Fuel Cell*, Electrochim. Acta, **49** (5), 2004, p. 821.
[19] KELLEY S. C., DELUGA G. A., SMYRL W. H., *Miniature Fuel Cells Fabricated on Silicon Substrates*, AIChE J. **48** (5), 2002, p. 1071.
[20] MOTOKAWA S., MOHAMEDI M., MOMMA T., SHOJI S., OSAKA T., *MEMS-Based Design and Fabrication of a New Concept Micro Direct Methanol Fuel Cell (μ-DMFC)*, Electrochemistry Communications, **6**, 2004, pp. 562–565.
[21] YU J., CHENG P., MA Z., YI B., *Fabrication of Miniature Silicon Wafer Fuel Cell with Improved Performances*, J. Power Sources, **124**, 2003, pp. 40–46.
[22] BUNKER C. E., MA B., SIMMONS K. J., ROLLINS H. W., LIU J., MA J., MARTIN C. W., DES MARTEAU D. D., SUN Y., *Steady-State and Time-Resolved Fluorescence Spectroscopic Probing of Microstructures and Properties of Perfluorinated Polyelectrolyte Membranes*, Journal of Electroanalytical Chemistry, **459**, 1998, pp. 15–28.
[23] MAYNARD H. L., MEYERS J. P., J. Vac. Sci. Technol. B, **20**, 2002, p. 1287.
[24] YU J. R., CHENG P., MA Z. Q., YI B. L., Electrochim. Acta, **48**, 2003, p. 1537.
[25] PAVIO J., BOSTAPH J., FISHER A., HALLMARK J., MYLAN B. J., XIE C. G., Advancing Microelectron., **29**, 2002, p. 1.
[26] BLUM A., DUVDEVANI T., PHILOSOPH M., RUDOY N., PELED E., J. Power Sources, **117**, 2003, p. 22.
[27] LU G. Q., WANG C. Y., *Electrochemical and Flow Characterization of a Direct Methanol Fuel Cell*, submitted for publication.
[28] STEWART M. P., BURIAK J. M., Adv. Mater., **12** (12), 2000, p. 859.
[29] HERINO R., in: L.T. Canham (Ed.), *Properties of Porous Silicon*, INSPEC, London, 1997.

[30] SIMION M., KLEPS I., NEGHINA T., ANGELESCU A., MIU M., BRAGARU A., DANILA M., CONDAC E., COSTACHE M., SAVU L., *Nanoporous silicon matrix used as biomaterial*, Journal of Alloys and Compounds, Volumes **434–435**, pp. 830–832, 2007.
[31] MIU M., KLEPS I., PAVESI L., CRACIUNOIU F., IGNAT T., DINESCU A., SIMION M., *Nanostructured silicon for optical biosensors*, Proceedings of the 30th International Semiconductor Conference–CAS, 15–17 Oct., 2007, Sinaia, Romania, pp. 345–350.
[32] CHURCH S., *Del. firm installs fuel cell*, The News Journal, January 6, 2006, p. B7.
[33] GORBANYUK T. I., EVTUKH A. A., LITOVCHENK V. G., SOLNEV V. S.,. PAKLOV E. M, Thin Solid Films, **495**, 2006, pp. 134–138.
[34] LUDVIGSSON M., LINDGRAIN J., TEGENFELDT J., Electrochim. Acta, **45**, 2000, p. 2267.

Gold Nanoparticles for SEIRS

Teodora IGNAT[1], Fouad MAROUN[2], Phillippe ALLONGUE[2]

[1]National Institute for Research and Development in Microtechnologies (IMT-Bucharest), Laboratory of Nanotechnology, IMT-Bucharest, Romania, 077190

[2]Laboratoire PMC, CNRS-Ecole Polytechnique, 91128 Palaiseau, France

Abstract. An important application in the emerging field of plasmonics is the development of substrates capable of providing large electromagnetic enhancements for surface-enhanced spectroscopies. In this work, gold nanoislands were deposited on a semiconductor surface according to a special arrangement which increases the infrared sensitivity. The high sensitivity of surface enhanced infrared absorption allows the observation of changes in the chemical nature of the carboxyl head group of the 11-mercaptoundecanoic acid during pH changing. An analysis of the vibrational spectra suggests that by changing the pH, the carboxyl head group of the self assembled monolayer of thiol molecule can be deprotonated and re-protonated after adsorption without losing the adsorbed 11-mercatoundecanoic molecule.

1. Introduction

Infrared spectroscopy (IR) allows the study of electrochemical reactions by probing the chemical species to the surface or near the surface electrodes. Unfortunately, the sensitivity is much lower in the case of metals as in the case of semiconductors. In particular, the use of attenuated-total-reflection (ATR) geometry which allows a wining of at least a 10 factor in sensitivity is applicable only in the case of semi-conductors. The low sensitivity in the case of metals is therefore a major handicap when it comes to discussing electrochemical and intermediary reactions present in quantities below the monolayer. The resonant excitation of plasmons in metallic nanostructures can provide large field enhancements on the surfaces of metals, and thus providing dramatic increases in the detected spectroscopic signals for molecules adsorbed on their surfaces [1]. The most widely used surface enhance spectroscopy (SES) is surface enhanced Raman scattering (SERS), where the electromagnetic enhancement factor is proportional to the fourth power of the incident field on the molecule [2]. Recently, the interest is focused in another type of SES, surface enhanced infrared absorption (SEIRA) [3–6]. Even the electromagnetic enhancement in SEIRA is only proportional to the square of the electro-

magnetic field, SEIRA plays important role in the field of chemical and biological sensing since it probes dipole-active vibration modes, and possesses sufficient sensitivity to detect weak signals on the level of monolayer.

It is well known that the maximum electromagnetic enhancement in a plasmonic nanostructure occurs for resonant excitations of the plasmons in the visible and UV regions of the spectrum [7–10]. So, designing and fabricating of nanostructures with reproducible plasmon resonance across the broad of IR region of the spectrum come as primary reason when thinking why SEIRA has received much less attention than SERS.

However, the plasmon resonances of metallic nanoparticles are strongly dependent on structure and composition [11].

In this work, we are studying gold metal nanoislands deposited on the surface of a semiconductor according to a special arrangement which increases the infrared sensitivity. Indeed, it was observed that the deposition in the form of a dense arrangement of nanoislands on an insulating substrate or semiconductor can increase the IR electromagnetic field on its surface. The origin of this increase is the presence of collective electromagnetic resonance of metal islands in the IR, while the resonance of an isolated island is generally in the visible. The gap resonance to the IR is due to the collective character and is even larger when the interactions between islands are bigger. To facilitate the understanding of this phenomenon of IR increased sensitivity, we have prepared a regular arrangement of metal nanoislands. In this paper, we show first of all how it is possible to prepare by electrochemical deposition a regular network of gold nano-islands on silicon. Then have been studied by IR spectroscopy adsorption and modification of a thiol molecule, 11-mercaptoundecanoic acid on the surface of gold nanoislands. We also could highlight that, the protonation and reprotonation of the carboxyl head group of the 11-mercaptoundecanoic acid after exposure in a solution of pH = 8 and pH = 2, can be made without losing the thiol molecule signal during pH changing.

2. Experimental

Silicon samples were cut from 1 to 10 Ωcm (111) wafers (n-type, P doped) with a miscut angle of 20 precisely oriented towards <11-2>. The careful adjustment of the miscut orientation is necessary to obtain straight and parallel monatomic steps terminated by monohydride sites. Prior to etching, samples were cleaned in (98% H_2SO_4)/(30% H_2O_2) 2:1 mixture and rinsed with bidistilled water. The H-termination was obtained by chemical etching in oxygen-free 40% NH_4F to avoid the formation of triangular etch pits on the (111) terraces. 50 mM $(NH_4)_2SO_3$ was used as oxygen scavenger. A final rinse in bidistilled water was performed after etching. An InGa eutectic on the back side was performed to assure the ohmic contact. The sample was then mounted with its lateral edges protected by an electrolytic scotch tape to expose only the well-defined (111) face to solution.

Gold was deposited from 0.1 mM $KAu(CN)_2$ + 0.2 mM NaCN + NaOH 2M, using a three-electrode electrochemical cell connected to a potentiostat. The reference electrode was a mercury sulfate electrode (MSE) and all potentials are quoted against this reference of potential. The counter electrode was an Au grid.

For the preparation of 11-mercaptoundecanoic acid monolayers, the gold substrates were immersed in a 2 mM aqueous solution for a period of 24h.

3. Results and discussion

To obtain a regular system of gold nanoisland, we start from a hydrogenated Si (111) surface prepared in a NH_4F solution. This treatment, associated with a particular choice of disorientation of the crystal against (111) plans, provide a Si surface, formed by plane terraces without pitting, separated by monoatomiques and parallel steps. Obtaining a Si surface with parallel steps is a necessary condition for obtaining a regular system of gold nano-islands.

In order to improve the size dispersion of the gold islands at steps, one must decouple the nucleation stage from the growth by using 'double-potential-step electrodeposition'. In this procedure, the first step of potential controls the density of nuclei along the silicon steps and the second one allows the growth of the existing nuclei. In the case of gold growth on stepped H–Si(111), the optimum sequence is applying −2 V for few seconds(Fig. 1a), to promote strong hydrogen evolution reaction (HER) at the silicon steps and saturate them with gold nuclei, and then −1.5 V for several tens of seconds, to grow the gold islands without nucleating new islands[12].

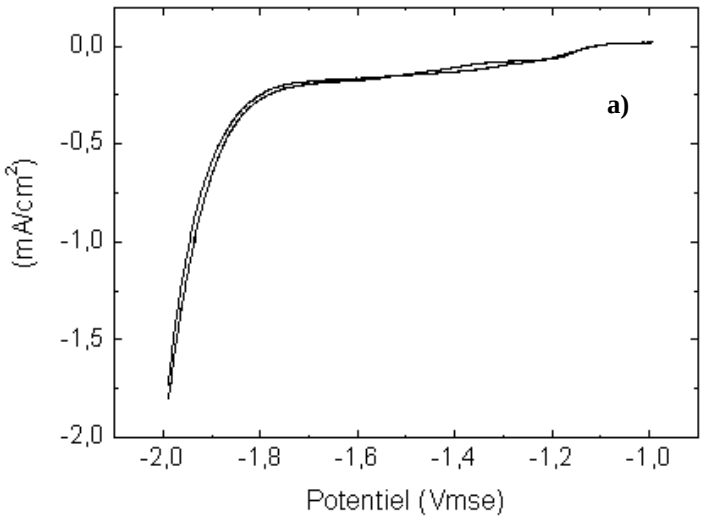

Fig. 1a.

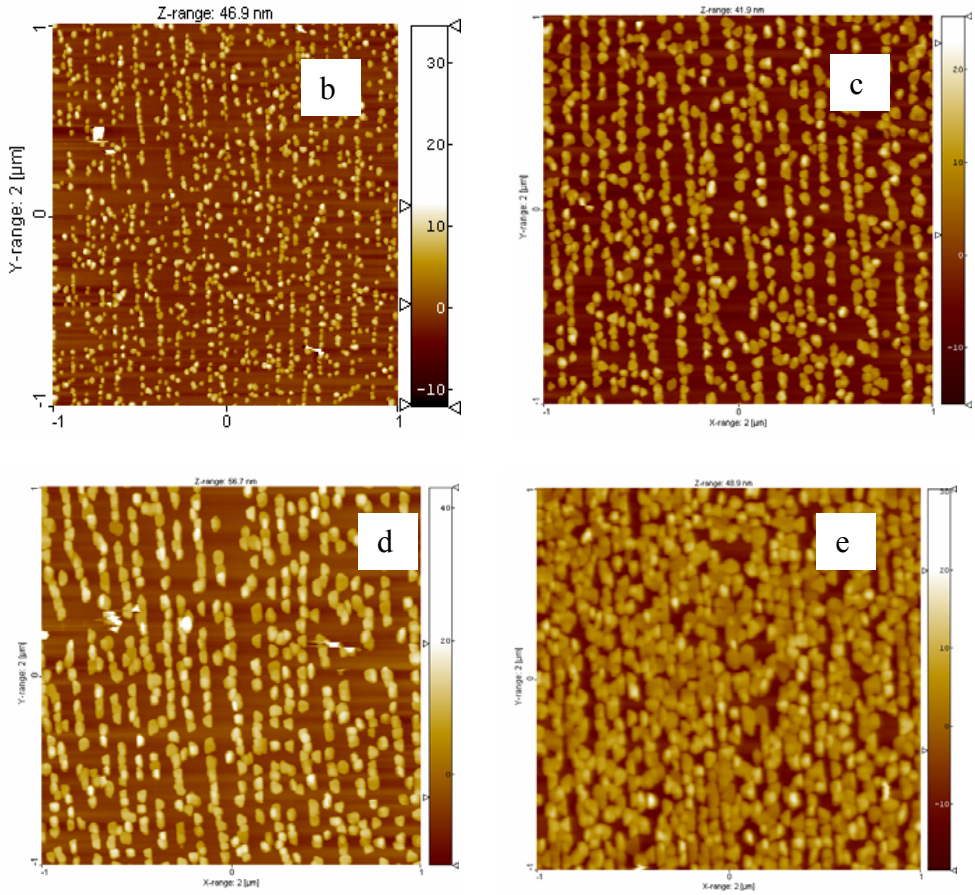

Fig. 1. a) Potential *vs.* current density for gold nano-island deposition; AFM images. Different gold deposits: b) 4 s at −2V and 10 s at −1.5 V; c) 4 s at −2V and 30 s −1.5 V; c) 4 s at −2V and 50 s at −1.5 V; d) 4 s at −2V and 100 s at −1.5 V.

In the b-e images gold nanoislands are separate by an average inter-islands distances of 118 nm in the case of b), 98 nm c), 90 nm d) and 50 nm e).

A first way to characterize the optical properties of gold nanoislands is to compare the absorbance of different deposits in function of the regularity of the Si steps and in function of the polarization of the incident light.

In Fig. 2 the fabricated deposits consist of rather monodisperse gold islands with 2×10^5 islands cm^{-1} along the steps, which is equivalent to an average distance of 50 nm between the centers of islands.

We observed that the absorbance in function of the wavenumber for the same gold deposit depends on the orientation of the polarization of light rather than the Si steps. The absorbance is always greater when the polarization of light is parallel to the board steps and smaller when it is perpendicular to the steps (Fig. 2c). This is

understandable when Au network is anisotropic with a density of nano-islands along the upper steps of 25% (in deposits from Fig. 2) perpendicular to the steps (which is identical to the density marches because of the selective nucleation). What is remarkable is that the absorbance is very sensitive to the regularity of gold nano-islands lines, so the regularity of the steps. Indeed, the two surfaces from Fig. 2 have the same density of steps but with a more regular spacing for Fig. 2b than for Fig. 2a. In addition, these two surfaces have the same total density and correspond to the same quantity of electrodeposited gold. The difference in average size of gold nano-islands comes from the shape of the AFM tip. This difference in regularity of the inter-steps spacing induces significant differences in absorbance spectra (Fig. 2c), the sample with a more regular spacing being more absorbent.

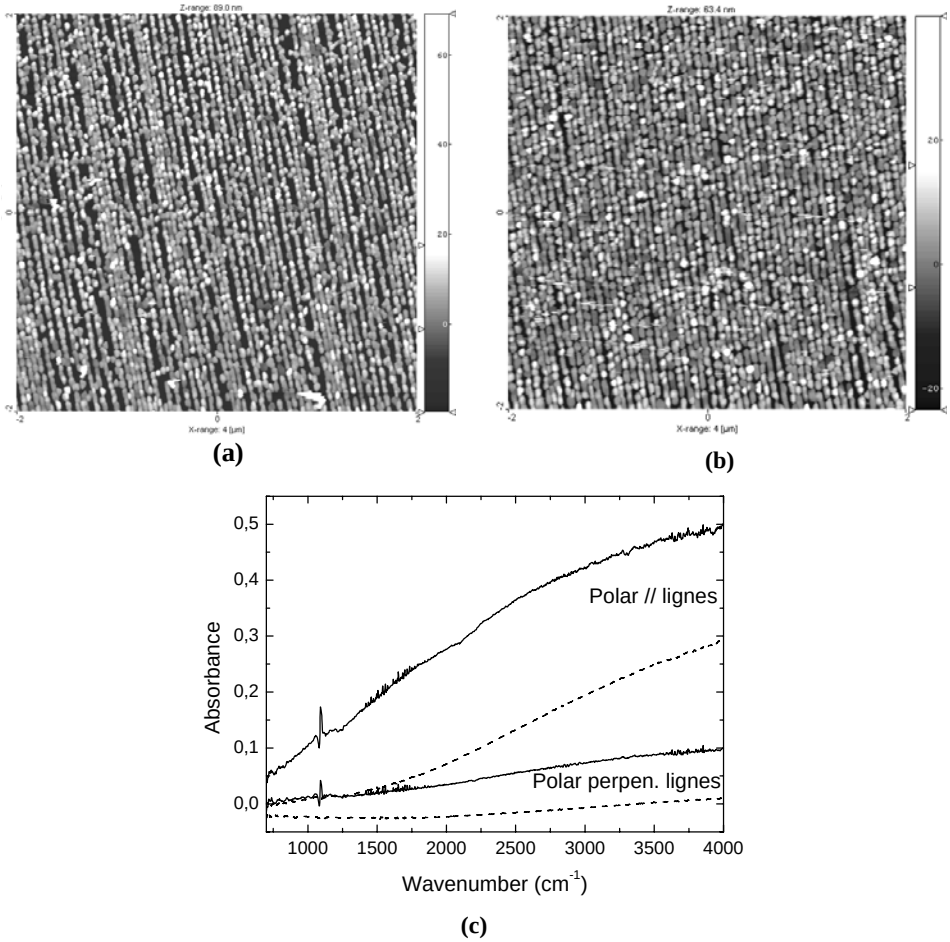

Fig. 2. AFM images(4 μm×4 μ m): (a) and (b) 4 s at −2V and 100 s at −1.5 V; (c) infrared absorption spectra corresponding to the two gold deposits, dotted line for the image (a) and plain line for the image (b).

In order to investigate the enhancement of infrared sensitivity 11-mercaptoundecanoic acid from 1 mM solution in ethanol was adsorbed on the Au/Si samples.

Previously, the gold nano-island surface was cathodic treated in an acid solution in order to desorb cyanide molecule adsorbed on the surface of gold deposits. The presence of characteristics peaks of the11-mercaptoundecanoic acid in the IR spectra, at 2845 and 2913 cm^{-1} corresponding to the alkyl chains and CH_2 groups, and at 1710 cm^{-1} associated with the vibrations of the C=O carboxylic group (Fig. 3), demonstrates the absorbance of the11-mercaptoundecanoic acid on the surface of gold nano-islands. In order to evaluate the enhancement in IR sensitivity, we compared the intensity of the specific 11-mercaptoundecanoic acid peaks (1710 cm^{-1}, 2845 cm^{-1} and 2913 cm^{-1}) with those peaks of a monolayer of undecanoic acid grafted directly on silicon surface (Fig. 3, the top spectrum). For a 100 s gold deposit time and for a polarization of the light parallel to the steps direction, the peak area of C=O (0.148) at 1710 cm^{-1} is 20 times greater and peaks area of CH_2 (0.029) is 7 times greater than in the case of undecilenic acid molecule grafted directly on silicon. This increase is almost 2 times greater for a polarization of light parallel to the gold nano-island lines compared to the light polarization perpendicular on the gold nano-island. This comes from the largest proximity of gold nano-islands following this direction. This system open the way for a quantitative study of the effect of enhancement depending on the morphology of metal deposition.

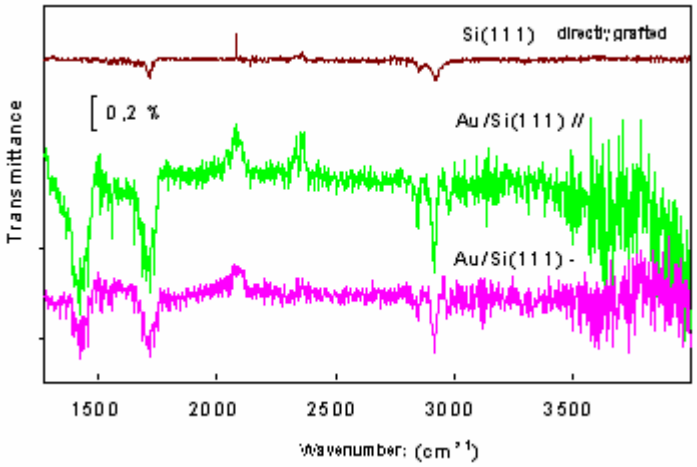

Fig. 3. Infrared spectra, of a silicon surface grafted with 11-undecylenic acid (upper spectrum) and a surface Au /Si functionalized with 11-mercaptoundecanoic acid (the bottom two spectra corresponding to two directions the polarization of light compared to the lines of gold).

This gold nano-islands /silicon structure allow us to demonstrate the effect of deprotonation and reprotonation of carboxyl head group of the self assembled

monolayer of thiol molecule after exposure to an alkaline (pH = 8) or acidic (pH = = 2) solution. The IR emphasized with great sensitivity these changes; two symmetrical peaks corresponding to the 1423 cm^{-1} and antisymmetric (1555 cm^{-1}) vibrations of the specific COO-groups are observed (Fig. 4). These experiences show the possibilities of using this type of gold deposits to study by infrared spectroscopies chemical or electrochemical reactions on the gold surface.

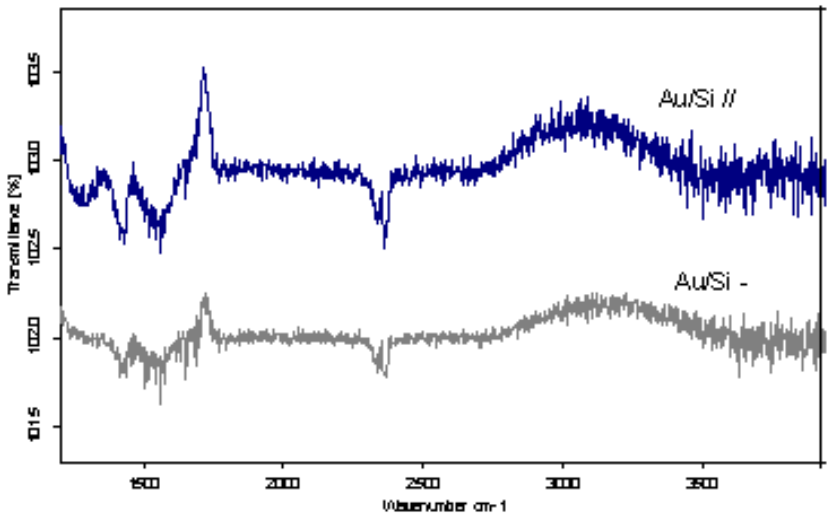

Fig. 4. IR spectra of deprotonated 11-mercaptoundecanoic acid for the two directions of the polarization of light.

4. Conclusions and perspectives

We have shown that IR-resonant gold nanoislands on Si are excellent substrates for SEIRA, producing high quality spectra across a broad 700–3500 cm^{-1} range required for vibrational spectroscopy. The analysis of the infrared signal of self-assembled monolayer of 11-mercaptoundecanoic acid on gold nano-islands have shown large SEIRA enhancement factors, in the 100 range, by using these substrates. These results open up new opportunities for the development of SEIRA as a reliable and highly useful technique for molecular spectroscopy, with numerous applications in chemical/electrochemical and biochemical sensing.

Acknowledgments. The authors gratefully acknowledge the support of the Marie Currie Fellow "*Nanoelectrochemistry: from the synthesis of nanomaterials to functionality – Functionalization of silicon surfaces for bioelectronics*" and to the Romanian Ministry of Education and Research through the contract no. ID_884/2007(PNII – IDEI programme), TD 437/2007 (CNCSIS grant).

References

[1] JIANG X., ATAKA K., HEBERLE J., J. Phys. Chem. C, 2008, **112**, pp. 813–819.
[2] JOHANSSON P., XU H. X., KALL M., *Surface-Enhanced Raman Scattering and Fluorescence Near Metal Nanoparticles*, Phys. Rev. B, 2005, **72**, p. 035427.
[3] ATAKA K., HEBERLE J., *Biochemical Applications of Surface-Enhanced Infrared Absorption Spectroscopy*, Analyutical and Bioanalytical Chemistry, 2007, **388**, pp. 47–54.
[4] GIBSON J. W., JOHNSON B. R., *Density-Matrix Calculations of Surface Enhanced Raman Scattering for p- Mercaptoaniline on Silver Nanoshells*, J. Chem. Phys., 2006, **124**, p. 064701.
[5] JANESKO B. G., SCUSERIA G. E., *Surface Enhanced Raman Optical Activity of Molecules on Orientationally Averaged Substrates: Theory of Electromagnetic Effects*, J. Chem. Phys., 2006, **2006**, p. 124704.
[6] GOUDE Z. E., LEUNG P. T., *Surface Enhanced Raman Scattering from Metallic Nanoshells with Nonlocal Dielectric Response*, Solid State Commun., 2007, **143**, pp. 416–420.
[7] SOUMEN B., SUROJIT P., *Controlled interparticle spacing for surface-modified gold nanoparticle aggregate Langmuir*, 2008, **2**4, 10, pp. 5562–5568.
[8] OUBRE C., NORDLANDER P., *Optical Properties of Metallodielectric Nanostructures Calculated using the Finite Difference Time Domain Method*, J. Phys. Chem. B, 2004, **108**, pp. 17740–17747.
[9] JAIN P. K., EL-SAYED M. A., *Universal Scaling of Plasmon Coupling in Metal Nanostructures: Extension from Nanoparticle Pairs to Nanoshells*, Nano Lett., 2007, **7**, pp. 2854–2858.
[10] KELLY K. L., CORONADO E., ZHAO L. L., SCHATZ G. C., *The Optical Properties of Metal Nanoparticles: The influence of Size, Shape, and Dielectric Environment*, J. Phys. Chem. B, 2003, **107**, pp. 668–677.
[11] ALLONGUE P., MAROUN F., *Self-ordered electrochemical growth on single-crystal electrode surfaces*, J. Phys.: Condens. Matter., **18**, 2006, pp. S97–S114.

Fabrication of Periodic Arrays of Metallic Nanoholes and their Structural and Plasmonic Properties

V. CÂNPEAN, S. AŞTILEAN

Nanobiophotonics Laboratory, Institute for Interdisciplinary
Experimental Research and Faculty of Physics, Babes-Bolyai University,
M. Kogalniceanu 1, 400084 Cluj-Napoca, Romania
E-mail: vcanpean@phys.ubbcluj.ro

Abstract In this work we implemented a new variant of classical nanosphere lithography that combines the reactive ion etching (RIE) of self-assembled film of polystyrene nanospheres with metal deposition to fabricate gold films with periodic arrays of nanoholes. This method allows us to introduce the control over the array periodicity by choosing the initial diameter of spheres, the metallic hole diameter by RIE etching time as well as the film thickness. The films morphology was characterized by AFM whereas their optical properties were measured using optical fibre microreflectometry and transmission. Our objective is to understand how the structural parameters (hole diameter) interplay onto the plasmonic response of films in order to enhance the light transmission as well as plasmonic local field.

1. Introduction

The desire to use and control photons in a manner analogous to the electrons in solids has generated a great interest on the study of nanoscale materials. Among them, nano-sized plasmonic materials have attracted numerous experimental and theoretical studies due to their intriguing optical properties, properties determined by the surface plasmons. A surface plasmon (SP) is a collective oscillation of free electrons inside a metal-dielectric surface. According to Maxwell's theory, electromagnetic surface waves can propagate along a metallic surface or on metallic films. Their dispersion relation ω(k) lies right of the light line which means that the surface plasmons have a longer wavevector than light waves of the same energy and thus they can't be directly excited using light. By imposing a periodic array of nanoholes upon a metallic film the light and plasmons wavevector can be matched through the momentum of the periodic array, satisfying Bragg equation:

$$\vec{k}_{sp} = \vec{k}_x \pm i\vec{G}_x \pm i\vec{G}_y \,, \tag{1}$$

where $\vec{k}_{sp}$ is the surface plasmon wave vector, $\vec{k}_x$ is the component of the incident wave vector that lies in the plane of the sample, $\vec{G}_x$ and $\vec{G}_y$ are the reciprocal lattice vectors.

A fundamental constrain in manipulating light at nanoscale is the extremely low transmission through subwavelength apertures. According to the theoretical results predicted by Bethe [1], transmission through a single aperture smaller than the wavelength of light scales as:

$$T \propto \left(\frac{r}{\lambda}\right)^4, \tag{2}$$

where r is the radius of the subwavelength aperture and λ is the wavelength of light. Accordingly, for a hole of 150 nm diameter, one expects transmission efficiency on the order of 10^{-3}. In 1998, Ebbesen and co-workers [2] found that the transmission of light through a periodic array of subwavelength holes is drastically enhanced. Using a silver film with periodic array of holes with diameter of 150 nm, the authors observed an enhanced transmission with efficiencies about 1000 times higher than that expected. This result has generated numerous theoretical [3-6] and experimental studies [7–9]. Apart from its fundamental interest, this extraordinary transmission effect has potential applications in a number of areas, ranging from biophotonics to near-field microscopy, omnidirectional absorbers and sensing.

In this work we fabricated subwavelength metallic holes arrays by implementing a nano-lithographic method inspired from the classical nanosphere lithography [10], in which we combine the self-assembling of polystyrene nanospheres with reactive ion etching (RIE) and metal deposition and studied the structural and plasmonic properties of the fabricated structures. This method allows us to introduce the control over the array periodicity by choosing the initial diameter of spheres, the metallic hole diameter by RIE etching time as well as the film thickness. The transmission and reflectivity spectra are characterized by well-defined maxima and minima of which the positions are determined by the geometry of the holes. Transmission with up to 3 times enhancement was obtained, with intensities highly dependent upon the holes diameters. Due to the high sensitivity of the plasmon resonances involved in this process, the fabricated structures are ideal multifunctional plasmonic substrates for Surface Plasmon Resonance (SPR) and Surface Enhanced Raman Spectroscopy (SERS) sensors.

2. Experimental section

Our strategy to fabricate periodic arrays of nanoholes in gold films consists of three major steps: convective assembly of polystyrene spheres on glass substrate (Fig. 1a), reactive ion etching with oxygen to tailor the sizes of the polystyrene beads (Fig. 1b) and gold film deposition and beads removal by sonication in toluene (Fig. 1c).

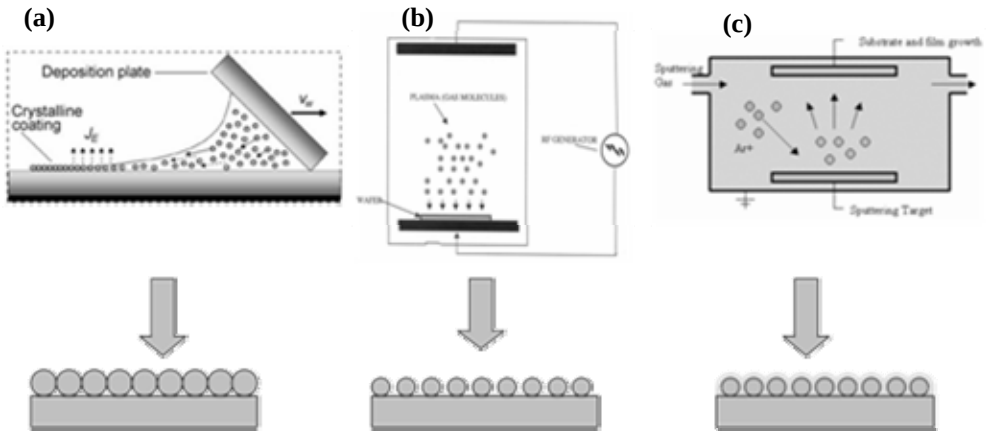

Fig. 1. Metallic nanohole array fabrication process: **(a)** Convective assembly; **(b)** Reactive Ion Etching; **(c)** Metal deposition.

Thorough cleaning of glass microscope slides was used to ensure hydrophilic surfaces. This process consisted in several steps: first the glass slides were sonicated in isopropylic alcohol for degreasing. After carefully rinsing the slides in ultra pure water, they were boiled in Piranha solution, followed by cleaning in ultra pure water and drying. Then a colloidal solution of polystyrene beads of 0.450 μm ± 0.011 μm in diameter was deposited on these samples. In our implementation of the convective assembly process used to deposit the coatings, a droplet of liquid suspension (~10 μL) was injected into the wedge formed between two inclined glass slides, a sample substrate and a deposition plate, where it was entrapped by capillarity. The liquid meniscus was withdrawn horizontally across the substrate by translating the deposition plate at controlled speeds. All coatings were deposited at ambient laboratory temperature, using a closed glass chamber to maintain a constant humidity. The diameters of the polystyrene beads coated substrates were then tailored by RIE with oxygen using a modified DC/RF sputtering device, where the coated substrate was used as target, thus the oxygen ions being accelerated towards the substrate. The etching process preceded at a pressure of 60 mTorr and a radio frequency (RF) power of 10W, with various etch periods (20, 25, 35, 45 s). After 45 s of etching, the entire array of spheres was eliminated from the substrate. Over the tailored array of nanospheres, a thin gold film of 40 nm thickness was deposited by thermal evaporation at a pressure of $3 \cdot 10^{-6}$torr.

3. Results and discussion

Figure 2 shows typical AFM images of the structures through the fabrication process steps. After the convective assembly of the spheres in step 1, AFM data (Fig. 2a) showed that the polystyrene array exhibited ordered hexagonal close-

packed arrangement over large areas. The period of the deposited layer is determined by the diameter of the spheres of 450 nm. The tailoring of the size of the polystyrene spheres array by oxygen RIE thinned the diameter of the spheres (Fig. 2 b). After the oxygen RIE, the separation between spheres increased as the size of the spheres decreased. RIE exposures of 45 s or longer resulted in total removal of the polystyrene spheres and thus they were not used in our experiment. After metal deposition and polystyrene sphere removal by sonication in toluene, a gold film with periodic array of nanoholes was left on the glass slide. The diameter of the holes was determined by the diameter of the tailored polystyrene spheres, whereas the period of the array of holes was determined by the initial diameter of the spheres, which was not affected by the etching process.

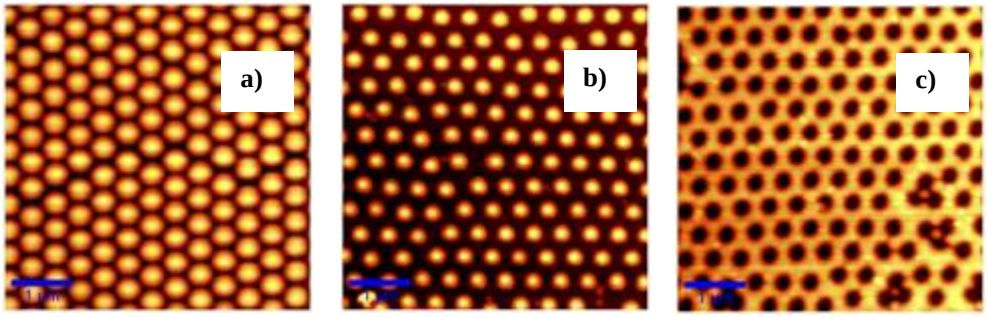

Fig. 2. AFM images of **a)** 450 nm PS monolayer; **b)** array of etched PS; **c)** metallic nanohole array.

Figure 3 depicts the optical transmission spectra of gold film perforated with an array of holes with diameters of 180 nm and 280 nm together with the transmission of reference flat film.

For a thin, flat film of 50 nm thickness, the transmission band around 500 nm originates from bulk optical properties of metal and can be explained in terms of electron transitions and recombination between the filled *d*-bands in metal and the Fermi level in conduction band [11]. However the transmission features of perforated films should be assignable to a contribution from the excitation of free electrons involved in surface plasmonic waves. It is meaningful that the transmission spectra of the perforated film with holes of 280 nm diameter exhibit maximum transmission which is of 36% at 564 nm (relatively to perfect transmissible reference), while for the film with holes of 180 nm diameter the maximum transmission of 33% is achieved at 553 nm. This leads to an increase of the transmission of 8.6 times for the holes of 280 nm diameter and 7.7 times for the holes of 180 nm diameter compared to the transmission of the flat gold film.

The excitation of surface plasmon is demonstrated also in Fig. 4 where is presented the optical reflectivity spectra of the holes array with diameters of 180 and 280 nm, at normal incidence together with that of a flat gold film.

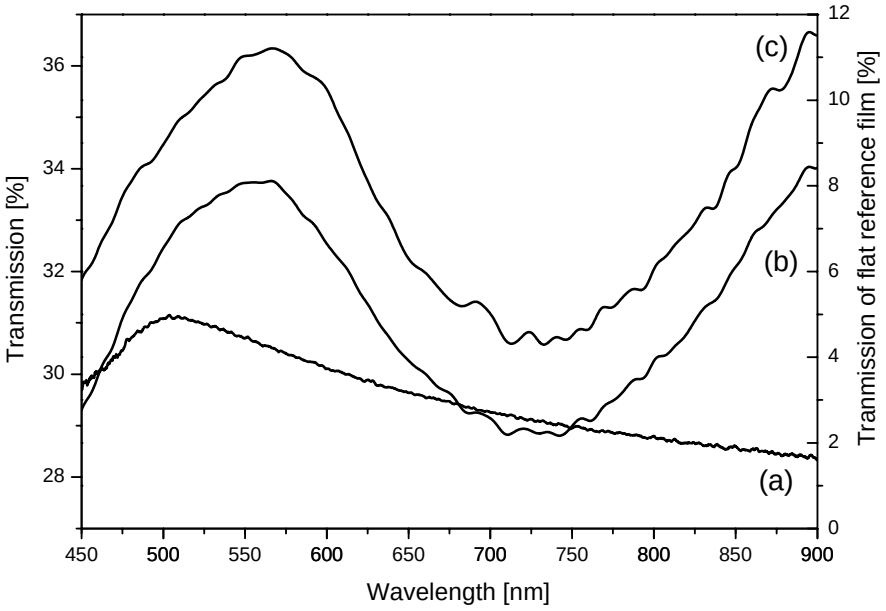

Fig. 3. Optical transmission spectra of gold film flat (a) and perforated with an array of holes of 180 nm (b) and 280 nm (c) diameter.

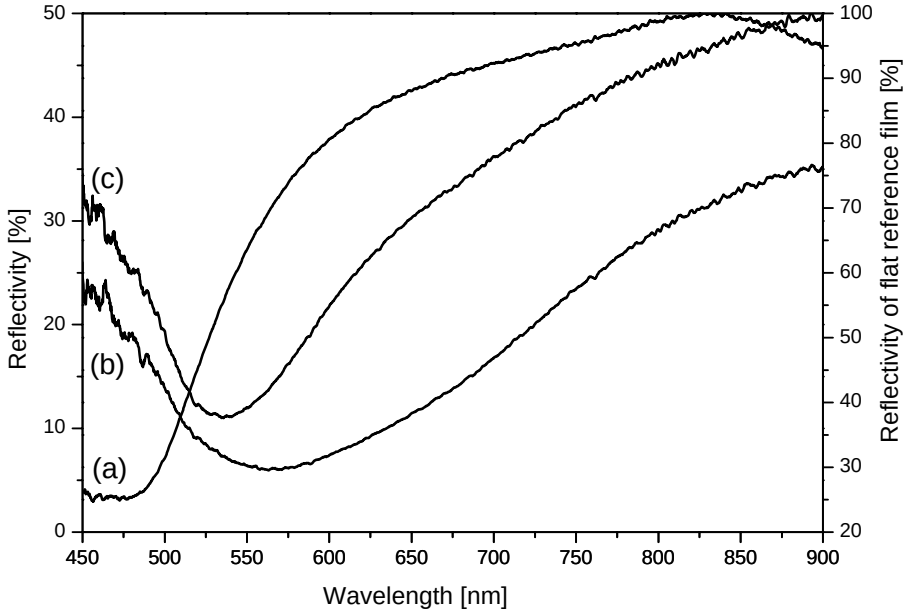

Fig. 4. Optical reflectivity spectra of gold flat film flat (a) and perforated with arrays of holes of 280 nm (b) and 180 nm (c).

Here the minimum of reflectivity is red shifted from the reflectivity edge at 505 nm of bulk film. The array of holes with diameters of 280 nm exhibit a minimum reflectivity at 568 nm with an intensity of 6%; as the hole array size decreases to 180 nm the minimum reflectivity shifts to 536 nm and increases to 11%.

The perforated metallic films exhibit both transmission and reflectivity spectral features different from that of the reference continuous film. In particular the transmission is amplified while the reflectivity is red shift and both effects are depended upon the diameter of the holes. This confirms that the nanostructuration brings new optical properties to noble-metal due to optical excitation of surface plasmons. In our case the surface plasmons excitation operates by coupling of the incident light to surface plasmons waves on air/metal interface, then by combining a direct (bulk) transmission with transmission through the holes mediated by localized plasmons and, finally re-emission of light by scattering of surface plasmons at the second metal/glass interface [12].

4. Conclusion

In this work we presented a simple, inexpensive and versatile method for the fabrication of metallic films perforated with subwavelength arrays of nanoholes. By optimal choosing the experimental parameters we can tune the structure's surface plasmon resonance over the desired spectral range. The optical properties of the fabricated structures were studied revealing an enhanced transmission with spectral position highly dependent on the period of the array.

The periodic arrays of subwavelength nanoholes in metallic thin films are among the most promising structures for applications in light manipulation at the subwavelength range. These structures enable an increase by several orders of magnitude of the transmission when the surface plasmon resonance condition is achieved. Moreover, the excitation of the surface plasmons leads to a strong enhancement of the local electromagnetic field, making these structures promising multifunctional substrates for surface plasmon – mediated molecular spectroscopic methods. Among these methods SERS can be a very sensitive method capable of single-molecule detection. SPR based sensors are gaining much interest in biochemical and biomedical sensing due to the high sensitivity of plasmon resonance on the changes in the dielectric constant of the surrounding medium.

Acknowledgments. This work was partially supported by the Romanian National Authority for Research in the frame of the CEEX program (Project No. 71/ 2006) and by The National University Research Council in the frame of the PN-II program (Project No. TD-28/2007).

References

[1] BETHE H. A., *Phys. Rev.* **66** (1944) p. 163.
[2] EBBSEN T. W., LEZEC H. J., GHAEMI H. F., THIO T., WOLFF P. A., *Nature* **391** (1998) p. 667.
[3] MARTIN-MORENO L., GARCIA-VIDAL F. J., LEZEC H. J., PELLERIN K. M., THIO T., PENDRY J. B., EBBESEN T. W., *Phys. Rev. Lett.* **86** (2001) p. 1114.
[4] POPOV E., NEVIERE M., ENOCH S., REINISCH R., *Phys. Rev. B* **62** (2000) p. 16100.
[5] ASTILEAN S., LALANNE PH., PALAMARU M., *Optics Communication* **175** (2001) p. 265.
[6] JIA W., LIU X., *Phys. Lett. A* **344** (2005) p. 451.
[7] LESUFFLER A., IM H., LINDQUIST N. C., OH S-H., *Appl. Phys. Lett.* **90** (2007) p. 243110.
[8] GHAEMI H. F., THIO T., GRUPP D. E., EBBESEN T. W., LEZEC H. J., *Phys. Rev. B* **58** (1998) p. 6779.
[9] SHUFORD K. L., RATNER M. A., GRAY S. K., SCHATZ G. C., *Appl. Phys. B* **84** (2006) p. 11.
[10] HULTEEN J. C., VAN DUYNE R. P., J. Vac. Sci. Technol. A **13** (1995) p. 1553.
[11] MOORADIAN A., *Phys. Rev. Lett.* **22** (1969) p. 185.
[12] GENET C., EBBESEN T. W., *Nature* **445** (2007) p. 36.

Investigation of the Binding Constant of Biocompatible Gold Nanoparticles to Bovine Serum Albumine Using Fluorescence and LSPR Spectroscopy

M. IOSIN[1], F. TODERAS[1], P. L. BALDECK[2], S. ASTILEAN[1]

[1]Faculty of Physics, Babes-Bolyai University, 400084, Cluj-Napoca, Romania
E-mail: iosinmonica@yahoo.com
[2]Laboratoire de Spectrométrie Physique, Université Joseph Fourier & CNRS UMR5588
Saint Martin d'Hères, France

Abstract. We investigate the adhesion of Bovine Serum Albumine (BSA) to gold nanoparticles by measuring the spectral shift of Localized Surface Plasmon Resonance (LSPR) and the fluorescence quenching of tryptophan residue in BSA after protein binding to the surface of metal. The spectroscopic data allow the calculation of constant binding (Kb) between the protein and colloidal gold and the numbers of specific binding sites.

1. Introduction

Despite the remarkable speed of development of nanoscience, relatively little is known about the interaction of nanoscale objects with biological systems. In the past few years there has been a surge of interest in nanomedicine and nanotoxicology for understanding bio/non-bio interfaces. When nanoparticles enter a biological fluid, they become coated with proteins that may transmit or induce biological effects due to altered protein conformation and perturbed function. A deep understanding of the biological effects of nanoparticles requires knowledge of the equilibrium and kinetic binding properties of proteins that associate with the particles. In particular, gold nanoparticles (AuNPs) are attractive for bio-nanotechnolgy due to their chemical stability and biocompatibility. Indeed, in contrast to cadmium containing quantum dots and other toxic or immunogenic nanoparticles, AuNPs have little or no long-term toxicity or other adverse effects in vivo. Colloidal gold has been safely used to treat rheumatoid arthritis for half a century. In the past few year great progress has been made in the synthesis of metal nanoparticles (NPs) and control over their size [1–3] and shape [4–6]. Beyond their biocompatibility and surface chemical properties, AuNPs strongly interact with light, a phenomenon

called *plasmon resonance* whereby light induces collective oscillations of conductive metal electrons at their surface. Excitation of plasmon resonances lead to a dramatic enhancement of the nanostructure light absorption and scattering cross-sections as well as of the local electromagnetic field bound to the metal surface. Apart to the dependence of particle shape, the position of the surface plasmon absorption band is highly dependent on the dielectric constant of the medium surrounding the particles. As result of chemical or electrostatic interaction between AuNPs and any molecular layer surrounding nanoparticles, there will be a change in the index of refraction which will be translated into a shift of surface plasmon resonance. This is the mechanism by which operates the local surface plasmon resonance (LSPR) spectroscopy in biodetection. Among AuNPs, rod-like shape nanoparticles are especially attractive for such sensing, due to their two plasmon resonant bands, one situated in visible and other in near-infrared (NIR), the second one being very sensitive to the local environment.

In this paper, we use the LSPR spectroscopy to prove the adhesion of BSA to the surface of spheroidal and rod-like AuNPs. Also, we use fluorescence spectroscopy to asses the affinity strengthens of protein binding to the metal surface. In recent years, the fluorescence quenching technique was applied extensively to study the interactions of different biomedical molecules and serum albumins [7–10] and the effect of metal ion on the bindings of serum albumins and other substances [11]. In this study, based on the method of Tedesco *et al.* [12], the binding constant and the numbers of binding sites between colloidal gold and serum albumins were calculated. There were three reasons for choosing Bovine Serum Albumin (BSA) in this study: (a) BSA is present in plasma where plays an important physiological role, (b) BSA is a protein model with well-known structure, and (c) BSA exhibits two tryptophan residues, one located on the surface and other in the hydrophobic pocket.

2. Experimental

$HAuCl_4 \cdot 4H_2O$, Na_3citrate and Bovine Serum Albumin were purchased from commercial sources (Aldrich) and used as received. Gold nanospheres of 18 nm average diameter were synthesized with the wet chemical method of Turkevich *et al.* [13]. For the synthesis of nanorods particles, a seed-mediated growth method at room temperature in two steps has been employed. In the first step a seed spheres solution of 3-5 nm gold nanocrytals was prepared. In the second step, the growth of gold nanorods from as prepared seed nanoparticles in presence of CTAB, sodium borohydride, $AgNO_3$ and ascorbic acid was used. The nanorods were concentrated and separated from solution by centrifugation. The supernatant, containing mostly CTAB molecules and gold ions, was removed and the solid part containing rods was redispersed in ultrapure water. The as synthesized nanorods in water are coated with a bilayer of CTAB molecule being stable at room temperature for

many months. The BSA solution is made by dissolving BSA in water to a concentration of 1 mg/mL.

The UV-VIS absorption spectra were recorded with a Jasco V-530 UV-VIS spectrophotometer. Fluorescence spectra were recorded on a Jasco LP-6500 spectrofluorimeter equipped with 1.0 cm quartz cells and the slit width was 1 nm/3 nm.

3. Results and discussion

Figure 1 shows the UV-Vis LSPR spectra of as prepared AuNPs in the presence and absence of BSA solution. UV-Vis absorption measurements (see curve a in Fig. 1) indicated that the maximum wavelength of the surface plasmon resonance (SPR) band of gold nanoparticles in aqueous suspension was 520 nm. When albumin solution was added to the preformed AuNPs solution, an increase in absorbance and a slight red-shift of 3 nm in the maximum absorbance value was observed, compared to that of control GNPs, which indicated the formation of bioconjugates (Fig. 1A).

The absorption spectrum of BSA aqueous solution exhibits an absorbance maximum at 278 nm which correspond to aromatic residues tryptophan and tyrosine absorption. In addition, from the ultraviolet absorption (UV) spectra shown in Fig. 1B, the absorption peak of pure BSA at 278 nm, moved to lower wavelength and the intensity of this protein characteristic peak decreases when different concentration of gold nanoparticles were added into BSA, which indicated that there was interaction between them. The blue shift indicated that tryptophan residues were placed in a more hydrophobic environment and less exposed to the solvent [14]. In contrast, obvious changes of SPR band were observed for GNP after conjugating with the albumin.

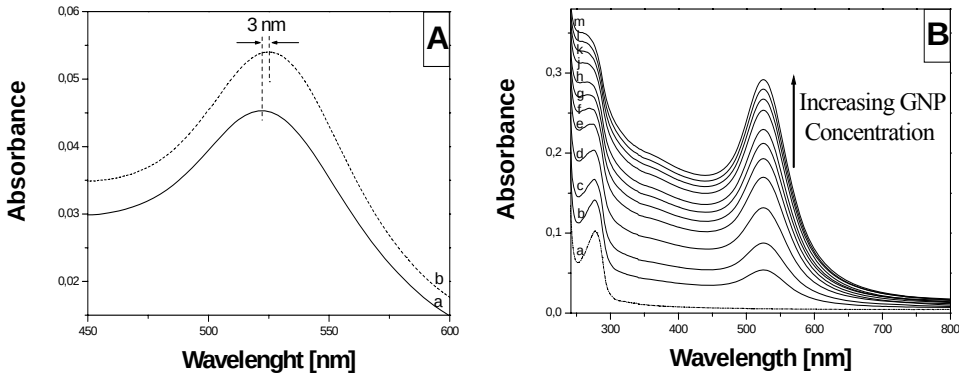

Fig. 1 A. The UV-VIS absorption spectra of pure colloidal gold solution (a), BSA-gold nanoparticles conjugates (b); **B.** Absorption spectra of BSA containing different concetrations of gold nanospheres. The [BSA]/[Au] ratio was maintained at values of (a) 0, (b) 0.1, (c) 0.2, (d) 0.3, (e) 0.4, (f) 0.5, (g) 0.6, (h) 0.7, (j) 0.8, (k) 0.9, (l) 1, (m) 1.1

For gold nanorods, the plasmon absorption splits into two bands [15]. The long wavelength plasmon band originates from the longitudinal mode of oscillation of the free electrons along the long axis of the rod, while the short wavelength plasmon band originates from the transverse mode perpendicular to the former one. As the aspect ratio of the gold nanorods increases, the longer wavelength plasmon absorption band gradually red shifts [16]. Here, gold NRs of aspect ratio 2 have a transverse band at 518 nm and a longitudinal plasmon band at 674 nm (Fig. 2A – curve a). Addition of BSA solution led to visible changes in the surface plasmon bands (Fig. 2A – curve b), the longitudinal band are red shifted with BSA addition. This shows a strong electromagnetic coupling in the longitudinal plasmon band of the gold nanorods because the BSA molecules were adsorbed onto the end of gold nanorod. In contrast, the transverse band did not show a similar change to the longitudinal band, indicating the absence of electromagnetic coupling in the transverse plasmon band.

In order to demonstrate the interaction between BSA and gold nanorods we monitoried the spectral changes in Fig. 2B. The aggregation effect was observed as result of addition of gold nanorods to pure BSA solution. It is observed that there is a red shift as well as broadening of the longitudinal plasmon band.

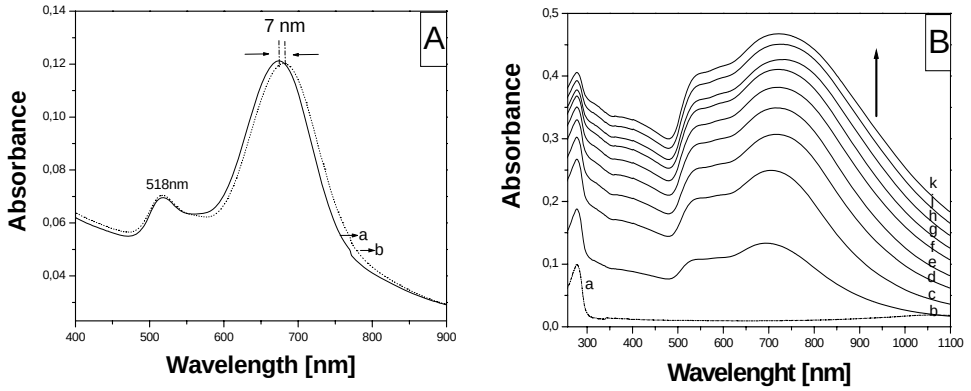

Fig. 2. A. The UV-VIS absorption spectra ofl gold nanorod solution (a), BSA-gold nanorods conjugates (b); **B.** Absorption spectra of BSA containing different concetrations of gold nanorods. The [BSA]/[Au] ratio was maintained at values of (a) 0, (b) 0.1, (c) 0.2, (d) 0.3, (e) 0.4, (f) 0.5, (g) 0.6, (h) 0.7, (j) 0.8, (k) 0.9.

Fluorescence Study. From the fluorescence spectra, we could obtain some information on the binding of protein to the surface of different shape gold nanoparticles, such as the binding mechanism, binding constant and binding site. BSA has three intrinsic fluorophores: tryptophan, tyrosine and phenylalanine that can be quenched. In fact, because phenylalanine has a very low quantum yield and

the fluorescence of tyrosine is almost totally quenched if it is ionized, or near an amino group, a carboxyl group, or a tryptophan, the intrinsic fluorescence of BSA is almost contributed by tryptophan alone [17].

Effect of gold nanospheres on BSA spectra. Herein, the fluorescence spectrum was monitored using excitation at 280 nm and emission within the region from 290 to 450 nm. From Fig. 3A, it could be seen that BSA had a strong fluorescence emission peak at 336 nm, whereas gold nanoparticles had no intrinsic fluorescence. The choice of 280 nm as the excitation wavelength was to avoid the contribution from tryptophan residues. The fluorescence intensity of BSA was decreased with the increasing of concentration of colloidal gold, which indicated that the colloidal gold quenched the fluorescence of BSA. The red shift of up to 4 nm (from 336 to 340 nm) with the increasing of gold nanospheres concentration corresponds to the changes of the polarity around tryptophan residues.

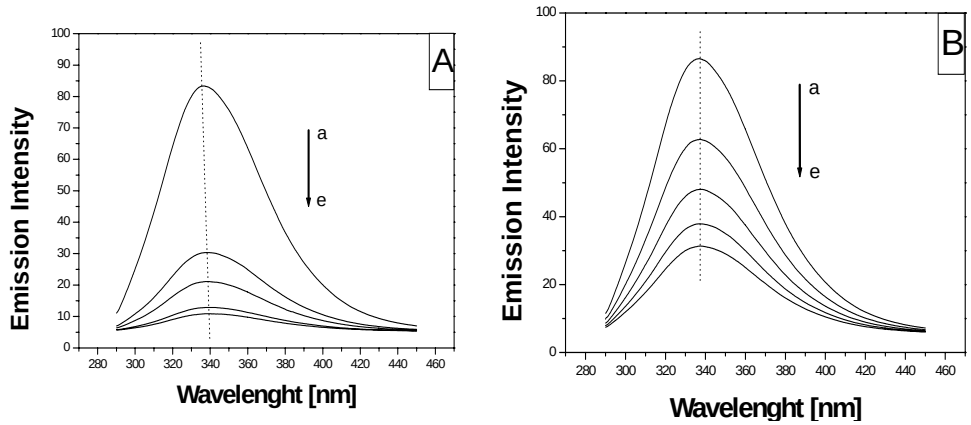

Fig. 3. The fluorescence quenching spectra of Tryptophan residues by different concentration of gold nanosphere **(A)** and gold nanorod **(B)**. The [BSA]/[Au] ratio was maintained at values of (a) 0, (b) 0.1, (c) 0.2, (d) 0.3, (e) 0.4.

Effect of gold nanorods on BSA spectra. To understand the effect of gold nanorods on the tryptophan environment of the protein, the intrinsic fluorescence of BSA in the presence of increasing concentrations of gold nanorods in the molar ratio of [BSA]/[rods] was studied. The fluorescence spectra of the protein in the presence of gold nanorods are shown in Fig. 3B. It was observed that the fluorescence intensity of BSA-gold nanorod decreased regularly with the increasing concentration of gold nanorod, but that there was no significant λ_{em} shift with the addition of gold nanorod, which indicated that gold nanorod can quench the inner fluorescence of BSA and that the interaction between gold nanorod and BSA has occurred. When the binding sites of the gold nanoparticles are totally saturated by BSA molecules, the fluorescence emission intensity becomes constant and no changes should be observed for any further BSA addition.

The binding constant K_A and the number n of binding sites. The relationship between fluorescence quenching intensity and the concentration of quenchers can be described using the method of Tedesco *et al.* The method was introduced to calculate the binding constants and the numbers of binding sites between colloidal gold and serum albumins.

In this equation $(F_0 - F)/(F - F_\infty) = ([M]/K_{diss})^n$, F_0 and F_∞ are the relative fluorescence intensities of the protein alone and the protein saturated with the [gold] and n is the number of binding sites per BSA. The slope of the double-logarithm plot obtained from the experimental data is the number of equivalent binding capacity (n), whereas the value of log[gold] at $\log[(F_0 - F)/(F - F_\infty)] = 0$ equals to the logarithm of the dissociation constant (K_{diss}). The reciprocal of K_{diss} is the binding constant K_b. The result (Table 1) illustrates that there is a greater constant binding between gold nanospheres and BSA than that of the nanorods and BSA.

Table 1. Binding constant (K_b) and binding capacity (n) of gold nanoparticles with BSA

	K_b	n
Gold nanosphere	2.34×10^{11}	1.37
Gold nanorod	0.5×10^{5}	0.38

4. Conclusions

The main purpose of this paper is to study the bindings of colloidal gold and serum albumins using the fluorescence quenching technique. The addition of BSA into the gold nanorod solution resulted in preferential binding to the two ends of the gold nanorods. On the other hand, for gold nanospheres the protein is adsorbed on the surface on the metallic gold nanoparticles. The gold nanospheres binding sites and thus the binding constant with BSA are greater than that of the nanorods due to the higher surface area where the protein can be adsorbed.

It can be expected that the fluorescence quenching technique could provide a promising tool to study the interactions of colloidal gold and proteins. Surface functionalization is a critical issue in the development of gold nanorods and other nanoparticles for applications in site-directed targeted imaging or therapy.

Acknowledgement. This work was supported by the National University Research Council, partially from the project IDEI No. 407 / 2007 and the Project No. TD-65/2007.

References

[1] FRENS G., Nat. Phys. Sci., **241**, p. 20, 1973.
[2] ALIVISATOS A. P., Science, **271**, p. 933, 1996.
[3] LANDES C. F., LINK S., MOHAMED M. B., NIKOOBAKHT B., EL-SAYED M. A., Pure. Appl. Chem., **74**, p. 1675, 2002.
[4] EL-SAYED M. A., Acc. Chem. Res., **34**, p. 257, 2001.
[5] SAU T. K., MURPHY C. J., J. Am. Chem. Soc., **126**, p. 8648, 2004.
[6] WIRTZ M., MARTIN C. R., Adv. Mater., **15**, p. 455, 2003.
[7] KLAJNERT B., BRYSZEWSKA M., Bioelectrochemistry, **55**, p. 33, 2002.
[8] JIANG C. Q., GAO M. X., MENG X. Z., Spectrochim. Acta, Part A **59**, p. 1605, 2003.
[9] GIRI R., Spectrochim. Acta, Part A **60**, p. 757, 2004.
[10] CUI F. L., FAN J.,. LI J. P, HU Z. D., Bioorg. Med. Chem., **12**, p. 151, 2004.
[11] DREVENSEK P., TUREL I., ULRIH N. P., J. Inorg. Biochem., **96**, p. 407, 2003.
[12] TEDESCO A. C., OLIVEIRA D. M., LACAVA Z. G. M., AZEVEDO R. B., LIMA E. C. D., MORAIS P. C., J. Magn. Magn. Mater., **272–276**, p. 2404, 2004.
[13] XIE H., TKACHENKO A. G., GLOMM W. R., RYAN J. A., BRENNAMAN M. K., PAPANIKOLAS J. M., FRANZEN S., FELDHEIM D. L., Anal. Chem., **75**, p. 5797, 2003.
[14] XIE H., Anal. Chem., **75**, p. 5797, 2005.
[15] LINK S., MOHAMED M. B., EL-SAYED M. A., J. Phys. Chem. B, **103**, p. 3073, 1999.
[16] JANA N. R., GEARHEART L., MURPHY C. J., Adv. Mater., **13**, p. 1389, 2001.
[17] SULKOWSKA A., J. Mol. Struct., **614**, p. 227, 2002.

Comparative Study of Some Oxidoreductases' Immobilization on Films, Micro- and Nanoparticle Supports

Elena NEAGU[1], Gabriela PAUN[1], Veronica MOROEANU[1],
Viorica PARVULESCU[2], G. L. RADU[3]

[1]Center of Bioanalysis, National Institute of Research -Development for Biological Sciences, Bucharest, 296 Splaiul Independenței, 060031, Bucharest, Romania
[2]*Ilie Murgulescu* Institute of Chemistry Physics, Spl. Independentei, Nr. 202, 060021 Bucharest, Romania
[3]Faculty of Applied Chemistry and Materials Science, *Politehnica* University of Bucharest, 313 Splaiul Independentei, Romania

Abstract. A comparative study of laccase and peroxidase (oxidoreductases) immobilization on polymeric supports and silica nanoparticles (SBA15 and SBA15 NH_2) is presented. Two types of biocompatible polymeric supports were obtained: films of sodium alginate/chitosan/hyaluronic acid, simple and with magnetic nanoparticles, and microparticles of chitosan and/or sodium alginate (as polymers) ± hyaluronic acid. Such supports were used to immobilize laccase and peroxidase by two methods: direct immersion and after support activation with 2.5% glutaraldehyde. For comparison, some supports based on silica, simple or functionalized (SBA15 and SBA15 NH_2) also were used to immobilize above mentioned enzymes. The immobilization yields of peroxidase on microparticles were calculated, the highest ones being obtained in case of supports activated with glutaraldehyde: 98,89% for chitosan microparticles and 98,86% for those of alginate + chitosan. In case of peroxidase immobilized on silica supports, simple and functionalized (SBA15 and SBA15 NH2), the immobilization yields were lower against that obtained using organic supports, namely, 98% and respectively 96,26%. As regards the laccase immobilization, the obtained immobilization yields using chitosan microparticles were 99,8%, while using silica supports they were above 90,8% and 90,7%. The properties of the used polymers and their structure determine the possibility to use them as raw materials in obtaining biocompatible supports in order to immobilize some biological active substances (enzymes, drugs).

1. Introduction

The immobilized enzymes opened new perspectives for processes in which the enzymatic biocatalysators intervene, facilitating their running in continuous system, the treatment in optimum conditions of some diluted solutions, the enzyme

disappearance from environment resulted after transformation and avoiding the undesired secondary products.

The including of enzymes into an immobilization support is based on their placing within the structure of a polymeric matrix or membrane, such structure being chosen as to impede enzyme release, but allowing the substrate penetration and release of the reaction products. Because the enzyme binds in no way to matrix or membrane, this represents the most used method applied to immobilize a great number of enzymes, microbial cells and cell organelles. The enzyme proprieties are almost not changed, and losses of enzimatic activities are negligible.

The enzymes immobilization by forming support-enzyme bounds is the oldest and among most used immobilization methods. The physical adsorption, ionic binding and chelating are the most attractive methods for industrial applications, because even if the strength of formed bound is weak, the possibility to reuse the support exists.

The supports used to immobilize the enzymes by covalent binding are classified by their origin into inorganic and organic ones being based on synthetic or natural polymers.

The cases in which the support, in its primary state, contains the reactive groups necessary to immobilize the enzyme are rare, excepting a series of organic compounds of synthesis. Therefore, before the immobilization the selected supports are activated with reagents compatible to enzyme structure.

Table 1. Main characteristics and applications of natural polymers

Polymers	Characteristics, uses
Chitosan and derivates	– natural polycation; – biocompatible, non-toxic; – able to form gels and films; – widely used in systems of controlled release (ex. gels, membranes, microspheres)
Alginate	– extracted from marine alga; – able to form relatively easily gels; – relative biocompatible; – microstructure and viscosity depend on its chemical composition; – used to realize: • the matrix to immobilize the cells and enzymes; • the systems of controlled release of bioactive substances; • the injectable microcapsules used in treatment of degenerative diseases and hormonal deficiencies.
Carragenan	– Sulphatat polysaccharide obtained from red algae; – able to form wide range of gels, at room temperature; – excellent thermo resistant properties; – used for microencapsulating
Hyaluronic acid	– excellent lubrication agent; – potential therapeutic agent.

The polymeric materials – simple or composite – constitute a very actual object characterized by peculiar dynamics, due to their wide range uses within the medical and pharmaceutical domains.

The main characteristics of most important natural polymers used as supports for enzyme immobilization are shown in Table 1.

The magnetic nanoparticles represent another type of supports used to immobilize some active biologic components, including the enzymes.

In recent years important successes were achieved in the technological processes to obtain magnetic microspheres, magnetic nanospheres or ferro-fluids. The techniques based on some complex magnetic biocompatible systems were applied in numerous fields like drug targeting, molecular biology, diagnostic, isolation and purification of cells, radioimmunoassay, hyperthermia, purification of nucleic acids.

As regards the forms of supports, these could be polymeric membranes, microspheres or nanoparticles.

The choice of support represents a problem of especial importance to obtain an immobilized enzimatic preparation.

It is enough difficult a material selected in this scope to concomitantly fulfil all conditions imposed to a suitable support, namely:

- high affinity against proteins;
- availability of reactive groups for direct reactions with protein free groups;
- easiness to be transformed into various physical forms;
- toxic free;
- physiological compatibility (for applications in food industry and those of medical nature);
- low price.

The research scope was to obtain some polymeric supports as films of alginate/chitosan/hyaluronic acid, films of chitosan with magnetic nanoparticles, and microparticles based on chitosan and mixes of sodium alginate/chitosan/hyaluronic acid.

These supports were used to immobilize some oxidoreductases – laccase and peroxidase – by two methods: through *adsorption on solid support* and *covalent binding* after support activation with 2.5% glutaraldehyde.

Besides the supports prepared of natural polymers, inorganic silica supports, simple and functionalized (SBA15 and SBA15 NH_2) and phosphate polymeric supports were also comparatively used to immobilize same enzymes.

Laccase (EC 1.10.3.2.), also named 1,4-benzendiol oxydase, represents an enzyme, which contains copper and is found in most plants and microorganisms.

The laccases are glycoproteins, their basic subunit being a single polypeptide chain of 50–70 kDa; their carbohydrate content is of 10–45%, they contain 4 copper atoms, and their optimum pH ranges between 4 and 7.3, in function of the substrate.

The laccase catalyzes the oxidation of mono-, di- and polyphenols to quinones, of aminophenols, polyamines, lignin, as well as of aryldiamines and concomitantly reduces the oxygen to water [2–4].

The laccase of *Trames versicolor* (an enzyme used in present project experiments) was immobilized on nanoparticles and caolinit through adsorption or covalent binding on supports previously activated by reticulation with glutaraldehyde [4], on activated agarose with p-benzoquinone [5], on electrodes of carbon fibres by adsorption after their reticulation with glutaraldehyde or carbodiimida [6], on silica particles [7], on polyamide membrane through covalent binding [8], on microfiltration membranes of polyviniliden difluoride (PVDF) [9] etc.

The laccase has applications especially in food industry, where its principal role is to remove the phenol compounds responsible of oxidation of cut vegetables, fruit juices, beer and vine turbidity [10]; as well as in textile industry to remove the colorants within the washing waters [11, 12], in nanobiotechnolgy by development of some biosensors for clinical and environment applications [13–15], in synthesis of some organic compounds [16–18], for treatment of some waste waters with high load of polyphenols [19–23].

Peroxidase (donor: H_2O_2-oxidoreductase, the other enzyme used in our experiments, is found both in vegetal and animal reigns, is distributed in mitochondria, peroxisomes and catalyses the dehydrogenation of great number of organic compounds, like: phenols and aromatic amines, hydroquinones, especially derivates of benzidine.

With few exceptions, the peroxidases are hemoproteins and catalyzes the reaction:

$$\underset{\text{donor}}{RH_2} + H_2O_2 \rightarrow \underset{\text{donor oxidat}}{R} + 2H_2O,$$

where RH_2 is a compound of organic nature belonging to very different chemical groups: aromatic amines, phenols, flavins, cytochromes.

But peroxidases, which act like oxidases:

$$DH_2 + O_2 \rightarrow D + H_2O_2$$

or monooxigenases:

$$DO_2 + O_2 + NADPH \rightarrow D\text{-}OH + NADP^+ + HO^-$$

also exist.

The horseradish peroxidase is most well studied, being a glycoprotein with content of 18% carbohydrates, having a molecular weight of 40200, an optimum pH of 6.0, and isoelectric point at 7.2 pH. The ratio of optical densities $D.O._{403\ nm}$/ $D.O._{257\ nm}$, named Renheitzahl (RZ), is usually determined on pure peroxidase preparations as test of preparation purity. RZ varies between 4.19 and 2.50 – RZ = 3.04 in case of homogenous enzymatic preparations.

The horseradish peroxidase shows a high specificity. Its activity is detected with H_2O_2, MeOOH, Et OOH.

The peroxidase from horseradish HRP was immobilized on alkylaminated glass and functionalized by glutaraldehyde to determine the oxalate in urine [24]. HRP was covalent immobilized on functionalized polyacrylonitril membranes PAN functionalized with carbodiimida 1-ethyl-3-(3-dimethylaminopropyl) (EDC). The silica microbeads derived by silanization were also coupled with HRP after activation with EDC or glutaraldehyde [25]. HRP was covalent immobilized on glass to remove 4-chlorophenol from water solutions [26].

A new biosensor for H_2O_2 was realized based on biohydrogel obtained by immobilization of horseradish peroxidase HRP on polyhydroxylcellulose PHC, prepared by mixing the polyvinylalcohol with carboxymethyl hydroxyethyl cellulose, a biosensor which was electrochemically and electroanalytically tested [27].

A new generation of biosensors was built starting from HRP immobilized through the sol- gel technology (SG) on modified electrode = nanotube of carbon (CNT). CNT promotes the effect of electron transfer between HRP and electrode surface, while the net of sol-gel furnishes an environment biocompatible for HRP immobilized enzyme which maintains its bioelectrolytic activity to reduce H_2O_2 and is able to respond to rapid changes of H_2O_2 concentrations [28].

The literature data indicate that, due to carboxyl groups in its molecule, the peroxidase could be immobilized through covalent binding on different supports, among which it could be named the membranes of polyacrylonitril [25].

2. Experimental part

Two of oxidoreductase enzymes were studied, respectively the *peroxidase* and *laccase*, which were immobilized on various functionalized supports in order to study the effects of such enzyme immobilization in function of nature of those supports.

The materials used in our experiments were:

1. Enzymes
   - Peroxidase, VI-A type from horseradish (Sigma)
   - Laccase from *Trametes versicolor* (Fluka)
2. Substrates for enzymes
   - Hydrogen peroxide (Chimopar) 0,0017 M, prepared through dilution of 1 mL of H_2O_2 30% in 100 mL of distilled water – for peroxidase
   - Syringaldazine (Sigma) – 0.216M solution prepared in absolute methanol – for laccase
3. Used supports
   3.1. – Microparticles of alginate/chitosan
   3.2. – Microparticles of alginate

3.3. – Microparticles of chitosan with hyaluronic acid
3.4. – Microparticles of chitosan
3.5. – Film of chitosan with magnetic nanoparticles
3.6. – Film of chitosan with hyaluronic acid
3.7. – Film of sodium alginate

3.8. 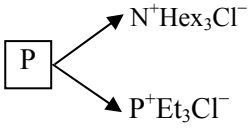

3.9. 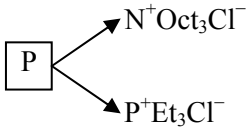

3.10. S-NH_2
3.11. SBA-15

4. Reagents necessary to determine the enzimatic activity of the two enzymes: 4 – aminoantipirina 0.0025 M with phenol 0.17 M; Potassium phosphate buffer 0.1 M pH = 6.5.

2.1. Supports' preparing

The biocompatible supports as microparticles were obtained from three polymers: chitosan 1.5%, sodium alginate 5% and hyaluronic acid 0.5%. After dissolution the polymeric solutions were poured in drops into 5% sodium hydroxide solution within which it promptly precipitates by forming microparticles.

Also, 1.5% PEG in order to increase the viscosity and 10% glycerol as porogenous agent were used.

The coagulation solution is maintained under stirring more about 5 minutes after appearance of microparticles, after which the stirring is stopped, the sodium hydroxide was filtered and obtained microparticles were washed with distilled water and dried at room temperature during 48 hours.

Preparing the chitosan films with magnetic nanoparticles:

The magnetic nanoparticles were obtained by co-precipitation of ferric and ferrous ions with NH_4OH in hydrothermal conditions; supports initially had a hydrophilic character after which they were functionalized with aminopropylsilane – APTS.

The chitosan films with magnetic nanoparticles were obtained from 1% chitosan solution prepared in 1% acetic acid, to which 1% PEG were added to increase the viscosity, mixed 2 hours till dissolution. In such solution the magnetic nanoparticles were added in 2:1 (chitosan:nanoparticles) weight ratio, the mix was sonicated several hours till homogenization.

Then, the solution was applied on glass and the solvent vaporization was performed at room temperature during 3–4 hours, then several hours into oven at 50°C. After solvent vaporization the dry formed pellicles are post-treated with 5% sodium hydroxide during 50–60 min, at 80°C, and finally the pellicles are washed with distilled water to remove the excess of hydroxide.

Biocompatible supports as films: as polymers were used 1.5% chitosan, 5% sodium alginate and 0.5% hyaluronic acid + additives poly ethylen glycol (PEG) and 2% acid acetic.

The following supports were obtained:

– *Pellicles:*

M1 =1% chitosan + 1% PEG + NPM (magnetic nanoparticles) in mass ratio of 2:1,
M2 =1.5% chitosan + 1% PEG + 0.5% HA in ratio of 25:1,
M3 = 5% alginate.

– *Microparticles:*

CH = 1% chitosan + 1.5% PEG,
CH – HA = 1.5% chitosan + 1% PEG + 0,5% HA,
Alg = 2% sodium alginate, further precipitation with 0.2 M $CaCl_2$,
Alg – CH = 2% alginate + 1% chitosan.

2.2. Oxidoreductases' immobilization on supports

The *peroxidase and laccase* immobilization on polymeric supports was realized by two methods:

a) on active surface of supports, *after their activation* with 2.5% glutaraldehyde 5 hours (2 ml), after which the supports were washed with 0.2 M phosphate buffer, pH 7.5 (for peroxidase) respectively 0.1 M phosphate buffer pH 6.5 (for laccase) after which the enzyme was added.

b) through *direct immersion of* supports in the enzymatic solution.

On supports 1 ml enzyme was placed and the supports were leaved in contact with enzyme 24 hours.

2.3. Determination of peroxidase activity

The peroxidase activity is usually determined based on the oxidation rate of pirrogaloll, a method which many times proved to be inadequate. A large variety of hydrogen donors were used to determine the enzyme activity, many systems including components with carcinogenic potential such as – di anizidina.

An improved method was realized by using 4 – aminoantipirine as hydrogen donor (Trinder, 1966). The reaction rate is determined through measuring the absorbance increase at 510 nm, an increase resulted by decomposition of hydrogen peroxide. By decomposition of one micromol of hydrogen peroxide at 25°C and pH = 7, in specific conditions results one unit.

It was worked with a peroxidase to which an enzimatic activity of 155 U/mg was determined.

Used reagents

– 0.2 M phosphate buffer pH = 7;
– 0.0017 M hydrogen peroxide, prepared by dilution of 1 mL 30% H_2O_2 in 100 mL distilled water. Then 1 mL of such solution was diluted with 50 mL 0.2 M phosphate buffer, pH = 7;
– 0.0025 M 4 – aminoantipirina with 0.17 M phenol prepared by dissolution of 810 mg phenol in 40 mL distilled water, to which 25 mg 4 – aminoantipirina was added and is diluted to a final volume of 50 mL with distilled water.

Work procedure

– The spectrophotometer was adjusted to 510 nm and 25°C.
– In each cuve was pipetted:
– 1.4 mL 4 – aminoantipirina solution + 1.5 mL 0.0017 M H_2O_2
– It was incubated in spectrophotometer at 25°C 3–4 minutes to equilibrate the temperature.
– 0.1 mL diluted enzyme was added and the absorbance increase was determined at 510 nm for 4–5 minutes.

Result calculation

ΔA_{510}/min for linear portion of curve was calculated with formula:
Enzyme units / mg = ΔA_{510}/min / 6.58×mg enzyme / mL mix.

2.4. Determination of laccase activity

The laccase activity was determined with a spectrophotometer based on the oxidation rate of siringaldazina along time, according to the reaction [66]:

$$\text{Siringaldazina} + O_2 \xrightarrow{\text{Laccase}} \text{oxidated Siringaldazina} + 2H_2O$$

Work procedure

The following reagents (mL) were pipetted in each cuve:

	Sample	Control
Deionized water	–	0.5
Phosphate buffer pH = 6,5	2.2	2.2
Enzyme solution	0.5	–

It was incubated in a spectrophotometer termostated at 30°C until the solutions reach such temperature, after which in each cuve (sample and control) 0.3 mL siringaldazina were introduced and immediately the absorbance variation was recorded at wavelength of 530nm during about 10 minutes. ΔA_{530nm}/min variation was calculated both for samples and control.

Result calculation

ΔA_{530}/min for linear portion of curve was calculated with formula:

$$\text{Units/ml enzyme} = \frac{\left(\Delta A_{530nm}\text{Proba/min} - \Delta A_{530}\text{Martor/min}\right)\times \text{dil.}}{\left(0{,}001\times 0{,}5\right)}$$

where:

dil. = dilution factor,

0.001 = change in A_{530nm} / min / units of laccase at pH 6.5 and 30°C in 3 ml reaction mix,

0.5 = volume (mL) of used enzyme.

3. Results and discussion

The results obtained at peroxidase immobilization on polymeric supports are presented in the Table 2 and Fig. 1.

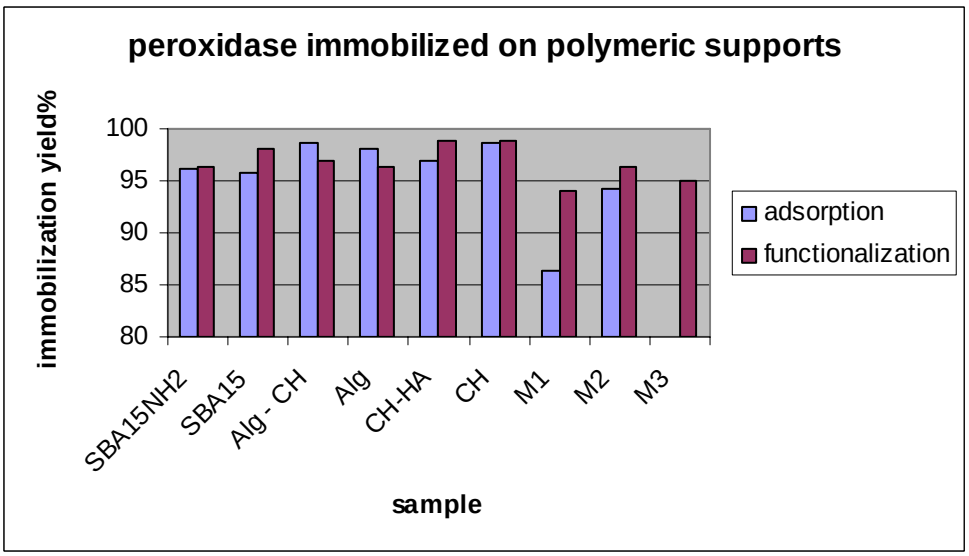

Fig. 1.

Table 2. Peroxidase immobilization on supports

Crt. No.	Sample	Immobilization type	Support weight, mg	A.E. UI/ support	A.E. UI/ mg support	Immobilization yield %
1	Microparticles SBA 15 NH_2	adsorption	14.5	30.41	2.09	96.23
		activation with glutaraldehyde	25.57	30.42	1.18	96.26
2	Microparticles SBA 15	adsorption	13.5	30.29	2.24	95.8
		activation with glutaraldehyde	12.4	31.19	2.51	***98***
3	Microparticles Alg - CH	adsorption	37.77	31.16	0.82	***98.6***
		activation with glutaraldehyde	28.22	30.7	1.08	97
4	Microparticles Alg	adsorption	30.54	30.97	1.01	98
		activation with glutaraldehyde	28.8	30.43	1.05	96.3
5	Microparticles CH - HA	adsorption	21.5	30.65	1.42	97
		activation with glutaraldehyde	30	31.24	1.04	***98.86***
6	Microparticles CH	adsorption	50	31,17	0.6	***98.6***
		activation with glutaraldehyde	32	31,25	0.97	***98.89***
7	Film M1	adsorption	49.24	27.3	0.55	86.39
		activation with glutaraldehyde	54	29.71	0.55	94
8	Film M2	adsorption	11.43	29.8	2.60	94.3
		activation with glutaraldehyde	7.9	30.45	3.85	96.36
9	Film M3	activation with glutaraldehyde	52.58	30.01	0.57	94.96

At peroxidase imobilization on polymeric supports was observed:

– an increased immobilization yields ranging between 86.39–98.89% by both immobilization methods, both for inorganic supports and organic ones,
– generally, after the functionalization with glutardialdehyde the obtained yields were slightly higher than in case of direct immersion for major part of supports,
– most suitable supports for peroxidase immobilization were those containing chitosan and especially as microparticles.

An enzyme with enzymatic activity of 56.34 U/mg was used to immobilize the laccase on polymeric supports and the obtained results are presented in Table 3 and Fig. 2.

In Fig.2 are presented by comparison the results obtained to immobilize the laccase on supports in function on the immobilization method:

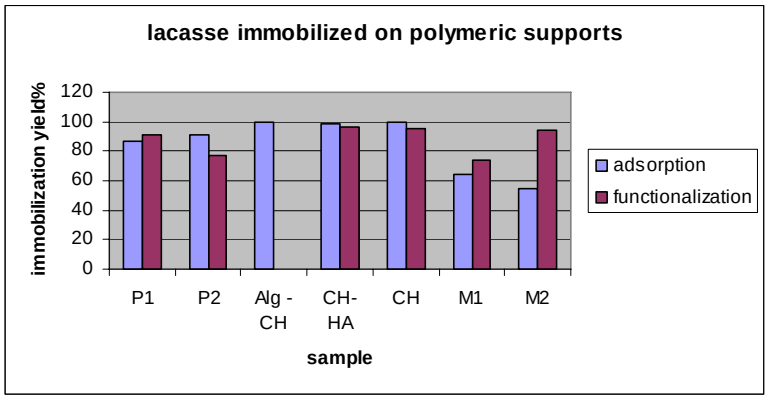

Fig. 2.

Table 3. Results obtained to immobilize the ***laccase*** on polymeric supports

Crt. No.	Sample	Immobilization type	Support weight, mg	A.E. UI/ support	A.E. UI/ mg support	Immobilization yield %
1	P1	adsorbtion	33.4	48.7	1.45	86.4
		activation with glutaraldehyde	31.24	51.16	1.63	**90.8**
2	P2	adsorbtion	29.2	43.68	1,49	77.5
		activation with glutaraldehyde	25.7	51.09	1,98	**90.7**
3	Microparti-cles Alg – CH	adsorbtion	26.8	56.024	2,09	***99.4***
4	Microparti-cles CH – HA	adsorbtion	17.3	55.5	3,20	***98.5***
		activation with glutaraldehyde	19.4	54.5	2,80	**96.7**
5	Microparti-cles CH	adsorbtion	54	53.66	0,99	***99.8***
		activation with glutaraldehyde	37.4	56.28	1,50	**95.2**
6	Film M1 (CH+NPM)	adsorbtion	30.89	36.41	1,17	64.6
		activation with glutaraldehyde	27.7	14.63	0,52	74
7	Film M2 (CH+HA)	adsorbtion	5.9	30.98	5,25	54.9
		activation with glutaraldehyde	10.4	53.164	5,11	**94.3**

Where:
P1 = inorganic support based on silica,
P2 = inorganic support based on silica,
Alg = sodium alginate,
CH = chitosan,
HA = hyaluronic acid,
NPM = magnetic nanoparticles.

Following the results obtained in immobilization experiments of laccase it was concluded that:

– the obtained immobilization yields were above 90% for all studied supports excepting the laccase immobilized on chitosan film with magnetic nanoparticles, where the immobilization yield was of 74% in case of film activation with glutaraldehyde and of 64.4% in case of adsorption on support;
– the supports as microparticles containing chitosan seemed to be most suitable to immobilize the laccase, especially through method of direct immersion;
– the film containing magnetic nanoparticles NPM registered the lowest immobilization yields to immobilize both studied enzymes, and significantly lower in case of laccase.

In Figs. 3 and 4 are comparatively presented the results obtained to immobilize the two studied enzymes in case of direct immersion and after the functionalization of supports.

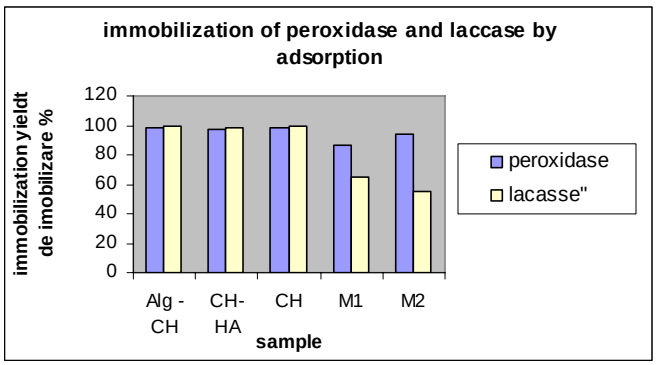

Fig. 3.

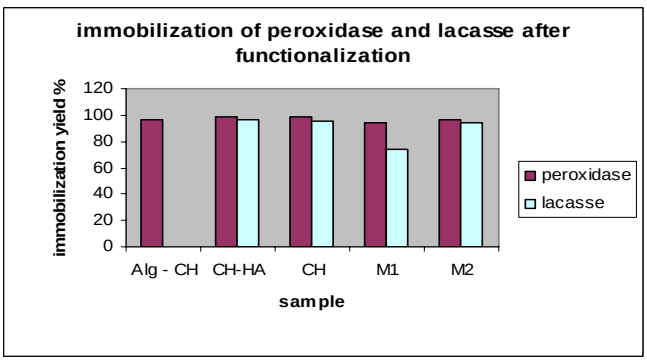

Fig. 4.

3. 1. Testing the stability in order to reuse the obtained immobilized systems

The stability of the supports immobilized with peroxidase and lacasse for which initial highest immobilization yields were obtained, was tested at their reuse. In this scope the supports were washed with phosphate buffer solution after determination of enzymatic activity and the preservation yields after each reuse were calculated (Tables 4 and 5 and Figs. 5 and 6).

Table 4. Results obtained to reuse peroxidase

Support type	Immobilization type	Initial yield %	Preservation yield after first reuse (%)	Preservation yield after second reuse (%)
Film M1	adsorption	86,39	82,9	80
	functionalization	94	92,6	91,4
Film M2	adsorption	94,3	93,48	92,8
	functionalization	96,36	95,9	94,9
Microparticles CH	adsorption	98,3	97,8	97
	functionalization	98,9	98,7	98
Microparticles CH-HA	adsorption	97	96,7	95
	functionalization	98,86	98,79	98
SBA 15 NH_2	adsorption	96,23	95,79	95
	functionalization	98,5	96,26	95
SBA 15	adsorption	98,6	95,4	94,9

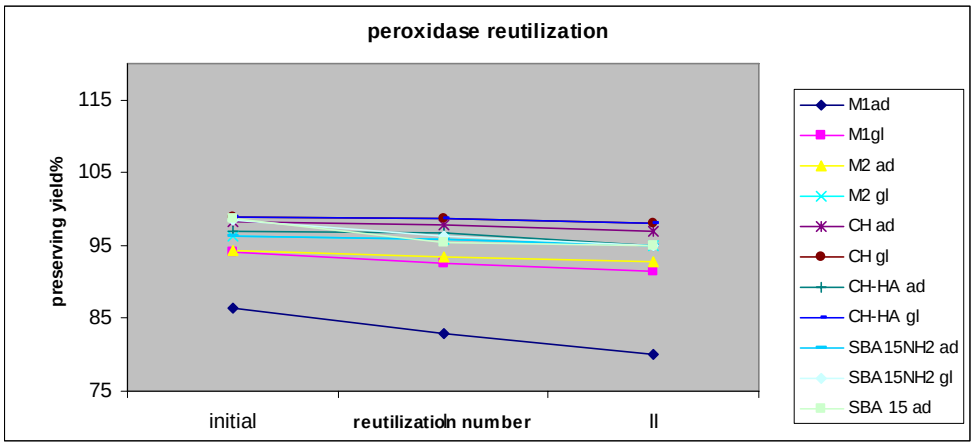

Fig. 5.

Table 5. Results obtained to reuse lacasse

Sample	Immobilization type	Immobilization yield %	Preservation yield after first reuse (%)	Preservation yield after second reuse (%)
P1	functionalization	90,8	89	87
P2	adsorbtion	90,7	89,5	88
Alg – CH	adsorbtion	99,4	97	95,5
CH-HA	adsorbtion	98,5	97	94
	functionalization	96,7	96	95,5
CH	adsorbtion	99,8	98,2	97
	functionalization	95,2	94	93
M2	adsorbtion	94,3	93	92,5

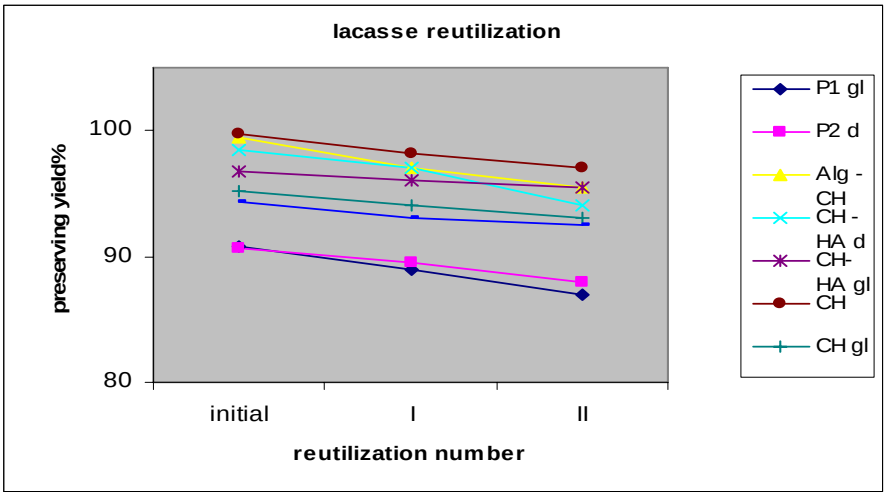

Fig. 6.

By reusing the enzymes was observed that the peroxidase and lacasse preserved in high extent the enzymatic activity, the obtained preservation yields being only by few units lower, for all studied supports.

4. Conclusions

- At immobilization of two oxidoreductase enzymes, *peroxidase* and *laccase* on polymeric supports, generally, high immobilization yields were obtained in range of 64.6 – 99.8%, by both immobilization methods – direct immersion and after functionalization with glutaraldehyde;
- The immobilization yields were higher using *peroxidase* than *laccase* especially after the supports' functionalization;

- At *laccase* immobilization on supports were generally obtained better results after functionalization with glutaraldehyde;
- The films with NPM –M3- generally gave results merely poor to immobilize both studied enzymes and by both methods, too;
- The most suitable supports among those studied by us to immobilize the *peroxidase* and *laccase* generally were those containing chitosan, especially as microparticles;
- The supports immobilized with peroxidase had greater level of preservation the enzimatic activity, when they were reused.

References

[1] SAFARIK I., SAFARIKOVA M., *Magnetic Nanoparticles and Biosciences*, Monatshefte fur Chemie, **133**, pp. 737–759, 2002.
[2] SOLOMON E. I., SUNDARAM U. M., MACHONKIN T. E., Chem Rev., **96**, pp. 2563–2605, 1996.
[3] YAROPOLOV A. I., SKOROBOGAT'KO O. V., VARTANOV S. S., VARFOLOMEYEV S. D., *Laccase. Properties, catalytic mechanism, and applicability*, Appl. Biochem. Biotechnol., **49**, pp. 257–280, 1994.
[4] HU X., ZHAO X., HWANG H.-M., Chemosphere, Volume **66**, Issue 9, pp. 1618–1626, 2007.
[5] MATEESCU M.-A., AGOSTINELLI E., WELTROWSKA G., WELTROWSKI M., MONDOVI B., BioMetals, Vol. **3**, No. 2, June 1990.
[6] FREIRE R. S., DURÁN N., KUBOTA L. T., Talanta**,** Volume **54**, Issue 4, pp. 681–686, 2001.
[7] CHAMPAGNE P.-P., RAMSAY J. A., Applied Microbiology and Biotechnology, Vol. **77**, No 4, pp. 819–823, 2007.
[8] SILVA C., SILVA C. J., ZILLE A., GUEBITZ G. M., CAVACO-PAULO A., Enzyme and Microbial Technology, Volume **41**, Issues 6–7, pp. 867–875, 2007.
[9] JOLIVALT C., BRENON S., CAMINADE E., MOUGIN C., PONTIÉ M., Journal of Membrane Science, Volume **180**, Issue 1, pp. 103–113, 2000.
[10] CRECCHIO C., RUGGIERO P., PIZZIGALLO M. D. R., *Polyphenoloxidases immobilized in organic gels: properties and applications in the detoxification of aromatic compounds*, Biotechnol. Bioeng., **48**, 585–591, 1995.
[11] RIU J., SCHÖNSEE I., BARCELO D., *Determination of sulfonated azo dyes in groundwater and industrial effluents by automated solid-phase extraction followed by capillary electrophoresis/mass spectrometry*, J. Mass Spectrom., **33**, 653–663, 1998.
[12] SETTI L., GIULIANI S., SPINOZZI G., PIFFERI P. G., *Laccase catalyzedoxidative coupling of 3-methyl 2-benzothiazolinone hydrazone and methoxyphenols*, Enzyme Microb. Technol., **25**, 285–289, 1999.
[13] HAGHIGHI B., GORTON L., RUZGAS T., JÖNSSON L. J., *Characterization of graphite electrodes modified with laccase from Trametes versicolor and their use for bioelectrochemical monitoring of phenolic compounds in flow injection analysis*, Anal. Chim. Acta, **487**, p. 314, 2003.
[14] LEECH D., DAIGLE F., *Optimisation of a reagentless laccase electrode for the detection of the inhibitor azide*, Analyst, **123**, 1971–1974, 1998.
[15] GOMES S. A. S. S., NOGUEIRA J. M. F., REBELO M. J. F., *Amperometric biosensor for polyphenolic compounds in red wine*, Biosens. Bioelectron., **20**, 1211–1216, 2004.

[16] ROY J. J., ABRAHAM T. E., ABHIJITH K. S., SUJITH KUMAR P. V., THAKUR M. S., *Biosensor for the determination of phenols based on Cross-Linked Enzyme Crystals (CLEC) of laccase*, Biosens. Bioelectron, **21**, 206–211, 2005.
[17] FRITZ-LANGHALS E., KUNATH B., *Synthesis of aromatic aldehydes by laccase mediator assisted oxidation*, Tetrahedron Lett., **39**, 5955–5956, 1998.
[18] AKTA N, TANYOLAÇ A., *Reaction conditions for laccase catalyzed polymerization of catechol*, Bioresour Technol., **87**, 209–214, 2003.
[19] SCHÄFER A., SPECHT M., HETZHEIM A., FRANCKE W., SCHAUER F., *Synthesis of substituted imidazoles and dimerization products using cells and laccase from Trametes versicolor*, Tetrahedron, **57**, pp. 7693–7699, 2001.
[20] DURANTE D., CASADIO R., MARTELLI L., TASCO G., PORTACCIO M., DE LUCA P. *et al.*, *Isothermal and non-isothermal bioreactors in the detoxification of waste waters polluted by aromatic compounds by means of immobilised laccase from Rhus vernicifera*, J. Mol. Catal. B Enzym., **27**, pp. 191–206, 2004.
[21] EDWARDS W., LEUKES W. D., BEZUIDENHOUT J., *Ultrafiltration of petrochemical industrial wastewater using immobilised manganese peroxidase and laccase: application in the defouling of polysulphone membranes*, J Desalin., **149**, pp. 275–278, 2002.
[22] LUCAS M., DE LA RUBIA T., MARTINEZ J., *Oxidation of low molecular weight aromatic components of olive-mill wastewaters by a Trametes versicolor laccase*, Polyphenols Actual., **23**, pp. 36–37, 2003.
[23] JOLIVALT C., BRENON S., CAMINADE E., MOUGIN C., PONTIÉ M., *Immobilization of laccase from Trametes versicolor on a modified PVDF microfiltration membrane: characterization of the grafted support and application in removing a phenylurea pesticide in wastewater*., J. Membr. Sci., **180**, pp. 103–113, 2000.
[24] YOTOVA L. K., IVANOV I. P., Biotechnology Techniques, Vol. **13**, No. 4, 1999.
[25] LEIRIÃO P. R. S., FONSECA L. J. P., TAIPA M. A., CABRAL J. M. S., MATEUS M., Applied Biochemistry and Biotechnology, Vol. **110**, No. 1, 2003.
[26] BÓDALO A., BASTIDA J., MÁXIMO M. F., MONTIEL M. C., GÓMEZ M., MURCIA M. D., Bioprocess and Biosystems Engineering, 2008.
[27] FENG L., WANG L., HU Z., TIAN Y., XIAN Y., JIN L., Microchimica Acta, March, 2008.
[28] WANG J., GU M., DI J., GAO Y., WU Y., TU Y., Bioprocess and Biosystems Engineering, Vol. **30**, No. 4, 2007.

This volume is promoted by the Commission “Science and Technology of Microsystems” of the Romanian Academy with the technical and financial support of the National Institute in Research and Development in Microtechnologies (IMT−Bucharest, http://www.imt.ro), and by the Romanian Ministry of Education and Research. The volume is part of the “Micro- and Nanoengineering” series (coordinator – Professor Dan Dascălu, member of the Romanian Academy).